Functionalization and Interpenetration in Metal Organic Frameworks (MOFs) for Reversible H_2 Storage

Thesis Submitted to

Academy of Scientific & Innovative Research (AcSIR) for the degree of

Doctor of Philosophy

in

Chemical Sciences

By

Pradip S. Pachfule

(Registration Number: 10CC12J26024)

Research Supervisor

Dr. Rahul Banerjee

Physical and Materials Chemistry Division,
CSIR-National Chemical Laboratory,
Pune-411008

May-2014

CERTIFICATE

This is to certify that the work presented in the thesis entitled "**Functionalization and Interpenetration in Metal Organic Frameworks (MOFs) for Reversible H_2 Storage**" submitted to Academy of Scientific & Innovative Research (AcSIR) by Pradip S. Pachfule, was carried out by the candidate at the CSIR-National Chemical Laboratory Pune, under my supervision. Such materials as obtained from other sources have been duly acknowledged in the thesis.

Dr. Rahul Banerjee, **Date:**

(Research Supervisor),

Physical and Materials Chemistry Division,

CSIR-National Chemical Laboratory,

Pune-411008.

CANDIDATE'S DECLARATION

I hereby declare that the thesis entitled "**Functionalization and Interpenetration in Metal Organic Frameworks (MOFs) for Reversible H_2 Storage**" submitted for the award of degree of ***Doctor of Philosophy*** in Chemical Sciences to Academy of Scientific & Innovative Research (AcSIR). This work has not been submitted by me to any other institution or university. This work was carried out by me at the CSIR-National Chemical Laboratory, Pune, India, under the supervision of Dr. Rahul Banerjee. Such materials as obtained from other sources have been duly acknowledged in the thesis.

Pradip S. Pachfule **Date:**

CSIR-National Chemical Laboratory,

Pune–411 008.

Dedicated to My Loving Family

Acknowledgement

First and foremost, I would like to express my heartfelt and sincere gratitude to my research supervisor ***Dr. Rahul Banerjee****, who introduced me to an interesting world of Crystallography and Metal-Organic Frameworks. Whose motivation, inspiration, encouragement and persistent guidance have leaded me to realise my dream to reality. I am thankful for his patience, motivation, timely advice and the continuous support provided during every stage of my research work.*

I extend my sincere thanks to the Director of CSIR-NCL ***Dr. Sourav Pal****,* ***Dr. Shivram*** *(former Director), Head of Physical and Materials Chemistry Division* ***Dr. Anil Kumar*** *for their kind help and encouragement during the course of this work. I extend my sincere gratitude to all my DAC members* ***Dr. Darbha Srinivas****,* ***Dr. Sayam Sengupt*** *and* ***Dr. Prakash Wadgaonkar*** *and SAO chairman* ***Dr. C. G. Suresh*** *for their timely suggestions and instructions throughout my Ph.D program. I am also very much thankful to* ***Dr. Sreekumar Kurungot*** *and* ***Dr. David Diaz′ Diaz′*** *and their group members for their kind help for characterizations and analyses. I wish to sincerely thanks to* ***Prof. Jianwen Jiang*** *and his lab-members for computational studies. I would like to acknowledge* ***Dr. Kumar Vanka, Prof. Sandeep Verma, Dr. Raju Mondal, Dr. Debajyoti Ghoshal, Dr. Lallan Mishra, Dr. Biju, Dr. D. Srinivasa, Dr. Mrs. Puranik*** *and* ***Dr. Rajesh Gonnade*** *for their suggestions and valuable guidance during the work.*

I would like to offer equally my sincere thanks to Dr. Gurame, Dr. Pujari, Dr. Rajmane, Dr. Jadhav, Dr. Deshmukh, Dr. Ubale, Dr. Basutkar, Dr. Chavan, Dr. Nimkar, Dr. Mahajan, Gawali Madam and Bhore Madam for their valuable suggestions and advice.

I have high regards for my seniors and colleagues who have provided me with unconditional support and help during my Ph D. course. My lab seniors Dr. Subash Sahoo, Dr. Manas Panda, Dr. Jayashri Thote, Dr. Gobinda Das and Dr. Digambar Shinde, who have trained and helped me in lab work, are greatly acknowledged. I would also thank all my colleagues Chandan, Tamas, Arijit, Subhadeep, Tanay. Sharath, Bishnu, Suman, Harshitha and Bikash for their help, support and keeping a constant joyful atmosphere in laboratory.

I would like to thank my seniors Dr. Nagesh Khupse, Dr. Kiran Patil, Dr. Prakash Sane, Deepak Jadhav, Ankush Bhise, Dhanraj Shinde, Mangesh Mahajan and Pankaj Dharamwar. I would like to specially thank Chinmay, Shekhar, Digambar, Vishal and Kiran for their constant help, suggestions and for unconditional support during thick and thin. I also thank my beloved friends Vinayak, Majid, Atul, Bhausaheb, Dnyaneshwar, Nagesh, Manik, Satej, Soma, Nitin, Sam, Yashawant, Master, Pravin, Ramu, Sandip, Narayan, Dr. Amol, Rupesh, Sachin, Vijay, Gajanan, Amol, Datta, Anil, Siddhu, Raja Das and Swapnil for their individual

support and encouragement during my carrier. Also my thanks to the friends from NCL and outside Rajashree, Sayali, Bharati, Bhagya, Aashwini, Deepti, Vrushali, Bhavana, Beena, Rupali, Rasika, Nisha, Neha, Smita, Sneha and Prajitha for their constant help and support.

I greatly acknowledge my loving brother ***Sudhir,*** *Sister in Law* ***Sarita****, nephew* ***Kartik*** *and niece* ***Vaishnavi*** *for encouraging me both spiritually and scientifically, without whose support my ambition can hardly be realized. I would also like to thank borther in law Mr. Santosh, Mr. Namdev, and my sister Sandhyatai, Vidyatai for their love, kindness and support. I thank my all family members and my better half Shital for their constant love and motivation. I specially thank Sister in Law Vaishali and Lovely Apurva for making the cheerful environment around me.*

I would like to thank my loving parents ***Shashikant*** *and* ***Mangal*** *for giving unconditional love, constant support and encouragement without their support I never would have been able to achieve my goals. My sincere gratitude to my Grandfather* ***Sahebrao****and grandmother* ***Chandrabhaga****, for their love and care.*

My greatest regards to the Almighty for bestowing upon me the courage to face the complexities of life and complete this dissertation successfully and for inculcating in me the dedication and discipline.

I offer my sincere regards to people, teachers who have inspired me directly or indirectly in research carrier.

I am grateful to CSIR, New Delhi, for awarding the research fellowship and Dr. Pal, Director, and Dr. Shivram, former director, CSIR-National Chemical Laboratory to carry out my research works, extending all infrastructural facilities and to submit this work in the form of a thesis for the award of Ph. D degree. I am also thankful to Academy of Scientific & Innovative Research (AcSIR) for giving me a chance to complete one the dream in my life.

– Pradip S. Pachfule

Contents

Abstract

Abstract

The thesis entitled **"Functionalization and Interpenetration in Metal Organic Frameworks (MOFs) for Reversible H_2 Storage"** has been divided into six chapters.

Chapter 1: Introduction to Metal Organic Frameworks (MOFs) and Hydrogen (H_2) Storage

Chapter 2: Fluorinated Metal Organic Frameworks (*F*-MOFs) for Enhanced Hydrogen (H_2) Uptake

Chapter 3: Effect of Fluorination on Hydrogen (H_2) Adsorption in Copper-Tetrazolate Based Metal Organic Frameworks (MOFs)

Chapter 4: Functionalized Interpenetrated Metal Organic Frameworks (MOFs) for Reversible Hydrogen (H_2) Uptake

Chapter 5: Carbon Nanofiber-Metal Organic Framework (CNF-MOF) Hybrids for Enhanced Hydrogen (H_2) Uptake

Chapter 6: Conclusions and Future Prospects

Chapter 1: **Introduction to Metal Organic Frameworks (MOFs) and Hydrogen (H_2) Storage**

Recent years have witnessed a huge level of research on the synthesis of porous functional materials named Metal Organic Frameworks (MOFs), using diverse organic spacers with different metals. One of the major reasons for MOF research is the expectation of achieving the U.S. Department of Energy (DoE) targets on H_2 storage for on-board and vehicular applications. Although carbon nanotubes, zeolites, activated

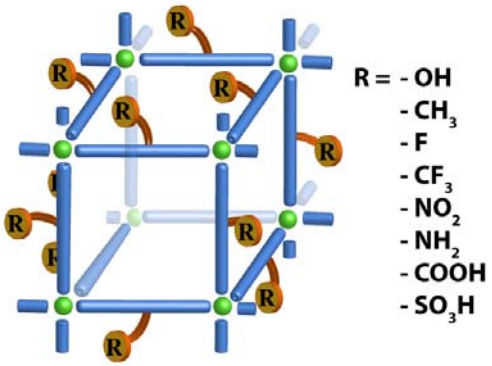

Figure 1. Cartoon representation of Functionalized Metal Organic Frameworks.

carbon, and metal hydrides have been extensively studied and potentially applied in several ways for H_2 storage, still there are limitations for using these materials as they are expensive, shows strong interaction with adsorbents, problems in regeneration of adsorbents, etc. MOFs on the other hand have shown promise over these materials because of their fascinating structures, exceptionally high surface areas, uniform yet tunable pore sizes, and well defined adsorbate-MOF interaction sites. Various strategies such as extending pore sizes comparable to the adsorbed molecules, increasing surface area and pore volume, utilizing catenation and creation of open metal sites have been explored, to achieve the DoE target for H_2 storage. Similarly, insertion of functionalized links holding functional groups like –F, $–NH_2$, –OH, –COOH, etc. on the organic spacer has also been proven to have a good impact on enhancing the H_2 and CO_2 gas adsorption properties. The improved interaction between the gaseous molecule and the functionalized framework brings hydrogen molecule in close proximity with several aromatic rings to improve the H_2 uptake capacities of MOFs *via* increased adsorption enthalpy.

In similar attempts for improving H_2 uptake in MOFs, the considerable attention has been given towards the synthesis of interpenetrated/catenated MOFs. Framework interpenetration, by which the pores of one framework are inter-grown by one or more independent frameworks, is a commonly observed phenomenon in MOFs. It was believed

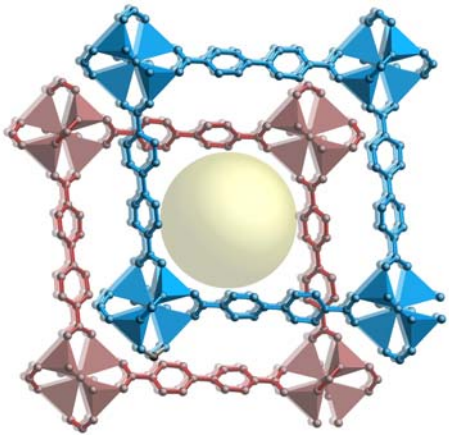

Figure 2. Representation of interpenetrated Metal Organic Framework.

that favorable interactions exist between aromatic rings of MOFs and hydrogen molecules. Since, microporous interpenetrated MOFs would be ideal candidates for the sorption of small gaseous molecules, interpenetration can be utilized to strengthen the interaction between the gaseous molecule and the framework by an entrapment mechanism, in which hydrogen molecules remains in close proximity with several aromatic rings from interpenetrating networks.

In these regards, looking towards the H_2 storage materials; functionalized and interpenetrated MOFs could become a best choice as MOFs adsorbs gas molecules reversibly in an efficient manner. Compared to traditional zeolites and porous carbon materials, MOFs have very high number of pores and surface area, which allow higher hydrogen uptake in a given volume. The stored high amount of H_2 stored in these materials can be utilized as a fuel in Fuel Cells for the generation of energy with zero emission.

Chapter 2: Fluorinated Metal Organic Frameworks (*F*-MOFs) for Enhanced Hydrogen (H_2) Uptake

The H_2 storage capacity in MOFs can be enhanced in various ways, such as introducing open metal sites, increasing surface area and pore volume, functionalizing organic linkers, and utilizing catenation. Yang et al., in this regard, have explored for the first time the possibility of synthesizing Fluorinated Metal Organic Frameworks (*F*-MOFs) using perfluorinated polycarboxylate ligands with porous surfaces and exposed fluorine atoms for interesting H_2 storage properties. Later, Cheetham and co-workers and others also explored the interesting H_2 and CO_2 storage properties in partially fluorinated MOFs or mixed perfluorinated and nonfluorinated ligands. In all these reports researchers have agreed that MOFs with fluoro-lined or fluoro-coated channels are expected to possess enhanced affinity and selectivity toward gas adsorption compared to their non-fluorinated counterparts due to semi-ionic nature of C–F bonds.

In most of the synthetic attempts for fluorinated MOFs from fluorinated dicarboxylates, insertion of a co-ligands such as 4,4′-bipyridine's and 1,10-phenanthroline have wider applications in MOF synthesis; because of their ability to bridge multiple metal sites and their facile derivatization to provide bridging ligands with additional functionality. In these regards, in our synthetic attempts towards

partially fluorinated MOFs, using 4,4'-hexafluoroisopropylidine bis-benzoic acid and different co-ligands like 1,10–phenanthroline and 3-methyl pyridine several *F*-MOFs has been synthesized. The successfully isolated partially fluorinated MOFs like *F*-MOF-4, Cu-FMOF-4B, Zn-*F*-MOF-4B, *F*-MOF-6, Co-HFMOF-D, Co-HFMOF-W, Mn-HFMOF-D, Mn-HFMOF-W has been used for H_2 adsorption. These *F*-MOFs show H_2 uptake ranging from 0.45 wt% to 0.90 wt% depending upon the available porosity. Although H_2 adsorptions for these *F*-MOFs are moderate, they still are comparable with the H_2 adsorption of the highest capacity zeolites, some carbon materials, and some other HF-MOFs reported in the literature.

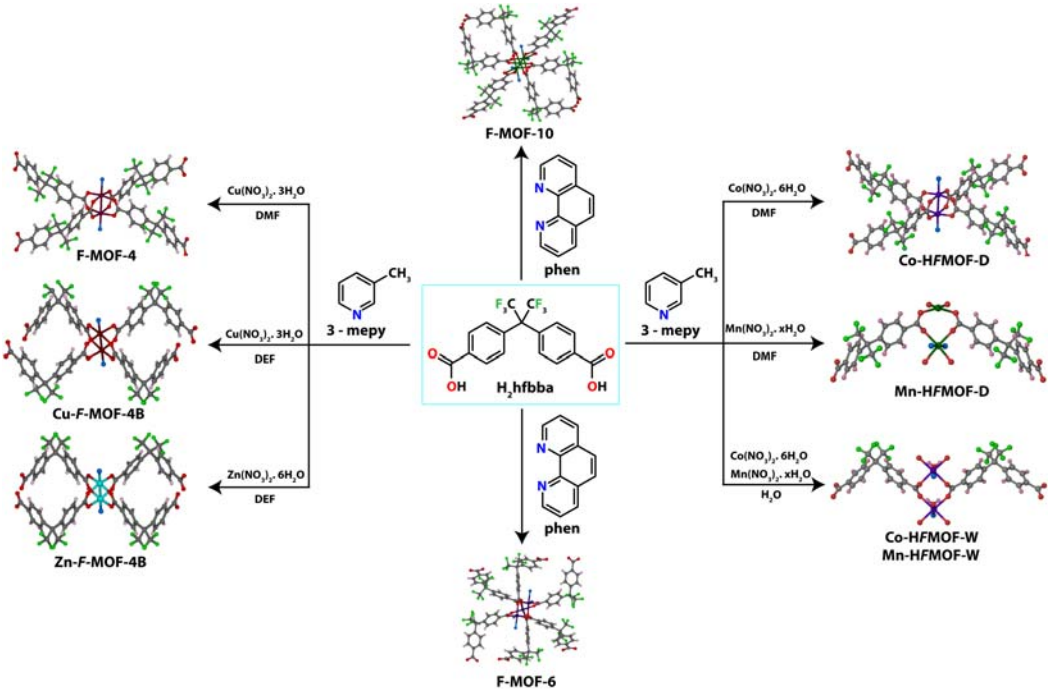

Figure 3. Synthesis of *F*-MOFs using 4,4′-hexafluoroisopropylidine bis-benzoic acid and different co-ligands like 1, 10–phenanthroline and 3-methyl pyridine.

Further, using a set of isostructural fluorinated and non-fluorinated MOFs, the effect of fluorine insertion on H_2 adsorption has been studied. The effect of partial introduction of fluorine atoms into the framework on the H_2 uptake properties of MOFs having similar structures has been analyzed experimentally and computationally in isostructural MOFs. Comparison of the H_2 and CO_2 adsorption in these isostructural fluorinated and non-fluorinated MOFs shows that high H_2 uptake in *F*-MOFs is not a

universal phenomenon, but is rather system-specific and differs from system to system.

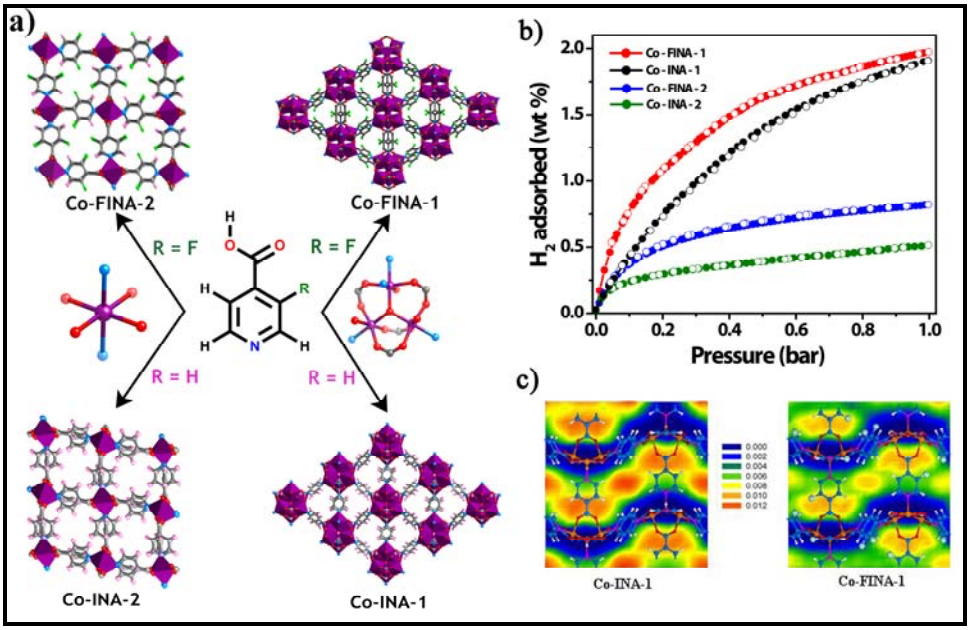

Figure 4. a) Synthesis of 2 set of isostructural fluorinated and non-fluorinated MOFs using isonicotinic acid and 3-fluoro isonicotinic acid based linkers with Co(II) as metal centers. b) H_2 adsorption isotherms in these MOFs. c) H_2 adsorption density counters observed computationally in Co-INA-1 and Co-FINA-1.

In the isostructural Co-INA-1 and Co-FINA-1, fluorination resulted in a similar H_2 uptake, whereas in Co-INA-2 and Co-FINA-2, fluorination resulted in an overall increase in H_2 uptake. From these results, it is clear that as fluorine atoms in F-MOFs are weakly interacting with gas molecules, other factors, such as pore size, curvature, and open metal sites, can also play crucial roles in the high gas uptakes in these F-MOFs.

Chapter 3: Effect of Fluorination on Hydrogen (H_2) Adsorption in Copper-Tetrazolate Based Metal Organic Frameworks (MOFs)

It is well documented in the literature that functionalized links having un-coordinated functional groups such as –F, $–NH_2$, –OH, –COOH, etc. on the organic spacer can also enhance the H_2 and CO_2 gas adsorption properties by increasing ligand-to-gas molecule interactions and adsorption enthalpy (Q_{st}) in MOFs. Theoretically, it is expected that fluorinated MOFs with exposed fluorine atoms into the pores should possess

significantly higher adsorption enthalpy for H_2 at near ambient temperatures due to strong interaction arising from the semi-ionic nature of the C−F bonds and adsorbing H_2 molecules. But, in practical aspects; particularly in the case of MOFs, the increasing van der Waals radii of fluorine atoms (1.47 Å) compared to the hydrogen (1.20 Å) need to be taken into consideration, as the slight changes in the pore sizes of these MOFs may result into the big difference in the adsorption capacities. In these regards, considering all the issues related towards advantages or disadvantages of fluorination for the improved H_2 uptake, at this status it is difficult to quote on the entire topic.

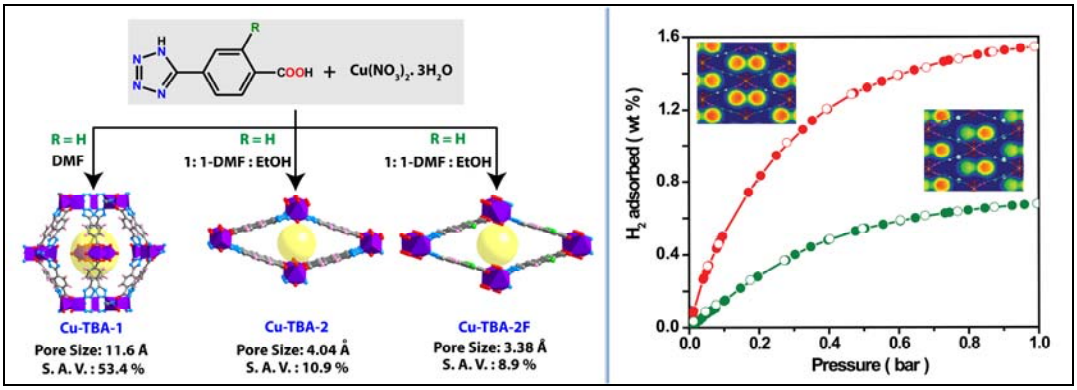

Figure 5. a) Synthesis of Cu-TBA-1, Cu-TBA-2 and Cu-TBA-2F using 4-(1H-tetrazole-5-yl)benzoic acid and 2-fluoro-4-(1H-tetrazole-5-yl)benzoic acid linkers. b) H_2 adsorption isotherms in Cu-TBA-2 and Cu-TBA-2F with H_2 adsorption density counters observed computationally.

In order to facilitate the studies regarding the effect of fluorination on H_2 uptake in MOFs, gas adsorption properties of three new MOFs named Cu-TBA-1, Cu-TBA-2 and Cu-TBA-2F has been reported in these studies. The phenomenon of structural isomerism has been observed in the Cu-TBA-1 and Cu-TBA-2 upon changing metal source during synthesis, whereas isostructural Cu-TBA-2 and Cu-TBA-2F has been achieved by changing the linker from 4-tetrazole benzoic acid (TBA) to 2-fluoro-4-tetrazole benzoic acid (2-F-4-TBA). By utilizing the structural similarities present in Cu-TBA-2 and Cu-TBA-2F, the effect of selectively introducing fluorine atoms into the MOFs for hydrogen uptake properties has been analyzed. In these studies, we have observed that Cu-TBA-1 and -2 adsorbs 1.16 and, 1.54 wt% of H_2, while Cu-TBA-2F adsorbs 0.67 wt% at 77 K and 1 atm. The direct comparison between iso-structural

partially fluorinated Cu-TBA-2F and non-fluorinated Cu-TBA-2 suggested that the enhancement of H_2 adsorption due to fluorination in MOFs is not an universal phenomenon, but it is rather system specific and can differ from system to system. The density distributions of adsorbed H_2 molecules in Cu-TBA-2 and -2F from simulation suggest that H_2 molecules are primarily adsorbed in the pores along the X-axis and the binding sites are mostly located in the pore centers. Based on the simulation, protruding fluorine atoms from 2-F-4-TBA appear to cause a steric hindrance and a lower adsorption for H_2. Nevertheless, thorough research work is necessary on H_2 adsorption on iso-structural fluorinated/nonfluorinated MOFs before we can conclusively indicate a positive/negative effect of fluorination on enhancement of H_2 adsorption in MOFs.

Chapter 4: Functionalized Interpenetrated Metal Organic Frameworks (MOFs) for Reversible Hydrogen (H_2) Uptake

MOFs possessing large sized pores are ultimately disadvantageous to H_2 storage, because H_2 molecules near the center of the pore are unlikely to experience any attraction from the potential surface of the pore walls. In these regards, the prominent way to reduce the number of large voids and increase framework-adsorbate interaction in a given structure is feasibly framework interpenetration. In principle, one should expect that the surface area for an interpenetrated framework will be reduced relative to its non-interpenetrated analogue, owing to the framework–framework interactions that should

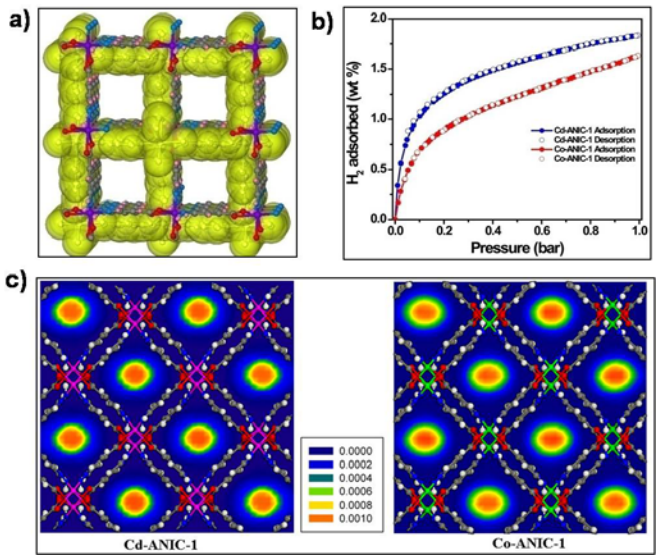

Figure 6. a) Interpenetrated crystal structure of isostructural Cd-ANIC-1 or Co-ANIC-1 MOFs. b) H_2 adsorption isotherms at 77 K and 1 atm pressure. c) Hydrogen adsorption density counters for Cd-ANIC-1 and Co-ANIC-1 MOFs.

arise upon desolvation, but catenation has shown some improvement in H_2 uptake in some MOF systems at 77 K and lower pressure region. Although, it is clear that the H_2 uptake at high pressure will be surely less due to the reduced pore volume; interpenetrated MOFs has been getting attention due to its low pressure region H_2 uptake with improved adsorption enthalpy.

In these regards, in continuation with the synthesis of functionalized MOFs for improved H_2 uptake, we have isolated a pair of partially interpenetrated amino functionalized MOFs holding diamondoid topology. Two isostructural, three dimensional, interpenetrated, amino functionalized MOFs, Cd-ANIC-1 and Co-ANIC-1 with amine-lined pores have shown high H_2 (77 K) uptake due to the framework interpenetration. The effect of interpenetration and amino functionalization on H_2 uptake properties of MOFs has been analyzed experimentally and computationally, in these isostructural MOFs. The adsorptions of H_2 in Cd-ANIC-1 and Co-ANIC-1 have also been validated by simulations, which show good agreement with experimental data. Collectively, these results points towards the discovery of new materials with amino functionalized interpenetrated frameworks synthesized from a simple isonicotinic acid derived link for high H_2 adsorption capacities.

Chapter 5: Carbon Nanofiber-Metal Organic Framework (CNF-MOF) Hybrids for Enhanced Hydrogen (H_2) Uptake

Hybrid materials design has emerged as the most modish research topics in recent years as it often results in new or modified properties than that of individual counterparts. Research on MOFs as well as carbon nanomorphologies like carbon nanotubes (CNTs), graphene (GE) and carbon nanofibers (CNFs) has picked up attention due to variety of applications like gas storage, sensing, drug delivery, catalysis etc. MOFs and nanocarbon morphologies so far have been well exploited in the literature separately. Despite the recent progresses in the construction of novel MOF-nanocarbon hybrid structures through different strategies and the improvement in the sorption capabilities of such hybrids, the nature of interaction between the MOF and nanocarbon components still possesses a limitation to the versatile exploration of such hybrids. The lack of proper chemical interactions among the indivisual counterparts of hybrid materials brings the limitations for their usages.

In these regards, we have performed synthesis of a Zn-terephthalate MOF-CNF hybrid by an in-situ [MOF@CNF] approach. By rationally tailoring the experimental parameters, we have achieved the selective one-dimensional confinement of highly crystalline and nanosized MOFs in inner cavity and in inner cavity as well as on the outer walls of CNF. A new strategy for the well ordered assembly of an otherwise thermodynamically less stable MOF in the inner cavity as well as on the outer wall of a CNF template has been reported for the first time. The synthesized hybrid material MOF-2@FCNF shows improved thermal stability as well as gas uptake over FCNF and MOF-2. At 1 atm pressure and 77 K, FCNF and MOF-2 adsorb 0.27 and 0.63 wt% H_2, while MOF@FCNF shows adsorption of 0.84 wt% of H_2. The significant increase of ~30 % in the H_2 uptake properties can be attributed to the modulated property characteristics of the hybrid material. The stabilization of the thermodynamically less stable variety of the MOF observed in this study may pave the way for future applications of these materials in unforeseen fields.

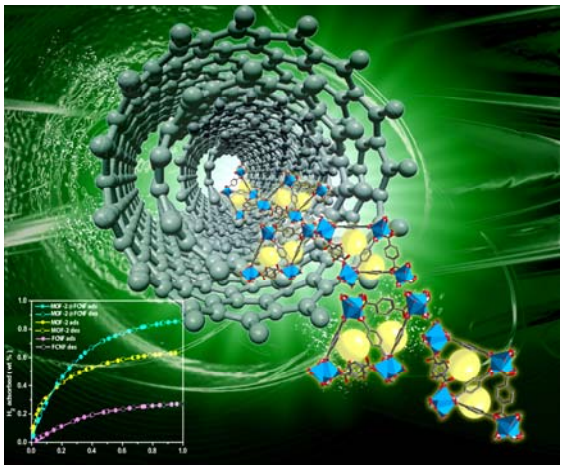

Figure 7. Cartoon representation MOF-2@CNF hybrids synthesized by in-situ approach.

Chapter 6: Conclusions and Future Prospects

This last chapter deals with the significant conclusions of the present study along with some of the emerging trends of these fascinating MOF materials as follows:

1. The intriguing structural aspects in addition to their high surface area's and pore volumes, makes MOFs suitable candidate for H_2 adsorption over literature reported materials like porous carbons, metal hydrides, zeolites, porous silica materials, etc.

2. The attempts followed for improvement in H_2 uptake capacities in MOFs includes increasing pore size, pore volume and surface area, creation of open metal sites, MOF functionalization, interpenetration or catenation, doping of metal nanoparticles, etc.

3. The *F*-MOF synthesized using a flexible fluorinated dicarboxylates building block

4,4′-hexafluoroisopropilidine bis-benzoic acid; 3-methyl pyridine/1,10-phenanthroline co-ligands, and different transition metal cations [Zn(II), Co(II), Mn(II) and Cu(II)] show moderate H_2 uptake despite of its very limited or negligible surface area.

4. The attempts towards synthesis of highly robust and porous MOFs using isonicotinic acid and 3-fluoro isonicotinic acid for high H_2 uptake proved to be rewarding to increase the overall H_2 uptake. From these results, it is clear that as fluorine atoms in *F*-MOFs are weakly interacting with gas molecules, other factors, such as pore size, curvature, and open metal sites, can also play crucial roles in the gas uptakes in these *F*-MOFs.

5. Using isostructural Cu-TBA-2 and Cu-TBA-2F MOFs, the effect fluorine insertion on H_2 uptake properties utilizing the experimental and computational results has been analyzed. The direct comparison between gas adsorption properties of iso-structural partially fluorinated Cu-TBA-2F and non-fluorinated Cu-TBA-2 suggested that enhancement of H_2 adsorption due to fluorination in MOFs is not an universal phenomenon, but it is rather system specific and can differ from system to system.

6. The interpenetrated, porous, functionalized Cd-ANIC-1 and Co-ANIC-1 MOFs with diamondoid topology showed high H_2 uptake as a result of interpenetration in the frameworks, which was further validated by simulation studies.

7. The selective one-dimensional confinement of highly crystalline and nanosized MOFs in inner cavity and in inner cavity as well as on the outer walls of CNF has been demonstrated. The hybrid material shows improved thermal stability as well as gas uptake over FCNF and MOF-2. The overall increase in the gas uptake properties of MOF-2@FCNF hybrid can be attributed to the modulated property characteristics of the hybrid material *via* gas diffusion.

Lastly, related promising developments and daunting challenges in this broad area are also discussed to extend the applications of functionalized and interpenetrated MOFs in view of the fundamental and technological interests ostensibly shown by a large number of interdisciplinary researchers encompassing physicists, chemists, biologists and engineers. Finally, some of the future prospects and precautions for the synthesis and applications of MOFs will be explained within the broad perspective of storage materials and its societal impact.

Chapter 1

Introduction to Metal Organic Frameworks (MOFs) and Hydrogen (H_2) Storage

1.1 Introduction:

Due to the limited resources of fossil fuels, a large part of ongoing research is going on for the development of alternative energy sources which are equally economical and more sustainable.[1] Also, the unlimited use of these fossil fuels is adversely affecting on the environmental conditions due to the pollutants emitted during use. These pollutants are causing various effects like adverse negative health effects, climate change, resource depletion and energy security concerns.[2] The continuous emission of these gases in large amount causes the environmental issues like global warming, causing the average surface temperature of the Earth to rise in response.[2b] In these regards, a necessity of renewable energy sources which are enormously available in nature is preferable. The natural resources like solar light, wind, biomass, nuclear and atomic fusion reactions are the available energy forms, which may lead towards the clean and highly rationalized energetic assets.[3] The high efficiency, easy availability and economical energy resources which emit minimum pollutants during the combustion/usage are the real time need for the energy aspects.[4] Although, solar and winds are reported as the clean and renewable energy sources, these resources hold flowing limitations:[5]

a. Solar energy can only be harnessed when it is daytime and sunny.

b. Large areas of land are required to capture the solar energy. Collectors are usually arranged together especially when electricity is to be produced and used in the same location.

c. Solar panels and wind turbines need to become cheaper than raw fossil fuels. This is the challenge posed by the diffuse nature of renewables.

d. Storage solutions need to become cheaper than fossil fuel refineries (e.g. power plants). This is the challenge posed by the intermittent nature of renewables.

Due to aforementioned reasons, there is an immense need of the energy sources, which will overcome these efficiency issues and can serve as a better option in near

future. Although not yet widely used as transportation fuel, an increase in research and development by both government and industry is working toward successful, and eventually commonplace, use of clean, economical, and safe production of hydrogen (H_2) as well as the greater availability of hydrogen fuel cell vehicles.[6] A big part of that excitement is that H_2 is a potentially emissions-free renewable fuel that can be produced not from foreign-sourced petroleum, but from domestic resources right here at home.[6c] The abundant supplies and high energy density possessed by H_2 holds the great promise for energy carrier for a future energy economy. The basic advantage of H_2 which can release energy cleanly without harmful emissions, which make it particularly attractive when considering the drivers for change as outlined above.[7] Furthermore, the increase in energy generation from renewable sources requires forms of energy storage as production fluctuates hugely with solar, wind and tidal activity. The energy stored in H_2 can later be released through electrochemical fuel cells that recombine hydrogen with oxygen, with no emissions of harmful gases.

1.2 Hydrogen Storage Materials and Challenges:

The storage of H_2 is one of these primary challenges to its successful implementation in an alternative energy economy that includes both mobile and static applications. Although, hydrogen has an excellent gravimetric energy density of around 120 MJ/kg, the volumetric energy density is considerably poorer in comparison to current fuels (e.g. 1 kg of H_2 occupying 11 m^3 at STP).[8] Consequently, a technique by which H_2 molecules can be packed more closely is needed (physisorption) rather than storing it by applying methods like compression, liquid storage, solid state storage, chemisorption, etc.[9] In order to achieve the current target set by the U. S. Department of Energy (DoE) for a vehicular hydrogen storage system, the ideal H_2 storage method has a good gravimetric density and volumetric density, equilibrium properties near ambient temperature and pressure, is reversible over many cycles, has fast transfer rate and is stable in air.[10] Further considerations are costs, recycling and charging infrastructures. Since, transport applications are often the most stringent as they require both high gravimetric and volumetric energy densities, the physisorption method has been put forward as one of the best way to store H_2 for those mentioned applications.

Porous materials like amorphous carbons, charcoals, metal hydrides, clathrates,

microporous polymers, zeolites, etc. have been used into the application of H_2 storage (*Figure 1.1*).[11] But these aforementioned materials are currently finding limited applications due to their very narrow possibilities for synthetic expansion. Structural resolution of amorphous carbons remains a problem due to a lack of long-range order, and building blocks for zeolite synthesis remain limited. Metal hydrides and clathrates mostly follow the chemisorption for H_2 storage than that of physisorption, showing the unsuitability for practical applications.[12] Also, the tedious and costly protocols for the synthesis find the further limitations for their usages in H_2 storage. As these amorphous materials lacks periodicity, large voids, and systematic adsorption sites, H_2 adsorption is unfeasible in these materials.

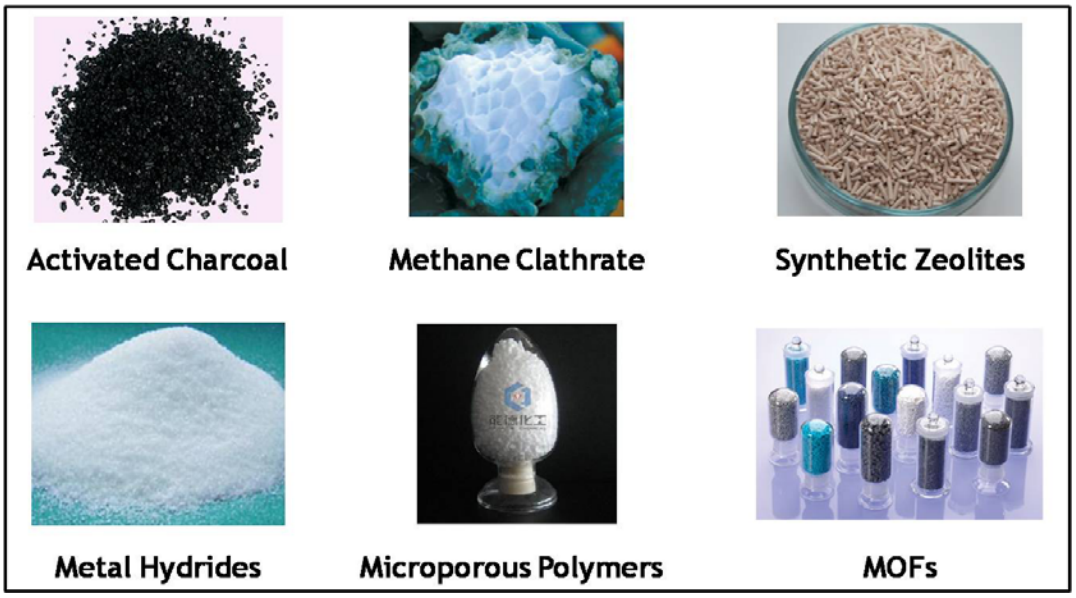

Figure 1.1 Representative literature reported porous materials used for H_2 adsorption and storage. [Source: Website and Wikipedia].

In this regards, a class crystalline and porous materials, MOFs, do not suffer from these limitations. Since, there is a wide array of organic units and metal centers that can be incorporated into MOFs, an incredibly diverse range of materials can be synthesized.[13] As these materials do not endure from the limitations of other porous materials in the expansion of the class, reversible adsorption and cost effectiveness, MOFs are considered as one of the prime material for H_2 storage. MOFs are considered as a good candidate for H_2 uptake, since these materials hold following advantages:

a. Commercial availability and easy synthesis.

b. Considerable stability at diverse applicative conditions.

c. Since, the metal-carboxylate and metal-hetero atoms (N, O, S, etc.) bonds formation is reversible; the formation of well-ordered crystalline MOFs with high porosity is visual.

d. Extremely large surface-areas and flexibility structures.

e. Robust architecture with high mechanical and thermal stabilities.

f. The ability to vary the size and nature of MOF structures without changing underlying topology gave rise to the isoreticular principle and its application in making MOFs with the large pore aperture and low density, which allows the selective inclusion of large molecules like vitamin, proteins as well tiny gas molecules.

g. The thermal and chemical stability of many MOFs has made them amenable to postsynthetic covalent organic and metal-complex functionalization. These capabilities enable substantial enhancement of gas storage in MOFs and have led to their extensive study in the catalysis of organic reactions, activation of small molecules, gas separation, biomedical imaging and proton, electron and ion conduction.

h. By expanding the length of the organic units, isoreticular expansion, pore size and surface area can be enhanced. Isoreticular modification and expansion can be applied to any MOF, and therefore this area has seen rapid expansion in recent years. Furthermore, unlike the case of amorphous carbons, the structure determination is possible for these frameworks due to the crystallinity that arises from the regular order of the MOF backbone.

i. As MOFs are crystalline materials with well ordered periodicity within the structure, the characterization is easy and rapid.

Due to aforementioned extraordinary properties of the MOFs over other materials, these materials are being repeatedly used for several applications including H_2 storage.

1.3 Synthesis of MOFs Materials for Hydrogen Storage:

Metal Organic Frameworks (MOFs) or Porous Coordination Polymers (PCPs) are organic-inorganic hybrids consisting of metal ions or clusters coordinated to rigid organic molecules to form one-, two-, or three-dimensional structures (*Figure*

1.2).[14] MOFs are composed of two major components: a metal ion or cluster of metal ions and an organic molecule called a linker. Usually metal ions or clusters include most of the metals from periodic table. The linkers involves organic components made up from aromatic, non-aromatic, aliphatic and coordinating carboxylate, imidazolate, triazolates, tetrazolate, pyridine based linkers, amino acids and its derivatives, etc.[15]

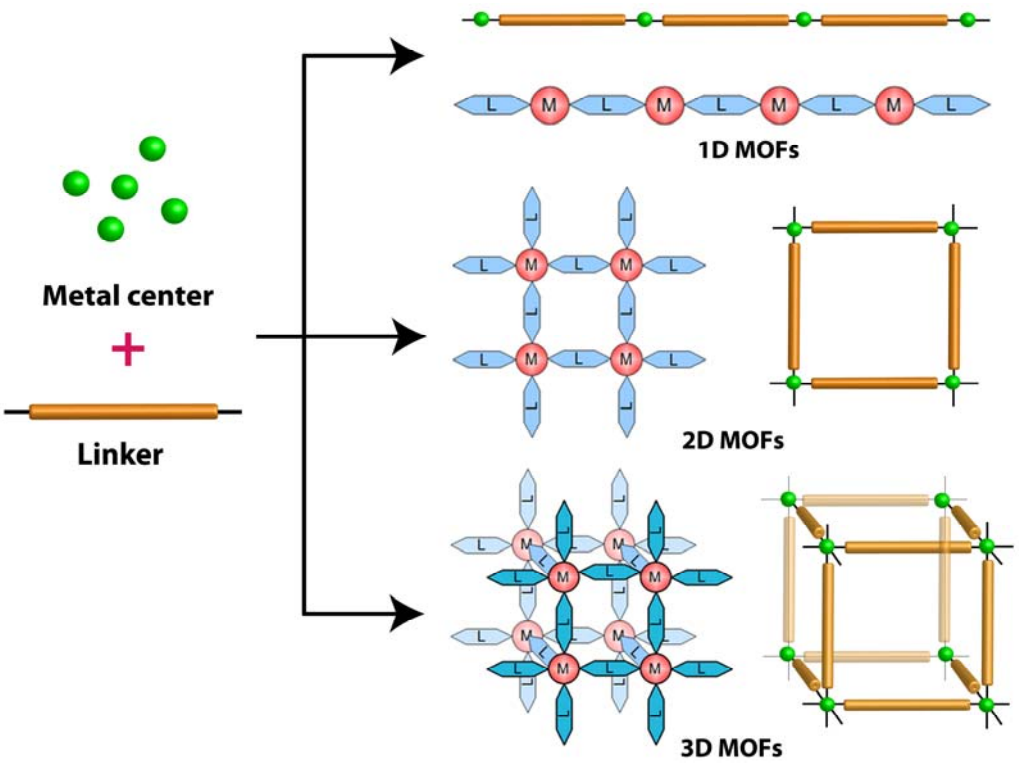

Figure 1.2 Scheme of synthesis of MOFs from metal centers and organic linkers to form 1D, 2D or 3D MOFs depending on degree of extension.

MOFs are crystalline materials and these materials need a crystal growth technique in order to produce a suitable crystal for X-ray diffraction analysis. Generally, the favoured methods for synthesis of crystalline MOFs are as follows:[16a]

1.3.1 Hydrothermal Synthesis:

Hydrothermal synthesis includes the crystallization of substances from high-temperature at high vapour pressures generated due to solvent of synthesis.[16b] The technique is typically employed in high temperature range and particularly below 200 ºC for aqueous and organic solvent systems using Teflon lined autoclave under autogenous pressure (*Figure 1.3*). Under these conditions, the solvent temperature can be increased above its

atmospheric pressure boiling point, while the solvent viscosity and dielectric constant of the solvent are reduced. Reduction of viscosity and dielectric constant also enhances the diffusion process and subsequently crystal growth.

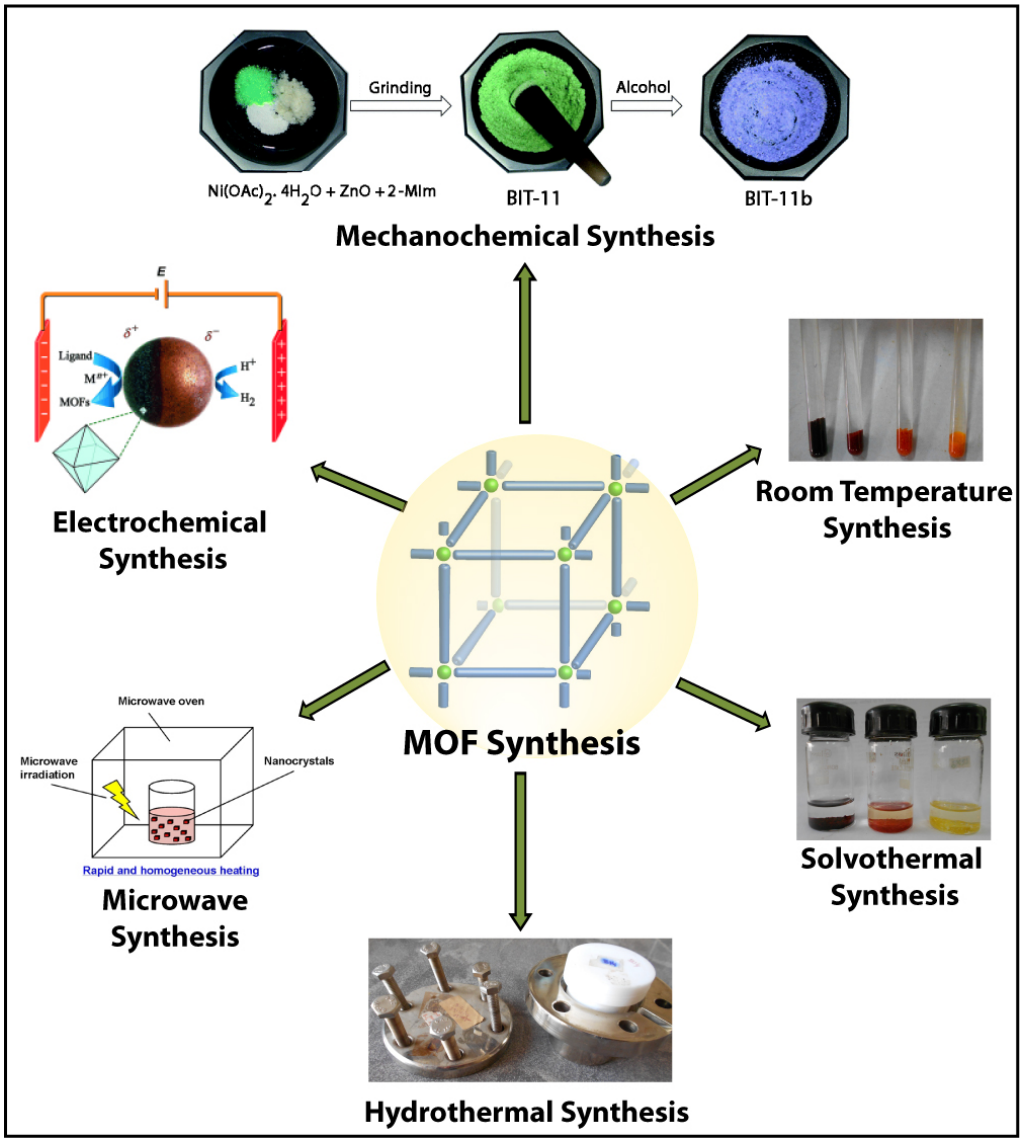

Figure 1.3 Various representative techniques utilized for the synthesis of MOFs from metal centers and organic linkers in suitable solvent media. [Source: Web and Wikipedia].

1.3.2 Solvothermal Synthesis:

Solvothermal synthesis is a method of producing crystalline MOFs, very similar to the hydrothermal route.[16c] The solvothermal synthesis route gains the benefit of both the sol-gel and hydrothermal routes, allowing the precise control over the size, shape

distribution, and crystallinity of MOFs by varying experimental parameters like reaction temperature and time, solvent type, surfactant type, precursor type, etc. (*Figure 1.3*).

1.3.3 Room Temperature Synthesis:

It is a distinct type of solvothermal synthesis, where the heating to the reaction mixture is not necessary to produce highly crystalline MOFs.[16d] Most prominently; the starting materials are mixed in solvent at ambient temperature and kept at room temperature for crystallization. Subsequent addition of bases like triethylamine, which causes deprotonation of the organic linker to precipitate the MOF are used during synthesis (*Figure 1.3*).

1.3.4 Microwave Assisted Synthesis:

Microwave-assisted synthesis relies on the interaction of electromagnetic waves with mobile electric charges.[16e] These can be polar solvent molecules/ions in a solution or electrons/ions in a solid. By applying the appropriate frequency, collision between the molecules will take place, which leads to an increase in kinetic energy, i.e. temperature, of the system. Due to the direct interaction of the radiation with the solution/reactants; MW-assisted heating presents a very energy efficient method of heating (*Figure 1.3)*.

1.3.5 Mechanochemical Synthesis:

Mechanical force can induce many physical phenomena (mechano-physics) as well as chemical reactions in presence of solvents.[16f] In mechanochemical synthesis, the mechanical breakage of intramolecular bonds followed by a chemical transformation takes place. Treatment of the starting materials for 2–10 min in a steel reactor containing a steel ball or mortar and pestle leads to a highly crystalline and single-phase product of MOFs with guest molecules in the pores (*Figure 1.3*). These can be removed by thermal activation to yield the guest-free porous compound.

1.3.6 Electrochemical Synthesis:

The electrochemical synthesis of MOFs was followed in order to prohibit the entry of anions like nitrate, perchlorate or halides during the syntheses, which are of concern to large-scale production processes (*Figure 1.3)*.[16g] The large scale synthesis of MOFs using metal precursors and linkers can be achieved following electrochemical synthesis. The highly crystalline and pure products are anticipated during this synthetic procedure.

1.4 Applications of MOFs:

Porous materials find their applications in gas storage, gas/vapor adsorption and separation, shape/size-selective catalysis, drug delivery, etc.[13] Conventionally, porous materials have been either organic or inorganic materials with available porosity. Most commonly used organic porous material is activated carbon, which is usually prepared by pyrolysis of carbon-rich materials and have high surface areas, high adsorption capacities, yet do not possess ordered structures.[17] Despite this lack of periodicity, porous carbon materials have many uses, including the separation and storage of gases, the purification of water, and solvent removal and recovery. Also, inorganic porous frameworks like zeolites possess highly ordered structures, which require an inorganic or organic template with strong interactions between the inorganic framework and the template during the synthesis.[11h,11i] The removal of the template from these materials can result in collapse of the framework. Although, inorganic frameworks suffer from a lack of diversity, as the variation of elements used seldom deviates from Al, Si and chalcogens; these materials have been used in separation and catalysis applications.

In order to take advantage of the properties of both organic and inorganic porous materials, porous hybrids, known as MOFs, can be generated that are both stable and ordered and possess high surface areas. MOFs are essentially coordination polymers formed in the most elementary sense by connecting together metal ions with polytopic organic linkers often resulting in fascinating structural topologies.[18] These materials have attracted a great deal of attention in the past decade due to its fascinating applications in gas storage, gas/vapor separation, size/shape/enantio-selective catalysis, luminescent and fluorescent materials, and drug delivery, etc (*Figure 1.4*).[14] Since, MOFs have following structural attractiveness; these materials have been successfully utilized for various applications:

a. Structural diversity due to possibility of synthesis of various MOFs by combining a range of metal centers and organic linkers. The ability to tune the framework architectures and properties in MOFs via the ligand and the metal ion provides a significant advantage over the zeolites because essentially an infinite number of variations are possible with predictable structures.

b. Easy synthesis and scale up following various strategies like room temperature

synthesis, electrochemical synthesis, etc is possible.

c. High porosity, tunable pore sizes, easy incorporation of functional groups is possible in MOFs. The dimensions and topology of channels can be tuned through organic synthesis by modifying the molecular structure of the organic ligand that bridges the metal ions.

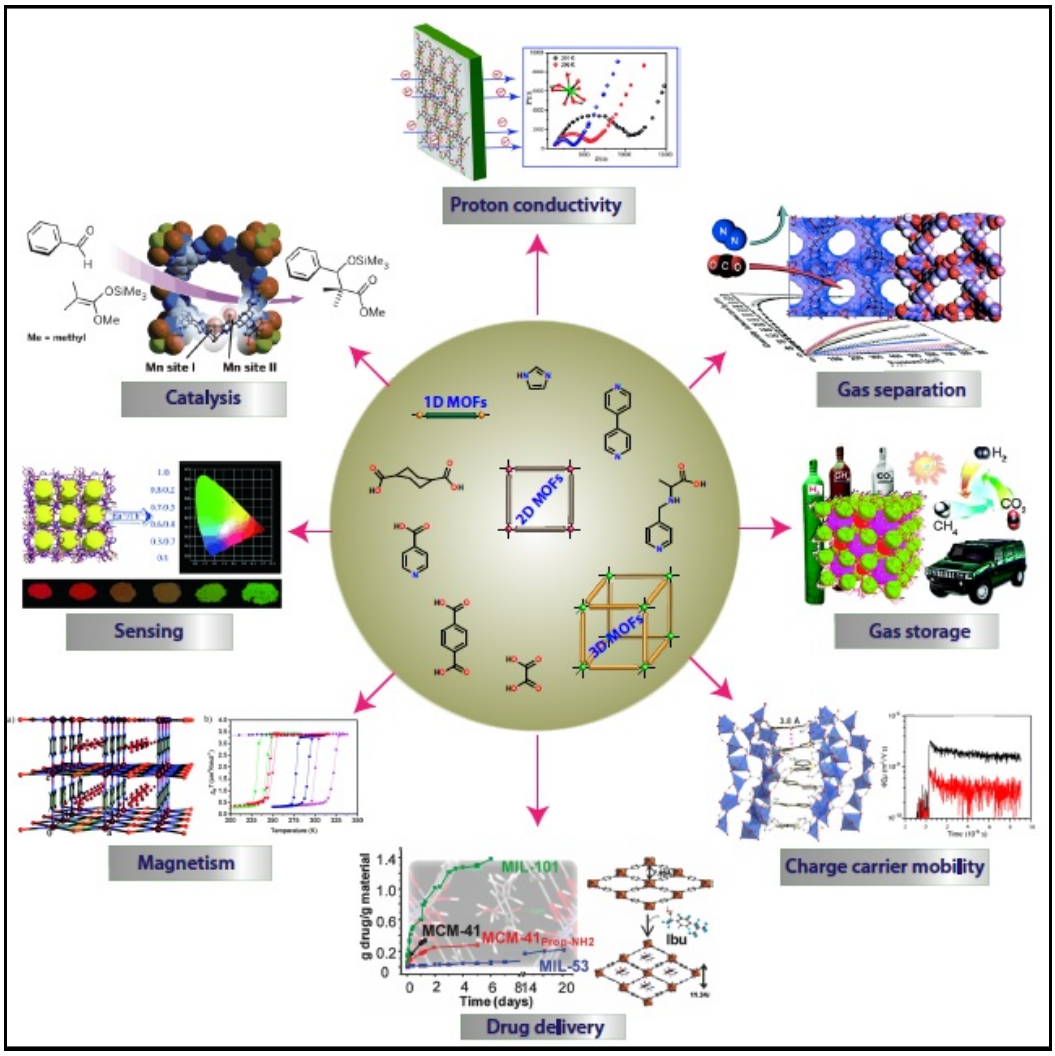

Figure 1.4 Synthesis of 1D, 2D and 3D MOFs using different kind of aromatic, non-aromatic, aliphatic linkers, for its various representative applications. [Reprinted with permission. Copyright: American Chemical Society, Royal Society of Chemistry and WILEY-VCH Verlag GmbH & Co. KGaA, Weinheim].

d. The surface properties of channels can be altered by appending different organic substituent's onto the organic ligand without changing the architecture of the

framework.

e. The prospect of predictable alteration of organic units to provide tailored materials for given applications.

Due to aforementioned reasons MOFs over other materials finds several applications as they possesses structural integrity. Although, MOFs have been successfully synthesized by various ways and potentially applied for several applications, utilization of these MOFs in following major aspects is demonstrated following experimental as well as computational pathways:

1.4.1 Hydrogen Storage:

The storage of H_2 is of course, a great challenge. The underlying possibility to use H_2 as a fuel for mobile or portable fuel-cell applications raises a very high interest in H_2 storage possibilities.[6] MOF-storage for H_2 works fully reversibly, avoids complicated heat treatments and recharging proceeds within seconds or minutes.[18] This is clearly an advantage over, e.g., metal hydrides, clathrates as storage materials. This makes, H_2 storage, the most important and attractive application of MOFs. As shown in Figure 1.5, the comparative uptake of H_2 by an empty tank without any porous materials and MOF filled container, thereby showing how important these MOFs are, for the world of today.

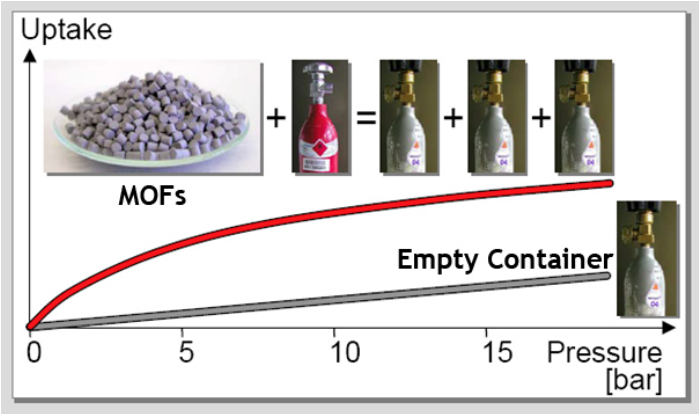

Figure 1.5 Comparative H_2 uptake in empty and MOF filled container. [Reprinted with permission from (18). Copyright 2012 American Chemical Society].

The solvent or guest molecules, which occupy the pore spaces in MOFs can be removed upon solvent exchange and heating under vacuum to generate a stable porous structure. Compared to their porous counterparts like zeolites and activated carbon,

MOFs have a much higher surface area (e.g. MIL-101 has a Langmuir surface area of 5900 m^2 g^{-1}).[19] The combination of different organic ligands and SBUs gives MOFs almost infinite geometrical and chemical variation.[19a] The availability of high resolution crystal structures of MOFs allows direct observation and comparison of pore size and geometry, which is almost impossible in other porous materials. Potential reaction sites on the organic ligands in MOFs renders post-synthetic modifications possible, leading to the introduction of additional active sites for stronger H_2 binding. All these characteristics of MOFs make them one of the most promising sorbent material for H_2 storage. The first MOF-based H_2 storage study performed in 2003 using MOF-5 showed H_2 uptake of 4.5 wt% (17.2 H_2 molecules per formula unit) at 77 K and 1 wt% at room temperature and 20 bar pressure.[20] With complete activation and protection of the sample from air and water, MOF-5 was observed to exhibit a record excess H_2 uptake of 7.1 wt% at 77 K and 40 bar.

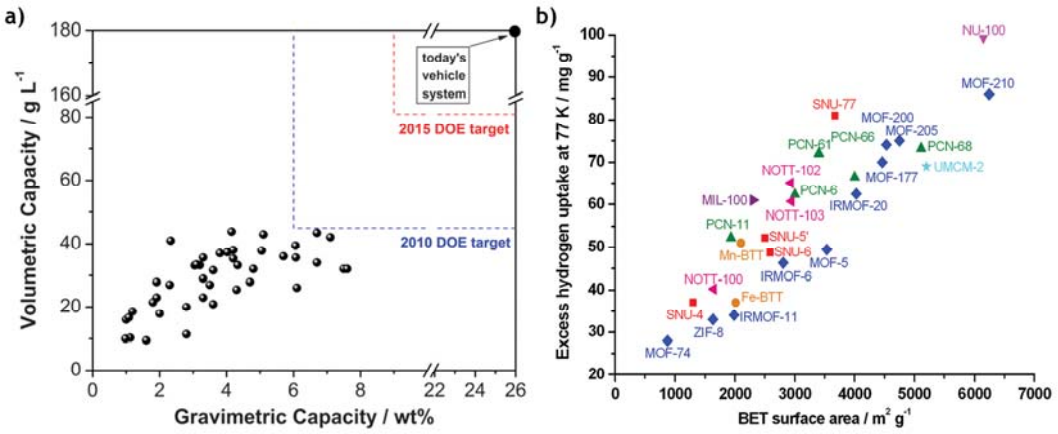

Figure 1.6 a) Current status of MOFs' hydrogen storage capacity at 77 K versus targets. b) Excess high pressure H_2 uptake capacities at 77 K versus BET surface areas for some highly porous MOFs. [Reprinted with permission from (18). Copyright 2012 American Chemical Society].

Using different possible combinations of organic linkers and metal centers; various MOFs with high porosity and subsequently H_2 uptake capacities has been reported in literature. As shown in Figure 1.6a, the H_2 uptake capacities in these MOFs are almost close to the DoE targets for vehicular applications.[18] These completely reversible and promising uptake capacities in these porous materials are very high compared to the traditional H_2 storage materials. Further, it has been shown through

calculations and experimental results that a qualitative linear relationship exists between the H_2 storage capacities at 77 K and the specific surface areas. As shown in Figure 1.6b, the high pressure H_2 uptake capacities of various MOFs show the directly proportional relationship between pore volume to the specific surface area. Therefore, in order to increase the H_2 uptake capacities at 77 K, higher specific surface area and higher pore volume should be created in the MOF. However, the H_2 storage capacity decreases sharply with increasing temperature, and none of the MOFs yet satisfies the proposed DoE target at room temperature. The MOFs are physisorption-based materials for H_2 storage, and their interaction energy with H_2 molecules is very weak. In these regards, several attempts have been performed to improve the H_2 uptake in MOFs *via* different possible strategies, which we have discussed in Section 1.5.

Table 1.1 Low pressure H_2 adsorption in Metal-Organic Frameworks at 77 K temperature and 1 atm pressure.

Name of MOFs	**H_2 uptake (wt%)**	**Name of MOFs**	**H_2 uptake (wt%)**
PCN-12[21a]	3.05	MOC-2[22h]	2.17
UTSA-20[21b]	2.80	UMCM-150[22i]	2.10
PCN-14[21c]	2.70	Ni\DOBDC[22j]	2.10
NOTT-103[21d]	2.56	Zn_2(BDC) (TMBDC)(DABCO)[22k]	2.10
PCN-11[21e]	2.55	$Ni_3(BTC)_2(3\text{-}PIC)_6(PD)_3$[23a]	2.10
HKUST-1[15c]	2.54	$(In_3O)(OH)(ADC)_2(IN)_2 . 4.67H_2O$[21k]	2.08
Cu_2(tptc)[21f]	2.52	$Zn_2(BDC)_2$ (DABCO)[22k]	2.00
NOTT-100[21d]	2.52	Mg\DOBDC[22j]	1.98
NOTT-140[21g]	2.50	PCN-6[23b]	1.90
MOF-505[21h]	2.48	NOTT-116[23c]	1.90
NOTT-101[21d]	2.46	CPM-6[23d]	1.88
NOTT-105[21d]	2.46	PCN-68[22c]	1.87
$Cu_4Cl(btt)_{3/8}$[21i]	2.42	Cd-ANIC-1[23n]	1.84
$Cu_6O(tzi)_3(NO_3)$[21j]	2.40	Co\DOBDC[22j]	1.81
PCN-12′[21a]	2.40	IRMOF-3[23e]	1.80
PCN-10[21e]	2.34	PCN-66[22c]	1.79
$(In_3O)(OH)(ADC)_2(NH_2IN)_2 . 2.67H_2O$[21k]	2.31	$Zn_2(C_2O_4)(C_2N_4H_3)_2.(H_2O)_{0.5}$[23f]	1.70
NU-100[22a]	2.29	Co-ANIC-1[23n]	1.64

NOTT-112[22b]	2.30	$[Co_4(OH)_2(p\text{-}CDC)_3DMF_2]_n$[23g]	1.61
NOTT-109[21d]	2.28	ZTF-1[23h]	1.60
PCN-61[22c]	2.25	CUK-1[23i]	1.60
Mn-BTT[22d]	2.25	$H_3[(Cu_4Cl)_3\text{-}(BTTri)_8]$[23j]	1.58
Cu_2(qptc)[22e]	2.24	Zn\DOBDC[22j]	1.54
NOTT-106[21d]	2.24	Bio-MOF-11[23k]	1.50
NOTT-107[21d]	2.21	ZIF-11[23l]	1.37
$[Zn_2(1)(DMF)_2]_n(DMF)_m$ [MOF(4)][22f]	2.20	MOF-5[23m]	1.32
NOTT-102[21d]	2.19	ZIF-8[23l]	1.30
$[Zn_3(OH)(p\text{-}CDC)_{2.5}(DEF)_4]$[22g]	2.10	MOF-177[23m]	1.25

1.4.2 CO_2 Adsorption and Storage:

The increasing level of atmospheric CO_2 is one of the greatest environmental concerns.[2] These emissions, mainly as a result of combustion of coal, oil, and natural gas are projected to continue to increase in the future due to economic growth and simultaneous industrial development, since, these carbon free energy systems are not well developed. In these regards, despite of the sequestration pathway, carbon capture systems (CCS) must capture the CO_2 from flue gas in an efficient and reversible fashion. Although utilization of alkanolamines and aqueous ammonia-based liquids for CO_2 capture is well settled on the industrial and

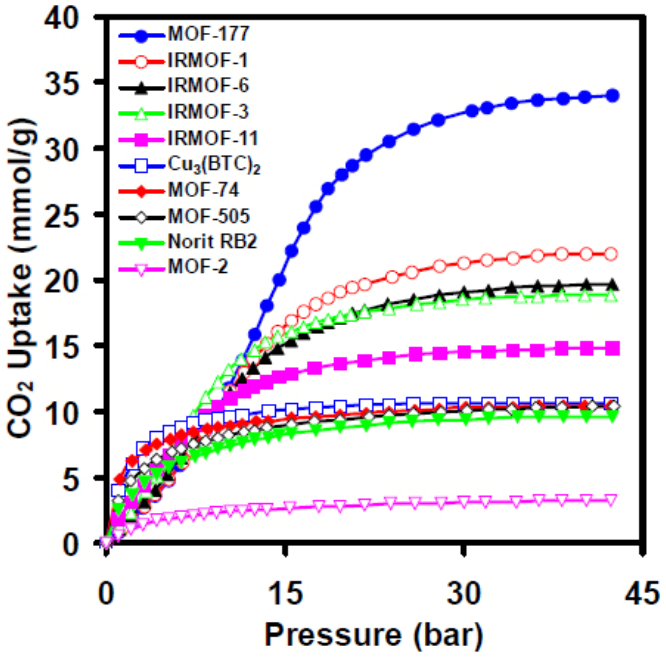

Figure 1.7 Comparative high pressure CO_2 uptake properties of literature reported MOFs and activated charcoal Norit RB2. [Reprinted with permission from (23m). Copyright 2004 American Chemical Society].

domestic levels, the difficulties due to regeneration of these CCS brings the limitations for their usages.[24] Also, solid porous adsorbent materials like zeolites, porous alumina, porous silica and activated charcoals or carbons has been used for selective capture of CO_2 from flue gases, but their amorphous structures, with limited stability in environmental conditions restricts their uses on industrial scale.[25] From an applications point of view, their extraordinary surface areas, finely tunable pore surface properties and potential scalability to industrial scale have made MOF materials an attractive target for CO_2 capture systems (*Figure 1.7*).[26] Highly crystalline structures with predictable topologies, tunable pore sizes, and functionalizable pores with functional groups incorporated *via* linkers or post-synthetic modification makes MOFs as eligible materials for highly efficient CO_2 capture systems.

The high CO_2 uptake in interpenetrated MOFs than that of its non-interpenetrated analogues has been achieved (*Figure 1.8a*).[27a] Since, it has been observed that MOFs possessing open metal sites enhances the performance by providing a mechanism for the separation of polar/non polar gas pairs such as CO_2/CH_4; synthesis of MOFs having open metal sites has been reported vastly in the literature (*Figure 1.8b* and *1.8c*).[27b,27c] For example, in HKUST-1 high CO_2 uptake has been achieved as a result of open metal sites;[27d] whereas in the case of Mg-MOF-74 as a result of open metal Mg-sites high CO_2 uptake and separation of CO_2 from flue gases has been achieved.[27e] The selective adsorption mechanism may occur due to the coordination of CO_2 to the metal center in an end-on fashion, i.e. O=C=O····Metal centre. The MOFs having free functional groups, i.e. surface functionalized frameworks enhances the capacity and selectivity of MOFs for CO_2 adsorption by grafting a functional group with a high affinity for CO_2 (e.g. amine, arylamine, alkylamine, hydroxyl groups, etc.). These functional groups enhance the selective interaction between CO_2 and the functionalized molecule as well as the constriction in the pore space of functionalized framework compared to the parent non-functionalized material (*Figure 1.8e*). The high CO_2 uptake observed in Bio-MOF-11 and ZTF-1 are the examples of high CO_2 uptake in functionalized MOFs.[23h,23k,23n] The utilization of porous materials with highly electronegative functionalities like –F, $–CF_3$ etc. having optimal adsorption thermodynamics and kinetics for CO_2 separation at room temperature has

been successfully achieved (*Figure 1.8d*).[27f]

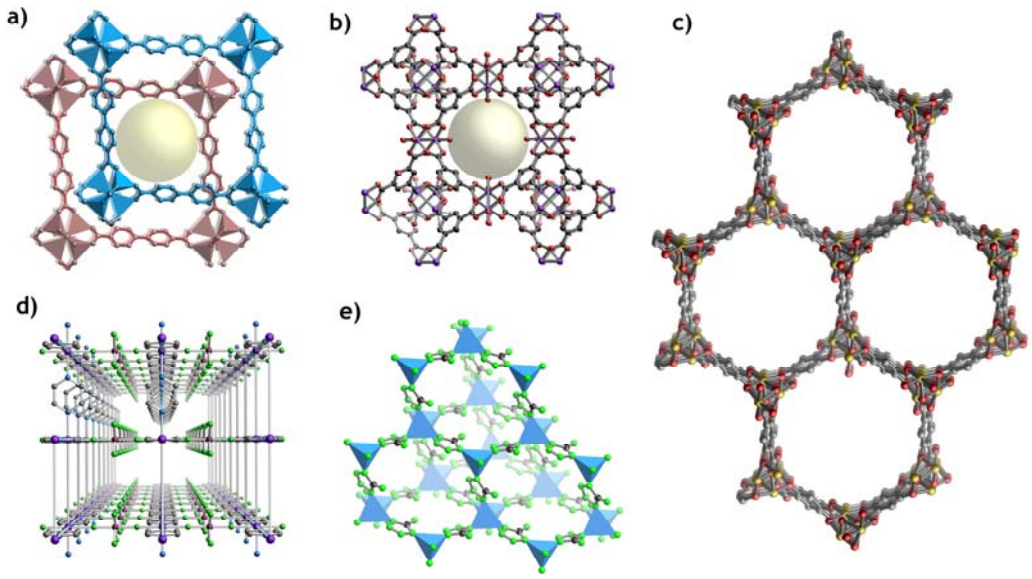

Figure 1.8 Representive MOFs reported for CO_2 capture and separation. a) Interpenetrated structure of IRMOF-8 for CO_2 capture. b) Structure of HKUST-1 and c) Mg-MOF-74 which possesses open metal sites shows high CO_2 capture as separation for later case. d) Structure of SIFSIX-3-Zn shows high separation of CO_2 from flue gases. e) Structure of ZTF-1 shows high CO_2 uptake at low pressure.

As discussed earlier, although materials with high CO_2 uptake capacities are important for various applications, the necessity of another kind of porous substances which can selectively adsorb CO_2 from mixture of gases are very important for industrial applications. The preferential uptake of CO_2 from mixture of gases like N_2, CO, H_2, CH_4, etc. is desired to separate the harmful gases from others in order to avoid the environmental issues. In these regards, MOFs with open metal sites, functional groups are mostly used as these MOFs adsorb the CO_2 very strongly over other gases due to high affinity. The successful utilization of several MOFs like SIFSIX-2-Cu, SIFSIX-2-Cu-I, SIFSIX-3-Zn, Mg-dobdc, IRMOFs, ZIFs, etc. having functional groups or open metal sites is successfully achieved.[27] The higher separation factor desired in porous materials has been successfully acquired in Mg-MOF-74, due to CO_2 adsorption over large temperature range as shown in Figure1.9.[27e]

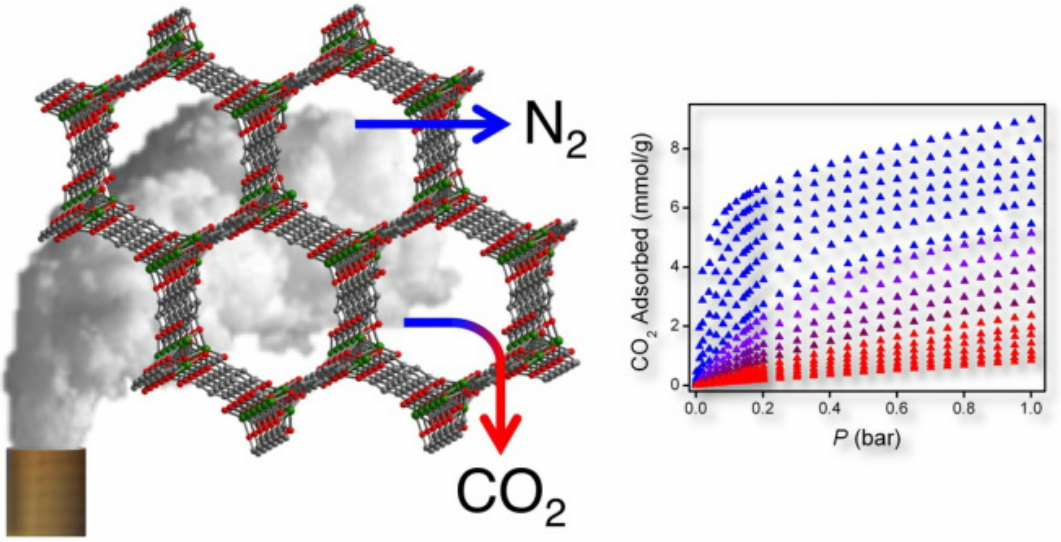

Figure 1.9 Selective gas adsorption in Mg-MOF-74 and separation of CO_2 from other gases as a result of open metal sites and subsequent high CO_2 uptake capacity over large temperature range. [Reprinted with permission from (27e). Copyright 2009 National Academy of Sciences, USA].

Table 1.2 Low pressure CO_2 adsorption capacities for Metal-Organic Frameworks at 273 and 298 K temperature and 1 atm pressure:

Name of MOF	CO_2 uptake (mmol/g)		Name of MOF	CO_2 uptake (mmol/g)	
	273K	298K		273K	298K
Mg\DOBDC[22j]	NA	8.08	MOF-505[21h]	NA	3.27
Co\DOBDC[22j]	NA	7.11	$H_3[(Cu_4Cl)_3$-$(BTTri)_8]$[23j]	NA	3.25
Ni\DOBDC[22j]	NA	5.80	$(In_3O)(OH)(ADC)_2$ $(NH_2IN)_2$. 2.67 H_2O[21k]	NA	3.21
Zn\DOBDC[22j]	NA	5.51	CPM-6[23d]	4.76	2.90
UTSA-20[21b]	NA	5.01	TMA@ Bio-MOF-1[28f]	4.5	NA
HKUST-1[15c]	NA	4.72	TEA@ Bio-MOF-1[28f]	4.2	NA
Zn + 4,4' bipy + (BTA-TBA)[28a]	NA	4.10	TBA@ Bio-MOF-1[28f]	3.5	NA
Bio-MOF-11[23k]	6.0	4.01	UMCM-150[22i]	NA	2.80
$[Zn_2(1)(DMF)_2]_n(DMF)_m[MOF(4)]$[28b]	5.80	NA	$Zn_2(BDC)_2$ $(DABCO)$[22k]	NA	2.71
$[Zn_3(OH)(p$-	NA	4.00	CPM-5[23d]	3.62	2.43

$CDC)_{2.5}]_n$[28c]					
Cd-ANIC-1[23n]	4.72	3.84	ZIF-78[28g]	3.348	2.23
ZTF-1[23h]	5.35	3.79	ZIF-96[28h]	NA	2.16
$Zn_2(C_2O_4)(C_2N_4H_3)_2.(H_2O)_{0.5}$[23f]	4.30	3.78	IRMOF-3[23e]	NA	2.14
Co-ANIC-1[23n]	4.22	3.48	$(In_3O)(OH)(ADC)_2(IN)_2 . 4.67\ H_2O$[21k]	NA	2.08
CUK-1[23i]	NA	3.48	MOF-177[23m]	NA	1.72
YO-MOF[28d]	NA	3.39	ZIF-69[28g]	3.03	1.69
SNU-M10[28e]	NA	3.30	MOF-5[23m]	NA	0.92

1.4.3 Methane (CH_4) Storage:

Natural gas is another good candidate for on-board fuel which has comparatively lower hazardous gas emissions. The main component of natural gas is methane (> 95 %). Methane has a comparable gravimetric heat of combustion with gasoline, but it suffers from the lack of effective storage. For example, liquefied natural gas requires cryogenic conditions (112 K), compressed natural gas operates at pressures about 200 bar, etc.[29] Unlike for hydrogen, the heat of adsorption for methane (about 20 kJ/mol) is already within the ideal scope for practical usage. DoE has set a methane storage target i.e. 180 v/v at ambient temperature and pressure range no more than 35 bar.[30] Although, some of the carbon materials, silica, zeolites, etc. have already reached this target, they have limited packing density, amorphous structure, limited surface area and tedious synthetic protocols.[31] Thus, the focus has been on increasing the surface area of the porous sorbent. After the first methane sorption study using MOFs in 1997, the studies on methane uptake in MOFs has been picked up very promptly.[32] Table 1.3 summarizes the surface area, porosity and methane uptake data for selected MOFs. The breakthrough result obtained in MOFs showed that the methane uptake in MOFs can exceed the DoE targets as well.

Since, MOFs present a unique blend of the benefits of both zeolites and porous carbons; superior applications of these materials for methane uptake are seen to be paving.[33] The crystalline nature and ordered porosity of the materials make absolute characterization a simple task, and permit in-depth structural and host–guest studies to be conducted. Additionally, exceptionally high surface areas may be obtained and the character of the framework is easily adjusted by incorporation of functional groups or

post-synthetic modification of the system.[34] The first reported measurement of methane uptake by a porous MOF in 1997 showed possible applications of MOFs for methane

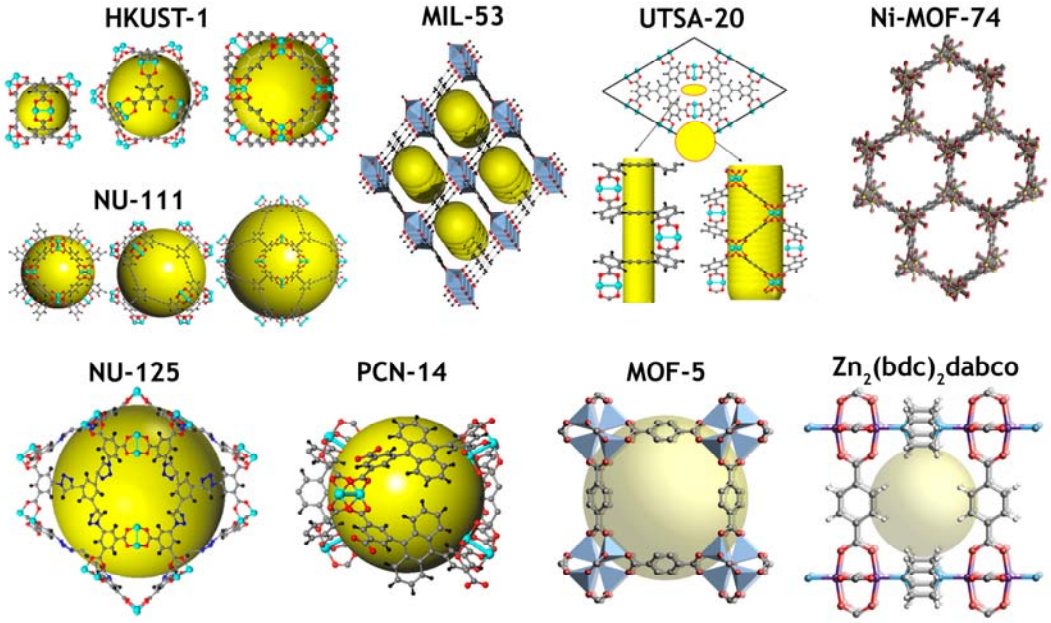

Figure 1.10 Representative examples of MOFs showing methane uptake at ambient temperature and higher pressure range. [Reprinted with permission from (29c). Copyright 2013 American Chemical Society].

storage.[32] While, volumetric storage capacity has been emphasized, to date, the reported volumetric storage capacity of a MOF is usually calculated from the gravimetric capacity and the crystallographic density of the material. This leads to an idealized maximum volumetric capacity for the framework, as it would be impractical to grow a single crystal large enough to accommodate enough methane for any practical use. However, the application of MOFs in methane storage has not received nearly as much attention as that for hydrogen storage or carbon dioxide capture. In the curiosity to explore methane uptake properties in MOFs, several researchers have investigated MOFs having high volumetric and gravimetric uptake. The representative MOFs and their methane uptake capacities at ambient temperature and high pressure are showed in Figure 1.10 and Figure 1.11. A compilation of reported methane uptake in high capacity MOFs, in addition to other thoroughly studied MOFs, is provided in Table 1.3:

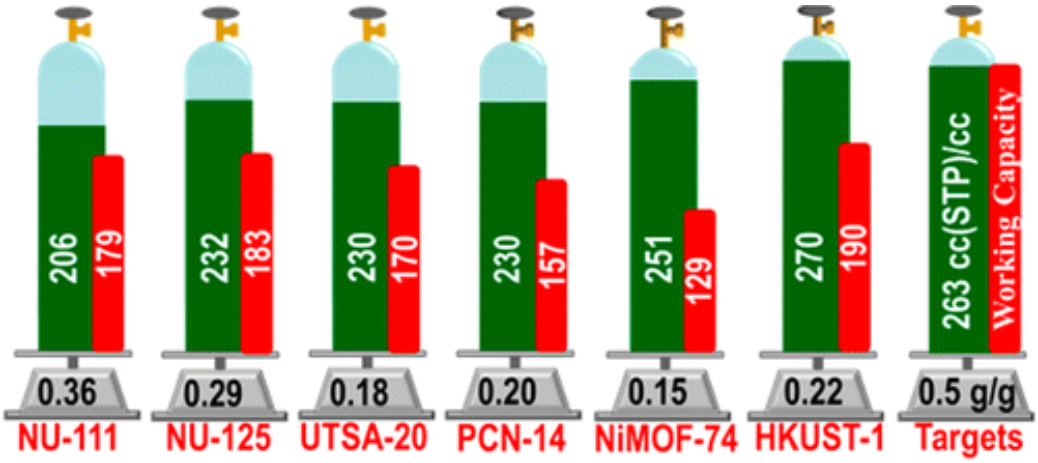

Figure 1.11 Methane uptake capacities in few well known MOFs at ambient temperature and 65 bar pressure showing uptake of methane in porous MOFs in response to the targets from DoE. [Reprinted with permission from (29c). Copyright 2013 American Chemical Society].

Table 1.3 Recent reports of methane storage in MOFs achieved at ambient temperature and high pressure range.

MOFs	**BET Surface area (m^2g^{-1})**	**Pore volume (cm^3g^{-1})**	**Density**	**CH_4 uptake (cc/cc) STP**
MIL-53 (Al)[33d]	1100	0.59	0.98	155 (35 bar)
MIL-101[35a]	2693	1.303	0.31	56 (60 bar)
PCN-14[21c]	1753	0.87	0.83	220 (35 bar)
$Zn_2(bdc)_2dabco$[35a]	1448	0.75	0.87	202 (75 bar)
$Cu_3(btc)_2$[35b]	1502	0.76	0.88	165 (35 bar)
IRMOF-1/MOF-5[35c]	1870	0.60	0.65	110 (36 bar)
HKUST-1[35a]	1502	0.78	0.88	267 (60 bar)
Ni-MOF-74[35d]	1350	0.51	1.21	251 (60 bar)
UTSA-20[31b]	1620	0.66	0.91	230 (60 bar)
NU-125[29c]	3120	1.29	0.58	232 (60 bar)
NU-111[29c]	4930	2.09	0.41	206 (60 bar)

1.4.4 Catalysis:

The applications of MOFs as catalytically active species have been increased over the years for due to following reasons:[36]

a. In case of MOFs, it is possible to further functionalize the pores found within MOFs in order to make the material catalytically active.

b. The pores present in MOFs may also be fine tuned in their chemical characteristics and according to the necessity of catalytic reactions.

c. Since, MOFs can form large and crystalline pores quite easily, catalytic reactions can easily take place within MOF pores.

In addition to the aforementioned reasons, MOFs are considered as good catalysts as they contain 'single-site' active species, in which every active site is in an identical environment due to the crystalline nature of MOFs. As shown in Figure 1.12, the various strategies and functional groups can be incorporated in MOFs *via* metal centers, linkers and post-synthetic modifications in order to acquire catalytic activities in MOFs.[37]

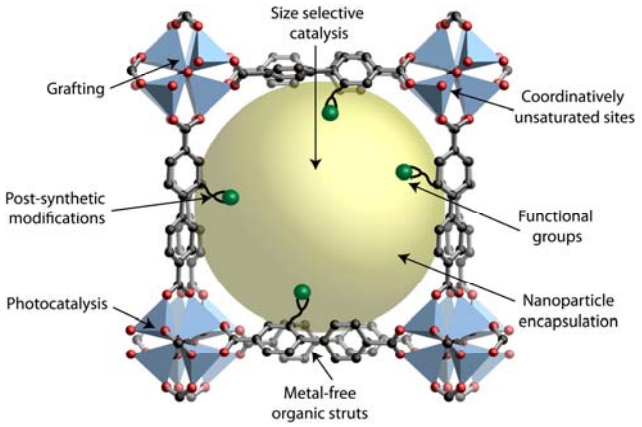

Figure 1.12 Different functionalities and strategies for the inclusion of catalytic moieties into MOF scaffold.

MOFs can be used as catalytic supports, whereby the MOF is used as a carrier for an active site e.g. MOF-5.[11a] The porous MOFs and ZIFs with considerable stability have been successfully utilized as a catalytic support in many catalytic reactions such as use in the epoxidation of propylene with molecular oxygen by incorporating Ag into MOF-5, H_2O_2 synthesis from the elements utilizing Pt on MOF-5, the synthesis of methanol from synthesis gas utilizing Cu on MOF-5, and also in the hydrogenation of cycloctene by incorporating Pd onto MOF-5.[38a] The Au and Ag nanoparticle incorporated ZIFs and MOFs have been effectively utilized as catalyst for nitro reduction reaction to produce commercially important amines and other reagents.[38b] The

various as synthesized or post-synthetically modified MOFs have been used for the synthesis of various commercially important chemicals, to catalyze organic transformation reactions (e.g. Suzuki, Sonogashira, Heck, etc.), various oxidation and reduction reactions, tandem and cascade reactions.[38c-38e]

Table 1.4 Literature reported examples of MOF based catalysts and summary of active functionalities involved in these MOFs as catalytic centers:

MOF Metal	MOF Linker	Active Centre	Catalytic Reaction
Cu	4,4′-bipyridine	Metal	Allylic oxidation[39a]
Zn	1,4-benzene dicarboxylic acid (IRMOF-1)	Metal	Cycloaddition of CO_2 and epoxides[39d]
Cu	1,2,4,5-benzenetetracarboxylic acid, 2,2'-bipyridine	Metal	Oxidation of olefins[39b]
Zn	1,4-benzene dicarboxylic acid, 2-amino terephthalic acid	Linker and Metal	Cycloaddition of CO_2 and epoxides[39c]
Zn	2-aminoterephthalic acid (IRMOF-3)	Linker	Knoevenagel reaction[39d]
Cr	1,4-benzene dicarboxylic acid, ethylenediamine (ED-MIL-101)	Coordinated ethylene-diamine	Knoevenagel reaction[39e]
Zn	2-methyl imidazole (ZIF-8)	Incorporated Au/Ag/Pd/Pt nanoparticles	Nitro reduction, CO oxidation, Suzuki coupling[38]
Cu	Imidazole [$Cu(im)_2$]	Metal	Oxidation of activated alkanes, 1,3-dipolar cycloaddition[39f]
Zn	Porphyrin [ZnPO-MOF]	Zn(II) - porphyrin sites	Acyl transfer between N-acetylimidazole and pyridylcarbinols[39g]
Co	Benzimidazole (Co-ZIF-9)	Metal and coordinated N-atoms	Photocatalysis and water splitting[39h]

As shown in Figure 1.12 and Table 1.4, many components of MOFs can be used within a catalytic reaction such as using the SBU as the active centre and also having the active centre being introduced to the MOF by post-synthesis modification.[40] The active catalytic centers in MOFs mainly includes linker functionalities achieved directly *via* incorporated linkers or post synthetic modifications, metal centers, metal connected organic moieties, encapsulated metal nanoparticles, etc. (*Table 1.4*). Due to high porosity, periodic arrangement of pores or cavities, considerable stability and crystalline architectures, the applications of MOFs as catalysts are finding several opportunities. The most remarkable characteristic of MOFs relevant for catalysis, which makes them unique, is the lack of non-accessible dead volume. Furthermore, due to the very open architecture, the self diffusion coefficients of molecules in the pore system are slightly lower than in the bulk solvent, which means mass transport in the pore system is not hindered. In addition, the ordered structure offers the opportunity to spatially separate active centers. As a result of their high surface areas, MOF-based catalysts contain a very high density of fully exposed active sites per volume (*Figure 1.13*).[38] This characteristic results in enhanced activity, and thus a more effective catalytic system.

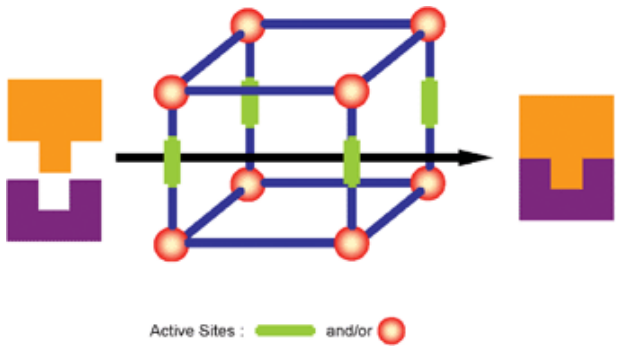

Figure 1.13 Active sites present into the MOFs which acts as catalytic centers during transformation. [Reprinted with permission from (38e). Copyright 2009 Royal Society of Chemistry].

Along with aforementioned applications of MOFs for H_2 storage, CO_2 adsorption and storage, methane storage, catalysis; there are several applications of MOFs has been reported into the literature for gas separation, proton conductivity, charge carrier mobility, magnetism, drug delivery, luminescence and sensors, etc (*Figure 1.4*). As a result of intriguing porous structures along with tunable pore sizes; MOFs have applied potentially for various appliances. Most of aforementioned applications of MOFs are based on the porosity or surface area available for the

adsorption of gas, solvent or analytes. As discusses in earlier Section 1.1, in order to store the high amount H_2 at lower as well as higher pressure range for its applications in fuel cell technology; MOFs have shown promising uptake as compared to other H_2 storage materials due to presence of highly porous structures. Well defined periodicity, high surface area, high stability to normal atmospheric conditions and easy scale up of MOFs shows its potential to serve as H_2 storage materials for fuel cell application, effectively. Although, MOFs have shown very high H_2 uptake capacities in response to DoE targets; there are several strategies put forward to improve the uptake capacities to large extent. In order to improve the interaction between framework and adsorbing H_2 molecules for efficient uptake at lower pressure following strategies have been demonstrated depending on experimental and computational outcomes. Herein, the improved interaction between the gaseous molecule and the functionalized framework brings hydrogen molecule in close proximity with several aromatic rings to improve the H_2 uptake capacities of MOFs via increased adsorption enthalpy.

1.5 Strategies for H_2 Uptake Improvement in MOFs:

There are several approaches have been demonstrated for improvement in H_2 uptake, the following strategies have found to be effective:

1.5.1 Increasing Pore Size, Pore Volume and Surface Area.

1.5.2 Creation of Open Metal Sites.

1.5.3 MOF Functionalization via Functional Group Incorporation.

1.5.4 Interpenetration or Catenation.

1.5.5 Doping of Metal Nanoparticles and Alkali Metals in MOFs.

Since, the MOFs synthesized or modified according to the aforementioned strategies adsorb H_2 effectively at low as well as high pressure; we will discuss these factors in details:

1.5.1 Increasing Pore Size, Pore Volume and Surface Area:

The correlation between H_2 uptake and various physical attributes of MOFs has been discussed in large context in the last few years. H_2 uptake seems to be proportional to heat of adsorption at low pressures, surface area at moderate pressures and pore

size/free volume at high pressures.[18] Various attempts to determine strong correlations between these physical attributes and H_2 uptake at low and high temperatures over a range of pressures have been made.[41] As shown in Figure 1.6b, there is roughly linear relationship between BET surface area or pore volume and the 77 K saturation hydrogen uptake data for selected MOFs at high pressure. But this linear relationship seems to be valid for high pressure H_2 uptake; whereas the same affiliation at low pressure H_2 uptake does not follow the similar trends.[18] The probable reason for this is the accumulation of all the free space available into MOF structure at high pressure, which is impossible in the case of low pressure uptake studies.

Table 1.5 Porosity and H_2 uptake studies in representative IRMOFs:

Name of MOF	**Linker**	**Pore Diameter (Å)**	**Framework Free Volume (%)**	**BET Surface Area (m^2/g)**	**H_2 uptake (wt%)**
IRMOF-3	2-amino-1,4-benzene dicarboxylic acid	9.6	78.7	2446	1.42
IRMOF-1 (MOF-5)	1,4-benzene dicarboxylic acid	11.2	79.2	3362	1.32
IRMOF-8	2,6-Naphthalene-dicarboxylic acid	12.6	84.4	4461	1.5
IRMOF-9	Biphenyl-4,4′-dicarboxylic acid	10.6	74.7	2613	1.17

The linear relationship between pore size and surface area in the case of MOFs is validated using literature reported IRMOFs as shown in Figure 1.14. As pore size increases as a consequence of increased linker length, pore volume increases; which further results into the increase in surface area upto few extent. But, the further increase in the linker length results into the formation of interpenetrated framework formation with decreased pore size, pore volume and surface area.[42] As a result of decreased surface area and % free volume available for adsorption of H_2 molecules, the overall H_2 uptake in these MOFs decreases considerably. As shown in Figure 1.14, the direct impact of linker length on the overall increase in surface area is visible upto certain extent. After that although linker length increases, surface area does not increases

rationally (*Table 1.5*).[23m] Although, interpenetrated MOFs can show elevated H_2 uptake compared to its non-interpenetrated analogues due to improved interaction between framework and adsorbing gas molecules, this improvement is possible only in the case of low pressure studies in few cases. But at high pressure, due to decreased pore volume H_2 uptake does not increases linearly (*Figure 1.14*).

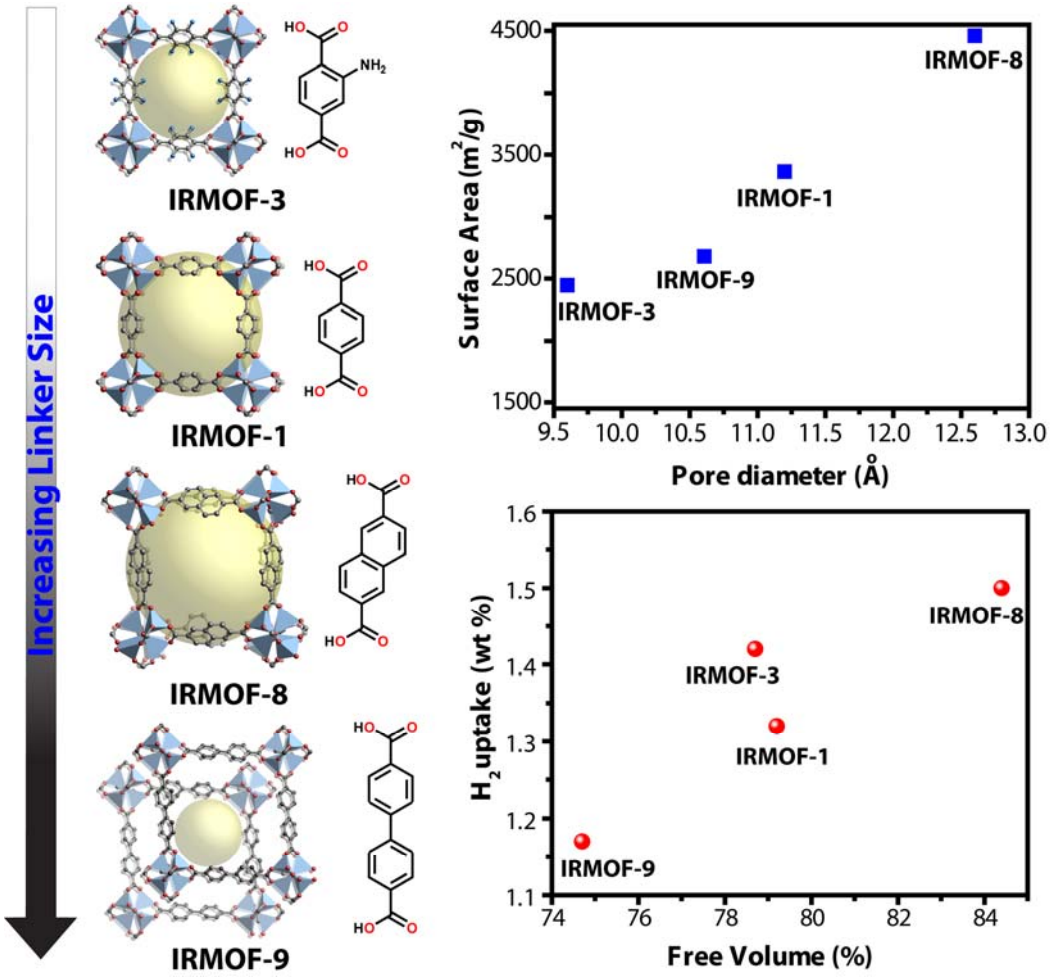

Figure 1.14 A schematic illustration showing the effect of increasing linker length on the surface area and subsequently on the H_2 uptake properties in MOFs. The increasing linker length for MOF synthesis further results into the interpenetration in frameworks decreasing the total pore volume and surface area significantly as shown in the case of IRMOF-9.

As shown in Figure 1.15, the H_2 uptake capacities of MOFs are directly related with the surface areas in the low surface area (100–2000 m^2/g), but the same relationship is not valid in the case where surface area exceeds 2000 m^2/g.[18,42] It seems

that at 1 atm pressure, the surface area greater than 2000 m^2/g cannot be fully covered with H_2 molecules, since at low pressure, H_2 will preferentially bind on the sites that have large affinity for H_2. In addition, low-pressure H_2 adsorption may be influenced by other factors such as pore size, catenation, ligand functionalization, and open metal sites. For example, the H_2 uptake capacity at 77 K and 1 atm for doubly interpenetrating SNU-77 (1.80 wt%)[43] having surface area of 3670 m^2/g (pore size of 8.0 Å), is higher than that of MOF-177 (1.24 wt%)[23m] that has higher surface area of 4750 m^2/g (pore size 11.8 Å) in the non-interpenetrating MOF. The factors influencing the H_2 uptake of porous MOFs at low pressure are not only related to the surface area, but these includes the other factors such as interpenetration, open metal sites, affinity of adsorbing gas molecules towards the framework, etc. On the other hand, the H_2 uptake capacities at high pressures show a qualitative relationship with the surface areas. As the surface area increases, the high pressure H_2 uptake capacity at 77 K increases probability due to the availability of free space for the adsorption of gas molecules. In summary, only increment in the surface area is not enough to achieve the high H_2 uptake at low pressure range, but it involves other structural factors as well.

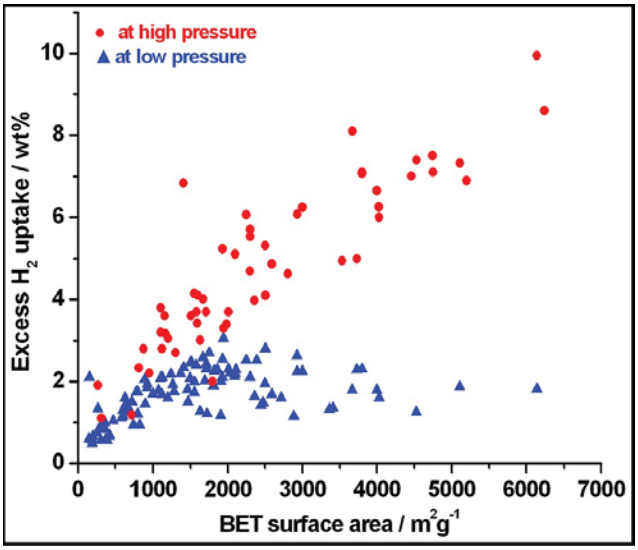

Figure 1.15 A plot showing the relationship between H_2 uptake capacities and surface areas of various MOFs at low pressure (1 atm) and high pressures (10–90 bar). [Reprinted with permission from (18). Copyright 2012 American Chemical Society].

1.5.2 Creation of Open Metal Sites:

It has been observed that coordinatively unsaturated metal sites present in MOFs show high hydrogen binding affinities.[42] During the H_2 uptake these unsaturated or open metal sites serve as the first loading sites due to high affinity. The MOFs having metal

coordinated solvent or gust molecules can generate the open metal sites. Solvent or guest molecules can be removed from the metal centers of MOFs without causing any structural collapse.[44] The solvent exchange with low boiling solvents followed by thermal activation at high vacuum can create open metal sites without collapsing the basic MOF framework integrity (*Figure 1.16*). The maintained crystallinity in these MOFs, with unsaturated metal coordination creates centers with high affinity for gas molecules.

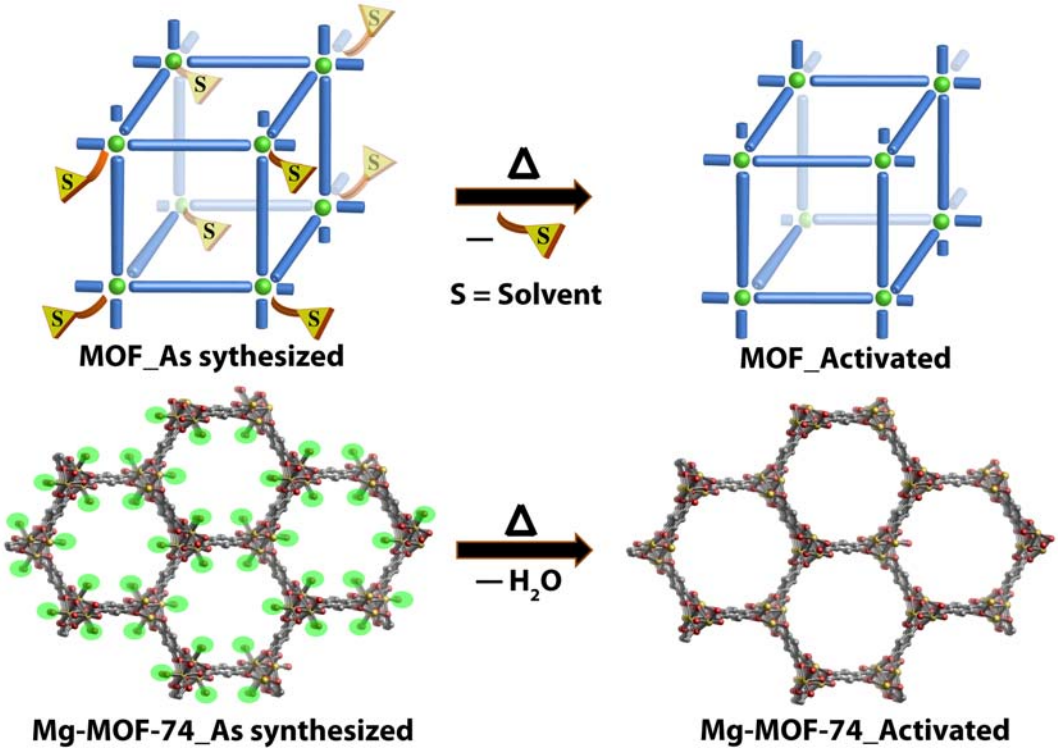

Figure 1.16 A schematic representation showing creation of open metal sites in MOFs. The removal of coordinated solvent molecules from the metal center under specific condition crates unsaturated metal centers. A representative example of Mg-MOF-74 is presented herein.

A series of MOFs having open metal sites derived from M (Mg, Ni, Zn, Co) and 2,5-dihydroxyterephthalic acid is reported into the literature, where these active sites for H_2 adsorption are present. Among this series, CPO-27-Ni (Ni-MOF-74) shows an initial adsorption enthalpy of 13.5 kJ mol^{-1}, which is among the highest reported value in literature for H_2 uptake.[45] A trend of increasing binding energies of Zn < Mn < Mg < Co < Ni have been observed in these MOFs, which is closely correlated with the cationic

radius of the exposed metal site. Further, open metal sites generated in $[Cu_3(BTC)_2(H_2O)_3]_n$ (HKUST-1) constructed from benzene-1,3,5-tricarboxylate and Cu paddle-wheel SBUs showed efficient H_2 uptake.[15c] A comparison of the H_2 storage capacities for three isostructural MOFs with and without open metal sites validated the importance of open metal sites for improved H_2 uptake. The H_2 sorption capacities of SNU-5 (2.87 wt%) having open metal sites at 77 K and 1 atm pressure is much higher than those SNU-4 (2.07 wt%) and SNU-5′ (1.83 wt%), which are without unsaturated metal centers.[46] The isosteric heats of H_2 adsorption for SNU-4, SNU-5' and SNU-5 were 5.96–7.24, 5.91–6.53 and 4.43–11.60 kJ mol^{-1}, respectively. These results suggest that the presence of open metal sites in MOFs lead to the higher H_2 uptake capacity and higher isosteric heat of H_2 adsorption as well as a higher surface area and pore volume. The list of representative MOFs having open metal sites is summarized in Table1.6.

Table 1.6 Literature reported representative examples of MOFs with open metal sites and their H_2 uptake properties at 77 K and 1 atm pressure as well as Isosteric Heat (Q_{st}) of H_2 adsorption:

Name of MOF	**Surface Area (m^2/g)**		**H_2 Uptake (wt %)**	**Isosteric Heat (Q_{st}) (kJ mol^{-1})**
	BET	**Langmuir**		
Mg_2(dobdc) [Mg-MOF-74][47a]	1510	-	2.2	10.3
Mn(NDC)[47b]	191	-	0.57	-
$Cu_6O(tzi)_3(NO_3)$[21j]	2847	3223	2.4	9.5
Zn_2(dhtp)[38b]	783	1132	1.77	8.3
$Zn_3(OH)(cdc)_{2.5}$[38b]	152	-	2.1	7.0
$Cr_3(BTC)_2$[47c]	1810	2040	1.9	7.4
$Fe_4O_2(BTB)_{8/3}$[47d]	1121	1835	2.1	-
$Cu_3(TATB)_2$ (catenated) PCN-6[23b]	-	3800	1.9	6.2
$Cu_3(TATB)_2$ (noncatenated) PCN-6′[47e]	-	2700	1.35	6
Cu_2(bptc) NOTT-100[21d]	1670	-	2.59	6.3

Cu_2(qptc) NOTT-102[21d]	2932	-	2.24	5.4
Cu_2(abtc) SNU-5[46]	-	2850	2.84	8.2
Cu_2(bdcppi) SNU-5′[46]	-	2450	2.1	5.8
Cu_3(BHB)[21b]	1156	-	2.9	-
Cu_3(ttei)[22a]	6143	-	1.82	6.1
Cu_3(L, hexacarboxy-late) PMOF-2(Cu)[47g]	3730	4180	2.29	9.2
$Cd_2(Tzc)_2$[39g]	230	339	0.55	11.4

1.5.3 MOF Functionalization via Functional Group Incorporation:

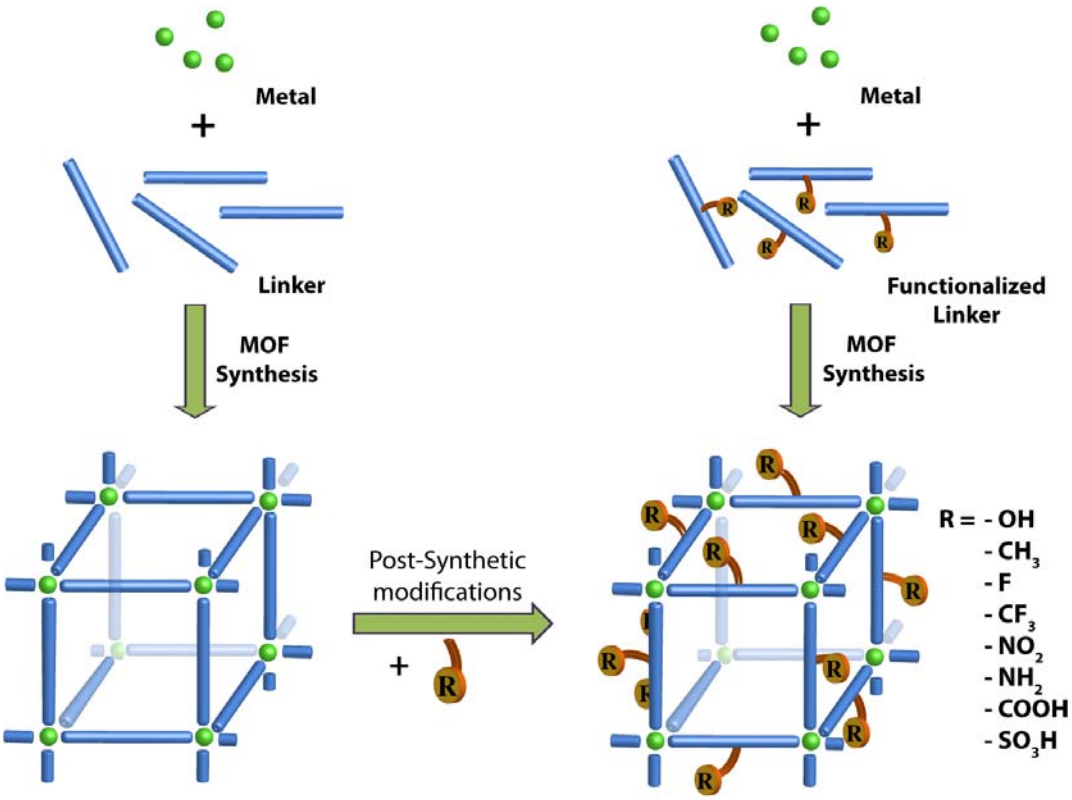

Figure 1.17 A schematic representation showing synthesis of functionalized MOFs *via* direct incorporation of linkers having functional groups or post synthetic modifications.

The organic linker can play an important secondary role in increasing hydrogen adsorption, although the metal sites and/or the SBU are the preferential adsorption sites for H_2.[48a] The increased interaction between adsorbing gas molecules and linkers *via*

functional groups or aromatic rings improves the gas uptake significantly, which was confirmed using experimental as well as theoretical calculations.[48b] The insertion of functionalized links holding functional groups like –F, $–NH_2$, –OH, –COOH, etc. has proved to have good impact on enhancing the H_2 adsorption properties.[49] Recently, computational studies proved that the choice of both ligand and metal center plays an important role in gas-framework interactions.[48] The improved interaction between framework components further results into the increment in isosteric heat (Q_{st}) of H_2 adsorption, which is needful for gas uptake at lower pressure range (*Figure 1.17*).[49]

In the case of IRMOF series, by the utilization of basic structural motif of $Zn_4(\mu_4\text{-}O)(CO_2)_8$ SBUs and different dicarboxylates linkers; series of MOFs have been synthesized with various functionalities (*Figure 1.18*).[23m,38b] From the gas uptake studies performed on these MOFs, it is clear that increasing the aromaticity of this central portion, from a simple phenyl ring (MOF-5/IRMOF-1) to cyclobutylbenzene (IRMOF-6) to naphthalene (IRMOF-8) increases the H_2 uptake dramatically, from 0.5 wt% to 1.0 wt% and 1.5 wt%, respectively (*Figure 1.16*).[50] The enhancement in the affinity of the ligand for the dihydrogen molecule is further enhanced by chemical MOF functionalization by the introduction of electron-donating groups to the central portion of the ligand. As shown in Figure 1.18, the replacement of 1,4-benzene dicarboxylic acid linker in MOF-5 with organic linkers having –Br, $–NH_2$ and $–CH_3$ groups afforded IRMOF-2, IRMOF-3 and IRMOF-18, respectively (*Figure 1.18*). An enhancement in gas uptake properties was found in these functionalized IRMOFs in practice. On the contrary, a lack of H_2 uptake enhancement was reported for pillared square grid net based MOFs constructed by ligands where all phenyl –H atoms replaced by either –F atoms or $–CH_3$ groups.[22k] This may be due to partial restriction of the pore size or blocking of the high-affinity metal-based binding sites by the larger ligand, effectively canceling out any benefit derived from electronic enhancement of the ligand. The improved H_2 adsorption enthalpy (upto 8 KJ/mol) in the partially fluorinated MOFs, wherein fluorine lined pores enhance the interaction with adsorbed H_2 molecules has been reported.[51a] As a result of complete fluorination in MOFs, the unique hysteretic adsorption of H_2, which shows a promising way for filling up H_2 at high pressure but stored at lower pressure has been reported into the literature.[51b] The strong interaction of

the semi-ionic C–F bonds with interacting H_2 molecules is the driving force for increased adsorption enthalpy, which leads to the higher adsorption at low pressure and elevated temperature.[52]

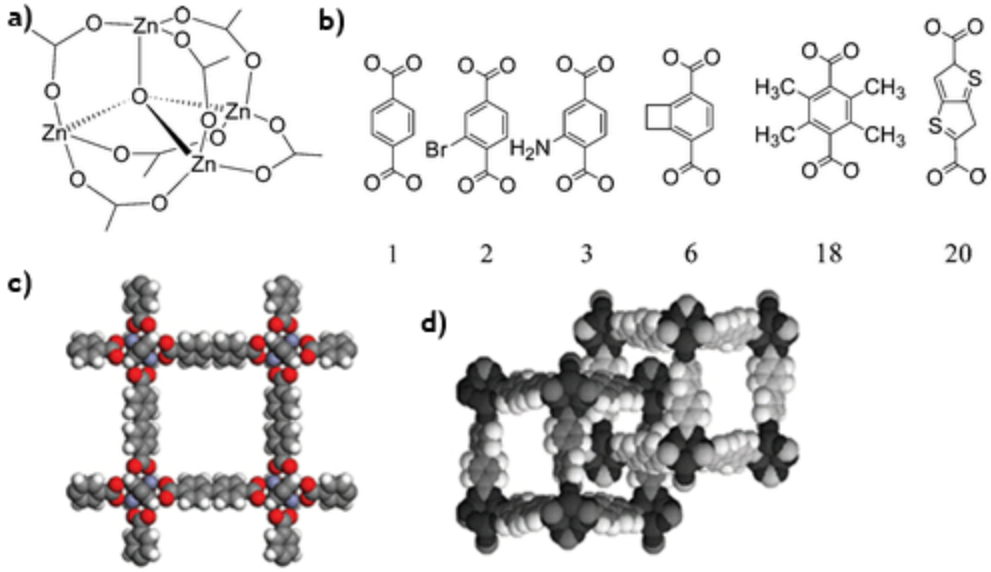

Figure 1.18 Synthesis of IRMOFs by utilizing $Zn_4(\mu_4\text{-}O)(CO_2)_8$ SBUs and carboxylate based organic linkers with functional groups. [Reprinted with permission from (38b). Copyright 2011 American Chemical Society].

Although various types of linker functionalizations are reported in the literature, the fluorine functionalized MOFs found to be appealing for H_2 uptake studies. The list of fluorine functionalized MOFs is summarized in Table 1.7:

Table 1.7 Hydrogen uptake properties of fluorine containing MOFs collected at 77 K* as a representative example of functionalized MOFs for H_2 uptake:

Name of MOF#	**H_2 Uptake (wt%)**	**Name of MOF#**	**H_2 Uptake (wt%)**
$[Zn_2(tfbdc)_2(dabco)]$[22k]	1.78	$[Co(hfbba)(3\text{-}mepy)(H_2O)]$[51f]	0.67
$[Co_3(hfbba)_6(phen)_2]$[51c]	0.90	$[Mn_2(hfbba)_2(3\text{-}mepy)]\cdot(H_2O)$[51f]	0.60
$[Cu_2(hfbba)_2(3\text{-}mepy)_2]\cdot(DMF)_2(3\text{-}mepy)$[51d]	0.58	$[Zn_2(hfipbb)_2(bpdab)]\cdot 2DMF$[51g]	0.87 [20 atm]
$[Zn_5(triazole)_6(tfbdc)_2(H_2O)_2]\cdot(4H_2O)$[51a]	0.43	$[Cd_2(hfipbb)_2(DMF)_2]\cdot 2DMF$[51g]	0.57 [20 atm]

[Cu(hfipbb)(H_2hfipbb)$_{0.5}$][51e]	0.23	[Cu(hfipbb) (H_2hfipbb)$_{0.5}$][51e]	1.1 [48 atm]
[Co_2(hfbba)$_2$(3-mepy)$_2$]·(DMF)$_3$[51f]	0.78	[Ag_2 (Ag_4-Tz_6)][51b]	2.33 [64 atm]
[Mn(hfbba)(3-mepy)(H_2O)][51f]	0.72		

*Here it should be noted that wherever pressure and temperature is not mentioned, there pressure is 1 atm and temperature is 77 K.
#tfbdc = Tetrafluoroterephthalic acid, dabco = 1,4-diazabicyclo[2.2.2]octane, hfbba = 4,4′-(Hexafluoroisopropylidene) bis(benzoic acid), phen = 1,10-phenanthroline, 3-mepy = 3-methyl pyridine, triazole = 1,2,4-triazole, Tz = 3,5-bis(trifluoromethyl)-1,2,4-triazole.

1.5.4 Interpenetration or Catenation:

The ongoing studies on the H_2 uptake in MOFs have confirmed that smaller pores actually take up H_2 more effectively than very large ones.[42a] Ideally, pore sizes ranging from 4 to 5 Å, which are comparable to the kinetic diameter of H_2 (~2.8 Å) seems to be ultimate for H_2 adsorption in porous MOFs.[22k] Pores of this size allow the dihydrogen molecule to interact with multiple portions of the framework rather than just one SBU or organic linker, increasing the interaction energy between the framework and H_2.[53] This increased interaction between adsorbing gas molecules and framework ingredients like SBU, linkers, etc. results into the improvement in isosteric heat (Q_{st}) of H_2 adsorption giving high uptake at low pressure.

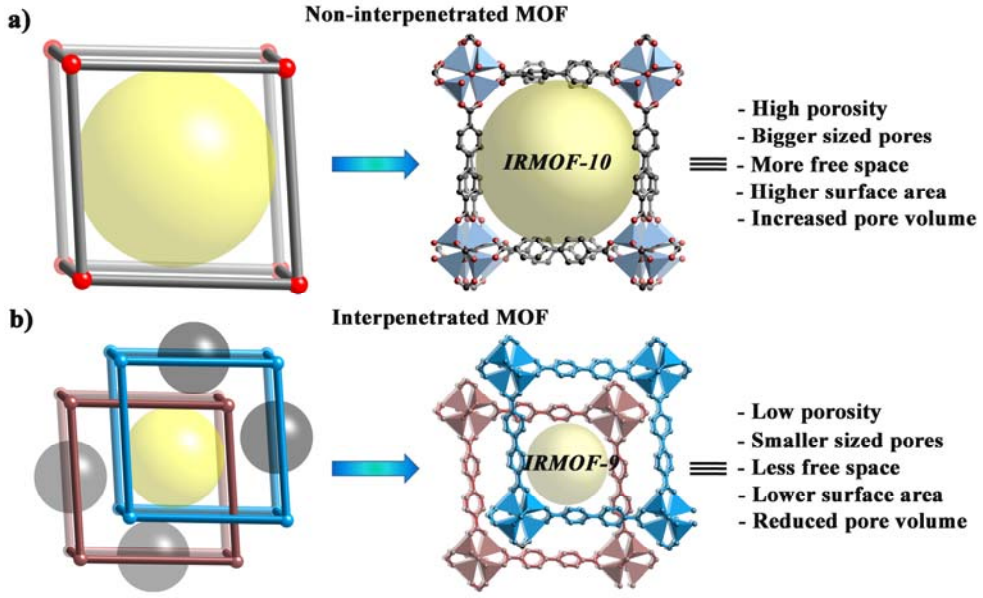

Figure 1.19 Structural representations of interpenetrated and non-interpenetrated MOFs IRMOF-9 and IRMOF-10 and its cartoon representation.

In general, if big pores should be generated in a MOF that is synthesized from an extended organic building block, an interpenetrated framework often resulted, since nature prefers to form a compact structure and reduce the free space. From the surface area, pore size and pore volume point of view, the phenomenon of interpenetration is contradictory (*Figure 1.19*). But as discussed earlier, for H_2 uptake rather than very large pores, small sized pores just fitable to the kinetic diameter of H_2 are favorable.[53b,53c] The typical effect of interpenetration on porosity is to subdivide large single pores, each bounded by the entire organic linker, into several smaller ones, each bounded by smaller portions of the organic linker. The dividation of bigger pores into the smaller ones creates the additional sites for H_2 adsorption, which causes the increment in the adsorption enthalpy and subsequently H_2 uptake.

A representative example of direct structural and H_2 uptake comparison between interpenetrated and non-interpenetrated MOFs for H_2 uptake has been reported in literature, wherein interpenetrated PCN-6 and non-interpenetrated PCN-6' having same structural components are utilized.[23b,47e] The interpenetrated MOF named PCN-6 contains the coppercarboxylate paddlewheel SBU linked by a trigonal triazine-based ligand, and the catenation isomerism is controlled by the presence or absence of oxalic acid, which acts as a template (*Figure 1.20*). The non-interpenetrated MOF named as PCN-6' has a higher overall porosity, based on the solvent-accessible volume calculated from the single-crystal X-ray structure. However, the interpenetrated PCN-6 exhibits 133 % increase in volumetric hydrogen uptake, and 29 % increase in gravimetric hydrogen uptake; when compared to the non-interpenetrated PCN-6'. In another example of interpenetrated MOF, a highly interpenetrated structure of $Zn_4O(L)_3$ (L= 6,6'-dichloro-2,2'-diethoxy-1,1'-binaphthyl-4,4'-dibenzoate) with small pores, fourfold

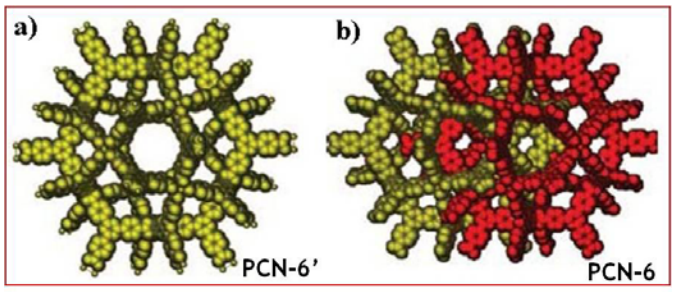

Figure 1.20 The structural representation of non-interpenetrated PCN-6′ and interpenetrated PCN-6 MOFs. [Reprinted with permission from (23b). Copyright 2006 American Chemical Society].

interpenetrating structure, open channels of less than 5 Å and BET surface area of only 502 m^2g^{-1} adsorbs 1.12 wt% of H_2 at room temperature and 48 bar.[42a] This H_2 uptake is very high compared to MIL-101 having hydrogen uptake of only 0.43 wt% under the same conditions, although it have high surface area of 5500 m^2g^{-1}.[54]

The importance of interpenetration for H_2 uptake was further confirmed by Grand Canonical Monte Carlo (GCMC) studies on two interpenetrated MOFs from the IRMOF series.[53] These studies demonstrated that the smaller pore size and multiplicity of networks allows the dihydrogen molecule to interact with the central phenyl rings of multiple linkers present therein, thus increasing the relevance of the non-coordinating portion of the ligand to H_2 storage.[53b] Both studies agree that the importance of a high heat of adsorption is greatest at low H_2 pressures, and that the overall pore volume becomes more important at higher loadings.[53c] The importance of interpenetration can be reflected in an increase in the H_2 uptake at 77 K and 1 atm as a result of an increase in the interaction energy and ΔH_{ads}.

1.5.5 Doping of Metal Nanoparticles and Alkali Metals in MOFs:

The doping of metal nanoparticles into the MOF matrix has been studied extensively for its various applications in catalysis, drug delivery and gas adsorption.[55] The phenomenon of H_2 adsorption in metal doped MOFs is also known as hydrogen spillover effect.[56] This hydrogen spillover effect has been known for a long time in the hydrogenation catalysts. It is defined as the dissociative chemisorption of hydrogen on the metal and the subsequent migration of atomic hydrogen onto the surface of the support such as alumina, carbon, etc.[56a] The support can be considered as the primary receptor for atomic hydrogen. It has been suggested that hydrogen spillover will play a much larger role in terms of H_2 storage at ambient temperatures, which is the preferred temperature for practical applications. These materials are getting attentions of researches due to the probable applications of these materials for H_2 storage at ambient conditions.

Hydrogen spillover in MOFs can be achieved by doping MOFs with metal nanoparticles.[57] As shown in Figure 1.21, the doing of nanoparticles into the MOFs can be achieved by two methods:

a. Incorporation of capped metal nanoparticles into the MOFs by mixing the

nanoparticles into the MOF precursor solutions during the synthesis. In this case, the formation of MOFs from its precursor solution takes place in presence of metal nanoparticles, wherein these nanoparticles gets incorporated inside MOF matrix.

b. Doping of metal nanoparticles into MOFs via post synthetic modifications. In this case, impregnation of metal nanoparticle precursor solution into the pre-synthesized MOF sample followed by successive reduction under mild conditions is desired.

The intra-framework generation of palladium nanoparticles (PdNPs) to enhance hydrogen storage was explored into SNU-3, where a redox-active ligand plays vital role was reported.[58a] The MOF resulting from the ligand catalyzed reduction of $Pd(NO_3)_2$ to nanoparticles of about 3.0 nm, showed increased H_2 uptake capacity at 77 K of 1.48 wt% compared to the 1.03 wt% of the pristine material, despite the decreased surface area and added weight.

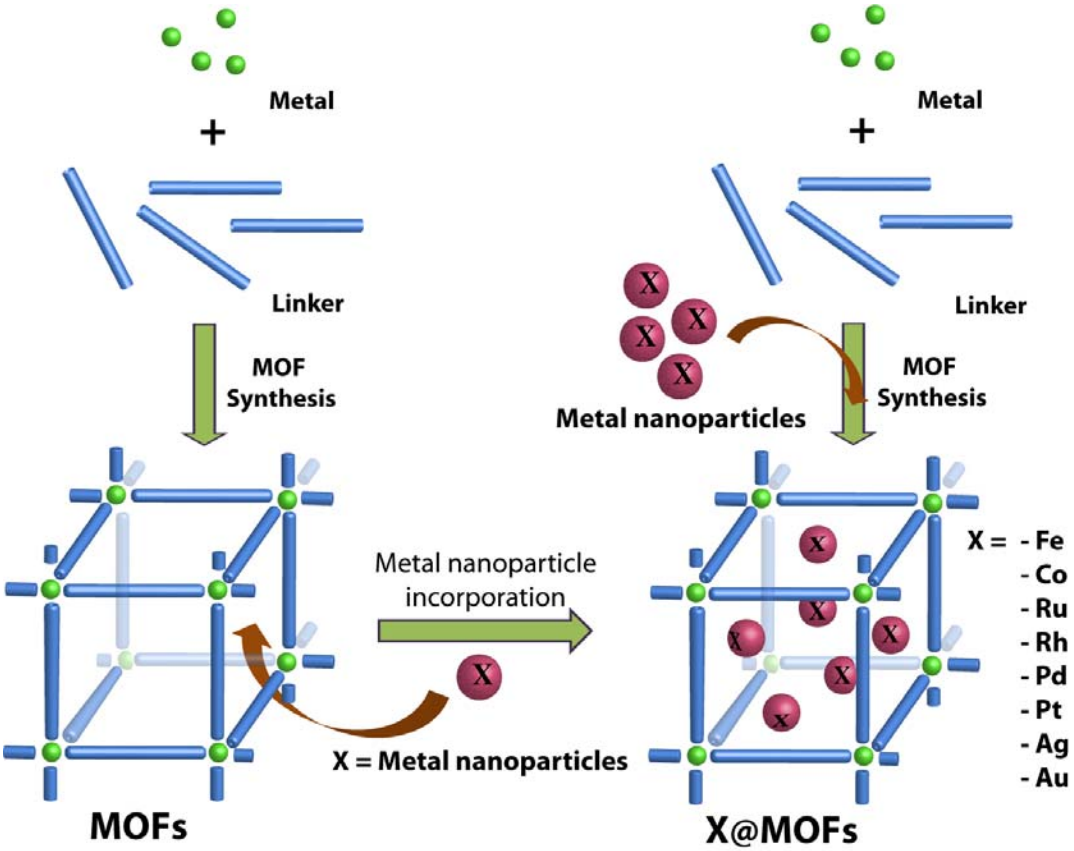

Figure 1.21 Schematic representations of metal nanoparticles doping into MOFs *via* direct incorporation during the synthesis or by post-synthetic modifications.

The further example of metal nanoparticles doping into MOFs includes the incorporation of PdNPs into MIL-100(Al).[58b] The fine distribution of approximately 2.0 nm in sized PdNPs generated in MOF framework induce a significant loss in BET surface area, total pore volume, and H_2 uptake at 77 K in the modified MOF. The nearly two fold increase in H_2 uptake observed at 298 K to 0.39 wt% has been partially attributed to β-hydride formation at low pressures and a spillover mechanism at pressures above 4.5 kPa (*Figure 1.22*). Increased H_2 storage by direct embedding of metal nanoparticles also has been reported for Pt-doped IRMOF-8, Pt-doped MOF-177, Ni-doped MIL-101, Pd-doped redoxactive MOF and Pd-doped MIL-100.[58c-58e] The aforementioned examples of metal nanoparticle doping into MOFs shows efficiency of these materials for H_2 uptake at room temperature and low pressure range. The effect of smaller size nanoparticles incorporation on the H_2 uptake properties has afforded the very high gas uptake capacities at room temperature.

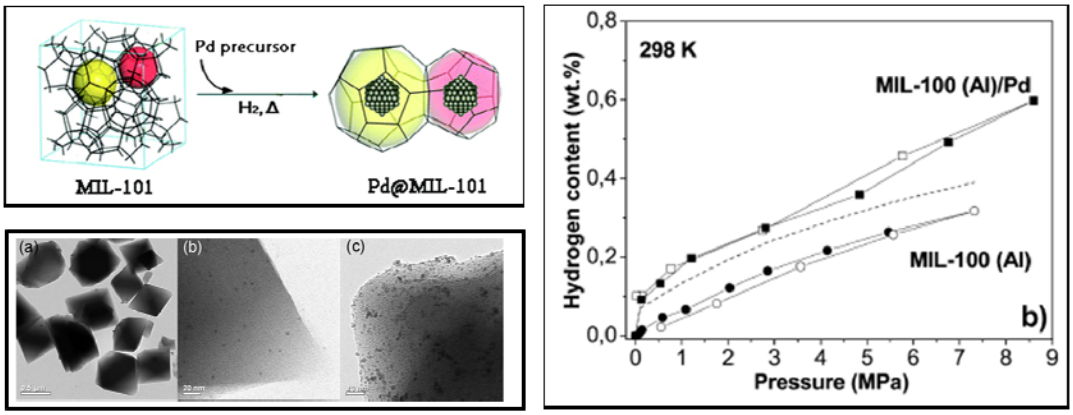

Figure 1.22 Schematic representations of synthesis of Pd@MIL-101 hybrid materials, TEM images and H_2 uptake studies at 298 K. Fine distribution of Pd nanoparticles into MIL-101 matrix is clearly visible in TEM images and clear improvement in H_2 uptake at room temperature for Pd nanoparticle doped MOF sample is visible. [Reprinted with permission from (58b). Copyright 2010 American Chemical Society].

In similar efforts to enhance the H_2 uptake at lower as well as ambient temperature, chemical doping into MOFs has received a considerable attention in the last few years, since calculations have shown that post-synthetic modification of MOFs with atomic or cationic metals like lithium can provide a route to surpass the DoE targets.[59] The computationally explored effects of lithium doping on various MOFs,

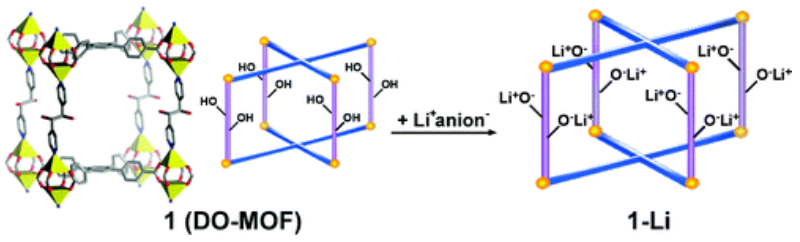

Figure 1.23 Doping of Li^+ achieved *via* solution method in DO-MOF by the means of free –OH groups present therein. [Reprinted with permission from (60c). Copyright 2009 American Chemical Society].

including IRMOF-14 showed that the single Li(0) per organic linker case can lead to a storage capacity that is 7.5 times larger than the un-doped IRMOF-14.[60a] The inclusion of hydroxyl group in MOF *via* linkers and then exchange of proton from the hydroxyl group with alkali metal ions like Li^+, Mg^{2+}, etc. has been reported.[59a,60b] As shown in Figure 1.23, the doping of Li^+ in DO-MOF has been achieved by the exchange of hydroxyl protons by replacing (*via* soaking) the initially present guest solvent molecules (DMF) with more volatile THF molecules and then stirring DO-MOF in an excess of $Li^+[O(CH_3)_3^-]$ in CH_3CN/THF (*Figure 1.23*).[60c] The extent of lithium loading was controlled by adjusting the stirring rate and time. In these doped MOFs, at low to intermediate levels of cation substitution, the activated metals appear to be naked, apart from alkoxide anchoring, resulting in unusual Q_{st} behavior and modest enhancement of H_2 sorption (~2 additional H_2 per added Li^+ at 77 K and 1 atm). Further, an analogue of MIL-53(Al) containing a free hydroxyl group that was post-synthetically modified to the lithium alkoxide functionalized MOF.[60d] The lithium doped samples prepared via aforementioned method showed a significant increase in hydrogen uptake capacity from 0.50 (for prestine MOF) to 1.7 wt% at 77 K, and doubled heats of adsorption at low coverage (5.8 *vs.* 11.6 kJ mol^{-1}).

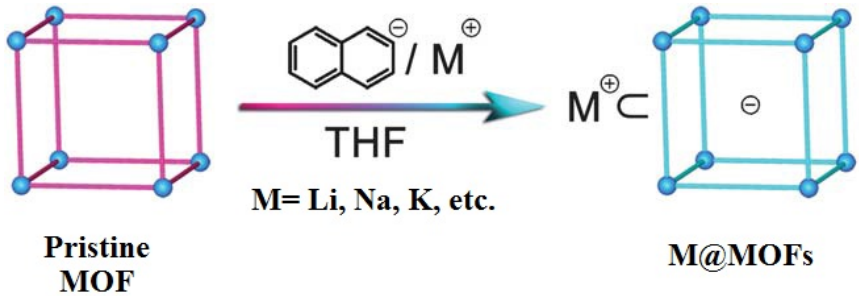

Figure 1.24 Representative method of doping metals into MOFs and chemical reduction of MOF using metal naphthalenide in THF (M = Li, Na, K). [Reprinted with permission from (59c). Copyright 2008 American Chemical Society].

As showed in Figure 1.24, an alternate strategy was employed for the chemical reduction of MOFs and doping it with alkali metal cations (Li^+, Na^+, K^+) for improved H_2 uptake.[59c] The average ΔH_{ads} value of 5.96 kJ mol^{-1} was observed for $Li^+@Zn_2(NDC)_2(diPyNI)$ case and highest H_2 uptake of 1.54 wt% was observed as a result of the K^+0.06/ligand doping, despite the greater contribution to the molecular weight of the framework. From the aforementioned examples of alkali metal doping into the MOFs, it is visual that high H_2 uptake can be achieved into the MOFs at lower as well as higher temperature range.

1.6 Conclusions:

As discussed in the Chapter, MOFs have very intriguing structural aspects in addition to their high surface area's and pore volumes. These properties makes MOFs suitable candidate for H_2 adsorption over other literature reported materials like porous carbons, metal hydrides, zeolites, porous silica materials, etc. Highly crystalline structures with predictable structures, tunable pore sizes, and functionalizable pores with functional groups incorporated *via* linkers or post-synthetic modification makes MOFs as eligible materials for gas adsorption, gas separation, catalysis, drug delivery, luminescence and sensors, etc. The attempts followed for improvement in H_2 uptake capacities in MOFs includes increasing pore size, pore volume and surface area, creation of open metal sites, MOF functionalization, interpenetration or catenation, doping of metal nanoparticles and alkali metals in MOFs, etc. Despite of the promising achievements in terms of H_2 storage in MOFs, the weak interaction between H_2 molecules and framework ingredients is the main obstacle for its further application and achievement of DoE targets. From the literature survey and expert reviews, it seems that in order to reach the DoE set targets for room temperature adsorption a strong initial heat of adsorption and large surface area and pore volume is desirable. This may be achieved by synthesis of highly porous MOFs with the incorporation of functional groups like –OH, –F, $–CF_3$, $–SO_3H$, –COOH, etc. *via* linkers or post-synthetic modifications. The initial heat of adsorption necessary for high H_2 uptake at low pressure can be achieved *via* highly electronegative groups present into the MOF pores and further uptake at high pressure can be accomplished by presence of high porosity.

1.7 References and Notes:

1. (a) D. Ahuja, M. Tatsutani, **2008**, *Sustainable Energy for Developing Countries,* Trieste: TWAS, Academy of Sciences for the Developing World). (b) W. Hafele, W. Sassin, *Resources and Endowments, An Outline of Future Energy Systems*, P.W. Hemily, M.N. Ozdas (eds.), *Science and Future Choice,* (Oxford: Clarendon Press, **1979**). (c) P. Ramchandra, D. Boucar, **2011**, *Green Energy and Technology*. Springer, London Dordrecht Heidelberg New York. (d) Intergovernmental Panel on Climate Change (**2007**), *Climate Change 2007,* Fourth Assessment Report, http://www.ipcc.ch/ipccreports/assessments-reports.html.

2. (a) J. Grigg, *Arch Dis Child,* **2002**, *86*, 79. (b) D. Lüthi, M. Le Floch, B. Bereiter, T. Blunier, J. M. Barnola, U. Siegenthaler, D. Raynaud, J. Jouzel, H. Fischer, K. Kawamura, T. F. Stocker, **2008**, *Nature, 453*, 379. (c) Health Effects of Climate Change in the UK (**2008**), UK Department of Health.

3. International Energy Outlook, (**2008**), *US Energy Information Administration*, http://www.eia.doe.gov/oiaf/ieo/highlights.html.

4. N.H. Stern, (**2007**), T*he Economics of Climate Change: The Stern Review,* Cambridge University Press.

5. (a) Disadvantages of wind energy, factors you need to consider, http://www.advantagesofsolarenergy4all.com/disadvantages-of-wind-energy.html#.U4JS-PlXOgQ. (b) H. Gunerhan, **2008**, *Environmental Impacts from the Solar Energy Systems*, http://www.lib.sie.edu.cn/tools/ebsco/ty2.pdf. (c) R. Sherif, **2009**, Concentrating Solar Energy-Technologies and Markets Overview, http://www.csmantech.org/Digests/2009/2009%20 Papers/3.2.pdf.

6. (a) A. Haryanto, S. Fernando, N. Murali, S. Adhikari, *Energy Fuels* **2005**, *19*, 2098. (b) R. K. Ahluwalia, T. Q. Hua, *Int. J. Hydrogen Energy*, **2011**, 37, 2891. (c) J. R. Bartels, M. B. Pate, *Int. J. Hydrogen Energy*, 35, 8371.

7. K. Lee, Economic feasibility of producing hydrogen using excess electricity from wind turbines on the Big Island of Hawaii, World renewable energy congress VIII, Denver, 3 September, 2004. http://www.sentech.org/Lee,%20K_Economic%20Feasibility%20Hawaii.pdf.

8. (a) J. Yang, A. Sudik, C. Wolverton, D. Siegel, *J. Chem. Soc. Rev.* **2010**, *39*, 656. (b) Based on their lower heating values, 1 kg H_2 = 120.21 MJ; 1 L low-sulfur gasoline = 31.67 MJ.

9. (a) K. L. Lim, H. Kazemian, Z. Yaakob, W. R. W. Daud, *Chem. Eng. Technol.*, **2010**, *33*,

213. (b) L. Zhou, *Renewable and Sustainable Energy Reviews*, **2005**, *9*, 395.

10. The DOE targets for the gravimetric and volumetric system for near-ambient temperature (from –40 to 85 °C) and moderate pressure (less than 100 bar) are 6.0 wt % (45 g/L) for the year 2010 and 9.0 wt% (81 g/L) for 2015. (a) DOE Office of Energy Efficiency and Renewable Energy Hydrogen, Fuel Cells & Infrastructure Technologies Program Multi-Year Research, Development and Demonstration Plan, available at http://www.eere.energy.gov/hydrogenandfuelcells/mypp. (b) FY-2006 Annual Progress Report for the DOE Hydrogen Program, **2006**, available at http://www.hydrogen.energy.gov/annual_progress.html. (c) S. Satyapal, *et al.* FY **2006** DOE Hydrogen Program Annual Merit Review and Peer Evaluation Meeting Proceedings, Plenary Session, available at http://www.hydrogen.energy.gov/annual_review06_plenary.html.

11. (a) C. Liu, Y. Y. Fan, M. Liu, H. T. Cong, H. M. Cheng, M. S. Dresselhaus, *Science*, **1999**, *286*, 1127. (b) P. Chen, X. Wu, J. Lin, K. L. Tan, Science, **1999**, *285*, 91. (c) T. Huang, *Nanotechnology That Will Change the World*; Enlighten Noah Publishing: **2002**, p 38. (d) R. T. Yang, *Adsorbents: Fundamentals and Applications*; Wiley: New York, **2003**, p 280. (e) S. Hynek, W. Fuller, J. Bentley, *Int. J. Hydrogen Energy* **1997**, *22*, 601. (f) H. Wang, Q. Gao, J. Hu, *J. Am. Chem. Soc.* **2009**, *131*, 7016. (g) Y. Fukai, *The Metal Hydrogen System*; U. Gonser, Ed.; Springer Series in Material Science; Springer-Verlag: New York, **1993**. (h) H. Imamura, N. Sakasai, *J. Alloys Compd*. **1995**, *231*, 810. (i) H. Imamura, N. Sakasai, Y. Kajii, *J. Alloys Compd*. **1996**, *232*, 218. (j) H. Imamura, N. Sakasai, T. Fujinaga, *J. Alloys Compd*. **1997**, *253-254*, 34. (k) G. Sandrock, *J. Alloys Compd*. **1999**, *293*, 877. (l) F. Schuth, B. Bogdanovi, M. Felderhoff, *Chem. Commun*. **2004**, 2249.

12. (a) I. K. Shah, P. Pre, B. J. Alappat, *Chem Sci Trans.*, **2013**, *2*, 1078. (b) I. K. Shah, P. Pre, B. J. Alappat, *Regeneration of adsorbents spent with Volatile Organic Compounds (VOCs)*, In Proceedings of International Conference on Environment and Industrial Innovation, Kualalumpur, **2011**.

13. (a) K. Sumida, D. L. Rogow, J. A. Mason, T. M. McDonald, E. D. Bloch, Z. R. Herm, T.-H. Bae, J. R. Long, *Chem. Rev.*, **2012**, *112*, 724. (b) C. Zou, Z. Zhang, X. Xu, Q. Gong, J. Li, C.-D. Wu, *J. Am. Chem. Soc.*, **2012**, *134*, 87. (c) Z. R. Herm, B. M. Wiers, J. A. Mason, J. M. van Baten, M. R. Hudson, P. Zajdel, C. M. Brown, N. Masciocchi, R. Krishna, J. R. Long, *Science*, **2013**, *360*, 960. (d) D.-X. Xue, A. J. Cairns, Y. Belmabkhout, L. Wojtas, Y. Liu, M. H. Alkordi, M. Eddaoudi, *J. Am. Chem. Soc.*, **2013**, *135*, 7660. (e) H. Deng, S. Grunder, K. E. Cordova, C. Valente, H. Furukawa, M. Hmadeh, F. Gándara, A. C. Whalley, Z. Liu, S. Asahina, H.

Kazumori, M. O'Keeffe, O. Terasaki, J. F. Stoddart, O. M. Yaghi, *Science*, **2012**, *336*, 1018. (f) K. J. Gagnon, H. P. Perry, A. Clearfield, *Chem. Rev.*, **2012**, *112*, 1034.

14. (a) M. Schröder, *Functional Metal-Organic Frameworks: Gas Storage, Separation and Catalysis*; (**2010**), Springer Berlin Heidelberg. (b) L. R. McGillivray, *Metal-Organic Frameworks: Design and Application*; (**2010**), Wiley-Blackwell.

15. (a) N. Stock, S. Biswas, *Chem. Rev.*, **2012**, *112*, 933. (b) J.-S. Chang, Y. K. Hwang, S. H. Jhung, Patent **WO2008/066293 A1**. (c) Q. M. Wang, D. Shen, M. Bülow, M. L. Lau, S. Deng, F. R. Fitch, N. O. Lemcoff, J. Semanscin, *Microporous Mesoporous Mater.* **2002**, *55*, 217. (d) M. Díaz-García, Á. Mayoral, I. Díaz, M. Sánchez-Sánchez, *Crystal Growth & Design,* **2014** *14*, 2479. (e) T. Ahnfeldt, J. Moellmer, V. Guillerm, R. Staudt, C. Serre, N. Stock, *Chem.—Eur. J.,* **2011**, *23*, 6462. (f) T. Friscic, D. G. Reid, I. Halasz, R. S. Stein, R. E. Dinnebier, M. J. Duer, *Angew. Chem., Int. Ed.* **2010**, *49*, 712. (g) U. Mueller, H. Puetter, M. Hesse, H. Wessel, **WO 2005/049892**.

16. (a) J. Lee, Z. Kim, T. Hyeon, *Adv. Mater.*, **2006**, *18*, 2073. (b) B. Sakintuna, Y. Yürüm, *Ind. Eng. Chem. Res.*, **2005**, *44*, 2893.

17. M. O'Keeffe, O. M. Yaghi, *Chem. Rev.*, **2012**, *112*, 675.

18. M. P. Suh, H. J. Park, T. K. Prasad, D.-W. Lim, *Chem. Rev.*, **2012**, *112*, 782.

19. (a) D.-Y. Hong, Y. K. Hwang, C. Serre, G. Férey, J.-S. Chang, *Adv. Funct. Mater.*, **2009**, *19*, 1537. (b) H. Li, M.; Eddaoudi, M.; O'Keeffe, O. M. Yaghi, *Nature,* **1999**, *402*, 276.

20. N. L. Rosi, M. Eddaoudi, D. T. Vodak, J. Eckert, M. O'Keeffe, O. M. Yaghi, *Science*, **2003**, *300*, 1127.

21. (a) X. –S. Wang, S. Ma, P. M. Forster, D. Yuan, J. Eckert, J. J. Lopez, B. J. Murphy, J. B. Parise, H. –C. Zhou *Angew. Chem. Int. Ed.* **2008**, *47*, 7263. (b) Z. Guo, H. Wu, G. Srinivas, Y. Zhou, S. Xiang, Z. Chen, Y. Yang, W. Zhou, M. O'Keeffe, B. Chen, *Angew. Chem. Int. Ed.* **2011**, *50*, 3178. (c) S. Ma, D. Sun, J. M. Simmons, C. D. Collier, D. Yuan, H.-C. Zhou, *J. Am. Chem. Soc.*, **2008**, *130*, 1012. (d) X. Lin, I. Telepen, A. J. Blake, A. Dailly, C. M. Brown, J. M. Simmons, M. Zoppi, G. S. Walker, K. M. Thomas, T. J. Mays, P. Hubberstey, N. R. Champness, M. Schroder, *J. Am. Chem. Soc.*, **2009**, *131*, 2159. (e) X. S. Wang, S. Ma, K. Rauch, J. M. Simmons, D. Yuan, X. Wang, T. Yildirim, W. C. Cole, J. J. Lspez, A. de Meijere, H. C. Zhou, *Chem. Mater.,* **2008**, *20*, 3145. (f) X. Lin, J. H. Jia, X. B. Zhao, K. M. Thomas, A. J. Blake, G. S. Walker, N. R. Champness, P. Hubberstey, M. Schroder, *Angew. Chem., Int. Ed.,* **2006**, *45*, 7358. (g) C. Tan, S. Yang, N. R. Champness, X. Lin, A. J. Blake, W. Lewis, M.

Schroder, *Chem. Commun.,* **2011**, 4487. (h) B. Chen, N. W. Ockwig, A. R. Millward, D. S. Contreras, O. M. Yaghi, *Angew. Chem. Int. Ed.* **2005**, *44*, 4745. (i) M. Dinca, W. S. Han, Y. Liu, A. Dailly, C. M. Brown, J. R. Long, *Angew. Chem., Int. Ed.*, **2007**, *46*, 1419. (j) F. Nouar, J. F. Eubank, T. Bousquet, L. Wojtas, M. J. Zaworotko, M. Eddaoudi, *J. Am. Chem. Soc.*, **2008**, *130*, 1833. (k) X. Gu, Z. –H. Lu, Q. Xu, *Chem. Commun.*, **2010**, *46*, 7400.

22. (a) O. K. Farha, A. O. Yazaydın, I. Eryazici, C. D. Malliakas, B. G. Hauser, M. G. Kanatzidis, S. T. Nguyen, R. Q. Snurr, J. T. Hupp, *Nature Chem.* **2010**, *2*, 944. (b) Y. Yan, X. Lin, S. Yang, A. J. Blake, A. Dailly, N. R. Champness, P. Hubbersteya, M. Schroder, *Chem. Commun*., **2009**, 1025. (c) D. Yuan, D. Zhao, D. Sun, Hong-Cai Zhou, *Angew. Chem. Int. Ed.* **2010**, *49*, 5357. (d) M. Dinca, A. Dailly, Y. Liu, C. M. Brown, D. A. Neumann, J. R. Long, *J. Am. Chem. Soc.* **2006**, 128, 16876. (e) X. Lin, J. Jia, X. Zhao, K. M. Thomas, A. J. Blake, G. S. Walker, N. R. Champness, P. Hubberstey, M. Schroder, *Angew. Chem.* **2006**, 118, 7518. (f) O. K. Farha, K. L. Mulfort, J. T. Hupp, *Inorg. Chem.,* **2008**, *47*, 10223. (g) O. K. Farha, A. M. Spokoyny, K. L. Mulfort, M. F. Hawthorne, C. A. Mirkin, J. T. Hupp, *J. Am. Chem. Soc.*, **2007**, *129*, 12680. (h) D. F. Sava, V.C. Kravtsov, J. Eckert, J. F. Eubank, F. Nouar, M. Eddaoudi, *J. Am. Chem. Soc.*, **2009**, *131*, 10394. (i) A. G. Wong-Foy, O. Lebel, A. J. Matzger *J. Am. Chem. Soc.* **2007**, *129*, 15740. (j) S. R. Caskey, A. G. Wong-Foy, A. J. Matzger, *J. Am. Chem. Soc.* **2008**, *130*, 10870. (k) H. Chun, D. N. Dybtsev, H. Kim, K. Kim, *Chem. Eur. J.* **2005**, *11*, 3521.

23. (a) X. B. Zhao, B. Xiao, A. J. Fletcher, K. M. Thomas, D. Bradshaw, M. J. Rosseinsky, *Science* **2004**, *306*, 1012. (b) D. Sun, S. Ma, Y. Ke, D. J. Collins, H. C. Zhou, *J. Am. Chem. Soc.* **2006**, *128*, 3896. (c) Y. Yan, I. Telepeni, S. Yang, X. Lin, W. Kockelmann, A. Dailly, A. J. Blake, W. Lewis, G. S. Walker, D. R. Allan, S. A. Barnett, N. R. Champness, M. Schroder, *J. Am. Chem. Soc.* **2010**, *132*, 4092. (d) S.-T. Zheng, J. T. Bu, Y. Li, T. Wu, F. Zuo, P. Feng, X. Bu, *J. Am. Chem. Soc.* **2010**, *132*, 17062. (e) F. Debatin, A. Thomas, A. Kelling, N. Hedin, Z. Bacsik, I. Senkovska, S. Kaskel, M. Junginger, H. Muller, U. Schilde, C. Jager, A. Friedrich, H. J. Holdt, *Angew. Chem. Int. Ed.* **2010**, *49*, 1258. (f) R. Vaidhyanathan, S. S. Iremonger, K. W. Dawson, G. K. H. Shimizu, *Chem. Commun*., **2009**, 5230. (g) O. K. Farha, A. M. Spokoyny, K. L. Mulfort, S. Galli, J. T. Hupp, C. A. Mirkin, *small*, **2009**, *5*, 1727. (h) T. Panda, P. Pachfule, Y. Chen, J. Jiang, R. Banerjee *Chem. Commun*., **2011**, 2011. (i) J. W. Yoon, S. H. Jhung, Y. K. Hwang, S. M. Humphrey, P. T. Wood, J. S. Chang, *Adv. Mater.* **2007**, *19*, 1830. (j) A. Demessence, D. M. D'Alessandro, M. L. Foo, J. R. Long, *J. Am. Chem. Soc.* **2009**, *131*, 8784. (k) J. An, S. J. Geib, N. L. Rosi *J. Am. Chem. Soc.* **2010**, *132*, 38. (l) K. S. Park, Z. Ni, A. P. Cote, J. Y. Choi, R. D. Huang, F. J. Uribe-Romo, H. K. Chae, M. O'Keeffe, O. M. Yaghi, *Proc. Natl. Acad.Sci. U. S. A.*, **2006**, *103*, 10186. (m) J. L. C. Rowsell, A. R. Millward, K. S. Park, O.

M. Yaghi, *J. Am. Chem. Soc.* **2004**, *126*, 5666. (n) P. Pachfule, Y. Chen, J. Jiang, R. Banerjee, *J. Mater. Chem.,* **2011**, *21*, 17737.

24. (a) F. Barzagli, F. Mani, M. Peruzzini, *Energy Environ. Sci.* **2010**, *3*, 772. (b) C.-H. Yu, C.-H. Huang, C.-S. Tan, *Aerosol Air Qual. Res.* **2012**, *12*, 745. (c) W. M. Budzianowski, Value-added carbon management technologies for low CO_2 intensive carbon based energy vectors, *Energy*, **2012**, 37.

25. (a) A.-H. Lu, G.-P. Hao, *Annu. Rep. Prog. Chem., Sect. A: Inorg. Chem.*, **2013**,*109*, 484. (b) A.-H. Lu, S. Dai, Porous Materials for Carbon Dioxide Capture, Springer-Verlag Berlin Heidelberg, **2014**.

26. (a) K. Sumida, D. L. Rogow, J. A. Mason, T. M. McDonald, E. D. Bloch, Z. R. Herm, T.-H. Bae, J. R. Long, *Chem. Rev.*, **2012**, *112*, 724. (b) Y. Liu, U. Z. Wang, H.-C. Zhou, *Greenhouse Gases: Sci. Technol.* **2012**, *2*, 239. (c) J. Liu, P. K. Thallapally, B. P. McGrail, D. R. Brown, J. Liu, *Chem. Soc. Rev.*, **2012**, *41*, 2308. (d) Z. Zhang, Y. Zhao, Q. Gong, Z. Li, J. Li, *Chem. Commun.*, **2013**, *49*, 653.

27. (a) A. R. Millward, O.M. Yaghi, *J. Am. Chem. Soc.*, **2005**, *127*, 17998. (b) P. D. C. Dietzel, R. E. Johnsen, H. Fjellvag, S. Bordiga, E. Groppo, S. Chavan, R. Blom, *Chem. Commun.* **2008**, 5125. (c) T. M. McDonald, D. M. D'Alessandro, R. Krishna, J. R. Long, *Chem. Sci.* **2011**, *2*, 2022. (d) S. S.-Y. Chui, S. M.-F. Lo, J. Charmant, A. G. Orpen, I. D. Williams, *Science*, **1999**, *283*, 1148. (e) D. Britt, H. Furukawa, B. Wang, T. G. Glover, O. M. Yaghi, *Proc. Natl. Acad. Sci. U. S. A.*, **2009**, *106*, 20637. (f) P. Nugent, Y. Belmabkhout, S. D. Burd, A.J. Cairns, R. Luebke, K. Forrest, T. Pham, S. Ma, B. Space, L. Wojtas, M. Eddaoudi, M. J. Zaworotko, *Nature*, **2013**, *495*, 80.

28. (a) O. K. Farha. C. D. Malliakas, M. G. Kanatzidis, J. T. Hupp, *J. Am. Chem. Soc.* **2010**, *132*, 950. (b) Y.-S. Bae, O. K. Farha, J. T. Hupp, R. Q. Snurr, *J. Mater. Chem.*, **2009**, *19*, 213. (c) Y. S. Bae, O. K. Farha, A. M. Spokoyny, C. A. Mirkin, J. T. Hupp, R. Q. Snurr, *Chem. Commun*., **2008**, 4135. (d) K. L. Mulfort, O. K. Farha, C. D. Malliakas, M. G. Kanatzidis, J. T. Hupp, *Chem. Eur. J.* **2010**, *16*, 276. (e) H. S. Choi, M. P. Suh, *Angew. Chem*. **2009**, *121*, 6997. (f) J. An, N. L. Rosi, *J. Am. Chem. Soc.* **2010**, *132*, 5578. (g) R. Banerjee, H. Furukawa, D. Britt, C. Knobler, M. O'Keeffe, O. M. Yaghi, *J. Am. Chem. Soc.* **2009**, *131*, 3875. (h) W. Morris, B. Leung, H. Furukawa, O. K. Yaghi, N. He, H. Hayashi, Y. Houndonougbo, M. Asta, B. B. Laird, O. M. Yaghi, *J. Am. Chem. Soc.*, **2010**, *132*, 11006.

29. (a) T. A. Makal, J. R. Li, W. Lu, H.-C. Zhou, *Chem. Soc. Rev.*, **2012**, *41*, 7761. (b) K.

Konstas, T. Osl, Y. Yang, M. Batten, N. Burke, A. J. Hill, M. R. Hill, *J. Mater. Chem.*, **2012**, *22*, 16698. (c) Y. Peng, V. Krungleviciute, I. Eryazici, J. T. Hupp, O. K. Farha, T. Yildirim, *J. Am. Chem. Soc.*, **2013**, *135*, 11887.

30. See DOE MOVE program at https://arpa-e-foa.energy.gov/.

31. (a) V. C. Menon, S. Komarneni, *J. Porous Mater.* **1998**, *5*, 43. (b) N. P. Stadie, M. Murialdo, C. C. Ahn, B. Fultz, *J. Am. Chem. Soc.*, **2013**, *135*, 990. (c) G. Férey, *Chem. Soc. Rev.*, 2008, **37**, 191. (d) R. Xu, W. Pang, J. Yu, Q. Huo, J. Chen, *Chemistry of Zeolites and Related Porous Materials: Synthesis and Structure*, John Wiley & Sons, Asia, Singapore, **2007**. (e) S. M. Auerbach, K. A. Carrado, P. K. Dutta, *Handbook of Zeolite Science and Technology*, Marcel Dekker, Inc., New York, **2003**. (f) D. W. Beck, *Zeolite Molecular Sieves*, John Wiley & Sons, New York, **1974**.

32. M. Kondo, T. Yoshitomi, H. Matsuzaka, S. Kitagawa, K. Seki, *Angew. Chem., Int. Ed.*, **1997**, *36*, 1725.

33. (a) Y. He, W. Zhou, R. Krishna, B. Chen, *Chem. Commun.* **2012**, *48*, 11813. (b) H. Wu, J. M. Simmons, Y. Liu, C. M. Brown, X. -S. Wang, S. Ma, V. K. Peterson, P. D. Southon, C. J. Kepert, H.-C. Zhou, Y. Yildirim, W. Zhou, *Chem.-Eur. J., 2010*, **16**, 5205. (c) K. Seki, *Chem. Commun*. **2001**, 1496. (d) S. Bourrelly, P. L. Llewellyn, C. Serre, F. Millange, T. Loiseau, G. Ferey, *J. Am. Chem. Soc.* **2005**, *127*, 13519. (e) P. L. Llewellyn, S. Bourrelly, C. Serre, A. Vimont, M. Daturi, L. Hamon, G. D. Weireld, J.-S. Chang, D.-Y. Hong, Y. K. Hwang, S. H. Jhung, G. Ferey, *Langmuir* **2008**, *24*, 7245.

34. (a) H. Deng, C. J. Doonan, H. Furukawa, R. B. Ferreira, J. Towne, C. B. Knobler, B. Wang, O. M. Yaghi, *Science*, **2010**, *327*, 846. (b) Z. Wang, S. M. Cohen, *Chem. Soc. Rev.*, **2009**, *38*, 1315. (c) F. A. Almeida Paz, J. Klinowski, S. M. F. Vilela, J. P. C. Tome, J. A. S. Cavaleiro, J. Rocha, *Chem. Soc. Rev.*, **2012**, *41*, 1088. (d) M. Servalli, M. Ranocchiari, J. A. Van Bokhoven, *Chem. Commun.*, **2012**, *48*, 1904. (e) K. K. Tanabe, S. M. Cohen, *Chem. Soc. Rev.*, **2011**, *40*, 498. (f) M. Kim, J. F. Cahill, K. A. Prather, S. M. Cohen, *Chem. Commun.*, **2011**, *47*, 7629. (g) S. M. Cohen, *Chem. Rev.*, **2012**, *112*, 970.

35. (a) I. Senkovska, S. Kaskel, *Microporous Mesoporous Mater.*, **2008**, *112*, 108. (b) S. Cavenati, C. A. Grande, A. R. E. Rodrigues, C. Kiener, U. Muüller, *Ind. Eng. Chem. Res.*, **2008**, *47*, 6333. (c) W. Zhou, H. Wu, M. R. Hartman, T. Yildirim, *J. Phys. Chem. C*, **2007**, *111*, 16131. (d) H. Wu, W. Zhou, T. Yildirim, *J. Am. Chem. Soc.*, **2009**, *131*, 4995.

36. (a) M. Yoon, R. Srirambalaji, K. Kim, *Chem. Rev.*, **2012**, *112*, 1196. (b) Y. Liu, W. Xuan,

Y. Cui, *Adv. Mater.*, **2010**, *22*, 4112.

37. (a) B. Kesanli, W. Lin, *Coord. Chem. Rev.* **2003**, *246*, 305. (b) W. Lin, *J. Solid State Chem.* **2005**, 178, 2486. (c) H. L. Ngo, W. Lin, *Top. Catal.* **2005**, *34*, 85. (d) L.; Ma, C. Abney, W. Lin, *Chem. Soc. Rev.* **2009**, *38*, 1248. (e) Y. Liu, W. Xuan, Y. Cui, *Adv. Mater.* **2010**, *22*, 4112. (f) W. Lin, *Top. Catal.* **2010**, *53*, 869. (g) K. Kim, M. Banerjee, M. Yoon, S. Das, *Top. Curr. Chem.* **2010**, *293*, 115.

38. (a) A. U. Czaja, N. Trukhan, U. Muller, *Chem. Soc. Rev.*, **2009**, *38*, 1284. (b) H.-L. Jiang, T. Akita, T. Ishida, M. Haruta, Q. Xu, *J. Am. Chem. Soc.*, **2011**, *133*, 1304. (c) F. X. Llabres i Xamena, A. Abad, A. Corma, H. Garcia, *J. Catal.*, **2007**, *250*, 294. (d) S. Hermes, M. Schroter, R. Schmid, L. Khodeir, M. Muhler, A. Tissler, R. Fischer, *Angew. Chem., Int. Ed.*, **2005**, *44*, 6237. (e) J. Lee, O. K. Farha, J. Roberts, K. A. Scheidt, S. T. Nguyen, J. T. Hupp, *Chem. Soc. Rev.*, **2009**, *38*, 1450.

39. (a) B. F. Sels, D. E. De Vos, P. A. Jacobs, *J. Am. Chem. Soc.*, **2001**, *123*, 8350. (b) Y.-J. Kim, D.-W. Park, *J. Nanosci. Nanotechnol.*, **2013**, *13*, 2307. (c) K. Brown, S. Zolezzi, P. Aguirre, D. Venegas-Yazigi, V. Paredes-García, R. Baggio, M. A. Novak, E. Spodine, *Dalton Trans.*, **2009**, 1422. (d) J. Gascon, U. Aktay, M. D. Hernandez-Alonso, G. P. M. van Klink, F. Kapteijn, *J. Catal.*, **2009**, *261*, 75. (e) P. Kasinathan, Y.-K. Seo, K.-E. Shim, Y. K. Hwang, U. H. Lee, D. W. Hwang, D.-Y. Hong, S. B. Halligudi, J.-S. Chang, *Bull. Korean Chem. Soc.*, **2011**, *32*, 2073. (f) I. Luz, A. León, M. Boronat, F. X. Llabrés i Xamena, A. Corma, *Catal. Sci. Technol.*, **2013**, *3*, 371. (g) A. M. Shultz, O. K. Farha, J. T. Hupp, S.T. Nguyen, *J. Am. Chem. Soc.*, **2009**, *131*, 4204. (h) S. Wang, W. Yao, J. Lin, Z. Ding, X. Wang, *Angew. Chem., Int. Ed.*, **2014**, *53*, 1034.

40. C. D. Wu, A. Hu, L. Zhang, W. Lin, *J. Am. Chem. Soc.*, **2005**, *127*, 8940.

41. (a) D. J. Collins, H.-C. Zhou, *J. Mater. Chem.*, **2007**, *17*, 3154. (b) J. Sculley, D. Yuan, H.-C. Zhou, *Energy Environ. Sci.*, **2011**, *4*, 2721.

42. (a) B. Kesanli, Y. Cui, M. R. Smith, E. W. Bittner, B. C. Bockrath, W. Lin, *Angew. Chem., Int. Ed.*, **2005**, *44*, 72. (b) S. T. Batten, R. Robson, *Angew. Chem., Int. Ed.*, **1998**, *37*, 1460.

43. H. J. Park, D.-W. Lim, W. S. Yang, T.-R. Oh, M. P. Suh, *Chem. Eur. J.*, **2011**, *26*, 7251.

44. (a) Y. K. Hwang, D.-Y. Hong, J.-S. Chang, S. H. Jhung, Y.-K. Seo, J. Kim, A. Vimont, M. Daturi, C. Serre, G. Ferey, *Angew. Chem., Int. Ed.* **2008**, *47*, 4144. (b) P. D. C. Dietzel, V. Besikiotis, R. Blom, *J. Mater. Chem.*, **2009**, *19*, 7362.

45. (a) W. Zhou, H. Wu, T. Yildirim, *J. Am. Chem. Soc.*, **2008**, *130*,15268. (b) N. Nijem, J.-F. O. Veyan, L. Kong, H. Wu, Y. Zhao, J. Li, D. C. Langreth, Y. J. Chabal, *J. Am. Chem. Soc*., **2010**, *132*, 14834. (c) S. A. FitzGerald, J. Hopkins, B. Burkholder, M. Friedman, J. L. C. Rowsell, *Phys. Rev. B: Condens. Matter Mater. Phys.*, **2010**, *81*, 104305. (d) P. D. C. Dietzel, P. A. Georgiev, J. Eckert, R. Blom, T. Strassle, T. Unruh, *Chem. Commun.*, **2010**, *46*, 4962. (e) J. G. Vitillo, L. Regli, S. Chavan, G. Ricchiardi, G. Spoto, P. D. C. Dietzel, S. Bordiga, A. Zecchina, *J. Am. Chem. Soc.*, **2008**, *130*, 8386.

46. Y.-G. Lee, H. R. Moon, Y. E. Cheon, M. P. Suh, *Angew. Chem. Int. Ed.* **2008**, *47*, 7741.

47. (a) K. Sumida, C. M. Brown, Z. R. Herm, S. Chavan, S. Bordiga, J. R. Long, *Chem. Commun.*, **2011**, *47*, 1157. (b) H. R. Moon, N. Kobayashi, M. P. Suh, *Inorg. Chem.*, **2006**, *45*, 8672. (c) K. Sumida, J.-H. Her, M. Dinca, L. J. Murray, J. M. Schloss, C. J. Pierce, B. A. Thompson, S. A. FitzGerald, C. M. Brown, J. R. Long, *J. Phys. Chem. C*, **2011**, *115*, 8414. (d) S. B. Choi, M. J. Seo, M. Cho, Y. Kim, M. K. Jin, D.-Y. Jung, J.-S. Choi, W.-S. Ahn, J. L. C. Rowsell, J. Kim, *Cryst. Growth & Des.*, **2007**, *7*, 2290. (e) S. Ma, D. Sun, M. W. Ambrogio, J. A. Fillinger, S. Parkin, H.-C. Zhou, *J. Am. Chem. Soc.*, **2007**, *129*, 1858. (f) S. Hong, M. Oh, M. Park, J. W. Yoon, J. S. Chang, M. S. Lah, *Chem. Commun.*, **2009**, 5397.

48. (a) J. L. C. Rowsell, O. M. Yaghi, *J. Am. Chem. Soc.*, **2006**, *128*, 1304. (b) O. Hubner, A. Gloss, M. Fichtner, W. Klopper, *J. Phys. Chem. A*, **2004**, *108*, 3019. (c) O. Hubner, A. Gloss, M. Fichtner, W. Klopper, *J. Phys. Chem. A* **2004**, *108*, 3019. (d) T. Yildirim, M. R. Hartman, *Phys. Rev. Lett.* **2005**, *95*, 215504. (e) V. K. Peterson, Y. Liu, C. M. Brown, C. J. Kepert, *J. Am. Chem. Soc.* **2007**, *128*, 15578. (f) J. L. C. Rowsell, J. Eckert, O. M. Yaghi, *J. Am. Chem. Soc.* **2005**, *127*, 14904. (g) Y. Liu, C. M. Brown, D. A. Neumann, V. K. Peterson, C. J. Kepert, *J. Alloys Compd.* **2007**, *446–447*, 385. (h) M. R. Hartman, V. K. Peterson, Y. Liu, S. S. Kaye, J. R. Long, *Chem. Mater.* **2006**, *18*, 3221. (i) H. Wu, W. Zhou, T. Yildirim, *J. Am. Chem. Soc.* **2007**, *129*, 5314.

49. (a) S. Couck, J. F. M. Denayer, G. V. Baron, T. Remy, J. Gascon, F. Kapteijn, *J. Am. Chem. Soc.***2009**, *131*, 6326. (b) Z. Chen, S. Xiang, H. D. Arman, P. Li, S. Tidrow, D. Zhao, B. Chen, *Eur. J. Inorg. Chem.* **2010**, 3745. (c) B. Arstad, H. Fjellvag, K. O. Kongshaug, O. Swang, R. Blom, *Adsorption* **2008**, *14*, 755. (d) J.-B. Lin, J.-P. Zhang, X.-M. Chen, *J. Am. Chem. Soc.* **2010**, *132*, 6654. (e) A. Torrisi, R. G. Bell, Mellot- C. Draznieks, *Cryst. Growth Des.* **2010**, *10*, 2839. (l) A. Sayari, Y. Belmabkhout, *J. Am. Chem. Soc.*, **2010**, *132*, 6312. (f) A. O. Yazaydin, R. Q. Snurr, T.-H. Park, K. Koh, J. Liu, M. D. LeVan, A. I. Benin, P. Jakubczak, M. Lanuza, D. B. Galloway, J. J. Low, R. R. Willis, *J. Am. Chem. Soc.* **2009**, *131*, 18198. (g) J. An, R. P.

Fiorella, S. J. Geib, N. L. Rosi, *J. Am. Chem. Soc.* **2009**, *131*, 8401.

50. A. G. Wong-Foy, A. J. Matzger and O. M. Yaghi, *J. Am. Chem. Soc.*, **2006**, *128*, 3494.

51. (a) Z. Hulvey, E. H. L. Falcao, J. Eckert, A. K. Cheetham, *J. Mater. Chem.* **2009**, *19,* 4307. (b) C. Yang, X. Wang, M. A. Omary, *J. Am. Chem. Soc.* **2007**, *129,* 15454. (c) P. Pachfule, C. Dey, T. Panda, K. Vanka, R. Banerjee, *Cryst. Growth & Des.*, **2010**, *10*, 1351. (d) P. Pachfule, C. Dey, T. Panda, R. Banerjee, *CrystEnggComm*, **2010**, *12,* 1600. (e) L. Pan, M. B. Sander, X. Huang, J. Li, M. Smith, E. Bittner, B. Bockrath, J. K. Johnson, *J. Am. Chem. Soc.*, **2004**, *126*, 1308. (f) P. Pachfule, R. Das, P. Poddar, R. Banerjee, *Inorg. Chem.,* **2011**, *50*, 3855. (g) W. Yang, X. Lin, A. J. Blake, C. Wilson, P. Hubberstey, N. R. Champness, M. Schroder, *Inorg. Chem.* **2009**, *48*, 11067.

52. H. Cheng, X. Sha, L. Chen, A. C. Cooper, M. Foo, G. C. Lau, W. H. Bailey, G. P. Pez, *J. Am. Chem. Soc*., **2009**, *131*, 17732.

53. (a) K. W. Chapman, P. J. Chupas, E. R. Maxey, J. W. Richardson, *Chem. Commun.*, **2006**, 4013. (b) H. Frost, T. Duren, R. Q. Snurr, *J. Phys. Chem. B*, 2006, 110, 9565. (c) P. Ryan, L. J. Broadbelt, R. Q. Snurr, *Chem. Commun.*, **2008**, 4132.

54. M. Latroche, S. Surble, C. Serre, C. Mellot-Draznieks, P. L. Llewellyn, J.-H. Lee, J.-S. Chang, S. H. Jhung, G. Ferey, *Angew. Chem. Int. Ed.*, **2006**, *45*, 8227.

55. (a) A. Corma, H. Garcia, *Chem. Soc. Rev.*, **2008**, *37*, 2096. (b) J. C. Fierro-Gonzalez, B. C. Gates, *Chem. Soc. Rev.*, **2008**, *37*, 2127.

56. (a) H. S. Cheng, L. Chen, A. C. Cooper, X. W. Sha, G. P. Pez, *Energy Environ. Sci.*, **2008**, *1*, 338. (b) L. F. Wang, R. T. Yang, *Energy Environ. Sci.*, **2008**, *1*, 268. (c) M.Suri, M. Dornfeld, E. Ganz, *J. Chem. Phys.*, **2009**, *131*, 174703. (d) B. D. Adams, C. K. Ostrom, S. Chen, A. Chen, *J. Phys. Chem. C*, **2010**, *114*, 19875.

57. (a) C. S. Tsao, M. S. Yu, C. Y. Wang, P. Y. Liao, H. L. Chen, U. S. Jeng, Y. R. Tzeng, T. Y. Chung, H. C. Wut, *J. Am. Chem. Soc.*, **2009**, *131*, 1404. (b) N. P. Stadie, J. J. Purewal, C. C. Ahn, B. Fultz, *Langmuir*, **2010**, *26*, 15481. (c) N. R. Stuckert, L. F. Wang, R. T.Yang, *Langmuir*, **2010**, *26*, 11963. (d) R. Campesi, F. Cuevas, M. Latroche, M. Hirscher, *Phys. Chem. Chem. Phys.*, **2010**, *12*, 10457.

58. (a) Y. E. Cheon, M. P. Suh, *Angew. Chem. Int. Ed*., **2009**, *48*, 2899. (b) C. Zlotea, R. Campesi, F. Cuevas, E. Leroy, P. Dibandjo, C. Volkringer, T. Loiseau, G. Ferey, M. Latroche, *J. Am. Chem. Soc.*, **2010**, *132*, 2991. (c) Y. Li, F. H. Yang, R. T. Yang, *J. Phys. Chem. C*, **2007**,

111, 3405. (d) Y. Li, R. T. Yang, *J. Am. Chem. Soc.*, **2006**, *128*, 726. (e) Y. Li, R. T. Yang, *J. Am. Chem. Soc.*, **2006**, *128*, 8136.

59. (a) D. Himsl, D. Wallacher, M. Hartmann, *Angew. Chem., Int. Ed.*, **2009**, *48*, 4639. (b) S. Yang, X. Lin, A. J. Blake, K. M. Thomas, P. Hubberstey, N. R. Champness, M. Schroder, *Chem. Commun.*, **2008**, 6108. (c) K. L. Mulfort, J. T. Hupp, *Inorg. Chem.*, **2008**, *47*, 7936.

60. (a) A. Mavrandonakis, E. Tylianakis, A. K. Stubos, G. E. Froudakis, *J. Phys. Chem. C*, **2008**, *112*, 7290. (b) K. L. Mulfort, T. M. Wilson, M. R. Wasielewski, J. T. Hupp, *Langmuir*, **2009**, *25*, 503. (c) K. L. Mulfort, O. K. Farha, C. L. Stern, A. A. Sarjeant, J. T. Hupp, *J. Am. Chem. Soc.*, **2009**, *131*, 3866. (d) Klontzas, E.; Mavrandonakis, A.; Tylianakis, E.; Froudakis, G. E. *Nano Lett.* **2008**, *8*, 1572.

Chapter 2

Fluorinated Metal Organic Frameworks (*F*-MOFs) for Enhanced Hydrogen (H_2) Uptake

2.1 Introduction:

The porous materials like functionalized and non-functionalized carbon nanotubes, zeolites, activated carbons, metal hydrides, etc. are considered as a potential materials for hydrogen (H_2) storage.[1] Although, inherent and intriguing properties of these materials showed high H_2 storage in these materials; still there are limitations for using these materials since these materials are expensive, shows strong interaction with adsorbents, difficulties in H_2 regeneration, etc.[2] MOFs, on the other hand, have shown promise over these materials because of potential structural and functional aspects associated due to the purely physisorptive nature of adsorption and easy regeneration procedure.[3] Various strategies such as extending pore sizes capable of fitting the adsorbed molecules, increasing surface area and pore volume, utilizing catenation, and creation of open metal sites have been explored, to achieve the high H_2 storage.[4] Similarly, insertion of functionalized links holding functional groups like –F, $–NH_2$, –OH, –COOH, etc. on the organic spacer has also been proven to have a good impact on enhancing the H_2 and CO_2 gas adsorption properties.[5] The improved interaction between the gaseous molecules and the functionalized framework brings H_2 molecules in close proximity with several aromatic rings to improve the H_2 uptake capacities of MOFs *via* increased adsorption enthalpy.[5,6]

The enhanced H_2 adsorption enthalpy achieved for the fluorine intercalated carbonous compounds have been validated in the literature using experimental as well as computational methods (*Figure 1*).[7] In these materials, the strong interaction of the semi-ionic C–F bonds with interacting H_2 molecules is the driving force for increased adsorption enthalpy, which leads to the higher adsorption at low pressure and elevated temperature.[7b] Since, enhanced H_2 adsorption enthalpy is feasible in case of fluorinated and amorphous materials lacking structural periodicity; the highly crystalline and fluorinated materials having well ordered structural periodicity are expected to have

very emerging outcomes for H_2 uptake. In these regards, fluorine functionalized MOFs (*F*-MOFs) proved to be advantageous for improved H_2 uptake with elevated adsorption enthalpy (Q_{st}) due to increased interactions between framework and adsorbing gas molecules as fluorine have high electronegativity.[6]

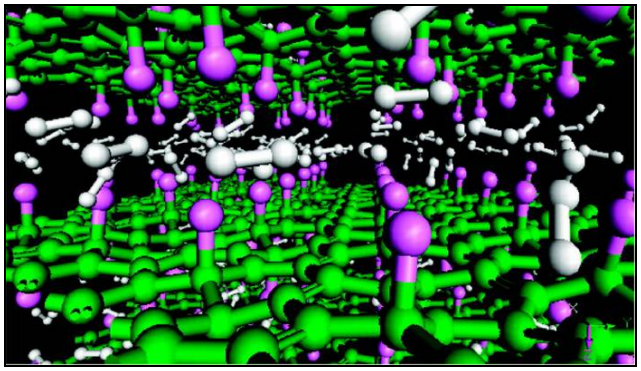

Figure 2.1 Fully optimized structures of the partially fluorinated graphite intercalation compounds with optimized H_2 molecules. [Reprinted with permission from (7a). Copyright 2009 American Chemical Society].

Furthermore, fluorinated MOFs (*F*-MOFs) with porous architecture showed its applications for the selective adsorption of hydrocarbons like methane, ethane, etc. compared to its non-fluorinated analogues.[20] Along this line, a report of fluorinated MOF represented a new class of porous materials with superior volumetric gas uptake.[8,6a,6b] The fluorine aligned channels present in the MOF structure have shown the unique hysteretic adsorption of H_2, which shows a promising way for filling up H_2 at high pressure but stored at lower pressure. Subsequently, a report on partially fluorinated MOFs highlighted the improved H_2 adsorption enthalpy (upto 8 KJ/mol), wherein fluorine lined pores enhances the interaction with adsorbed H_2 molecules. But, in contrary to aforementioned results, recent communications by few research groups, explains the decrease in overall H_2 uptake in partially fluorinated MOFs because of the decrease in pore size compared to its non-fluorinated counterparts, due to higher van der Waals radii of fluorine (1.47 Å) than hydrogen (1.20 Å) present on ligands.[10] From these results, it is clear that as fluorine atoms in partially fluorinated MOFs are weakly interacting with gas molecules, other factors, such as pore size, curvature, and open metal sites, can also play crucial role in the high gas uptakes within these *F*-MOFs.

Although, there are few reports on the *F*-MOFs synthesized using fluorinated linkers or fluorine containing anions, the current status does not determine the exact contributions of fluorine towards higher gas uptake due to unavailability of comparative

studies. There are literature precedents available, wherein gas uptake properties of fluorinated MOFs have been compared with its non-fluorinated counterpart, which have similar structure. But none of these reports explains the exact status of gas uptake properties in *F*-MOFs and effect of partial or full fluorination on gas adsorption properties. Since, in *F*-MOFs hydrophobic nature induced *via* highly electronegative fluorine atoms is visual; these MOFs have been effectively utilized for hydrocarbon adsorption or separation at room temperature.[11] In order to understand the status and current scenario of *F*-MOFs for gas as well as solvent adsorption, we have studied the literature reports, which are presented in following section:

2.2 Applications of *F*-MOFs:

The *F*-MOFs have high affinity towards adsorbing gas molecules, which shows improved enthalpy for H_2 adsorption. Similarly, the hydrophobic nature of these fluorine atoms introduced into the framework induces hydrophobicity in MOFs, which has been utilized for the applications in hydrocarbon adsorption/separation also.[7b] From the literature survey, it is visual that due to intriguing properties of *F*-MOFs these materials has been used for following applications:

2.2.1 Fluorinated MOFs for Gas Adsorption and Separation:

Porous MOFs with exposed fluorine atoms (*F*-MOFs) show "high" physisorptive H_2 adsorption enthalpy resulting in the enhancement of the H_2 adsorption properties. But, there have been reports of explicit comparison with nonfluorinated analogues, which impart a "disadvantage" of fluorination towards H_2 adsorption. The very first report on synthesis, structure and room-temperature H_2 adsorption of a novel [Cu-(hfipbb)(H_2hfipbb)$_{0.5}$] fluorine containing MOFs showed the probable application of *F*-MOFs for gas adsorption (*Figure 2.4a*).[12] The superior performance showed by FMOF-1 compared to as-received single walled carbon nanotubes (SWCNTs) and purified SWCNTs, emphasized the integrity of these MOFs for gas uptake. A promising H_2 storage capacity of 1.6 wt% at 48 atm and RT showed by [Cu-(hfipbb)(H_2hfipbb)$_{0.5}$] inspired the researchers for the synthesis of other *F*-MOFs with porous architectures containing fluorine atoms exposed to the pores. Further, reports of synthesis and gas adsorption properties of perfluorinated MOFs and the utilization of *F*-MOFs for hysteretic sorption of H_2 showcased a promising way for H_2 to be filled at high

pressures but stored at lower pressures (*Figure 2.2a*).[8] The volumetric adsorption capacity of FMOF-1 for H_2 at 77 K and 64 bar is as high as 41 kg/m^3, which can be attributed to the increased interactions between fluorine lined porous channels and adsorbing H_2 molecules giving rise to the high physisorptive H_2 adsorption enthalpy.

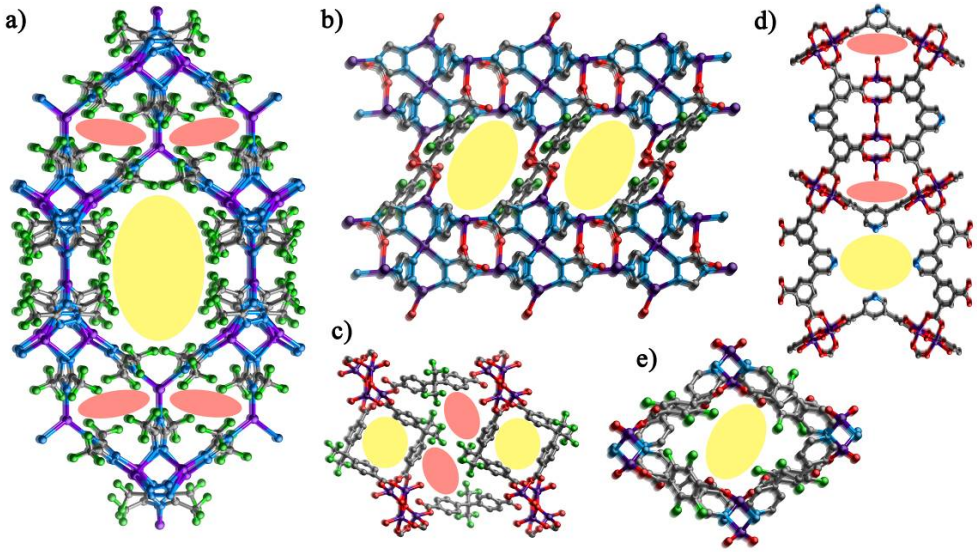

Figure 2.2 Representative literature reported perfluorined MOFs used for gas adsorption or separation. (a) Fully fluorinated FMOF-1.[8] (b) Partially fluorinated Zn_5(1,2,4-triazolate)$_6$(tetra fluoroterephthalate)$_2$(H_2O)$_2$·4H_2O MOF.[9] (c) Partially fluorinated FMOF-2 synthesized from 4,4'-(Hexafluoroisopropylidene)bis(benzoic acid).[14] (d) Representative structure of a series of Cu-based [1,1′:3′,1″-ter- phenyl]-(3,3″,5,5″)-tetracarboxylic acid functionalized MOFs.[15] (e) Partially fluorinated Zn(bpe)(tftpa)·cyclohexanone MOF.[13] (Hydrogen atoms and solvent molecules are omitted for clarity). Color code: Ag (violet), Cu, Zn (dark blue), N (blue), O (red), C (grey), F (green).

The utilization of smaller pores for high H_2 uptake with elevated adsorption affinity was successfully demonstrated with a partially fluorinated porous coordination polymer Zn_5(1,2,4-triazolate)$_6$(tetrafluoroterephthalate)$_2$(H_2O)$_2$·4H_2O.[9] This porous coordination polymer (PCP) exhibited high physisorptive H_2 adsorption enthalpy (8 kJ/mol) due to the interaction of fluorine atoms exposed to the pore surface with H_2 and small pore size comparable to the hydrogen's molecular diameter (*Figure 2.2b*). Similarly, a partially fluorinated MOF, Zn(bpe)(tftpa)·cyclohexanone, with fluorine atoms exposed to the pore surface, adsorbs 1.04 wt% H_2 at 77 K and 1 atm with an adsorption enthalpy of 6.2 kJ/mol, which signifies a trivial enhancement in the binding strength due to the presence of fluorine atoms *(Figure 2.2e)*.[13] The gas-induced

expansion and contraction of a fluorinated MOF named "FMOF-2" for highly selective CO_2, H_2S, and SO_2 adsorption showed breathing behavior towards selected gas molecules (*Figure 2.2c*).[14] The same MOF has been further used in the temperature dependent Kr/Xe selective adsorption.[16] An estimated Kr/Xe selectivity at 0.1 bar and 203 K shown by FMOFCu was attributed to the micro-tubes packed along the [101] direction connected through small bottleneck windows in FMOFCu. The effect of fluorination has been further explained in four iso-structural MOFs with various functionalized pore surfaces (–H, –N, $–CH_3$ and $–CF_3$), where MOFs were synthesized from a series of di-isophthalate ligands.[15] Among this series of MOFs, the MOF possessing free $–CF_3$ (PCN-308) groups in its framework, showed highest H_2 uptake of 2.67 wt% at 77 K and 1 bar and CO_2 uptake of 15.4 wt% at 297 K and 1 bar. Despite being holding lower surface area, PCN-308 showed higher heat of adsorption for H_2 and CO_2 than that of its non-fluorinated versions. In a recent report, adsorption of 0.74 wt% of H_2 at 77 K/1 atm pressure and 2.78 wt% of H_2 at 77 K/41 bar pressure with isosteric heat of H_2 adsorption (Q_{st}) value of ~7.9 kJ/mol at low coverage has been demonstrated.[17] In the partially fluorinated 3D MOF, $\{[Zn_4O(bfbpdc)_3\text{-}(bpy)_{0.5}(H_2O)]\cdot(3DMF)(H_2O)\}_n$ (bpy = 4,4′-bipyridine and bfbpdc = 2,2′-bistrifluoromethyl-biphenyl-4,4′-dicarboxylate) enhancement in gas adsorption was assigned to the presence of the exposed metal site and fluorine atoms in the pore surface of the framework.

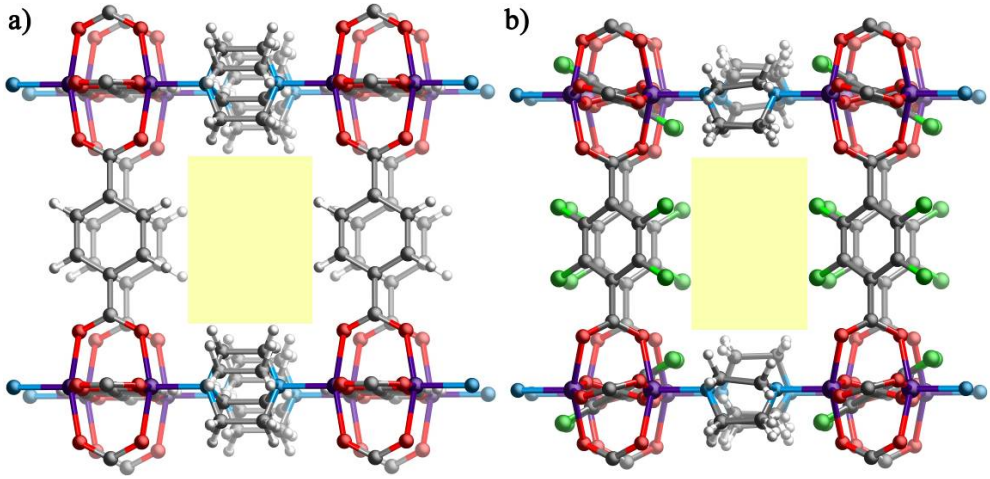

Figure 2.3 Comparative structure of the Zn containing 1,4-benzenedicarboxylic acid/2,3,5,6-tetrafluoro-1,4-benzenedicarboxylic acid and 1,4-diazabicyclo[2.2.2]octane based MOFs.[10a] Color code: Zn (violet), N (blue), O (red), C (grey), F (green). [Reprinted with permission from (10a). Copyright 2005 WILEY-VCH Verlag GmbH & Co. KGaA].

Although, aforementioned results showed advantages of fluorine functionalization for high H_2/CO_2 uptake with increased heat of adsorption, one relevant report demonstrated the disadvantages of fluorine functionalization towards the incremental gas adsorption.[10a] In this context author mentioned that "*from the gas-sorption point of view, fluorinated MOF has a disadvantage compared to its non-fluorinated analogue not because of the slightly reduced pore size, but because of its higher framework density originating from the fluorine atoms. The densities for fluorinated and non-fluorinated MOFs based on crystallographic analysis are 1.03 and 0.82 g/cm^3, respectively*." As shown in Figure 2.3, due to the increased atomic size of fluorine over hydrogen atom, the overall pore size decreases significantly in fluorinated MOF. The decreased free space for gas adsorption, further results into the overall decrease in the gas adsorption capacities. Also from the gas adsorption point of view, partially fluorinated tetrafluoroterephthalte based MOF (density = 1.03 g/cm^3) has disadvantage compared to non-fluorinated terephthalate based MOF (density = 0.826 g/cm^3), not because of the slightly reduced pore size, but because of its higher framework density originating from the fluorine atoms.[10b] Hence, it was evident in few cases that the fluorine functionalization was not fruitful leading towards the increase in gas uptake capacity.

2.2.2 Fluorinated MOFs for Gas Hydrocarbon Sorption or Separation:

The separation of a mixture of hydrocarbons is a commercially important process as it has a wide range of applications in the chemical and polymer industry.[18] Existing methods for separation of hydrocarbons from mixtures including fractional distillation are based on the difference in the boiling points of the constituents and requires high-energy costs due to their requirement of low temperatures and high pressure. In order to achieve energy effective separation, the exploitation of porous materials like zeolites, hydrophobic polymers, carbon containing materials (like SWCNTs, activated carbons), alumina compounds, etc. have been tried widely.[19,20] Particularly, the applications of modified Y zeolites (AgY and CeY) prepared using ion-exchange methods for hydrocarbons separation is well studied in literature.[21] The adsorption breakthrough and on site solvent washing experiments, as well as computer simulation performed for various Y zeolites showcased the adsorption and desorption behavior of sulfur

containing molecule (thiophene) and hydrocarbon (heptane). Similarly, a hydrophobic and crystalline polymorph of SiO_2, (named 'Silicalite') has been utilized as a molecular sieve for the selective adsorption of organic molecules over water.[22a] The adsorption of the benzene, toluene, dichloromethane, 1,1-dichloro-1-fluoroethane, etc. has successfully been demonstrated using hydrophobic Y-Type zeolite.[22b] So, the literature reports reveal that in order to achieve the adsorption and/or separation of the hydrocarbons using porous materials, hydrophobicity of the materials plays a crucial role. Due to the versatile nature of the pores and high pore volume, crystalline MOFs provide a cost effective alternative way to separate C1−C3 and higher hydrocarbons at higher temperature.[20] In response the above observations, hydrophobicity in MOFs has been achieved by incorporation of hydrophobic groups or atoms like methyl, ethyl, *n*-propyl, $-CF_3$, –F, etc. The hydrophobicity is induced into the FMOFs either via incorporation of anions like SiF_6^{2-}, PF_6^-, ZrF_6^{2-}, SbF_6^-, BF_4^-, etc. or through perfluorinated carboxylate, triazolate, tetrazolate etc. organic ligands. This hydrophobicity in these MOFs facilitates their stability in presence of water, which in turn helps them for the separation/adsorption of hydrocarbons.

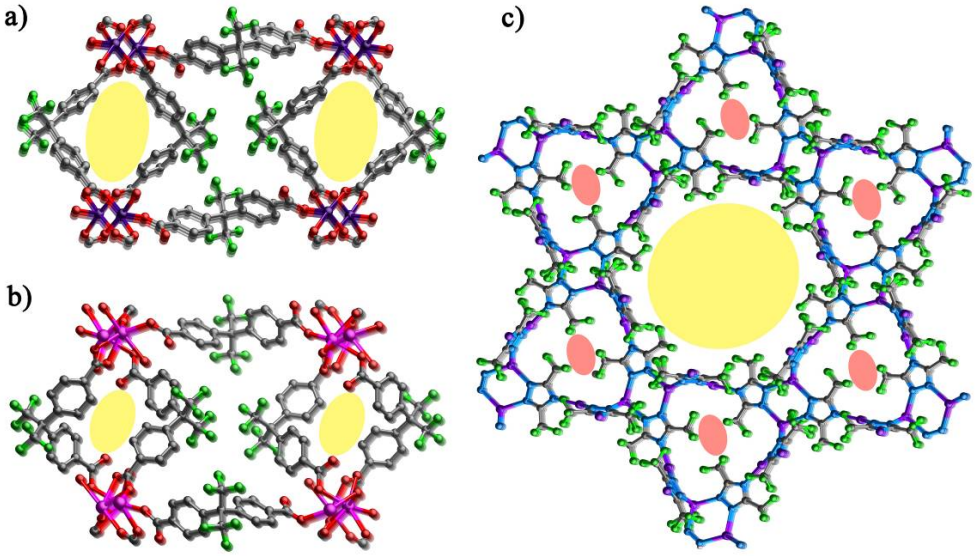

Figure 2.4 Representative examples of literature reported perfluorinated MOFs used for hydrocarbon adsorption or separation. (a) Partially fluorinated [Cu(hfipbb)(H_2hfipbb)$_{0.5}$] synthesized from 4,4'-(Hexafluoroisopropylidene)bis(benzoic acid).[11] (b) Partially fluorinated AEPF-1 synthesized from 4,4'-(hexafluoroisopropylidene)-bis(benzoic acid).[25] (c) Fully fluorinated FMOF-2 synthesized from perfluorinated ligand 3,5-bis(trifluoromethyl)-1,2,4-triazolate.[26] Color code: Cu/Zn (violet), Cd (Pink), N (blue), O (red), C (grey), F (green).

The development of teflon like channeled nanoporous MOF with a chiral and uni-nodal 4-connected net for hydrocarbon sorption has been reported in 2005.[23] Subsequently, a three dimensional [Cu(hfipbb)(H_2hfipbb)$_{0.5}$] MOF, with fluorine lined micro-channels showed strong interactions with hydrocarbons, causing to large values for the heat of adsorption.[24] Since, these channels are hydrophobic, they allow the separation of trace amount of water vapor present as an impurity with the non-polar hydrocarbon molecules. The shape and size selective [Cu(hfipbb)(H_2hfipbb)$_{0.5}$] MOF showed efficient method of separating normal C4 from their branched analogues, higher normal alkanes and olefins (*Figure 2.4a*). Similarly in a Ca-based metal–organic framework named AEPF-1 based on the organic linker H_2hfbba, reversible structural change upon removal or addition of guest solvent molecules has been showcased (*Figure 2.4b*).[25] The perfluorinated spongy and hydrophobic AEPF-1 shows selective adsorption of various organic compounds like toluene, benzene, isopropyl alcohol, 1-butanol, acetone and acetonitrile based on their size, shape and polarity.

Further, fluorine containing MOFs (FMOFs) with superior adsorption and hydrophobic properties toward oil spill cleanup and hydrocarbon storage have been reported in 2011 by Omary and co-workers (*Figure 2.4c*).[26] The Ag containing 3,5-bis(trifluoromethyl)-1,2,4-triazolate based fully perfluorinated MOFs with highly hydrophobic channels have been employed for hydrocarbon adsorption. The hydrophobic FMOFs with remarkable air and water stability exhibit a high affinity towards C6–C8 hydrocarbons of oil components. The *F*-MOFs (FMOF-1 and FMOF-2) can selectively adsorb C6–C8 hydrocarbons in preference to water, through a combination of hydrophobicity and capillary action. In another report, the separation of C3/C4 hydrocarbon mixture by adsorption using a mesoporous MIL-100(Fe) was recorded.[27] The fluorine containing MIL-100(Fe) shows preferential adsorption forisobutane over propane and propylene in a wide range of temperature (323–523 K) and pressure (0–300 kPa). Temperature dependent propane, isobutene and propylene adsorption at low pressures is demonstrated depending on the interaction of adsorbate with Fe(II) sites of the MOFs.

2.3 Synthesis of Fluorinated MOFs for Enhanced H_2 Uptake:

As discussed earlier, in few literature reports, porous *F*-MOFs with fluorine atoms exposed into the pores showed high physisorptive H_2 adsorption enthalpy resulting in the enhancement of the H_2 adsorption properties.[8,9] But, at the same time, few literature reports suggests the disadvantage of fluorination towards H_2 adsorption.[10] As a result, at this moment, it is very difficult to draw any conclusion regarding the impact of fluorination on H_2 and CO_2 adsorption. Thus, to conclude the effect of fluorination on H_2 uptake property of a MOF, systematic comparison between isostructural fluorinated and non-fluorinated MOFs is necessary. In these regards, in order to study the H_2 adsorption behaviors in *F*-MOFs, we started working on the synthesis and gas adsorption studies of fluorine containing MOFs synthesized from 4,4'-(Hexafluoroisopropilidine)bis benzoic acid (H_2hfbba) as linker and different *N*-donor linkers (*Figure 2.5*) with the aid of various metal centers (Mn, Co, Cu, Zn, etc.).[28b-28e]

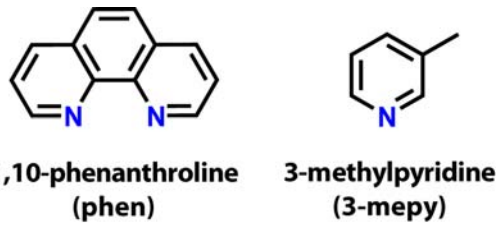

Figure 2.5 Nitrogen containing linkers used for the synthesis of *F*-MOFs.

During these studies, firstly we have utilized H_2hffbba as an organic linker not only due to the presence of fluorine into its backbone, but it also holds following advantages:

a. It's bent geometry and considerably long molecular backbones can induce formation of a moderately porous framework with many characteristics such as selective gas adsorption, gas storage and catalysis.

b. The twisted (V-shaped) conformation of this ligand may provide the ability to shape helical assembly with chirality in the resultant supramolecular architecture.

c. The different degrees of deprotonation of the ligands under different reaction conditions may result in variable coordination modes in the products.

d. Long molecular structure of this primary building unit may lead to the formation of microporous coordination frameworks with channels.

In addition to these aforementioned advantages of H_2hfbba linker towards the induction of porosity and helicity into the resultant *F*-MOFs; dicarboxylate linker show

different modes of coordination in various reaction conditions as showed in Figure 2.6. The major reason behind these various possible coordination modes in these types of carboxylate linkers may be the variable degree of deprotonation in different reaction conditions like temperature, pressure, solvent, pH, subsequent metal centre and co-linkers, etc. In these regards, in the *F*-MOFs represented in this context, the mostly observed coordination modes are μ_1^t–OC(=O), μ_2^b–OCO and μ_1^c–OCO (*Figure 2.6a–2.6c*). Although, there are several possible modes of attachments for H_2hfbba linker, most commonly observed modes of attachment for this linker are summarized in Figure 2.6.

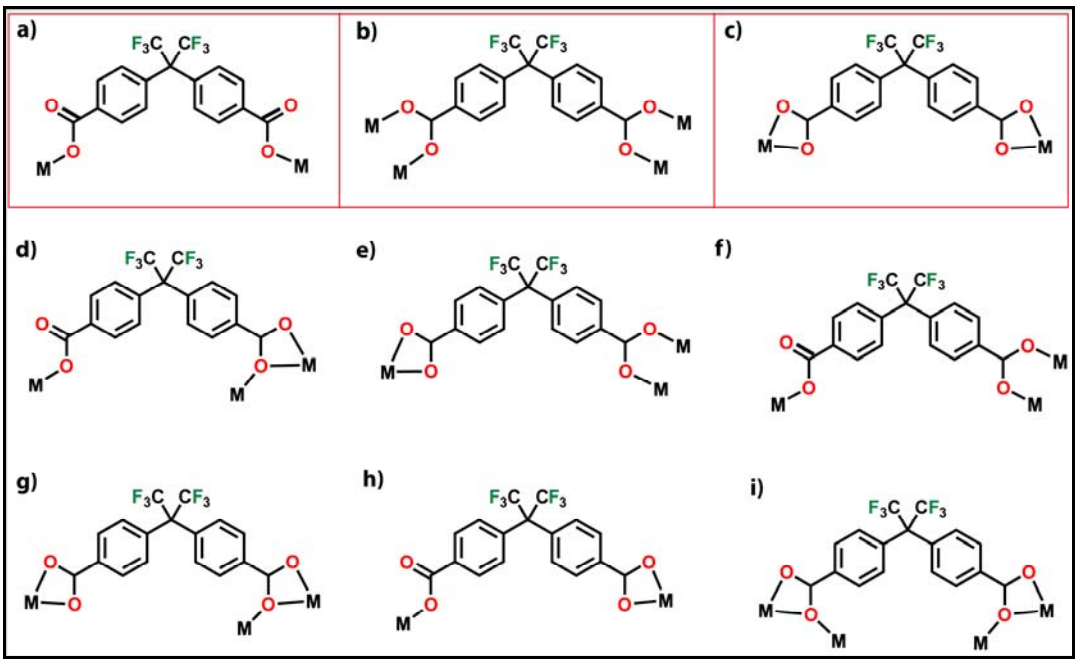

Figure 2.6 Commonly observed coordination modes during the MOF formation using perfluorinated H_2hfbba linkers. The coordination modes observed during the current studies are highlighted in red boxes (Figure 2.6a, 2.6b and 2.6c).

Since, we have used the V-shaped H_2hfbba as an organic linker for the synthesis of *F*-MOFs, there always lays a possibility of formation of small sized pores due to the twisted conformation. From the literature reports and obtained structures, it was clear that *F*-MOFs obtained using H_2hfbba linker usually forms the pores of 3–4 Å diameter, which shows adsorption of small gas molecules, but non-porous for the bigger sized gas/solvent molecules (*Figure 2.7*).[28] Mostly these structures get deformed due to the

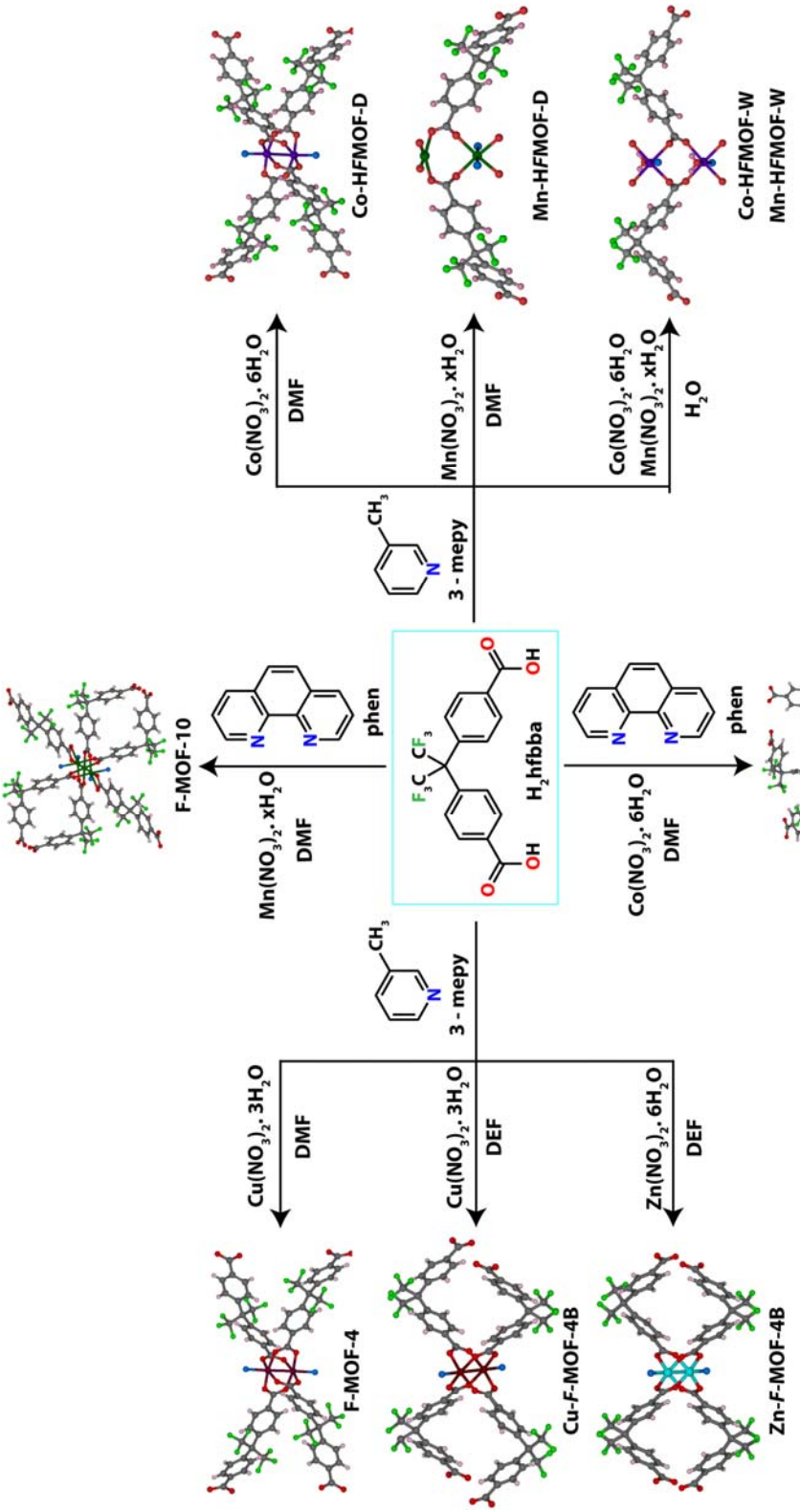

Figure 2.7 Scheme of synthesis of *F*-MOFs using H_2hfbba as a linker and 3-methyl pyridine, 1,10-phenanthroline co-linkers.

intrinsic flexibility in MOFs due to the bent natures of linkers. Additionally, in many of these MOF synthesis procedures addition of *N*-containing linkers was essential to get the crystalline product, in view of fact that without addition of these linkers usually precipitation occurs. These additionally inserted *N*-containing linkers caps the valences of metals centers coordinated therein, restricting the dimensionality of resulting *F*-MOFs. Also, the non-fluorinated analogue of H_2hfbba does not provide the isostructural MOF, albeit similar reactions condition has been maintained during the course of reaction. In view of these aspects, according to our perspective, the rigid organic linkers holding both nitrogen and carboxylate functionalities for the coordination with metal centers and free fluorine atoms will be the ideal candidate for *F*-MOF synthesis. In these pyridyl carboxylate following probabilities can be observed:

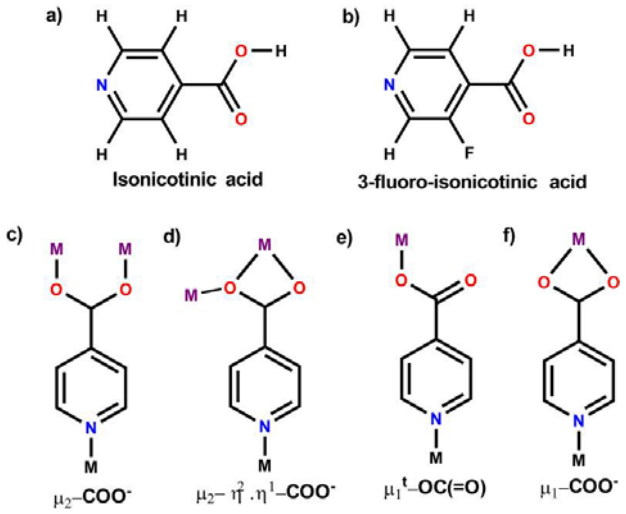

Figure 2.8 The structure and commonly observed coordination modes of INA and *F*INA linkers.

a. Carboxylic groups of such acids get partially or completely deprotonated depending upon the reaction conditions, resulting different coordination modes (monodentate, chelating, and/or bridging).

b. The effective incorporation of N, N'-donors on the same linkers will decorate the channels in MOFs to stabilize the structure and conveniently arrange the surface features of the compound (Figure 2.8).[30a,30b]

In these regards, we have selected isonicotinic acid (4-pyridinecarboxylic acid, INA) and its fluorinated analogue 3-fluoro-isonicotinic acid (3-fluoro-4-pyridinecarboxylic acid, *F*INA) as a building block due to following reasons:

a. The modular length of these linkers can produce the porous structures with reasonably high porosity.

b. The rigid structure of these linkers with rotatable carboxylate groups (having angular movement) at its terminals can undergo modification to produce different structures.[30]

c. Also, pyridyl rings in these linkers can show free rotation around the metal ion, thus limiting the degree of control over the final structure.

d. Since, both fluorinated and non-fluorinated nicotinic acid based linkers are available commercially; it will be easier to synthesize the isostructural MOFs with/without fluorine incorporated into its backbone. Using these structures, it will be more convenient to study the effect of fluorination on the gas adsorption properties in resulting MOFs.

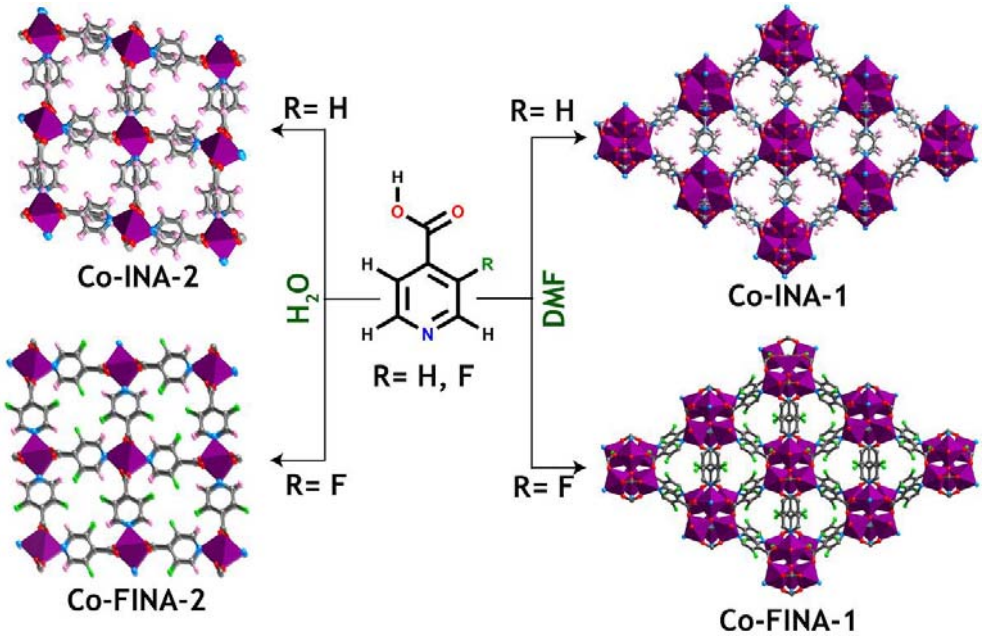

Figure 2.9 Scheme of synthesis of isonicotinic acid based fluorinated and non-fluorinated MOFs using INA and *F*INA linker in presence of DMF and H_2O solvents with the aid of Co(II) as metal centers. Color code: Co (Pink), N (blue), O (red), C (grey), F (green). [Reprinted with permission from (28a). Copyright 2012 WILEY-VCH Verlag GmbH & Co. KGaA].

As shown in Figure 2.8 and 2.9, during the course of reaction both these INA and *F*INA linkers can show various modes of attachments leading to the formation of diverse number of MOFs.[28a] In order to study the effect of partial fluorination on the H_2 uptake properties in MOFs, we have synthesized two isostructural pairs of non-fluorinated and fluorinated MOFs using INA/*F*INA linkers and Co(II) metal centers, respectively.

2.4 Result and Discussions:

2.4.1 MOF Synthesis using H_2hfbba and Isonicotinate Linkers:

Direct solution reactions (mixing or layering) of organic linker and metal solution at RT give rise to a microcrystalline precipitate in most of the MOF syntheses reactions. In order to achieve the large sized MOF crystals suitable for single crystal XRD studies, hydrothermal or solvothermal synthesis methods have been demonstrated as very promising techniques. Since, H_2hfbba is sparingly soluble in water at room temperature, the reaction linker with metals in water solvent are performed mostly in autoclave following hydrothermal synthesis.[11,14,25] The increased vapour pressure during high temperature heating of the reaction mixture dissolves the H_2hfbba linker in water, which further reacts with metals to form MOF crystals. Similarly, the solvothermal reaction of H_2hfbba with metals in the DMF solvent proceeds faster due to the high solubility of both linker as well as metals. The reaction of H_2hfbba and metals in absence of *N*-containing co-linkers mostly results into the formation of precipitate without reaction. In order to achieve the crystalline products, herein we have added the co-linkers like 3-methyl pyridine and 1,10-phenanthroline.[11b-11e] The effect of addition of co-linkers was clearly been visualized during the course of reaction, since we could isolate several MOFs by following this synthesis procedure. The *F*-MOFs achieved *viz*. $[Cu_2(hfbba)_2(3\text{-mepy})_2].(DMF)_2(3\text{-mepy})$ (***F*-MOF-4**), $[Cu_2(hfbba)_2(3\text{-mepy})_2]$ (**Cu-*F*MOF-4B**), $[Zn_2(hfbba)_2(3\text{-mepy})_2]$ (**Zn-*F*MOF-4B**), $Co_3(hfbba)_6(phen)_2$ (***F*-MOF-6**), $Mn_3(hfbba)_6(phen)_2$ (***F*-MOF-10**), $[Co_2(hfbba)_2(3\text{-mepy})_2].(DMF)_3$ (**Co-H*F*MOF-D**), $[Mn_2(hfbba)_2(3\text{-mepy})].(H_2O)$ (**Mn-H*F*MOF-D**), $[Mn(hfbba)(3\text{-mepy})(H_2O)]$ (**Mn-H*F*MOF-W**) and $[Co(hfbba)(3\text{-mepy})(H_2O)]$ (**Co-H*F*MOF-W**) by using H_2hfbba as a linker and 3-methyl pyridine and 1,10-phenanthroline show structural diversity.

The effect of physical parameters like solvent, temperature, pressure, etc. on the MOF growth has been studied in literature to large extent.[32] In such cases, with change in experimental conditions, each time new MOFs get formed. The synthesis of INA and *F*INA based porous MOFs was achieved by hydrothermal and solvothermal synthesis. Similarly, in the cases of INA and *F*INA linkers, by changing the solvent from H_2O and DMF, we have achieved two distinct MOF phases. Synthesis, structure and gas adsorption properties of four new MOFs designed from isonicotinic acid (INA) and its

fluorinated analogue 3-fluoro isonicotinic acid (*F*INA) along with Co(II) as metal center has been reported. $[Co_3(INA)_4(O)\ (C_2H_5OH)_3](NO_3)\cdot(C_2H_5OH)\cdot(H_2O)_3]$ **Co-INA-1** and $[Co(INA)_2\cdot(DMF)]$ **Co-INA-2** are structural isomers so as $[Co_3(FINA)_4(O)(C_2H_5OH)_2(H_2O)]$ **Co-FINA-1** and $[Co(FINA)_2\cdot(H_2O)]$ **Co-FINA-2**, but most important thing to note here is that Co-INA-1 and Co-FINA-1 are isostructural so as Co-INA-2 and Co-FINA-2 (**INA** = isonicotinic acid, **FINA** = 3-fluoro-isonicotinic acid). Effect of partial introduction of fluorine atoms into the framework on gas uptake properties of MOFs having similar structures has been analyzed experimentally and computationally, in isostructural MOFs.

2.4.2 Crystal Structure Description:

Crystal Structure of $[Cu_2(hfbba)_2(3\text{-mepy})_2]\cdot(DMF)_2$ (3-mepy) (*F*-MOF-4):[28e]

Asymmetric unit of *F*-MOF-4 (space group $P2_1/c$) comprises two crystallographically independent Cu^{+2} ion, two hfbba and two 3-mepy ligand, one lattice 3-mepy and three lattice DMF molecules (*Figure 2.10*). Both Cu^{+2} centers have almost the same coordination environments with a nearly ideal square-pyramidal sphere ($\tau \approx 0$)[32] enclosed by two hfbba ligands and one 3-methyl-pyridine ligand. The di-copper paddlewheel secondary building unit (SBU)[33] for *F*-MOF-4 with the Cu···Cu distance of 2.60 Å is shown in Figure 2.10a, expanded to show the four H_2hfbba ligands, each coordinated to a di-copper paddlewheel unit *via* one of their carboxylate groups.

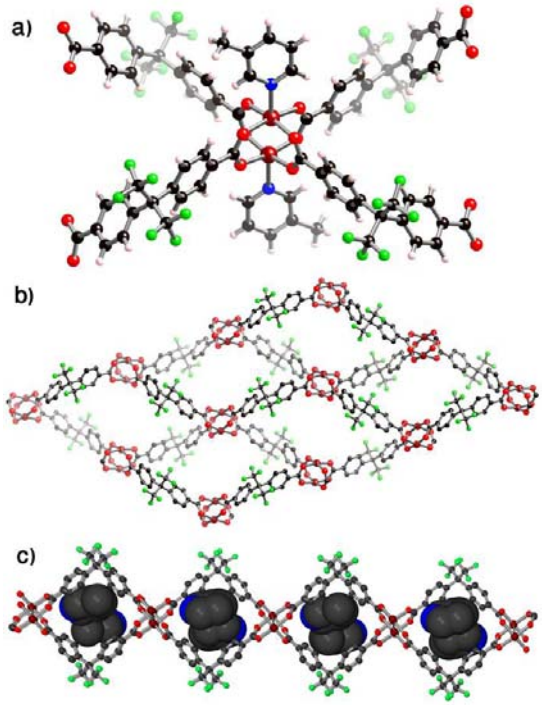

Figure 2.10 Crystal structure of *F*-MOF-4. (a) SBU showing the paddle-wheel motif of Cu(II). (b) 2D coordination layer in *F*-MOF-4 with Cu(II) paddle-wheel (view down b axis). (c) Coordination layer in *F*-MOF-4 (view down *a* axis). Color code: Cu (brown), N (blue), O (red), C (grey), F (green). [Reprinted with permission from (28e). Copyright 2010 Royal Society of Chemistry].

The second carboxylate group of each H_2hfbba ligand coordinates to another paddlewheel unit, generating the extended corrugated two dimensional sheets, as shown in Figure. 2.10b. Two 3-mepy ligands occupy the axial positions of the di-copper paddle wheel SBU. In *F*-MOF-4, the sheets stack along y axis affording square -shaped channels from the sheet cavities that run through the gross structure (*Figure 2.10c*). Similarly sheets stack along z axis affording hexagonal channels that run through the gross structure. The distance between equivalent atoms in neighboring sheets is approximately 3.5 Å. The $–CF_3$ groups of H_2hfbba ligands are directed to the outside of the larger square channels, whereas DMF and 3-methyl-pyridine guests reside inside the square shaped and hexagonal channels, respectively. The pore diameter is approximately 5.5 Å across, based on the largest sphere that could fit into the pore and be in contact with the van der Waals surface. Such a large void space within a framework often leads to molecular entanglement and two-fold interpenetration.

Crystal Structure of $[Cu_2(hfbba)_2(3\text{-mepy})_2]$ (Cu-*F*MOF-4B) and $[Zn_2(hfbba)_2(3\text{-mepy})_2]$ (Zn-*F*MOF-4B):[28c]

The asymmetric unit of Cu-*F*MOF-4B/Zn-*F*MOF-4B contains one crystallographically independent Cu^{2+} or Zn^{2+} ion, one H_2hfbba ligand, one 3-methyl pyridine ligand and one guest solvent molecule. Each octahedral Cu^{2+} or Zn^{2+} ion is surrounded by four oxygen atoms from H_2hfbba ligands [Cu/Zn–O distance ranges from 2.01 to 2.03 Å] and one nitrogen from 3-methyl pyridine ligand [Cu–N distance= 1.96 Å] as shown in Figure 2.11. Both Cu^{2+} centers of Cu-*F*MOF-4B have almost the same coordination environments with a nearly ideal square-pyramidal sphere ($\tau \approx 0$) enclosed by four hfbba ligands [Cu–O distance ranges from 2.01 to 2.03 Å] and one 3-methyl pyridine ligand [Cu–N distance= 1.96 Å]. The di-copper paddlewheel SBU for Cu-*F*MOF-4B with the Cu···Cu distance of 2.67 Å is shown in Figure 2.11b, expanded to show the four hfbba ligands, each coordinated to a di-copper paddlewheel unit *via* one of their carboxylate groups. Co-ligand 3-mepy molecules are assembled at top and bottom position. This di-copper paddlewheel extends further in *ab* plane to connect the next SBU giving rise to square shaped pores and further the 2D structure. 3-mepy molecules are inter-digited into the square shaped pores along the *c* axis. Space filling model shows the assembly of this square shaped pores to form 1D channel (*Figure 2.11c*).

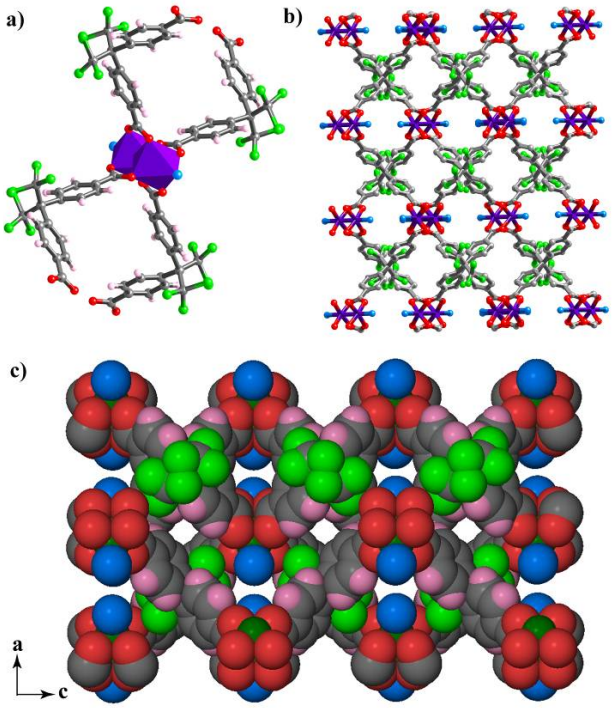

Figure 2.11 Crystal structure of Cu-*F*MOF-4B/Zn-*F*MOF-4B. (a) Polyhedral representation of the SBU showing the paddle-wheel motifs. (b) Inter-digited layered structure of Cu-*F*MOF-4B/Zn-*F*MOF-4B. (c) Packing diagram of Cu-*F*MOF-4B/Zn-*F*MOF-4B (view down b axis) showing channels. Color code: Cu (violet), N (blue), O (red), C (grey), F (green). [Reprinted with permission from (28c). Copyright 2011 American Chemical Society].

Topological simplification of Cu-*F*MOF-4B, by joining only Cu^{2+} centers, with ligand atoms, shows the formation of square shaped pores and mode of attachment of ligands with metal center. In the 2D structure of Cu-*F*MOF-4B separate layers are arranged in an offset fashion (*Figure 2.11b*). Each layer is displaced from its adjacent layer by a distance of 2.01 Å. The $-CF_3$ groups of H_2hfbba ligands are directed to the outside of the square channels while DEF molecules are occupying the interlayer region. The pore diameter for Cu-*F*MOF-4B is ~3.10 Å across, based on largest sphere that could fit into the pore and also remain in contact with van der Waals surface.[35]

Structure of $Co_3(hfbba)_6(phen)_2$ (*F*-MOF-6) and $Mn_3(hfbba)_6(phen)_2$ (*F*-MOF-10):[28d]

F-MOF-6 and –10 have very similar structure (a = 36.62; b =13.55; c = 26.37; β = 127.8 *vs.* a = 37.09; b =13.64; c = 29.67; β = 135.0) containing similar $[M_3(CO_2)_6]$ SBUs with three octahedral M^{2+} ions. Similar to the structure of *F*-MOF-6, in the case of *F*-MOF-10 also, Mn(1) and Mn(3) atoms are coordinated to two bidentate phenanthroline ligands [Mn–N distances, 2.22 and 2.24 Å] and six different hfbba ligands [Mn–O distances range from 2.08 to 2.26 Å] (*Figure 2.12a*). The coordination sphere of the central octahedral Mn^{2+} ion includes six oxygen atoms [Mn–O distances

range from 2.08 to 2.23 Å] from the bridging hfbba ligands (*Figure 2.12b*). This $[M_3(CO_2)_6]$ SBUs connects to six hfbba ligands which are arranged in a roughly octahedral manner around the trimer, bridging to six other trimers to form a 3D pcu network (*Figure 2.12c*).

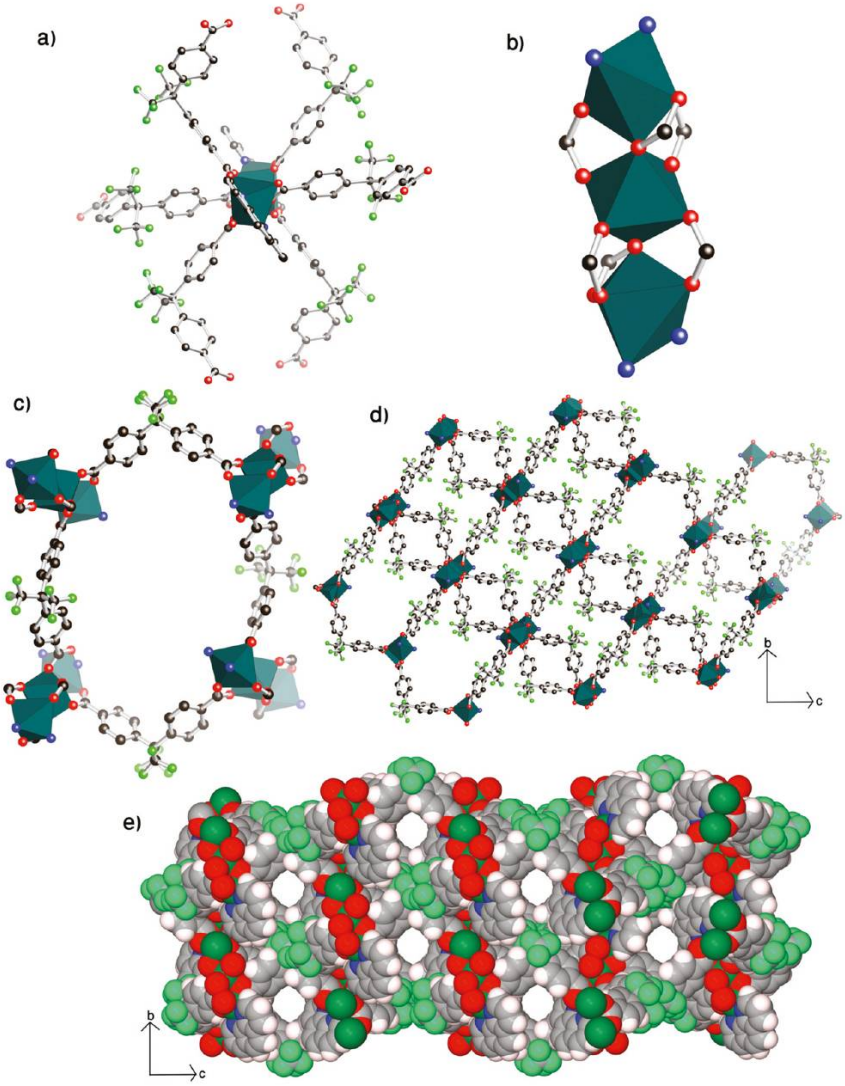

Figure 2.12 Crystal structure of *F*-MOF-6/*F*-MOF-10. (a) Polyhedral representation of the SBU of *F*-MOF-6/*F*-MOF-10 showing the coordination environment around Co/Mn. (b) $[M_3(CO_2)_6]$ SBUs with three octahedral M^{2+} ions. (c) Isolated cage in *F*-MOF-6/*F*-MOF-10. (d) 3D pcu network in *F*-MOF-6/*F*-MOF-10. (e) One-dimensional channels of *F*-MOF-6/*F*-MOF-10 shown in spacefill model. Color code: Co/Mn (green), N (blue), O (red), C (grey), F (green).

The framework in *F*-MOF-10 is also open, containing one-dimensional channels of 4.4 × 4.0 Å dimension (the channel size is measured by considering the van der Walls radii

of the constituting atoms) along the crystallographic *a* axis (*Figure 2.12e*). These channels are occupied by solvent molecules. However, calculations with *PLATON* show that the effective volume for the inclusion is 33 % of the crystal volume. Appearance of strong peaks at 1405 and 1606 cm^{-1} in the IR spectrum confirms the coordinated carboxylates.

Crystal structure of $[Co_2(hfbba)_2(3\text{-mepy})_2]\cdot(DMF)_3$ (Co-H*F*MOF-D):[28a]

Crystal structure of Co-H*F*MOF-D contains two crystallographically independent Co^{2+} ions, two hfbba ligands, two 3-methyl pyridine ligand and three lattice DMF molecules in its asymmetric unit (*Figure 2.13a*). Both Co^{2+} centers of Co-H*F*MOF-D have almost the same coordination environments with a nearly ideal square-pyramidal sphere ($\tau \approx 0$) enclosed by four hfbba ligands [Co–O distance ranges from 2.02 to 2.05 Å] and one 3-methyl pyridine ligand [Co–N=2.05 Å]. The di-cobalt paddlewheel SBU for Co-H*F*MOF-D with the Co···Co distance of 2.74 Å is shown in Figure 2.13a, expanded to show the four hfbba ligands, each coordinated to a di-cobalt paddlewheel unit *via* one of their carboxylate groups. The second carboxylate group of each hfbba ligand coordinates to another paddlewheel unit, generating the extended corrugated 2-D layered structure (*Figure 2.13b*). In Co-H*F*MOF-D, 3-methyl pyridine ligands occupy the axial positions of di-cobalt paddlewheel, blocking the pores. By joining only Co^{2+} centers with ligand atoms, topological simplification of Co-H*F*MOF-D shows the formation of square shaped pores and mode of attachment of ligands with metal center as shown in Figure 2.13c. In Co-H*F*MOF-D, the sheets stack along *b* axis affording square-shaped channels from the sheet cavities that run through the gross structure (*Figure 2.13d*) creating square grid topology. The distance between equivalent atoms in between neighboring sheets is approximately 3.5 Å. The $–CF_3$ groups of H_2hfbba ligands are directed to the outside of the larger square channels while one DMF molecule is sitting inside the pore and two are arranged in the interlayer region, respectively. The pore diameter for Co-H*F*MOF-D is ~3.10 Å across, based on largest sphere that could fit into the pore and also remain in contact with van der Waals surface. The $–CF_3$ groups of one channel in Co-H*F*MOF-D are located in between the edge of the square shaped channel with minimal interlayer void (*Figure 2.13d*). The two-dimensional parallel interpenetrating network is reinforced by the existence of other

non-covalent interactions like C-H···F hydrogen bonds (*D*, 3.32 Å; *d*, 2.77 Å; *θ*, 117.3º).[35]

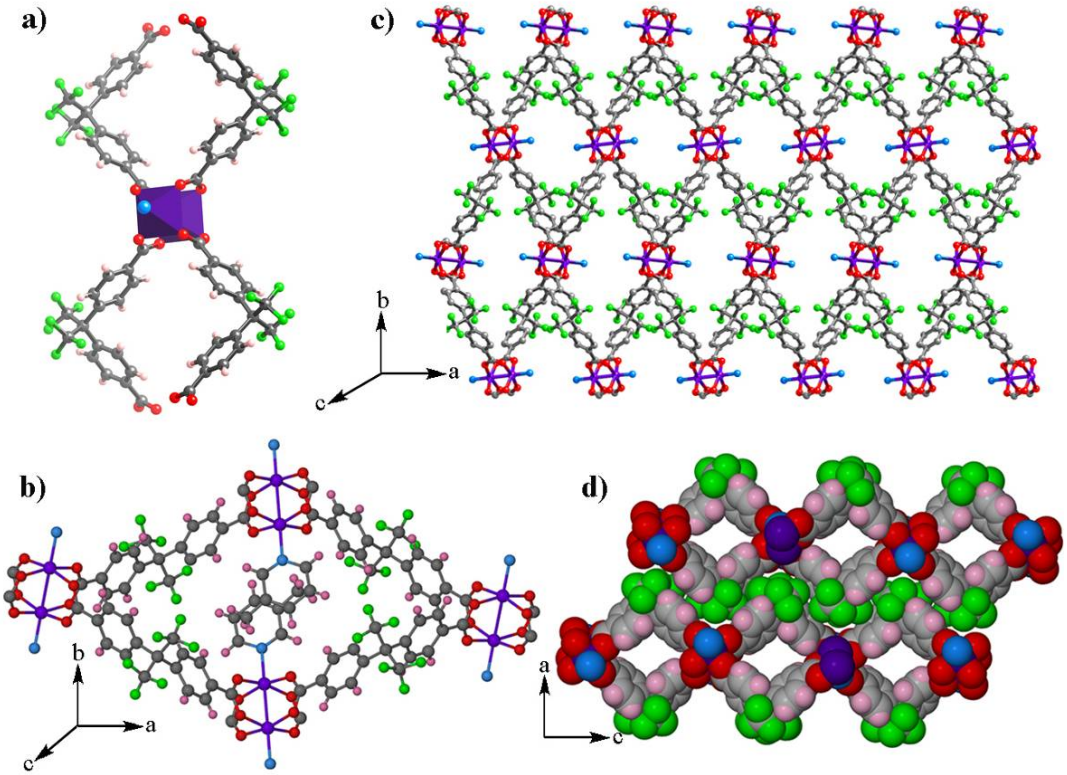

Figure 2.13 Crystal structure of Co-H*F*MOF-D. (a) Polyhedral representation of the SBU showing the paddle-wheel motif of Co^{2+}. Two 3-methylpyridine ligands occupy the axial positions. (b) One single unit of Co-H*F*MOF-D clearly showing the pointing 3-mepy groups into the pores. (c) 2-D coordination layer in Co-HFMOF-D with Co^{2+} paddle-wheel binuclear nodes (view down *c* axis). (d) Space fill model of Co-H*F*MOF-D (view down *b* axis) showing the 3.106 Å channels. Color code: Co (violet), N (blue), O (red), C (grey), F (green). [Reprinted with permission from (28b). Copyright 2011 American Chemical Society].

Crystal structure of $[Mn_2(hfbba)_2(3\text{-mepy})]\cdot(H_2O)$ (Mn-H*F*MOF-D):[28a]

In the two dimensional structure of Mn-H*F*MOF-D, asymmetric unit is composed of one Mn^{2+} ion, one hffbba ligand, one 3-methyl pyridine ligand and one lattice H_2O molecule. Two different types of co-ordination environments around Mn^{2+} are found in Mn-H*F*MOF-D. As a result there are two types of SBUs in the binuclear Mn-H*F*MOF-D unit (*Figure 2.14a*). Among these SBUs, one is in octahedral co-ordination geometry as four hfbba ligands [Mn_{oct}–O distance ranges from 2.15 to 2.18 Å] and two 3-methyl pyridine ligands [Mn–N=2.26 Å] are co-ordinated. Another SBU is in square planer co-

ordination sphere where only four hfbba ligands [Mn –O distance ranges from 2.11 to 2.15 Å and O–Mn–O angle ranges from 89.4º to 95.0º] are attached to metal center. In this structure, these octahedral and square planer metal centers are arranged alternatively along crystallographic *b* axis (*Figure 2.14b*). Crystal structure of Mn-H*F*MOF-D adopts a 2-D arrangement as the co-ordination of Mn^{2+}– hfbba – Mn^{2+} propagates along *c* axis and simultaneously Mn–CO_2–Mn propagates along *b* axis.

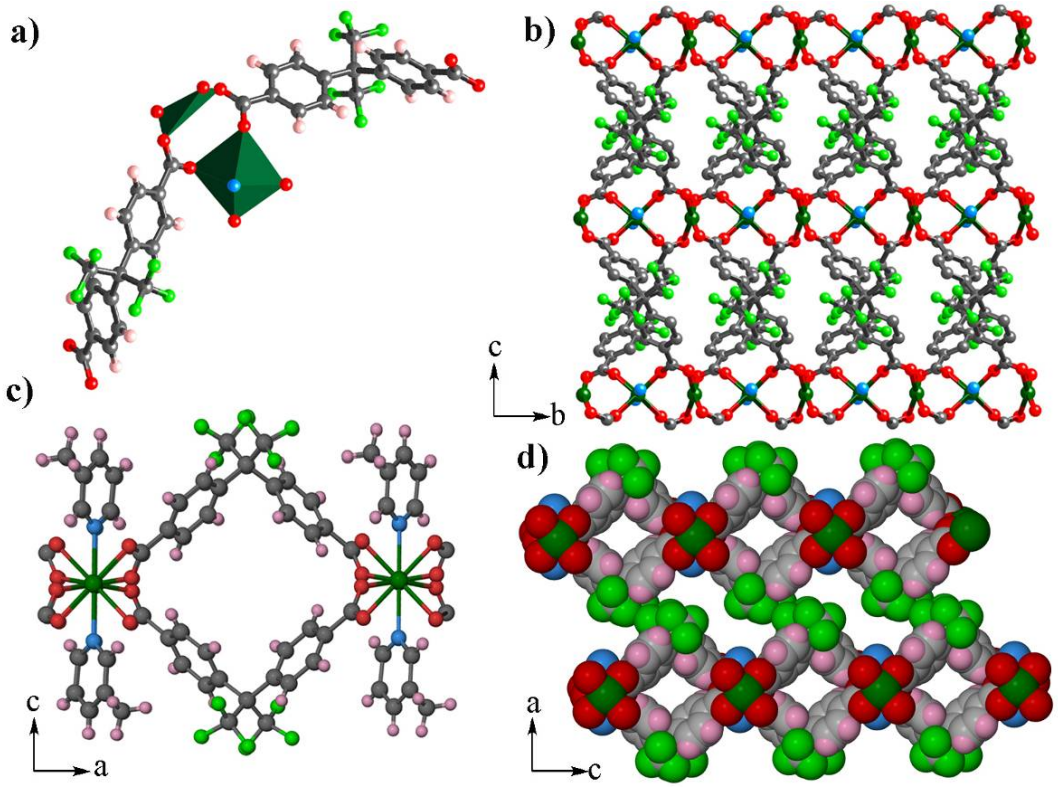

Figure 2.14 Crystal structure of Mn-H*F*MOF-D. (a) Polyhedral representation of the SBU showing the octahedral and square planar Mn^{2+} metal centers coordinated to H2hfbba linker. (b) 2-D coordination layer in Mn-HFMOF-D (view down *a* axis). (c) One single unit of Mn-H*F*MOF-D clearly showing coordinating 3-mepy groups. (d) Space fill model of Co-H*F*MOF-D (view down *b* axis) showing open channels. Color code: Mn (dark green), N (blue), O (red), C (grey), F (green). [Reprinted with permission from (28b). Copyright 2011 American Chemical Society].

Since the octahedral Mn^{2+} sites are blocked by 3-methyl pyridine, which is a monodentate ligand, the crystal structure fails to propagate along the crystallographic *a* axis. In the crystal structure of Mn-H*F*MOF-D, each hfbba ligand is connected to two Mn^{2+} metal centers i.e. octahedral and square planer respectively through zigzag fashion

as shown in Figure 2.14b. By joining only Mn^{2+} centers with ligand atoms, topological simplification of Mn-H*F*MOF-D shows the formation of zigzag network and mode of attachment of ligands with metal center (*Figure 2.14c*). In the structure of Mn-H*F*MOF-D, propagation of accessible square shaped pores of about 3.0 Å pore diameter is along the *b* axis in which lattice water molecules are sitting inside. Here, $-CF_3$ groups are protruding outside the adjacent channels within interlayer's which are spaced at 2.84 Å, in zigzag manner (*Figure 2.14d*). Unlike Co-H*F*MOF-D, $–CF_3$ groups of one channel in Mn-H*F*MOF-D are located on top of the square shaped channel edges with significant interlayer void. The two-dimensional parallel interpenetrating network is reinforced by the existence of other non-covalent interactions like C-H····F hydrogen bonds (*D*, 3.30 Å; *d*, 2.53 Å; *θ,* 140.5º).[35]

Crystal Structures of [Mn(hfbba)(3-mepy)(H_2O)] (Mn-H*F*MOF-W) and [Co(hfbba)(3-mepy)(H_2O)] (Co-H*F*MOF-W):[28a]

Three dimensional Mn-H*F*MOF-W and Co-H*F*MOF-W have been synthesized from H_2O, by hydrothermal conditions in acid digestion bomb at 120 °C. Mn-H*F*MOF-W and Co-H*F*MOF-W are iso-structural MOFs containing Mn^{+2} and Co^{+2} metal centers (see the unit cell dimensions in *Table 2.1 and 2.2*) in orthorhombic $Pna2_1$ space group. The asymmetric unit of Mn-H*F*MOF-W and Co-H*F*MOF-W contains one crystallographically independent Mn^{+2}/Co^{+2} ion, one hfbba ligand, one 3-methyl pyridine ligand, and one co-ordinated H_2O molecule (*Figure 2.15a*). Each octahedral Mn^{+2}/Co^{+2} ion is surrounded by four oxygen's from hfbba ligands [M–O distance ranges from 2.07 to 2.21 Å], one oxygen from H_2O [M–O distance = 2.16–2.22 Å] and one nitrogen from 3-methyl pyridine ligand [M–N distance = 2.12–2.24 Å]. In Mn-H*F*MOF-W and Co-H*F*MOF-W, metal–metal distance is 4.49 to 4.61 Å, which are connected through COO^- group of hfbba ligands. In the SBU of Mn-H*F*MOF-W and Co-H*F*MOF-W, on the adjacent metal center 3-methyl pyridine ligands are co-ordinated above and below positions alternatively (*Figure 2.15b*). The co-ordinated water molecule is co-ordinated on the opposite side of 3-methyl pyridine ligand. Four hfbba ligands are co-ordinated to adjacent metal centers from one carboxyl group which extends further joining to the next SBU. In the structure of Mn-H*F*MOF-W and Co-H*F*MOF-W, alternatively joined 3-methyl pyridine ligands are interdigited in the pores

by blocking them through *ab* plane.

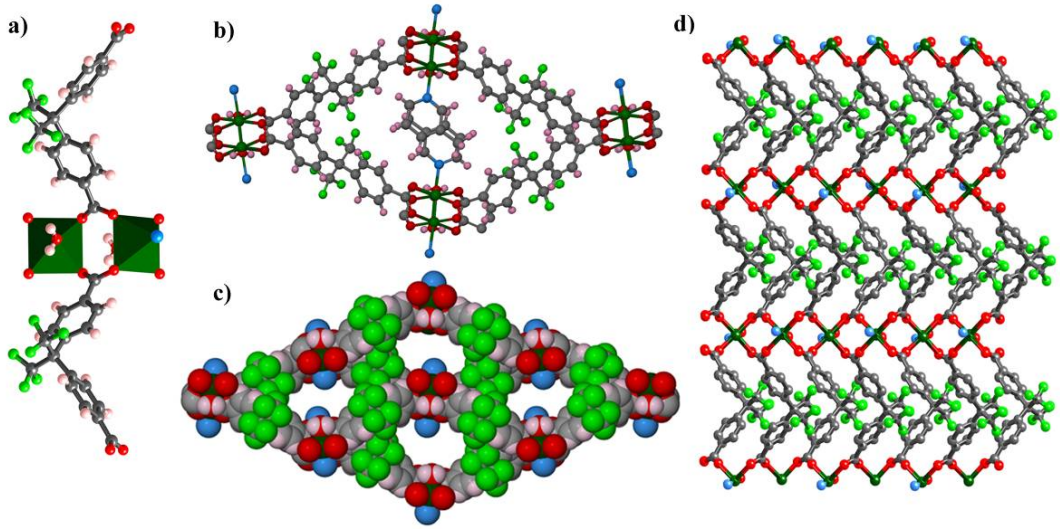

Figure 2.15 Crystal structures of Co-H*F*MOF-W and Mn-H*F*MOF-W. (a) Polyhedral representation of the SBU showing the presence of paddle-wheel Co^{2+}/Mn^{2+}. (b) One single unit of Co-H*F*MOF-W and Mn-H*F*MOF-W clearly showing the pointing 3-mepy groups into the pores. (c) Space fill model of Co-H*F*MOF-W and Mn-H*F*MOF-W. (d) 2-D coordination layer in Co-H*F*MOF-W and Mn-H*F*MOF-W (view down *c* axis). Mn/Co (dark green), N (blue), O (red), C (grey), F (green). [Reprinted with permission from (28b). Copyright 2011 American Chemical Society].

In these structures, each hfbba ligand co-ordinates with two adjacent metal centers through one of its carboxyl groups, which extends further forming the hexagonal pores along with interpenetration of 3-mepy and co-ordinated water molecules inside. Co-ordinated hfbba ligands form the zigzag type structure along the crystallographic ac plane (*Figure 2.15d*). By joining only Co^{+2}/Mn^{+2} centers with ligand atoms, topological simplification of Mn-H*F*MOF-W and Co-H*F*MOF-W shows the formation of zigzag network and mode of attachment of ligands with metal center as shown in Figure 2.15d. Since V-shaped H_2hfbba ligand co-ordinates with metals, it gives square shaped pores. Space filling model of these MOFs along crystallographic *ab* plane shows the formation of 1D channel assembling these square shaped pores (*Figure 2.15c*).

Using H_2hfbba linker and *N*-containing 3-mepy and 1,10-phenanthroline co-linkers, we tried to investigate the influence of the solvent and temperature on the formation and changes from 0D/1D to 3D architectures, when we change the solvent

from H_2O to DMF (*Figure 2.7*). However, for Zn(II), Mn(II) and Cu(II), a similar solvent change results in a 0D to 1D structural change. It is noteworthy that as soon as we use DMF as a solvent there is a dimensionality increase for the resulting *F*-MOFs.[28] A possible reason behind this could be the poor solubility of the H_2hfbba ligand in water. The poor solubility of the fluorinated dicarboxylic acid over the heterocyclic co-ligands may play an important role in the formation of the H-bonded/1D structures over 2D/3D structures. As H_2hfbba is the major structural building block, its limited abundance during the formation/crystallization due to its poor solubility in water may lead to the formation of the H-bonded/1D structures over 2D/3D frameworks. Structural comparison between *F*-MOF-4 and Cu-*F*-MOF-4B/Zn-*F*-MOF-4B indicates that a change in solvent of synthesis (DMF and DEF) resulted into diverse changes in resultant MOF architecture. Tetradentate bridging mode of H_2hfbba ligand coordinates with metal centers resulting in the formation of bimetallic tetracarboxylate clusters in all the *F*-MOFs, where apical positions are occupied by 3-picoline resulting into the formation of 2-fold parallel 2D→2D interpenetration or interdigitation with a 1D channel through crystallographic planes.

Similarly, using H_2hfbba linker and *N*-containing 3-methyl pyridine co-linker, we tried to investigate the influence of the solvent and temperature on the dimensionality in the resulting MOFs. We have synthesized four new polymeric frameworks Co-H*F*MOF-D, Co-H*F*MOF-W, Mn-H*F*MOF-D, and Mn-H*F*MOF-W as shown in Figure 2.7, which forms 2-D and 3-D networks with diverse architectures depending on the solvent of synthesis. We expected that the insertion of additional 3-methyl pyridine ligand in the synthesis media should have a crucial effect, as they induces the Π–Π stacking interactions affecting the dimensionality of the resulting polymeric framework, and therefore its square grid topology. In all the structures 3-picoline occupies the axial position of the $M_2N_2(\mu_2\text{-}CO_2)_2$ or $M_2N_1O_1(\mu_2\text{-}CO_2)_2$ the coordination sphere (*Figure 2.13–2.15*). Bimetallic clusters formed by coordination of metal centers with carboxylate groups play an important role in the determination of the architecture of the resultant framework. In the *F*-MOFs reported herein, the co-ordination mode is $\mu_2{}^b$–OCO, that is, both the carboxylate oxygen atoms are involved in the co-ordination with two M^{+2} atoms in monodentate fashion (*Figure 2.6*). Although

the co-ordination mode is same in all H*F*MOFs, their dimensionality, SBU, and resultant frameworks are totally different from each other. It seems that the solvent of synthesis and the conditions for reaction are affecting the network structures. Co-H*F*MOF-D and Mn-H*F*MOF-D synthesized from DMF have the 2-D structure, whereas Co-H*F*MOF-W [flack parameter: 0.01(2)] and Mn-H*F*MOF-W [flack parameter: 0.04-(2)][36] synthesized from H_2O have the isostructural 3-D architecture with an octahedral SBU in the same *Pna*2_1 space group as shown in Figure 2.15. The adoption of a non-centrosymmetric space group and *21* screw axis by these two *F*-MOFs could be attributed to the bent nature of the hfbba link.[28] But Co-H*F*MOF-D and Mn-H*F*MOF-D synthesized from DMF have different structures (Co-H*F*MOF-D, octahedral SBU with paddlewheel; Mn-H*F*MOF-D, octahedral and square planar SBU in same structure) with different space groups (C2/*c* in Co-H*F*MOF-D and C2 in Mn-H*F*MOF-D). Although combination of $hfbba^{2-}$ with M^{2+} can produce several possible bridging modes, we observe only three possible co-ordination mode $\mu1^{t}$–OC(=O), $\mu2^{b}$–OCO and $\mu1^{c}$–OCO along this series (*Figure 2.6*), even we have changed solvent and synthetic conditions. Within these H*F*-MOFs, Co-H*F*MOF-D and Mn-H*F*MOF-D show formation of 2-fold parallel 2-D→2D interpenetration with a 1-D channel through the crystallographic *ac* plane (*Figure 2.13 and 2.14*). Co-H*F*MOF-W and Mn-H*F*MOF-W on the other hand show formation of a 3-D framework with interdigited 3-methyl pyridine molecules (*Figures 2.15*). Also, in these two H*F*MOFs open metal sites can be observed as they contain the coordinated H_2O molecules which could be removed by strong evacuation.

Crystal Structures of $[Co_3(INA)_4(O)(C_2H_5OH)_3](NO_3)\cdot(C_2H_5OH)\cdot(H_2O)_3]$ Co-INA-1 and $[Co_3(FINA)_4(O)(C_2H_5OH)_2(H_2O)]$ Co-*F*INA-1:

The isostructural Co-INA-1[38] and Co-*F*INA-1, crystallizes in *Pnma* space group with 8-connected, oxo-centered [Co_3(O)] type SBU where open metal sites could be perceived. Since, Co-INA-1 and Co-*F*INA-1 have similar structure except replacement of INA with *F*INA; the structural details of isostructural Co-*F*INA-1 only represented herein. Each [Co_3(O)] metal cluster of Co-*F*INA-1 is connected to eight *F*NIC ligands through four bridging μ_2-COO^- groups, four pyridyl nitrogen atoms, two coordinated ethanol and one coordinated water molecule (*Figure 2.16a and 2.16d*).

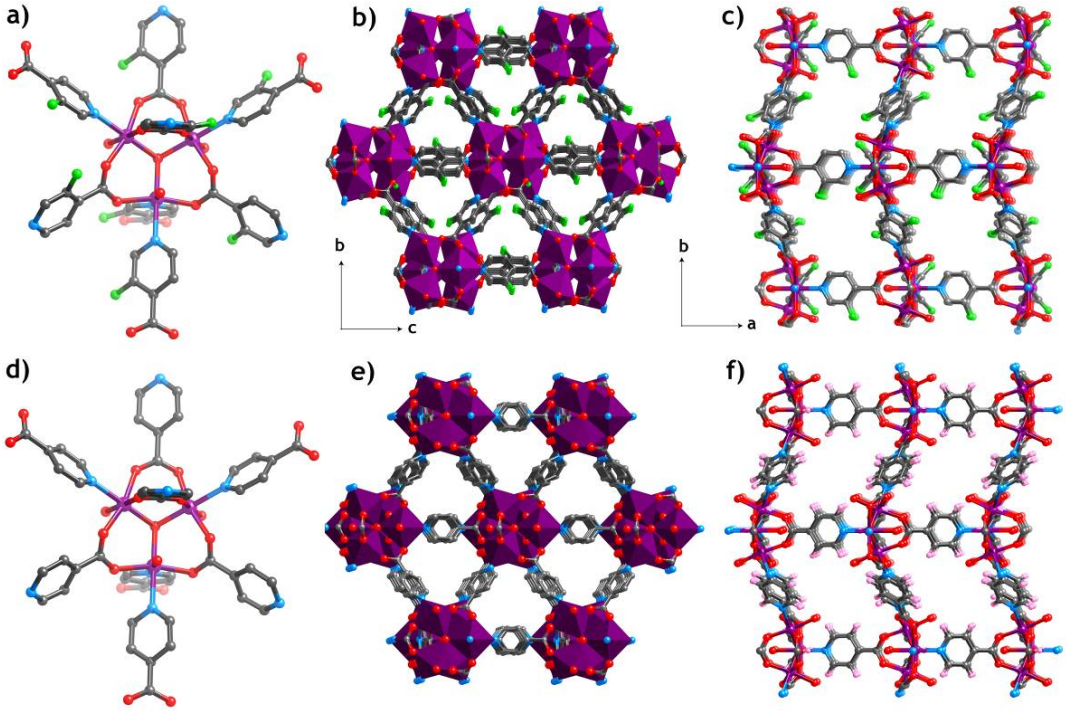

Figure 2.16 Crystal structure of Co-*F*INA-1 and Co-INA-1. (a), (d) Ball and stick representation of SBU of Co-*F*INA-1 and Co-INA-1. (b), (e) Packing diagram of Co-*F*INA-1 and Co-INA-1 along *a* axis. (c), (f) Packing diagram of Co-*F*INA-1 and Co-INA-1 along *c* axis. Co (pink), N (blue), O (red), C (grey), F (green). [Reprinted with permission from (28a). Copyright 2012 WILEY-VCH Verlag GmbH & Co. KGaA].

Each tri-metal cluster is connected to the eight similar tri-metal SBUs resulting into highly connected 3D framework with high porosity. In Co-*F*INA-1, two types pores are available, through *a* axis one dimensional channels with an aperture of 4.2 Å propagate (*Figure 2.16b and 2.16e*), while through *c* axis square shaped channels of 3.2 × 2.8 Å dimensions extends through the crystal structure (*Figure 2.16c and 2.16f*). The metal sites are coordinated to EtOH and water molecules pointing towards the pores, which in-turn can create the open metal sites. In each tri-metal oxo-center [Co_3(O)], two metal centers possesses identical coordination sphere (τ = 0), where each Co(II) connects to three μ_2-carboxyl oxygen atoms, one nitrogen from *F*NIC ligand, one ethanol molecule and one central μ_3-oxygen atom. Remaining third Co(II) metal center is connected to two μ_2-carboxyl oxygen, two *F*NIC–pyridyl nitrogen, one coordinating water molecule and one central μ_3-oxygen atom. The crystal structure of Co-INA-1 has higher porosity (5.0 Å) and solvent accessible void (39 %) than Co-*F*INA-1 (4.2 Å and

34.5 %) calculated using *PLATON*, due to smaller atomic size of hydrogen atoms than fluorine.

Crystal structure of [Co(INA)$_2$.(DMF)] Co-INA-2 and [Co(*F*INA)$_2$ •(H$_2$O)] Co-*F*INA-2:

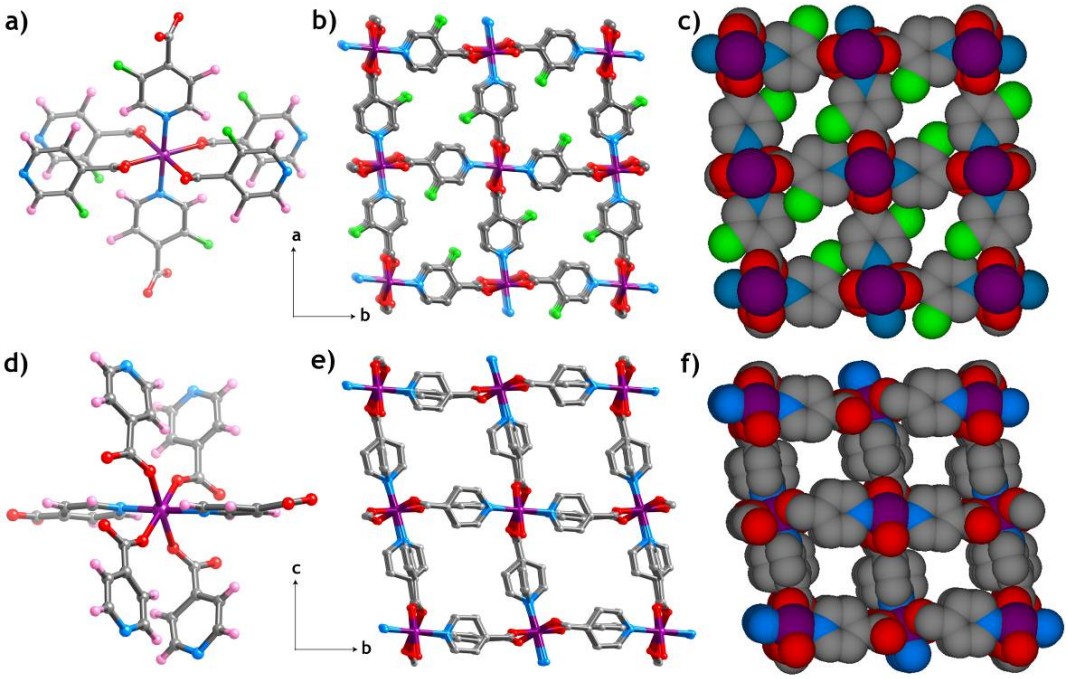

Figure 2.17 Crystal structure of Co-FINA-2 and Co-INA-2. (a), (d) Ball and stick representation of SBU of Co-FINA-2 and Co-INA-2. (b), (e) Packing diagram of Co-FINA-2 and Co-INA-2 along *c* and *a* axis, respectively. (c), (f) Space filling representation of Co-FINA-2 and Co-INA-2 along *c* and *a* axis, respectively. Co (pink), N (blue), O (red), C (grey), F (green). [Reprinted with permission from (28a). Copyright 2012 WILEY-VCH Verlag GmbH & Co. KGaA].

The three dimensional structure of Co-INA-2 and Co-*F*INA-2 crystallizes in *P*21 and *P*21/*c* space groups, respectively. In the crystal structure of Co-INA-2 and Co-*F*INA-2, the INA and *F*INA linkers coordinate through pyridinic nitrogen atoms and carboxylic acid groups in μ_2-OCO fashion. The crystal structure of Co-INA-2 and Co-*F*INA-2 consists doubly bridged infinite Co(II) carboxylate chains (*Figure 2.17a and 2.17d*). The pyridine functionalities of the INA and *F*INA ligands point outwards of the chains (*Figure 2.17b and 2.17e*). The resulting strands crosslink by N–Co coordination to generate the 3D framework. In Co-INA-2, each Co(II) metal center connects to the four INA ligands through one of their μ_2-carboxyl oxygen and two INA ligands through their

pyridyl nitrogen atoms. Each SBU connects to the next through INA ligands to generate the 3D structure. Co-INA-2 have 2.4 × 3.1 Å square shaped pores with 8.9 % solvent accessible void, where uncoordinated water molecules are sitting inside the pores (*Figure 2.17c and 2.17f)*. The Co-*F*INA-2 crystal structure shows the square shaped channels of 2.4 × 4.1 Å running through the structure with 51 % solvent accessible volume. Like isostructural Co-INA-1 and Co-*F*INA-1, the structures of Co-INA-2 and Co-*F*INA-2 are also isostructural.

Like isostructural Co-INA-1 and Co-*F*INA-1, the structures of Co-INA-2 and Co-*F*INA-2 are also isostructural. In the crystal structure of Co-INA-1, due to the presence of $[Co_3(OH)]$ metal cluster, additional positive charge on central tetra-coordinated oxygen atom has been balanced by the NO_3^- ions present in the pores. But in case of Co-*F*INA-1, the metal cluster itself is neutral $[Co_3(O)]$, which diminishes the possibility of presence of NO_3^- ions in the pores. The crystal structure of Co-INA-1 has higher porosity (5.0 Å) and solvent accessible void (39 %)[38] than Co-*F*INA-1 (4.2 Å and 34.5 %) calculated using *PLATON*, due to smaller atomic size of hydrogen atoms than fluorine. Comparison between the cell dimensions for the Co-INA-2 (a = 9.81 Å, b = 12.64 Å, c = 11.07 Å) and Co-*F*INA-2 (a = 4.96 Å, b = 12.35 Å, c = 11.81 Å) reveals that although the b and c axes are similar in dimensions, the a axis of the Co-INA-2 unit cell is approximately double of Co-*F*INA-2 (doubling of the a axis is expected from the randomization/disorder of the pyridine ring orientations in the Co-INA-2 structure).[39] The unit cell volume of the Co-*F*INA-2 crystal structure (698.9 A^3) is 51 % that of the Co-INA-2 unit cell volume (1355.0 A^3). Co-*F*INA-2 has higher pore dimensions (2.4 × 4.1 Å) compared to Co-INA-2 (2.4 × 3.1 Å), although in former case fluorine atoms are pointing into pores. Also Co-*F*INA-2 (14.5 %) has the higher solvent accessible void than that of Co-INA-2 (8.9 %), although latter have the higher cell volume and cell dimensions.

2.4.3 X-ray Powder Diffraction and Thermal Properties:

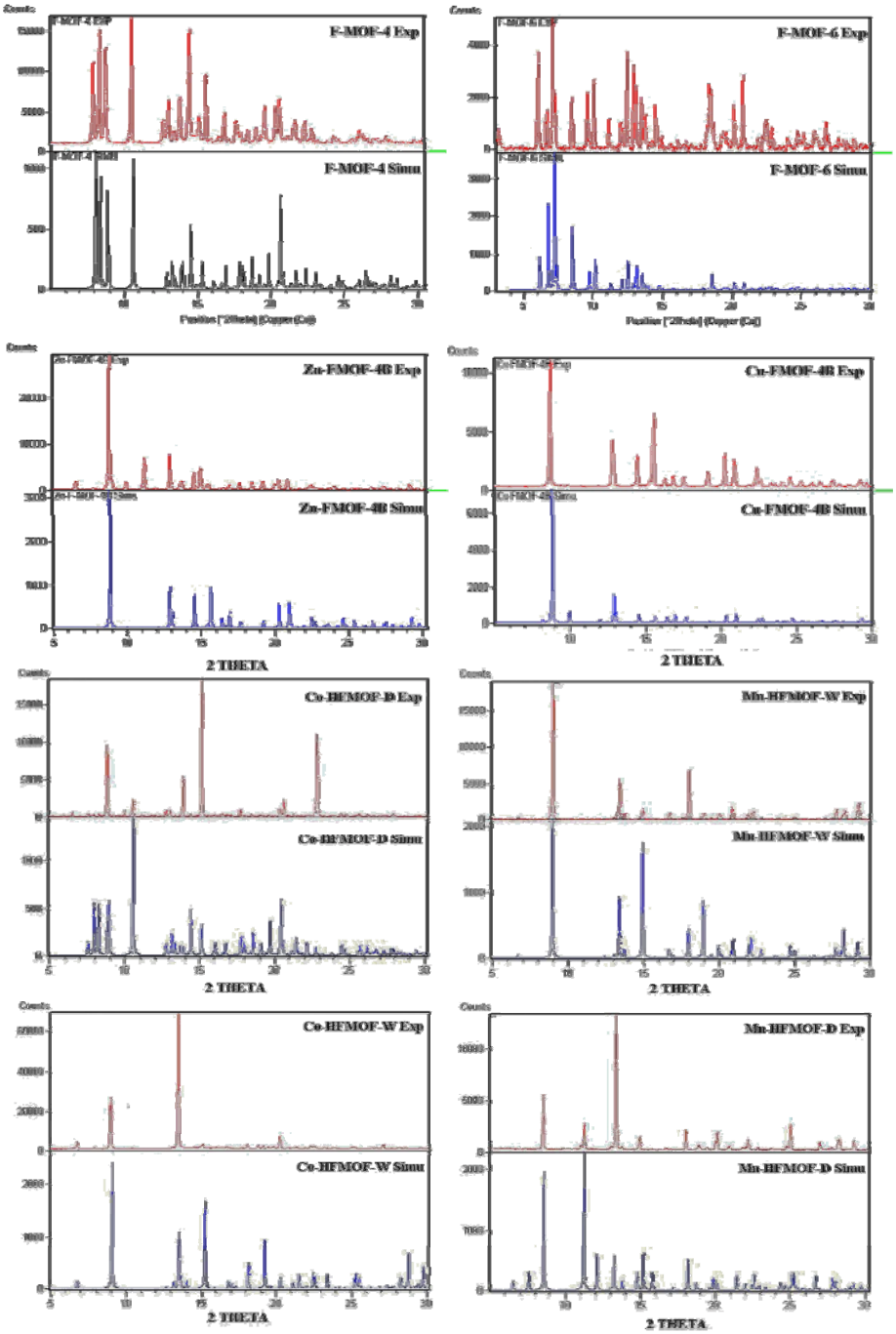

Figure 2.18 PXRD patterns for the as synthesized MOF samples of *F*-MOF-4, *F*-MOF-6, Zn-*F*MOF-4B, Cu-*F*MOF-4B, Co-H*F*MOF-D, Mn-H*F*MOF-W, Co-H*F*MOF-W and Mn-H*F*MOF-D. The matching profile of simulated XRD patterns from single crystal structure data with those of experimental one suggests the phase purity of synthesized MOFs.

Being achieved structural information of partially fluorinated MOFs synthesized using H_2hfbba linker by solvothermal/hydrothermal methods; the bulk phase of synthesized MOFs was characterized using PXRD, TGA and gas adsorption studies. PXRD experiments were carried out on all the complexes, to confirm the phase purity of the bulk materials. The PXRD patterns of the experimental and computer-simulated patterns of all the *F*-MOFs are shown in Figure 2.18. All the major peaks in the experimental PXRD patterns of *F*-MOF-4, *F*-MOF-6, Zn-*F*MOF-4B, Cu-*F*MOF-4B, Co-H*F*MOF-D, Mn-H*F*MOF-W, Co-H*F*MOF-W and Mn-H*F*MOF-D are matches quite well with that of simulated PXRD pattern from single crystal XRD structure, indicating their reasonable crystalline phase purity. Similarly, peak to peak matching profile of experimental and simulation PXRD patterns of these *F*-MOFs confirms the absence of impurities in the bulk phase MOF synthesized. The experimental patterns in few MOF cases have few diffraction lines that are un-indexed and some that are slightly broadened in comparison with those simulated patterns. This is probably due to the loss of DMF molecules from the lattice because of grinding during the analysis.

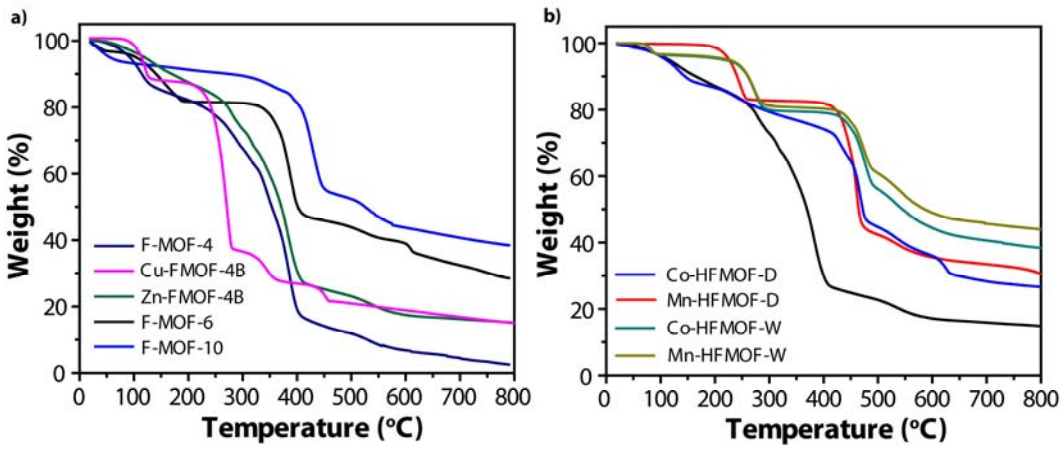

Figure 2.19 Overlay of TGA traces of as synthesized *F*-MOFs indicating their reasonable thermal stability.

To examine the architectural and thermal stability of synthesized *F*-MOFs, we prepared them at the gram scale to allow detailed investigation of the aforementioned properties. From thermogravimetric analyses (TGA) performed on the as synthesized MOFs samples represented in Figure 2.19, it was revealed that these compounds have high thermal stability. The TGA trace for *F*-MOF-6, *F*-MOF-10 and Cu-*F*MOF-4B

showed a gradual weight-loss step of upto 150 °C, corresponding to escape of all DMF/H_2O molecules from the pores followed by a sharp weight loss (300–450 °C) probably because of the decomposition of the framework. The TGA patterns of the *F*-MOF-4, Zn-*F*MOF-4B and Co-H*F*MOF-D show continuous weight loss from the temperature above 100 °C probably due to the loss of guest solvent molecules present into the pores of these MOFs. The TGA of Mn-H*F*MOF-D and Mn-H*F*MOF-W shows the sharp weight loss of 25–100 °C corresponding to escape of all H_2O molecules in pores followed by a plateau before a sharp weight loss (200–300 °C) probably because of the decomposition of the coordinated 3-methyl pyridine molecules. The TGA of Co-H*F*MOF-W shows a gradual weight loss step of 25–125 °C corresponding to the loss of coordinated and framework water molecules followed by the decomposition of the framework probably because of decomposition of 3-methyl pyridine molecules and escape of coordinated H_2O molecules.

Further, in order to furnish the phase purity of INA and *F*INA linker based MOFs, PXRD analyses were performed using bulk samples. All major peaks of experimental PXRDs matches well with simulated PXRDs, indicating their reasonable crystalline phase purity (*Figure 2.20*). The experimental PXRD pattern of Co-*F*INA-1 has a few diffraction lines that are un-indexed and some that are slightly broadened in comparison to the simulated pattern. This is probably due to the loss of DMF molecules from the lattice due to grinding at the time of sample preparation. Also in purpose of checking framework architecture and thermal stability of Co-*F*INA-1, Co-*F*INA-2 and Co-INA-2, we performed thermal gravimetric analyses (TGA) of these samples. From TGA it was revealed that these compounds have high thermal stability. The TGA traces of as synthesized Co-INA-2, Co-*F*INA-1 and Co-*F*INA-2 showed a gradual weight-loss step of 11.5 % (20–200 °C), 19.5 % (20–140 °C) and 8.7 % (20–160 °C) respectively corresponding to escape of DMF, EtOH and H_2O guest and coordinated solvent molecules from pores (*Figure 2.20*). The framework of Co-*F*INA-1 is stable upto 400 °C although coordinated and guest solvent molecules leaves the framework at 140 °C. After 400 °C the Co-*F*INA-1 framework decomposes with sharp weight loss. The framework of Co-*F*INA-2 have the more stability compared to Co-INA-2. Co-*F*INA-2 is stable upto 300 °C, whereas Co-INA-2 is stable upto 250 °C. This is followed by a

sharp weight loss probably due to the decomposition of the frameworks.

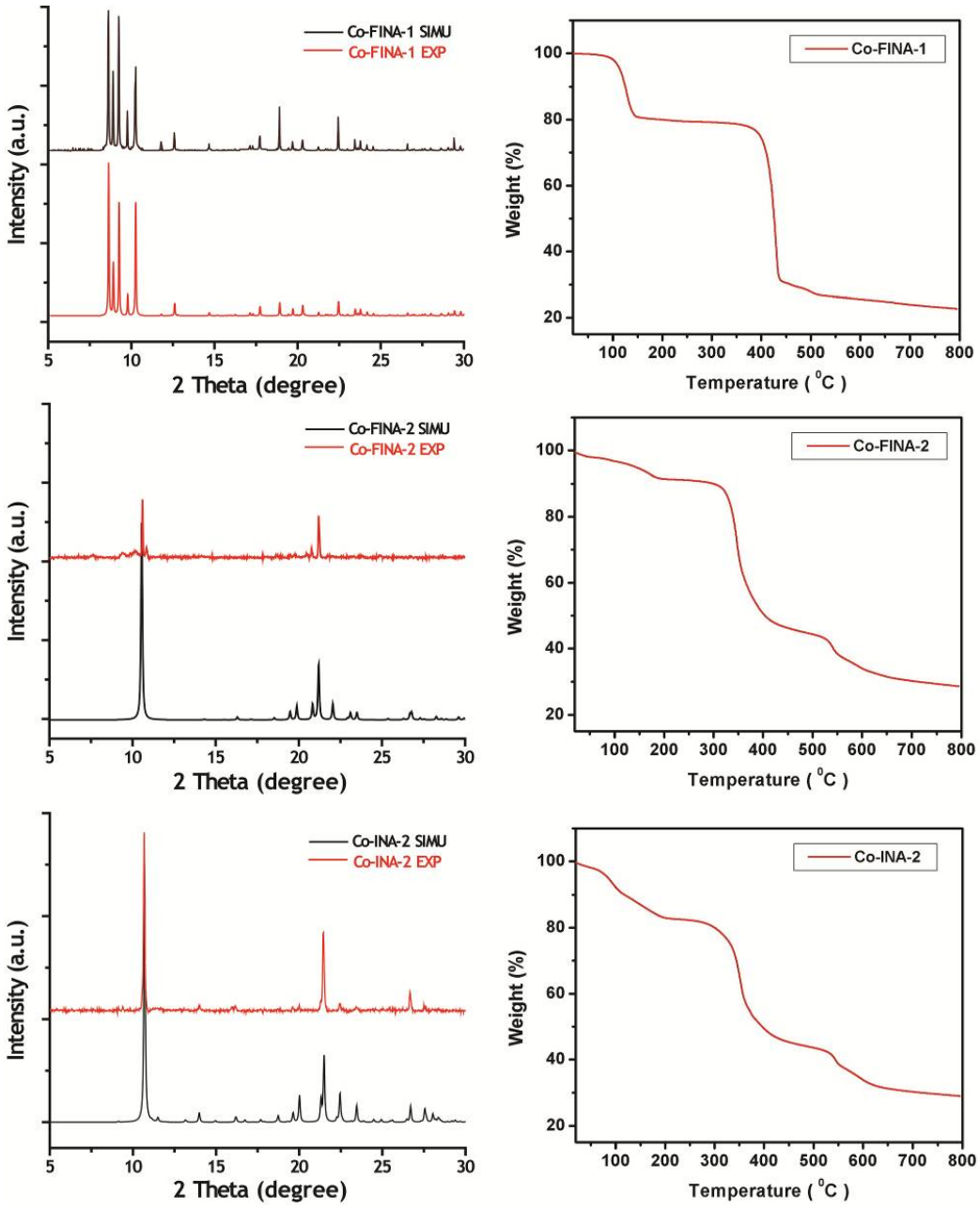

Figure 2.20 PXRD patterns and TGA profiles for the as synthesized MOF samples of Co-FINA-1, Co-FINA-2, and Co-INA-2. The matching profile of simulated XRD patterns from single crystal structure data with those of experimental one suggests the phase purity of synthesized MOFs. The thermal stability of Co-FINA-1, Co-FINA-2, and Co-INA-2 above 300 °C is visible from TGA profiles.

2.5 Gas Adsorption Properties:

2.5.1 Experimental Results:

Having all the structural information and phase pure samples of all the 2D and 3D MOFs synthesized using H_2hfbba linkers; we have investigated the gas adsorption behavior of these samples. Prior to the gas adsorption, the micro-crystals of each MOF were soaked in dry chloroform or 1:1 dry dichloromethane and methanol mixture for 12 h. Fresh 1:1 dry dichloromethane and methanol mixture was subsequently added, and the crystals were allowed to stay for an additional 48 h to remove coordinated and free solvates (DMF/DEF/H_2O/EtOH) present in framework. The sample was dried under a vacuum (<10^{-3} Torr) at room temperature for 12 h. In case, if the coordinated solvent

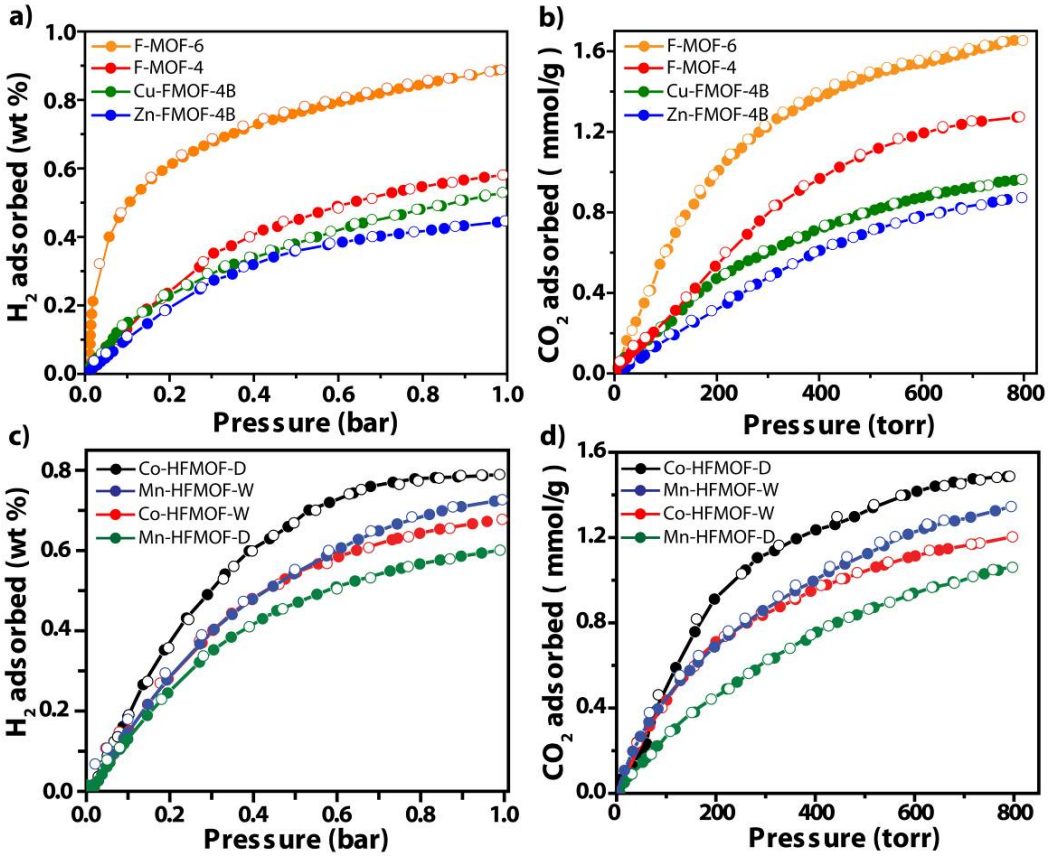

Figure 2.21 Gas adsorption analyses for *F*-MOFs. (a) and (b) H_2 (77 K) and CO_2 (298 K) adsorption isotherms for F-MOF-4, F-MOF-6, Cu-*F*MOF-4B and Zn-*F*MOF-4B. (c) and (d) H_2 (77 K) and CO_2 (298 K) adsorption isotherms for Co-H*F*MOF-D, Co-H*F*MOF-D, Co-H*F*MOF-W and Mn-H*F*MOF-W. Filled and open circles represent adsorption and desorption branches, respectively.

molecules on the secondary binding units (SBUs) remain in the framework at this stage; to remove these species, samples were heated at 60 °C for 12 h and 100 °C for 12 h under a dynamic vacuum. Since, all these *F*-MOFs synthesized using H_2hfbba linker was having porous structures with the pore sizes ranging from 3–5 Å, we have collected the N_2 adsorption isotherms at 77 K and 1 atm pressure. Except, *F*-MOF-4 (196 m^2/g) and *F*-MOF-6 (20 m^2/g); none other MOF in this series among synthesized *F*-MOFs have shown N_2 uptake. All of these *F*-MOFs are non-porous towards the N_2 uptake as they have a lesser aperture size than the kinetic diameter of N_2 (3.6 Å); however, these *F*-MOFs are able to take the H_2 (2.89 Å) and CO_2 (3.4 Å) as they have a lesser kinetic diameter. Furthermore, the low kinetic energy of the N_2 molecules, at 77 K results in N_2 molecules being unable to effectively enter small pores.

All these *F*-MOFs show reversible type-I H_2 and CO_2 adsorption isotherms at 77 K and 298 K, respectively. As shown in Figure 2.21, among these H_2hfbba based MOF series represented herein, *F*-MOF-6 show highest H_2 uptake upto 0.90 wt% as pressure approaches to 1 atm. In this series, *F*-MOF-4 having non-interdigitated square shaped pores showed H_2 and CO_2 uptake of 0.58 wt% and 1.27 mmol/g, respectively. The isostructural MOFs, Cu-*F*MOF-4B and Zn-*F*MOF-4B having square-shaped pores with interdigitated layered show nearly similar H_2 uptake upto 0.52 and 0.45 wt% as well as CO_2 uptake of 0.96 and 0.87 mmol/g, as pressure reaches to 1 atm. The uptake observed in *F*-MOF-4 and Cu-*F*MOF-4B/Zn-*F*MOF-4B is well justified as later have the non-interdigited pores accessible for gas adsorption. Further, iso-structural Co-H*F*MOF-W and Mn-H*F*MOF-W show nearly equal 0.67 and 0.72 wt% H2 uptake, and 1.20 and 1.34 mmol/g of CO_2 adsorption. In this context, Co-H*F*MOF-D showed higher H_2 (0.78 wt%) and CO_2 (1.48 mmol/g) uptake, whereas Mn-H*F*MOF-D shows the lower H_2 (0.60 wt%) and CO_2 (1.06 mmol/g) adsorption. This result is well anticipated as Co-H*F*MOF-D contains the robust paddle-wheel Co(II) motif with 3-methyl pyridine molecules pointing outward of the pore. As a result pores are accessible for adsorbing gas molecules. On the other hand, Co-H*F*MOF-W and Mn-H*F*MOF-W have blocking 3-methyl pyridine molecules into the pores. Although, H_2 adsorptions for these *F*-MOFs are moderate, they still are comparable with the H_2 adsorption of the highest capacity zeolites, some carbon materials, and some other *F*-MOFs reported in the literature.

Table 2.1 Summary of gas adsorption analyses of MOFs synthesized using H_2hfbba and INA/FINA linkers:

Sr. No.	Name of MOF	BET surface area (m^2/g)	H_2 uptake (wt%)[a]	CO_2 uptake (mmol/g)[b]
H_2hfbba linker based MOFs				
1	F-MOF-4[28e]	196	0.58	1.27
2	Cu-FMOF-4B[28c]	-	0.52	0.96
3	Zn-FMOF-4B[28c]	-	0.45	0.87
4	F-MOF-6[28d]	20	0.9	-
5	Co-HFMOF-D[28b]	-	0.78	1.48
6	Mn-HFMOF-D[28b]	-	0.60	1.06
7	Co-HFMOF-W[28b]	-	1.67	1.20
8	Mn-HFMOF-W[28b]	-	0.72	1.34
INA and FINA linker based MOFs				
9	Co-INA-1[28a]	544[c]	1.90	3.09
10	Co-FINA-1[28a]	547	1.97	3.00
11	Co-INA-2[28a]	92	0.52	1.78
12	Co-FINA-2[28a]	152	1.82	2.30

a H_2 uptake data represented is collected at 77 K and 1 atm pressure.
b CO_2 uptake data represented is collected at 298 K and 1 atm pressure.
c surface are represented in this table is Langmuir surface area adopted from Reference: *Inorg. Chem.*, **2011**, *50*, 232.

As shown in Figure 2.21 and table 2.1, we have achieved the moderate H_2 and CO_2 uptake in these *F*-MOFs synthesized using H_2hfbba linkers, despite in several cases surface area was negligible. From this obtained data it was clear that tiny pores present in these MOFs are the result of V-shaped bent structure of H_2hfbba linker used as building block, which restricts the formation of big channels favorable for higher amount of gas uptake. The twisted conformation of linker in these MOFs induces flexibility restricting the pore size below 4 Å, which in turn creates very small channels accessible for tiny gas molecules (H_2/CO_2) with very limited free space. The high framework density and low solvent accessible voids present in these MOFs as a result of their limited intrinsic porosity, adsorbs H_2 moderately. Since, we could not synthesize the isostructural non-fluorinated analogue for any of these *F*-MOFs; it is very difficult

to conclude the effect of fluorination on the gas adsorption.

In these regards, in order to achieve the porous MOFs with rigid framework for high H_2 uptake, we have collected the gas adsorption isotherms for MOFs synthesized using INA and *F*INA as a building block. In these MOFs, as seen from the crystal structures of Co-INA-1, Co-*F*INA-1, Co-INA-2 and Co-FINA-2; the modular length of these INA and *F*INA linkers produced the porous structures with reasonably high pore size and surface area due to higher porosity. Most importantly, in these cases, we could

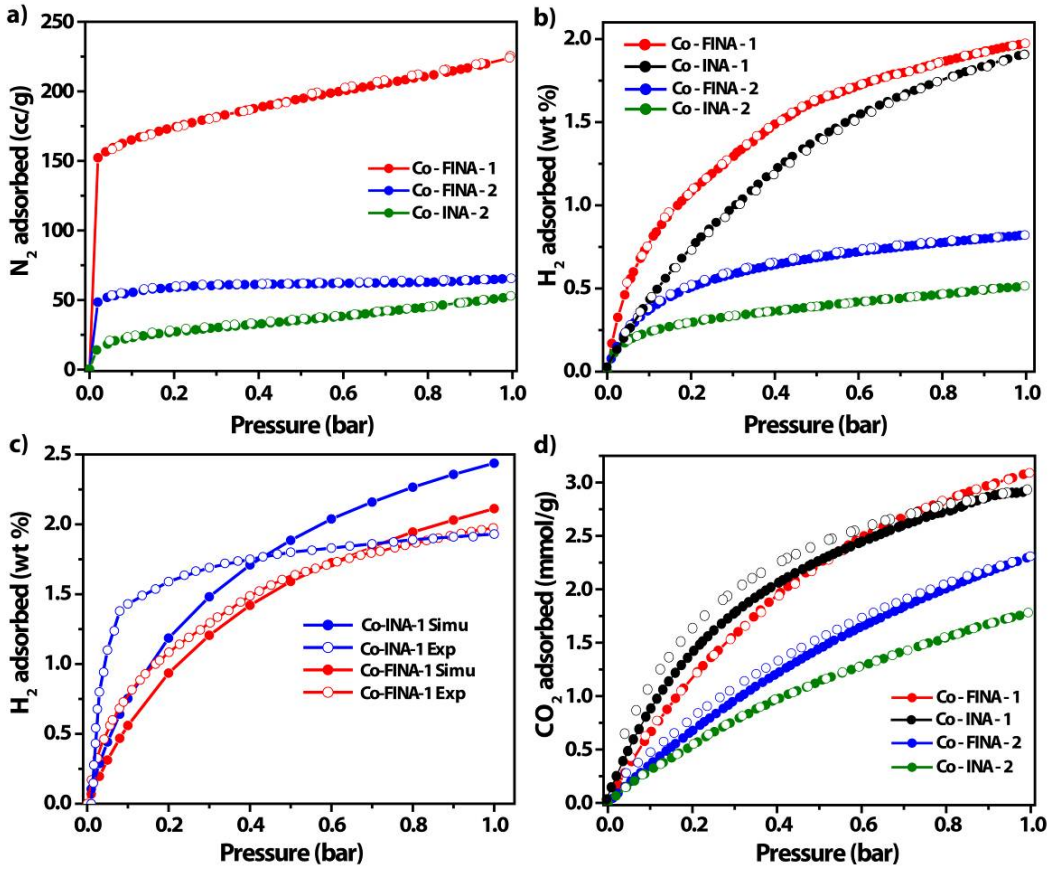

Figure 2.22 Gas adsorption analyses for Co-FINA-1, Co-INA-1, Co-FINA-2, and Co-INA-2. (a) N_2 adsorption isotherms for Co-FINA-1, Co-FINA-2, and Co-INA-2 collected at 77 K and 1 atm pressure. (b) H_2 adsorption isotherms for Co-FINA-1, Co-INA-1, Co-FINA-2, and Co-INA-2 collected at 77 K and 1 atm pressure. (c) Comparison between simulated and experimental H_2 adsorption isotherms for Co-FINA-1 and Co-INA-1 collected at 77 K and 1 atm pressure. (d) CO_2 adsorption isotherms for Co-FINA-1, Co-INA-1, Co-FINA-2, and Co-INA-2 collected at 298 K and 1 atm pressure. Filled and open circles represent adsorption and desorption branches, respectively. [Reprinted with permission from (28a). Copyright 2012 WILEY-VCH Verlag GmbH & Co. KGaA].

easily synthesize the isostructural MOFs with/without fluorine incorporated into its backbone. Since, using these isostructural MOFs (Co-INA-1/Co-*F*INA-1 and Co-INA-2/Co-*FI*NA-2) it will be more convenient to study the effect of fluorination on the gas adsorption properties in resulting MOFs, we have analyzed the adsorption behavior of these MOFs using N_2, H_2 and CO_2 gases. The isostructural MOFs, with and without fluorine atoms pointing into the pores will allow studying the electronic effect of these atoms present into the pores on the gas (especially H_2) uptake properties.

Analysis of crystal structure of Co-INA-1, Co-*F*INA-1, Co-INA-2 and Co-*F*INA-2 reveals that, these MOFs are porous with moderate solvent accessible void, despite being the presence of protruding fluorine atoms in the pores of Co-*F*INA-1 and Co-*F*INA-2. Unlike Co-*F*INA-1 and Co-INA-1, Co-*F*INA-2 possesses higher pore size and higher solvent accessible void than non-fluorinated Co-INA-2. These results motivated us to study the N_2, H_2 and CO_2 adsorption of these MOFs. Prior to gas sorption experiments, guest and possibly coordinated solvent molecules are removed by solvent exchange and thermal activation at an optimized temperature of 150 °C, under ultrahigh vacuum. The permanent porosity of Co-*F*INA-1, Co-*F*INA-2 and Co-INA-2 was confirmed by N_2 adsorption isotherms, as these MOFs have the pore size higher than the kinetic diameter of N_2 (3.6 Å). All these MOFs show reversible Type-I N_2 adsorption isotherms at 77 K temperature (*Figure 2.22a*). The Co-*F*INA-1 have the BET and Langmuir surface area of 547 and 841 m^2/g, which is higher than its non-fluorinated isostructural analogue Co-INA-1[37] (Langmuir surface area = 544 m^2/g). Although, Co-*F*INA-1 has smaller pores compared to Co-INA-1, it shows higher surface area possibly due to high stability of the framework. It has been mentioned in the literature that Co-INA-1 due to the slight shrinkage and/or partial collapse of the coordination framework after removing all coordinated and lattice solvents, shows less Brunauer–Emmett–Teller (BET) as well as Langmuir surface area. Whereas, Co-*F*INA-1 framework remains intact even after solvent removal also probably due to the presence of fluorine atoms into the pores. Co-INA-2 shows 92 m^2/g and 157 m^2/g of BET and Langmuir surface area, whereas its fluorinated isostructural analogue Co-*F*INA-2 has higher BET (152 m^2/g) as well as Langmuir surface area (238 m^2/g) as shown in Figure 2.22. The higher surface area of Co-*F*INA-2 than Co-INA-2 is justified

as former has the larger pores with higher solvent accessible void. It is noteworthy that for Co-*F*INA-1 and –2, fluorine insertion has increased the surface area than the non-fluorinated analogues.

Further, as we confirmed the permanent porosity of Co-INA-1, Co-INA-2, Co-*F*INA-1 and Co-*F*INA-2, we collected the H_2 and CO_2 adsorption isotherms for these MOFs. All these MOFs show reversible type-I isotherms at 77 K (H_2) and 298 K (CO_2) and 1 atm pressure. In addition, the absence of adsorption–desorption hysteresis indicates that H_2 and CO_2 is reversibly adsorbed by all the MOFs reported here. At 77 K, Co-FINA-1 adsorbs highest amount of H_2 in this series (1.97 wt%) as pressure approaches to 1 atm (*Figure 2.22b*). At 77 K, Co-INA-1 adsorbs almost similar amount of H_2, showing 1.90 wt% uptake as pressure approaches to 1 atm (as reported in literature). Similarly, Co-*F*INA-2 shows 0.82 wt% H_2 uptake at 77 K and 1 atm pressure. Co-INA-2, which is isostructural with Co-*F*INA-2, adsorbs lowest amount of H_2 (0.52 wt%) in this series of MOFs synthesized using INA and *F*INA linkers. Although Co-FINA-1 has smaller pores compared to Co-INA-1, it shows higher surface area as well as higher H_2 adsorption. A possible reason could be the aforementioned logic of pore shrinkage in Co-INA-1 due to loss of coordinated solvent molecules while evacuation. At higher pressure, Co-INA-1 and Co-*F*INA-1, Co-INA-1 has a higher H_2 adsorption over the entire pressure range. H_2 uptake in Co-*F*INA-2 and Co-INA-2 is well justified as Co-*F*INA-2 has much larger pores (2.4 × 4.1 Å *vs* 2.4 × 3.1 Å) with higher solvent accessible void (14.4 % *vs* 8.9 %) compared to the Co-INA-2, which is well supported by the BET and Langmuir surface area analyses. Further, the CO_2 adsorption properties of Co-INA-1, Co-*F*INA-1, Co-INA-2 and Co-*F*INA-2 shows same trends in adsorption capacities as seen in the case of H_2 uptake (*Figure 2.22d*). Co-*F*INA-1 adsorbs 3.09 mmol/g CO_2 at 298 K, which is highest uptake in this series. Co-*F*INA-2 adsorbs 2.30 mmol/g, while Co-INA-2 adsorbs 1.78 mmol/g of CO_2 at 298 K and as pressure approaches to 1 bar. These CO_2 uptake properties are well justified with respect to the BET and Langmuir surface areas of these MOFs. The H_2 and CO_2 uptake capacities shown by the Co-INA-1, Co-FINA-1, Co-INA-2, Co-*F*INA-2 are comparable with previously reported well known MOFs. The H_2 (77 K) and CO_2 (298 K) uptake shown by the Co-*F*INA-1 at 1 bar pressure is highest reported for the fully or

partially fluorinated MOFs reported in the literature. Co-*F*INA-1 outperforms the fluorinated MOFs [Ag_2 (Ag_4-Tz_6)][8] and [$Zn_2(tfbdc)_2(dabco)$],[10a] which have the H_2 uptake capacity of 1.0 wt% and 1.78 wt% respectively, at 1 bar pressure. The H_2 uptake shown by Co-*F*INA-1 at 77 K and 1 atm pressure is comparable to the MOFs like Mg/DOBDC,[4f] $Zn_2(BDC)_2$ (DABCO)[10a] and outperforms well known MOFs like PCN-6,[40a] PCN-68,[40b] PCN-66,[40b] NOTT-116,[40c] Co/DOBDC,[4f] Zn/DOBDC,[4f] IRMOF-3,[5g] CUK-1,[40d] Bio-MOF-11,[40e] MOF-177,[40f] MOF-5[40f] and ZIFs like ZIF-11[40g] and ZIF-8[40g] reported in literature. Also CO_2 uptake at 298 K and 1 atm pressure shown by the Co-*F*INA-1 outperforms MOFs like CPM-6,[41a] TMA@ Bio-MOF-11,[41b] UMCM-150,[41c] $Zn_2(BDC)_2(DABCO)$,[10a] IRMOF-3,[5g] $(In_3O)(OH)(ADC)_2(IN)_2 \cdot 4.67H_2O$,[5c] MOF-177, MOF-5 and ZIFs like ZIF-78[41d] and ZIF-69[41d]. The simultaneous H_2 and CO_2 uptake shown by the Co-*F*INA-1 stands better over some literature reported MOFs having higher surface area. The gas uptake shown by Co-*F*INA-2 is lower than Co-*F*INA-1, but still it is comparable with previously reported fluorinated and non-fluorinated MOFs.[6-17]

2.5.2 Computational/Theoretical Results:

As shown in Figure 2.22c, we could obtain the adsorption isotherms of H_2 in Co-INA-1 and Co-*F*INA-1 at 77 K, experimentally as well as by simulations also. The simulation results of H_2 adsorption in Co-*F*INA-1 agree fairly with the experimental data. In Co-INA-1, however, the calculated results underestimate the experimental data at low pressures, but overestimate at high pressures. The deviations between simulation and experimental results in Co-INA-1 might be attributed to the structural changes during experimental data collection. The simulation used the crystal structure prior to the removal of solvents, though solvents were not included in the simulation. Nevertheless, the crystal structure of Co-INA-1 was found to slightly shrink and/or partially collapse after removing all coordinated and lattice solvents. Therefore, the crystal structure in experimental measurement was different from the one in the simulation. It should be noted that the crystal structure of Co-*F*INA-1 remains intact even after solvent removal due to the presence of fluorine atoms. Comparing the simulation results in Co-INA-1 and Co-*F*INA-1, Co-INA-1 has a higher H_2 adsorption over the entire pressure range, since we did not considered the structural changes into the MOF during the activation and gas adsorption studies.

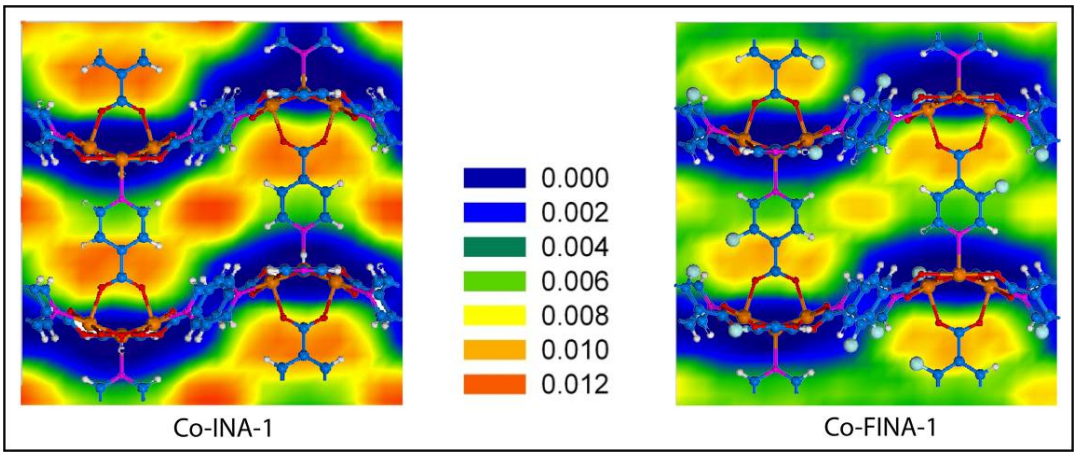

Figure 2.23 H_2 adsorption density contours for Co-INA-1 and Co-FINA-1 on the *XY* plane for H_2 adsorption in Co-INA-1 and Co-FINA-1 at 40 kPa. [Reprinted with permission from (28a). Copyright 2012 WILEY-VCH Verlag GmbH & Co. KGaA].

The density contours calculated to identify the favorable binding sites for H_2 in Co-INA-1 and Co-FINA-1 as shown in Figure 2.23. These density contours are shown on the *XY* plane for H_2 adsorption at 40 kPa. It is observed that H_2 molecules are primarily located in the 1-D channels and the binding sites are mostly located in the channel centers. The density in Co-FINA-1 is lower than in Co-INA-1, particularly in the regions near the fluorine atoms due to steric hindrance.

2.6 Conclusions:

In this contribution, we have successfully synthesized new *F*-MOF using a flexible fluorinated dicarboxylates building block 4,4′-(Hexafluoroisopropilidine)bis-benzoic acid; 3-methyl pyridine/1,10-phenanthroline co-ligands, and different transition metal cations [Zn(II), Co(II), Mn(II), and Cu(II)]. These materials exhibit a great degree of structural diversity despite similar structural components, i.e. dicarboxylate building block, heterocyclic *N*-containing co-ligands and transition metals. The moderate H_2 uptake shown by these materials, despite of its very limited or negligible surface area could possibly emerge as H_2 storage materials. The H_2 uptake shown by these partially fluorinated MOFs can be attributed to the V-shaped twisted conformation and flexible nature of 4,4′-(Hexafluoroisopropilidine)bis-benzoic acid, which restricts the expansion of cavities into the MOF structure.

The attempts towards synthesis of highly robust and porous MOFs using isonicotinic acid and 3-fluoro isonicotinic acid for high H_2 uptake proved to be rewarding to increase the overall H_2 uptake. Two pairs of isostructural fluorinated and non-fluorinated MOFs by using isonicotinic acid and its fluorinated analogue 3-fluoro isonicotinic acid have been synthesized. For the first time, we have achieved isostructural isomerism in fluorinated and non-fluorinated MOFs by using fluorinated and non-fluorinated ligands. The comparison of the H_2 uptake in these isostructural MOFs using experimental and simulation methods, emphasizes that improvement in H_2 uptake in *F*-MOFs is not a universal phenomenon, but is rather system-specific and differs from system to system. In isostructural Co-INA-1 and Co-*F*INA-1, fluorination resulted in almost similar H_2 uptake, whereas in Co-INA-2 and Co-*F*INA-2, fluorination resulted in an overall increase in H_2 uptake. Also, the H_2 uptake shown by Co-*F*INA-1 is the highest reported in the literature for *F*-MOFs, although the pore size is decreased due to fluorine atoms pointing into the pores. From these results, it is clear that as fluorine atoms in *F*-MOFs are weakly interacting with gas molecules, other factors, such as pore size, curvature, and open metal sites, can also play crucial roles in the gas uptakes in these *F*-MOFs. The replacement of flexible dicarboxylate linkers with rigid and hetero atom containing carboxylate linkers produces the highly porous MOFs without assistance of additional co-linker for high H_2 uptake.

2.7 Experimental Materials and Methods:

2.7.1 General Procedures:

All reagents and solvents for synthesis and analysis were commercially available and used as received without further purification. The Fourier transform (FT) IR spectra (KBr pellet) were taken on a Perkin Elmer FT-IR Spectrum (Nicolet) Spectrometer. Powder x-ray diffraction (PXRD) patterns were recorded on a Phillips PANalytical diffractometer for Cu-Kα_1 radiation (λ = 1.5406 Å), with a scan speed of 2° min^{-1} and a step size of 0.02° in 2θ. Thermo-gravimetric experiments (TGA) were carried out in the temperature range of 15–900 °C on a SDT Q600 TG-DTA analyzer under N_2 atmosphere at a heating rate of 10 °C min^{-1}. All low pressure gas adsorption experiments (up to 1 bar) were performed on a Quantachrome Quadrasorb automatic volumetric instrument.

2.7.2 X-Ray Crystallography:

All single crystal data were collected on a Bruker SMART APEX three circle diffractometer equipped with a CCD area detector (Bruker Systems Inc., 1999a)[14] and operated at 1500 W power (50 kV, 30 mA) to generate Mo Kα radiation (λ=0.71073 Å). The incident x-ray beam was focused and monochromated using Bruker Excalibur Gobel mirror optics.42 Crystals of all the MOFs reported herein were mounted on nylon CryoLoops (Hampton Research) with Paraton-N (Hampton Research). Data were integrated using Bruker SAINT software.[43] Data were subsequently corrected for absorption by the program SADABS.[44] The space group determinations and tests for merohedral twinning were carried out using *XPREP*.[45] In all cases, the highest possible space group was chosen. All structures were solved by direct methods and refined using the *SHELXTL 97* software suite.[46] Atoms were located from iterative examination of difference F-maps following least squares refinements of the earlier models. Hydrogen atoms were placed in calculated positions and included as riding atoms with isotropic displacement parameters 1.2-1.5 times U_{eq} of the attached C atoms. Data were collected at 100(2) or 298(2) K for all the MOFs reported. All structures were examined using the *Addsym* subroutine of PLATON[47] to assure that no additional symmetry could be applied to the models. All ellipsoids in ORTEP diagrams are displayed at 50 %,

Table 2.2 Comparison of crystal data and structure refinement for H_2hfbba based MOFs reported.

***F*-MOF**	***F*-MOF-4**	***F*-MOF -6**	***F*-MOF-10**	**Cu-*F*MOF-4B**	**Zn-*F*MOF-4B**	**Co-H*F*MOF-D**	**Co-H*F*MOF-W**
Empirical formula	$C_{29.97}H_{27.97}F_6N_{2.91}O_{5.5}Cu$	$C_{25}H_{13.33}F_6N_{1.33}O_{12}Co$	$C_{25.5}H_{14}F_6N_{1.33}O_4Mn$	$C_{23}H_{15}O_4F_6NCu$	$C_{29}H_{22}F_{5.92}N_2O_4Zn$	$C_{28}H_{20}F_6N_4O_7Co$	$C_{23}H_{17}F_6NO_5Co$
Formula weight	694.51	569.3	571.98	546.91	640.36	696.65	560.31
Temperature	100(2) K	100(2) K	100(2) K	293(2) K	293(2) K	293(2) K	293(2) K
Wavelength	0.71073 Å	0.71073 Å	0.71073 Å	0.71073 Å	0.71073 Å	0.71073 Å	0.71073 Å
Crystal system	Monoclinic	Monoclinic	Monoclinic	Orthorhombic	Orthorhombic	Monoclinic	Orthorhombic
Space group	$P2_1/c$	$C2/c$	$C2/c$	*Cmca*	*Cmc21*	$C2/c$	$Pna2_1$
Unit cell dimensions	*a* = 25.643(8) Å *b* = 11.004(3) Å *c* = 24.351(7) Å β =115.518°	a = 36.616(6)Å b = 13.551(2)Å c = 26.373(4)Å β = 127.80(2)°	a = 37.09(2) Å b = 13.643(7) Å c = 29.671(12) Å β = 135.04(2)°	*a* = 21.561(3) Å *b* = 14.717(2) Å *c* = 17.745(3) Å	*a* = 21.626(2) Å *b* = 14.662(17) Å *c* = 17.777(3) Å	*a* = 26.957(9) Å, *b* = 11.025(8) Å, *c* = 24.602(15) Å, β = 119.74(3)°	*a* = 26.194(8) Å, *b* = 10.524(5) Å, *c* = 8.243(4) Å
Volume (Å^3)	6201.0(3)	10340(3)	10609(9)	5630.7(15)	5636.8(13)	6349(7)	2272.4(19)
Z	4	4	2	8	8	8	4
Density (g/cm^3)	1.488	1.097	1.074	1.290	1.507	1.458	1.638
Goodness-of-fit on F^2	0.986	1.041	0.877	1.067	0.949	1.054	1.095
Final R indices [I>2sigma(I)]	R_1 = 0.0557, wR_2 = 0.1278	R_1 = 0.0858, wR_2 = 0.1915	R_1 = 0.1119, wR_2 = 0.2597	R_1 = 0.0960, wR_2 = 0.2410	R_1 = 0.0596, wR_2 = 0.1345	R_1 = 0.1297, wR_2 = 0.3308	R_1 = 0.0550, wR_2 = 0.1133
R indices (all data)	R_1 = 0.0990, wR_2 = 0.1439	R_1 = 0.1202, wR_2 = 0.2070	R_1 = 0.1465, wR_2 = 0.2990	R_1 = 0.1529, wR_2 = 0.2638	R_1 = 0.0967, wR_2 = 0.1542	R_1 = 0.1343, wR_2 = 0.3359	R_1 = 0.0641, wR_2 = 0.1168
CCDC No.	**745106**	**752227**	**752231**	**797251**	**797252**	**788025**	**788026**

Table 2.3 Comparison of crystal data and structure refinement for H_2hfbba and INA/FINA based MOFs reported.

***F*-MOF**	**Mn-H*F*MOF-D**	**Mn-H*F*MOF-W**	**Co-INA-1****	**Co-FINA-1**	**Co-INA-2**	**Co-FINA-2**
Empirical formula	$C_{23}H_{16}F_6NO_{4.5}Mn$	$C_{23}H_{17}F_6NO_5Mn$	$C_{30}H_{43}N_5O_{19}Co_3$	$C_{22}H_7F_5N_4O_{12}Co_3$	$C_{27}H_{16}N_5O_9Co_2$	$C_{12}H_4F_2N_2O_5Co$
Formula weight	547.31	556.32	954.5	791.11	672.31	353.10
Temperature	293(2) K	293(2) K	123(2) K	298(2) K	298(2) K	298(2) K
Wavelength	0.71073 Å	0.71073 Å	0.71073 Å	0.71073 Å	0.71073	0.71073 Å
Crystal system	Monoclinic	Orthorhombic	Orthorhombic	Orthorhombic	Monoclinic	Monoclinic
Space group	*C*2	*P*na2_1	P*nma*	*Pnma*	*P*2_1	*P*2_1/*c*
Unit cell dimensions	*a* = 28.086(8) Å, *b* = 7.583(2) Å, *c* = 12.109(3) Å, β = 105.461(5)°	*a* = 26.406(8) Å, *b* = 10.626(3) Å, *c* = 8.473(3) Å	*a* = 18.986(4) Å *b* = 19.683(4) Å *c* = 12.081(2) Å	*a* = 19.329(8) Å *b* = 20.088(9) Å *c* = 12.120(7) Å	*a* = 9.819(2) Å *b* = 12.6499(4) Å *c* = 11.0731(8) Å β = 99.852(4)°	*a* = 4.9627(7) Å *b* = 12.3597(6) Å *c* = 11.8167(5) Å β = 105.336(2)°
Volume (Å^3)	2485.6(8)	2377.3(7)	4514.6(2)	4706(4)	1355.1(4)	699.00(9)
Z	2	4	4	4	2	2
Density (g/cm^3)	1.463	1.554	1.298	1.117	1.648	1.678
Goodness-of-fit on F^2	1.010	1.052	1.075	1.097	0.839	1.146
Final R indices [I>2sigma(I)]	R_1 = 0.0682, wR_2 = 0.1675	R_1 = 0.0354, wR_2 = 0.0913	R_1 = 0.0882, wR_2 = 0.1006	R_1 = 0.1090, wR_2 = 0.3201	R_1 = 0.0535, wR_2 = 0.1384	R_1 = 0.0511, wR_2 = 0.1322
R indices (all data)	R_1 = 0.0959, wR_2 = 0.1797	R_1 = 0.0405, wR_2 = 0.0935	R_1 = 0.2559, wR_2 = 0.2653	R_1 = 0.1323, wR_2 = 0.3352	R_1 = 0.1035, wR_2 = 0.1542	R_1 = 0.0585, wR_2 = 0.1359
CCDC No.	**788027**	**788028**	**-**	**835979**	**835981**	**835980**

** The crystal data for Co-INA-1 is reported previously by Q. Chen, J.-B. Lin, W. Xue, M.-H. Zeng, X.-M. Chen, *Inorg. Chem.,* **2011**, *50*, 232.

probability level unless noted otherwise. Crystal data and details of data collection structure solution and refinement are summarized in Table 2.2 and 2.3. Crystallographic data (excluding structure factors) for the structures represented in this chapter have been deposited with the CCDC as deposition No. CCDC 745106, 752227, 752231, 797251, 797252, 788025–788028, 835979–835981 (See Table 2.2 and 2.3). Copies of the data can be obtained, free of charge, on application to the CCDC, 12 Union Road, Cambridge, CB2 lEZ, UK [Fax: + 44 (1223) 336 033; e-mail: deposit@ccdc.cam.ac.uk].

2.7.3 H_2 and CO_2 Adsorption Measurements:

Hydrogen adsorption-desorption experiments were conducted at 77 K using Quantachrome Quadrasorb automatic volumetric instrument. Ultrapure H_2 (99.95 %) was purified further by using calcium aluminosilicate adsorbents to remove trace amounts of water and other impurities before introduction into the system. For measurements at 77 K, a standard low-temperature liquid nitrogen dewar vessel was used. CO_2 adsorption-desorption measurements were done at 273 K and 298 K temperatures. Before gas adsorption measurements, the sample was activated at room temperature (for 12 h) and 100 ºC (for 24 h) under ultrahigh vacuum (10^{-8} mbar). About 75 mg of samples were loaded for gas adsorption, and the weight of each sample was recorded before and after out-gassing to confirm complete removal of all residual guest and coordinated solvent molecules. The same analyses were performed three times to confirm the repeatability and reusability of the materials.

2.7.4 Simulation Model and Method:

To unravel the effect of fluorine atoms on adsorption and identify the adsorption sites in gas–loaded structures, grand canonical Monte Carlo (GCMC) simulations were carried out for H_2 adsorption at 77 K in Co-INA-1 and Co-FINA-1. The experimentally determined desolvated crystal structures were used in the simulations. H_2 molecule was modeled as a two-site rigid molecule with H–H bond length of 0.74 Å. The Lennard-Jones interaction parameters of H-H interaction were σ = 2.59 Å and ε = 12.5 K.[48] The dispersion interactions of the framework atoms in Co-INA-1 and Co-FINA-1 were represented by the Universal Force Field (UFF).[49] The frameworks and H_2 molecules were treated as rigid. The Lorentz-Berthelot combining rules were used to calculate the cross LJ interaction parameters. The LJ interactions were evaluated using a spherical

cutoff of 18 Å with the long-range corrections added. The number of trial moves in the GCMC simulation was 2×10^7. The first 10^7 moves were used for equilibration and the subsequent 10^7 moves for production. Four types of trial moves were conducted for H_2 molecules, namely, displacement, rotation, regrowth at a new position, and swap with the reservoir.

2.7.5 Synthesis of MOFs:

The synthesis of various MOFs using H_2hfbba, INA, *F*INA as linkers and 3-methyl pyridine, 1,10-phenanthroline, 2,2'-bipyridine, 4,4'-dimethyl-2,2'-bipyridine as co-ligands in DMF, DEF, H_2O as solvents with the aid of Mn, Co, Cu and Zn as metal centers has been performed (*Figure 2.8 and 2.9*). As shown Figure 2.8 and Figure 2.9, using following synthetic procedures various MOFs has been synthesized.

$[Cu_2(hfbba)_2(3\text{-mepy})_2]\cdot(DMF)_2(3\text{-mepy})$ (*F*-MOF-4):[28e] 0.5 mL 3-methyl-pyridine stock solution (0.20 M) and 1.5 mL H_2hfbba stock solution (0.20 M) were mixed in a 5 mL vial. To this solution was added 0.5 mL $Cu(NO_3)_2\cdot 3H_2O$ stock solution (0.20 M). The vial was capped and heated to 85 °C for 96 h. The mother liquor was decanted and the products were washed with DMF (15 mL) three times. Blue colored crystals of *F*-MOF-4 were collected by filtration and dried in air (10 min) (Yield: 50 %; 0.0120 g depending on $Cu(NO_3)_2\cdot 3H_2O$).

***FT-IR* :** (KBr 4000-400 cm^{-1}): 3676 (br), 3068 (w), 3935 (m), 2657 (w), 2548 (w), 2331(s), 1944(m), 1816 (w), 1683 (m), 1632 (w), 1561 (w), 1410 (s), 1291 (w), 1239 (s), 1174 (w), 1090 (w), 1020 (w), 971 (w), 929 (w), 846 (m), 780 (s), 748 (w), 706 (w), 514 (m) and 494 (w).

Synthesis of $Co_3(hfbba)_6(phen)_2$ (*F*-MOF-6):[28d] Following similar synthetic protocol as *F*-MOF-5, synthesis of *F*-MOF-6 has been performed except the addition of $Co(NO_3)_2\cdot 6H_2O$ in place of $Cu(NO_3)_2\cdot 3H_2O$. Pink colored crystals of *F*-MOF-6 were collected by filtration and dried in air (10 min). [Yield: 70 %, 0.0203 g depending on $Co(NO_3)_2\cdot 6H_2O$].

***FT-IR* :** (KBr 4000-400 cm^{-1}): 3467 (br), 3077 (w), 2932 (w), 2857 (w), 2188 (w), 1950 (w), 1673 (s), 1612 (m), 1562 (w), 1403 (s), 1255 (m), 1212 (w), 1175 (s), 1090 (w), 1021 (m), 970 (m), 860 (m), 845 (m), 781 (s), 727 (s) and 659 (w).

Synthesis of $Mn_3(hfbba)_6(phen)_2$ (*F*-MOF-10):[28d] Following similar synthetic protocol as *F*-MOF-8, synthesis of *F*-MOF-10 has been performed except the addition of $Mn(NO_3)_2{\cdot}xH_2O$ in place of $Zn(NO_3)_2{\cdot}6H_2O$. Light yellow colored crystals of *F*-MOF-10 were collected by filtration and dried in air (10 min) (yield: 72 %). [Yield: 47 %, 0.0205 g depending on $Mn(NO_3)_2{\cdot}xH_2O$].

***FT-IR* :** (KBr 4000-400 cm^{-1}): 3353 (br), 3075 (w), 2934 (w), 2345 (w), 1947 (m), 1814(w), 1606 (s), 1555 (w), 1403 (s), 1292 (w), 1254 (w), 1211 (w), 1175 (w), 1102 (w), 1021 (s), 971 (w), 845 (s), 845 (s), 782 (w), 727 (m), 688 (w), 639 (w) and 468 (w).

Synthesis of $[Cu_2(hfbba)_2(3\text{-mepy})_2]$ (Cu-*F*MOF-4B):[28c] Following similar synthetic protocol as *F*-MOF-4, synthesis of Cu-*F*MOF-4 has been performed except the replacement of DMF solvent with DEF. Dark blue colored crystals of Cu-*F*MOF-4B were collected by filtration and dried in air (10 min). [Yield: 67 %, 0.0161 g depending on $Cu(NO_3)_2{\cdot}3H_2O$].

FT-IR: (KBr 4000-400 cm^{-1}): 3659 (m, br), 3071 (m, br), 2935 (w), 1632 (m), 1407 (s), 1239 (m), 1173 (s), 929 (m), 779 (m), 514 (m).

Synthesis of $[Zn_2(hfbba)_2(3\text{-mepy})_2]$ ·(3-mepy) (Zn-*F*MOF-4B):[28c] Following similar synthetic protocol as Cu-*F*MOF-4B, synthesis of Zn-*F*MOF-4B has been performed except the addition of $Zn(NO_3)_2{\cdot}6H_2O$ in place of $Cu(NO_3)_2{\cdot}3H_2O$. Colorless crystals of Zn-*F*MOF-4B were collected by filtration and dried in air (10 min). [Yield: 48 %, 0.0142 g depending on $Zn(NO_3)_2{\cdot}6H_2O$].

FT-IR: (KBr 4000-400 cm^{-1}): 3310 (m, br), 2941 (w), 1938 (w), 1644 (s), 1570 (m), 1410 (s), 1291 (m), 1174 (m), 929 (m), 780 (m) and 477 (m).

Synthesis of $[Co_2(hfbba)_2(3\text{-mepy})_2]$ ·$(DMF)_3$ (Co-H*F*MOF-D):[28b] Following similar synthetic protocol as *F*-MOF-4, synthesis of Co-H*F*MOF-D has been performed except the replacement of metal centre $Cu(NO_3)_2{\cdot}3H_2O$ with $Co(NO_3)_2{\cdot}6H_2O$. Dark pink colored crystals of Co-H*F*MOF-D were collected by filtration and dried in air (10 min) [Yield: 52 %, 0.0151 g depending on $Co(NO_3)_2{\cdot}6H_2O$].

FT-IR: (KBr 4000-400 cm^{-1}): 3393 (m, br), 2935 (w), 1944 (w), 1628 (m), 1406 (s), 1172 (s), 929 (m), 780 (m) and 481 (m).

Synthesis of [Co(hfbba)(3-mepy)(H_2O)] (Co-H*F*MOF-W):[28b] Hydrothermal reaction of $Co(NO_3)_2{\cdot}6H_2O$ (0.035, 0.12 mmol) with 0.5 mL 3-methyl pyridine and excess H_2hfbba (0.196 g, 0.50 mmol) in a 25 mL acid-digestion bomb using deionized water (7 mL) at 85 °C for 96 h produced pink colored crystals of Co-H*F*MOF-W. Crystals were collected by filtration, washed with ethanol, and dried in air (10 min). [Yield: 42 %, 0.0147 g depending on $Co(NO_3)_2{\cdot}6H_2O$].

FT-IR: (KBr 4000-400 cm^{-1}): 3203 (m, br), 3088 (w), 2528 (w), 1697 (m), 1609 (s), 1546 (m), 1392 (s), 1293 (m), 1171 (m), 930 (w), 786 (m), 725(m) and 512(w).

Synthesis of [Mn_2(hfbba)$_2$(3-mepy)]·(H_2O) (Mn-H*F*MOF-D):[28b] Following similar synthetic protocol as *F*-MOF-4, synthesis of Mn-H*F*MOF-D has been performed except the replacement of metal centre $Cu(NO_3)_2{\cdot}3H_2O$ with $Mn(NO_3)_2{\cdot}xH_2O$. Colorless crystals of Mn-H*F*MOF-D were collected by filtration and dried in air (10 min). [Yield: 47 %, 0.0134 g depending on $Mn(NO_3)_2{\cdot}xH_2O$].

FT-IR: (KBr 4000-400 cm^{-1}): 3225 (m, br), 1965 (m), 1624 (m), 1550 (s), 1390 (s), 1242 (s), 1171 (m), 957 (s), 784 (s), 555 (w).

Synthesis of [Mn(hfbba)(3-mepy)(H_2O)] (Mn-H*F*MOF-W):[28b] Following similar synthetic protocol as Co-H*F*MOF-W, synthesis of Mn-H*F*MOF-W has been performed except the replacement of metal centre $Co(NO_3)_2{\cdot}6H_2O$ with $Mn(NO_3)_2{\cdot}xH_2O$. Crystals were collected by filtration, washed with ethanol, and dried in air (10 min). [Yield: 61 %, 0.0213 g depending on $Mn(NO_3)_2{\cdot}xH_2O$].

FT-IR: (KBr 4000–400 cm^{-1}): 3207 (m, br), 3090 (w), 2528 (w), 1697 (m), 1610 (s), 1547 (m), 1390 (s), 1292 (m), 1248 (s), 1171 (m), 933 (w), 785 (m), 730 (m), 514 (w).

Synthesis of [$Co_3(INA)_4(O)(C_2H_5OH)_3$]($NO_3$)·($C_2H_5OH$) ·($H_2O$)$_3$] Co-INA-1:[37] A mixture of $Co(NO_3)_2{\cdot}6H_2O$ (1.0 mmol, 0.029 g), isonicotinic acid (1.0 mmol, 0.121 g), triethylamine (0.20 mL), and EtOH (10 mL) was sealed in a 15 mL teflon-lined stainless-steel parr bomb at 140 °C for 72 h, which was then slowly cooled to room temperature. The block red crystals obtained were filtered off, washed with EtOH and dried in air (30 min). (Yield: 21 mg, 75 % based on Co).

FT-IR: (KBr, 4000-400 cm^{-1}): 3372 (s), 1617 (s), 1550 (s), 1384 (vs), 1229 (w), 1058 (w), 1019 (w), 869 (w), 775 (m), 690 (m), 568 (w), 457 (w).

Synthesis of [Co(INA)$_2$ •(DMF)] Co-INA-2:[28a] 1.5 mL isonicotinic acid (0.20 M)

solution in DMF was taken in a 5 mL glass vial. 0.5 mL $Co(NO_3)_2 \cdot 6H_2O$ solution (0.20 M) in DMF was added to this solution. The vial was capped and heated to 85 °C for 72 h. The mother liquor was decanted and plate pink crystals were filtered off, washed with DMF and dried in air (10 min). (Yield: 17 mg, 58 % based on Co).

FT-IR: (KBr 4000-400 cm^{-1}): 3238 (br), 2894 (br), 1657 (w), 1566 (m), 1441 (s), 1372 (s), 1062 (w), 774 (m) and 684 (s).

Synthesis of $[Co_3(FINA)_4(O)(C_2H_5OH)_2\ (H_2O)]$ Co-FINA-1:[28a] A mixture of $Co(NO_3)_2 \cdot 6H_2O$ (1.0 mmol, 0.029 g), 3-fluoro-isonicotinic acid (1.0 mmol, 0.121 g), EtOH (2 mL) and DMF (5 mL) was sealed in a 25 mL teflon-lined stainless-steel parr bomb at 140 °C for 72 h, which was then slowly cooled to room temperature. The block pink crystals obtained were filtered off, washed with DMF and dried in air (30 min). (Yield: 15 mg, 50 % based on Co).

FT-IR: (KBr 4000-400 cm^{-1}): 3215 (br), 1654 (m), 1588 (s), 1381 (s), 1215 (s), 1062 (w), 801 (w) and 667 (w).

Synthesis of $[Co(FINA)_2.(H_2O)]$ Co-FINA-2:[28a] 1.5 mL 3-fluoro-isonicotinic acid (0.20 M) solution in DMF was taken in a 5 mL glass vial. 0.5 mL $Co(NO_3)_2 \cdot 6H_2O$ solution (0.20 M) in DMF was added to this solution. The vial was capped and heated to 85 °C for 72 h. The mother liquor was decanted and block pink crystals were filtered off, washed with DMF and dried in air (10 min). (Yield: 19 mg, 65 % based on Co).

FT-IR: (KBr 4000-400 cm^{-1}): 3212 (br), 2871 (br), 1661 (w), 1561 (m), 1539 (s), 1381 (s), 1231 (s), 1062 (w), 923 (w), 773 (m) and 688 (s).

2.8 References and Notes:

1. (a) A. Zukal, I. Dominguez, J. Mayerova, J. Cejka, *Langmuir*, **2009**, *25*, 10314. (b) R. V. Siriwardane, M. S. Shen, E. P. Fisher, J. Losch, *Energy Fuels*, **2005**, *19*, 1153. (c) Y. Belmabkhout, A. Sayari, *Adsorption*, **2009**, *15*, 318. (d) S. Kim, J. Ida, V. V. Guliants, J. Y. S. Lin, *J. Phys. Chem. B*, **2005**, *109*, 6287. (e) S. N. Kim, W. J. Son, J. S. Choi, W. S. Ahn, *Microporous Mesoporous Mater.*, **2008**, *115*, 497. (f) B. J. Kim, K. S. Cho, S. J. Park, *J. Colloid Interface Sci.*, **2010**, *342*, 575. (g) C. Chen, S.-T. Yang, W.-S. Ahn, R. Ryoob, *Chem. Commun.,* **2009**, 3627.

2. (a) J. Strom-Olsen, In *Method of Hydrogen Generation for Fuel Cell Applications and a Hydrogen-Generating System*, Patent Filing WO0185606, May **2001**, McGill University. (b) J. Irvine, *Theme issue: materials chemistry for hydrogen storage and generation*, *J. Mater. Chem.*, **2008**, *18*, 2295. (c) A. Zuttel, *et.al.*, In *Hydrogen Desorption From Lithiumtetrahydroboride (LiBH4)*, Proceedings, 14th World Hydrogen Energy Conference, June **2002**, Montreal, Canada.

3. (a) J. J. Perry Iv, J. A. Perman, M. J. Zaworotko, *Chem. Soc. Rev.*, 2009, **38**, 1400. (b) M. O'Keeffe, O. M. Yaghi, *Chem. Rev.*, **2012**, *112*, 675. (c) H. Furukawa, K. E. Cordova, M. O'Keeffe, O. M. Yaghi, *Science*, **2013**, *341*, 1230444. (d) M. Li, D. Li, M. O'Keeffe, O. M. Yaghi, *Chem. Rev.*, **2014**, *114*, 1343. (e) T. R. Cook, Y.-R. Zheng, P. J. Stang, *Chem. Rev.*, **2013**, *113*, 734. (f) C. Janiak, *Dalton Trans.*, **2003**, 2781. (g) S. T. Meek, J. A. Greathouse, M. D. Allendorf, *Adv. Mater.*, **2011**, *23*, 249. (h) L. J. Murray, M. Dinca, J. R. Long, *Chem. Soc. Rev.*, **2009**, *38*, 1294. (i) T. A. Makal, J.-R. Li, W. Lu, H.-C. Zhou, *Chem. Soc. Rev.*, **2012**, *41*, 7761. (j) M. P. Suh, H. J. Park, T. K. Prasad, D.-W. Lim, *Chem. Rev.*, **2012**, *112*, 782. (k) K. Sumida, D. L. Rogow, J. A. Mason, T. M. McDonald, E. D. Bloch, Z. R. Herm, T.-H. Bae, J. R. Long, *Chem. Rev.*, **2012**, *112*, 724. (l) J.-R. Li, J. Sculley, H.-C. Zhou, *Chem. Rev.*, **2012**, *112*, 869. (m) H. Wu, Q. Gong, D. H. Olson, J. Li, *Chem. Rev.*, **2012**, *112*, 836. (n) Z. Zhang, Y. Zhao, Q. Gong, Z. Li, J. Li, *Chem. Commun.*, **2013**, *49*, 653. (o) P. Nugent, Y. Belmabkhout, S. D. Burd, A. J. Cairns, R. Luebke, K. Forrest, T. Pham, S. Ma, B. Space, L. Wojtas, M. Eddaoudi, M. J. Zaworotko, *Nature*, **2013**, *495*, 80.

4. (a) X.-S. Wang, S. Ma, P. M. Forster, D. Yuan, J. Eckert, J. J. Lopez, B. J. Murphy, J. B. Parise, H.-C. Zhou, *Angew. Chem. Int. Ed.,* **2008**, *47*, 7263. (b) X. Lin, J. H. Jia, X. B. Zhao, K. M. Thomas, A. J. Blake, G. S. Walker, N. R. Champness, P. Hubberstey, M. Schroder, *Angew. Chem. Int. Ed.,* **2006**, *45*, 7358. (c) B. Chen, N. W. Ockwig, A. R. Millward, D. S. Contreras, O. M. Yaghi, *Angew. Chem. Int. Ed.,* **2005**, *44*, 4745. (d) M. Dinca, W. S. Han, Y. Liu, A. Dailly, C. M. Brown, J. R. Long, *Angew. Chem. Int. Ed.,* **2007**, *46*, 1419. (e) C. Tan, S. Yang, N. R.

Champness, X. Lin, A. J. Blake, W. Lewis, M. Schroder, *Chem. Commun.,* **2011**, *47*, 4487. (f) S. R. Caskey, A. G. Wong-Foy, A. J. Matzger, *J. Am. Chem. Soc.,* **2008**, *130*, 10870.

5. (a) S. Couck, J. F. M. Denayer, G. V. Baron, T. Remy, J. Gascon, F. Kapteijn, *J. Am. Chem. Soc.* **2009**, *131*, 6326. (b) A. Demessence, D. M. D'Alessandro, M. L. Foo, J. R. Long, *J. Am. Chem. Soc.* **2009**, *131*, 8784. (c) X. Gu, Z.-H. Lu, Q. Xu, *Chem. Commun.* **2010**, *46*, 7400. (d) R. Vaidhyanathan, S. S. Iremonger, G. K. H. Shimizu, P. G. Boyd, S. Alavi, T. K. Woo, *Science* **2010**, *330*, 650. (e) A. O. Yazaydin, R. Q. Snurr, T.-H. Park, K. Koh, J. Liu, M. D. LeVan, A. I. Benin, P. Jakubczak, M. Lanuza, D. B. Galloway, J. J. Low, R. R. Willis, *J. Am. Chem. Soc.* **2009**, *131*, 18198. (f) A. Torrisi, R. G. Bell, C. Mellot-Draznieks, *Cryst. Growth Des.* **2010**, *10*, 2839. (g) F. Debatin, A. Thomas, A. Kelling, N. Hedin, Z. Bacsik, I. Senkovska, S. Kaskel, M. Junginger, H. Muller, U. Schilde, C. Jager, A. Friedrich, H. J. Holdt, *Angew. Chem. Int. Ed.* **2010**, *49*, 1258. (h) J. L. C. Rowsell, O. M. Yaghi, *J. Am. Chem. Soc.* **2006**, *128*, 1304. (i) B. Chen, S. Xiang, G. Qian, *Acc. Chem. Res.* **2010**, ***43***, 1115. (j) Z. Chen, S. C. Xiang, H. D. Arman, P. Li, D. Y. Zhao, B. Chen, *Eur. J. Inorg. Chem.* **2010**, 3745. (k) Z. Chen, S. Xiang, H. D. Arman, J. U. Mondal, P. Li, D. Zhao, B. Chen, *Inorg. Chem.* **2011**, *50*, 3442. (l) Z. Chen, S. Xiang, H. D. Arman, P. Li, D. Zhao, B. Chen, *Eur. J. Inorg. Chem.* **2011**, 2227. (m) Z. J. Zhang, S. C. Xiang, X. Rao, Q. Zheng, F. R. Fronczek, G. D. Qian, B. Chen, *Chem. Commun.* **2010**, *46*, 7205.

6. (a) C. Yang, X. P. Wang, M. A. Omary, *Angew. Chem. Int. Ed.* **2009**, *48*, 2500. (b) R. A. Fischer, C. Woll, *Angew. Chem. Int. Ed.* **2008**, *47*, 8164. (c) Z. Hulvey, D. A. Sava, J. Eckert, A. K. Cheetham, *Inorg. Chem.* **2011**, *50*, 403. (d) W. Yang, X. Lin, A. J. Blake, C. Wilson, P. Hubberstey, N. R. Champness, M. Schroder, *Inorg. Chem.* **2009**, *48*, 11067. (e) C. A. Fernandez, P. K. Thallapally, R. K. Motkuri, S. K. Nune, J. C. Sumrak, J. Tian, J. Liu, *Cryst. Growth Des.* **2010**, *10*, 1037. (f) J. Seo, C. Bonneau, R. Matsuda, M. Takata, S. Kitagawa, *J. Am. Chem. Soc.* **2011**, *133*, 9005.

7. (a) H. Cheng, X. Sha, L. Chen, A. C. Cooper, M. Foo, G. C. Lau, W. H. Bailey, G. P. Pez, *J. Am. Chem. Soc*., **2009**, *131*, 17732. (b) T. Loiseau, G. Férey, *J. Fluorine Chem.*, **2007**, *128*, 413.

8. C. Yang, X. Wang, M. A. Omary, *J. Am. Chem. Soc*., **2007**, *129*, 15454.

9. Z. Hulvey, E. H. L. Falcao, J. Eckerta, A. K. Cheetham, *J. Mater. Chem*., **2009**, *19*, 4307.

10. (a) H. Chun, D. N. Dybtsev, H. Kim, K. Kim, *Chem. Eur. J.* **2005**, *11*, 3521. (b) P. Pachfule, Y. Chen, S. C. Sahoo, J. Jiang, R. Banerjee, *Chem. Mater.*, **2011**, *23*, 2908.

11. L. Pan, D. H. Olson, L. R. Ciemnolonski, R. Heddy, J. Li, *Angew. Chem. Int. Ed.* **2006**, *45*,

616.

12. L. Pan, M. B. Sander, X. Huang, J. Li, M. Smith, E. Bittner, B. Bockrath, J. K. Johnson, *J. Am. Chem. Soc.*, **2004**, *126*, 1308.

13. Z. Hulvey, D. A. Sava, J. Eckert, A. K. Cheetham, *Inorg. Chem*., **2011**, *50*, 403.

14. C. A. Fernandez, P. K. Thallapally, R. K. Motkuri, S. K. Nune, J. C. Sumrak, J. Tian, J. Liu, *Cryst. Growth Des.,* **2010**, *10*, 1037.

15. Y. Liu, J.-R. Li, W. M. Verdegaal, T.-F. Liu, H.-C. Zhou, *Chem. Eur. J*. **2013**, *19*, 5637.

16. C. A. Fernandez, J. Liu, P. K. Thallapally, D. M. Strachan, *J. Am. Chem. Soc.*, **2012**, *134*, 9046.

17. A. Santra, I. Senkovska, S. Kaskel, P. K. Bharadwaj, *Inorg. Chem.*, **2013**, *52*, 7358.

18. S. I. Semenova, *J. Membr. Sci*., **2004**, *231*, 189.

19. B. Smit, T. L. M. Maesen, *Nature,* **1995**, *374*, 42.

20. H. Wu, Q. Gong, D. H. Olson, J. Li, *Chem. Rev.* **2012**, *112*, 836.

21. L. Lin, Y. Zhang, H. Zhang, F. Lu, *J. Colloid Interface Sci.*, **2011**, *360*,753.

22. (a) E. M. Flanigen, J. M. Bennett, R. W. Grose, J. P. Cohen, R. L. patton, R. M. Kirchner, J. V. Smith, *Nature,* **1978***, 271*, 512. (b) J.-H. Yun, D.-K. Choi, *AIChE J.* **1998**, *44*, 1344.

23. A. Monge, N. Snejko, E. Gutierrez-Puebla, M. Medina, C. Cascales, C. Ruiz-Valero, M. Iglesias, B. Gomez-Lor, *Chem. Commun*., **2005**, 1291.

24. R. E. Morris, A. Burton, L. M. Bull, S. I. Zones, *Chem. Mater*., **2004**, *16*, 2844.

25. A. E. Platero-Prats, V. A. de la Pena-O'Shea, N. Snejko, A. Monge, E. Gutierrez-Puebla, *Chem. Eur. J.* **2010**, *16*, 11632.

26. C. Yang, U. Kaipa, Q. Z. Mather, X. Wang, V. Nesterov, A. F. Venero, M. A. Omary, *J. Am. Chem. Soc*. **2011**, *133*, 18094.

27. M. G. Plaza, A. M. Ribeiro, A. Ferreira, J. C. Santos, Y. K. Hwang, Y.-K. Seo, U.-H. Lee, J.-S. Chang, J. M. Loureiro, A.E. Rodrigues, *Microporous Mesoporous Mater.*, **2012**, *153*, 178.

28. (a) P. Pachfule, Y. Chen, J. Jiang, R. Banerjee, *Chem. Eur. J.*, **2012**, *18*, 688. (b) P. Pachfule, R. Das, P. Poddar, R. Banerjee, *Inorg. Chem.,* **2011**, *50*, 3855. (c) P. Pachfule, R. Das, P. Poddar, R. Banerjee, *Cryst. Growth & Des.*, **2011**, *11*, 1215. (d) P. Pachfule, C. Dey, T. Panda, K. Vanka, R. Banerjee, *Cryst. Growth & Des.*, **2010**, *10*, 1351. (e) P. Pachfule, C. Dey,

T. Panda, R. Banerjee, *CrystEnggComm*, **2010**, *12,* 1600.

29. (a) L.S. James. *Chem. Soc. Rev.*, **2003**, *32*, 276. (b) Q. Wei, M. Nieuwenhuyzen, L. S. James. Microporous Mesoporous Mater., **2004**, *73*, 97.

30. (a) R. Patra, H. M. Titi, I. Goldberg, *CrystEngComm*, **2013**, *15*, 2853. (b) R. Patra, H. M. Titi, I. Goldberg, *CrystEngComm*, **2013**, *15*, 2863. (c) R. Patra, H. M. Titi, I. Goldberg, *New J. Chem.*, **2013**, *37*, 1494. (d) R. Patra, H. M. Titi, I. Goldberg, *CrystEngComm*, **2013**, *15*, 7257. (e) A. Karmakar, H. M. Titi, I. Goldberg, *Cryst. Growth Des.*, **2011**, *11*, 2621.

31. (a) M. G. Goesten, E. Stavitski, J. Juan-Alcaniz, A. Martinez-Joaristi, A.V. Petukhov, F. Kapteijn, J. Gascon, *Catalysis Today*, **2013**, *205*, 120. (b) M. Sindoro, A.-Y. Jee, S. Granick, *Chem. Commun.*, **2013**, *49*, 9576. (c) C. Giacovazzo, *Fundamentals of Crystallography*, Oxford University Press, New York, **2002**. (d) K. M. McGrath, *Adv. Mater.*, **2001**, *13*, 989. (e) S. Mann, *Angew. Chem. Int. Ed.*, **2000**, *39*, 3393. (f) T. Ahnfeldt, N. Guillou, D. Gunzelmann, I. Margiolaki, T. Loiseau, G. Ferey, J. Senker, N. Stock, *Angew. Chem. Int. Ed.*, **2009**, *48*, 5163. (g) M. Haouas, C. Volkringer, T. Loiseau, G. Ferey, F. Taulelle, *Chem. Mater.*, **2012**, *24*, 2462. (h) P. P. Long, H. W. Wu, Q. Zhao, Y. X. Wang, J. X. Dong, J. P. Li, *Microporous Mesoporous Mater.*, **2011**, *142*, 489.

32. A. W. Addison, T. N. Rao, J. Reedijk, J. V. Rijn, G. C. Verschoor, *J. Chem. Soc., Dalton Trans.*, **1984**, 1349.

33. M. O'Keeffe, M. Eddaoudi, H. Li, T. Reineke, O. M. Yaghi, *J. Solid State Chem.*, **2000**, *152*, 3.

34. All calculations were done using Cerius2 software (Ver. 4.2, Accelrys); van der Waals radii taken into consideration are C, 1.70; H, 1.20; O, 1.52; N, 1.55; F, 1.47 Å; Cl, 1.79; Br, 1.89 Å.

35. (a) D. G. Golovanov, K. A. Lyssenko, M. Y. Antipin, Y. S. Vygodskii, E. I. Lozinskaya, A. S. Shaplov, *CrystEngComm,* **2005**, *7*, 53. (b) G. Althoff, G. Ruiz, V. Rodríguez, G. López, J. Pérez, C. Janiak, *CrystEngComm,* **2006**, *8*, 662. (c) S. Takahashi, T. Jukurogi, T. Katagiri, K. Uneyama, *CrystEngComm,* **2006**, *8*, 320. (d) A. R. Choudhury, T. N. Guru Row, *CrystEngComm,* **2006**, *8*, 265. (e) R. Mariaca, N.-R. Behrnd, P. Eggli, H. Stoeckli-Evans, J. Hulliger, *CrystEngComm,* **2006**, *8*, 222. (f) E. D'Oria, J. J. Novoa, *CrystEngComm,* **2008**, *10*, 423. (g) G. R. Desiraju, T. Steiner, *The weak hydrogen bond*. In*IUCr Monograph on Crystallography*; Oxford Science: Oxford, **1999**; Vol. 9. (h) J. Ruiz, V. Rodríguez, C. D. Haro, E. Espinosa, J. Pérez, C. Janiak, *Dalton Trans.,* **2010**, *39*, 3290.

36. (a) H. D. Flack, *Acta Crystallogr*. **1983**, *A39*, 876. (b) H. D Flack, G. Bernardinelli, *Acta*

Crystallogr. **1999**, *A55*, 908.

37. Q. Chen, J.-B. Lin, W. Xue, M.-H. Zeng, X.-M. Chen, *Inorg. Chem.,* **2011**, *50*, 2321.

38. The solvent-accessible void calculations mentioned herein are carried out in the bare structure by removing all the solvent molecules from the framework manually, assuming that all the solvent molecules leave the framework during solvent exchange and strong evacuation.

39. Q. Wei, M. Nieuwenhuyzen, S. L. James, *Microporous Mesoporous Mater*., **2004**, *73*, 97.

40. (a) D. Sun, S. Ma, Y. Ke, D. J. Collins, H. C. Zhou, *J. Am. Chem. Soc.*, **2006**, *128*, 3896; (b) D. Yuan, D. Zhao, D. Sun, H.-C. Zhou, *Angew. Chem., **2010***, *122*, 5485. (c) Y. Yan, I. Telepeni, S. Yang, X. Lin, W. Kockelmann, A. Dailly, A. J. Blake, W. Lewis, G. S. Walker, D. R. Allan, S. A. Barnett, N. R. Champness, M. Schroder, *J. Am. Chem. Soc.,* **2010**, *132*, 4092. (d) J. W. Yoon, S. H. Jhung, Y. K. Hwang, S. M. Humphrey, P. T. Wood, J. S. Chang, *Adv. Mater.,* **2007**, *19*, 1830. (e) J. An, S. J. Geib, N. L. Rosi, *J. Am. Chem. Soc.,* **2010**, *132*, 38. (f) J. L. C. Rowsell, A. R. Millward, K. S. Park, O. M. Yaghi, *J. Am. Chem. Soc.,* **2004**, *126*, 5666. (g) K. S. Park, Z. Ni, A. P. Cote, J. Y. Choi, R. D. Huang, F. J. Uribe-Romo, H. K. Chae, M. O′Keeffe, O. M. Yaghi, *Proc. Natl. Acad. Sci. USA,* **2006**, *103*, 10186.

41. (a) S.-T. Zheng, J. T. Bu, Y. Li, T. Wu, F. Zuo, P. Feng, X. Bu, *J. Am. Chem. Soc.*, **2010**, *132*, 17062. (b) J. An, N. L. Rosi, *J. Am. Chem. Soc.*, **2010**, *132*, 5578. (c) A. G. Wong-Foy, O. Lebel, A. J. Matzger, *J. Am. Chem. Soc.*, **2007**, *129*, 15740. (d) R. Banerjee, H. Furukawa, D. Britt, C. Knobler, M. O′Keeffe, O. M. Yaghi, *J. Am. Chem. Soc.*, **2009**, *131*, 3875.

42. *SMART, Version 5.05*; Bruker AXS, Inc.: Madison, Wisconsin, **1998**.

43. Bruker **(2004)**. *SAINT-Plus* (Version 7.03). Bruker AXS Inc., Madison, Wisconsin, USA.

44. G. M. Sheldrick, **(2002)**. *SADABS* (Version 2.03) and *TWINABS* (Version 1.02).University of Göttingen, Germany.

45. G. M. Sheldrick, **(1997)**. *SHELXS '97*. University of Göttingen, Germany.

46. G. M. Sheldrick, **(1997)**. *SHELXTL '97*. University of Göttingen, Germany.

47. A. L. Spek, **(2005)**. PLATON, *A Multipurpose Crystallographic Tool*, Utrecht University, Utrecht, The Netherlands.

48. R. F. Cracknell, *Phys. Chem. Chem. Phys.* **2001**, *3*, 2091.

49. A. K. Rappe, C. J. Casewit, K. S. Colwell, W. A. Goddard, W. M. Skiff, *J. Am. Chem. Soc.* **1992**, *114*, 10024.

Memorandum

The results of this chapter have already been published in *Inorganic Chemistry,* **2011**, *50*, 3855-3865 [**Title:** Structural, Magnetic, and Gas Adsorption Study of a Series of Partially Fluorinated Metal Organic Frameworks (HF-MOFs)]; *Crystal Growth & Design*, **2011**, *11*, 1215-1222 [**Title:** Solvothermal Synthesis, Structure, and Properties of Metal Organic Framework Isomers Derived from a Partially Fluorinated Link]; *Crystal Growth & Design*, **2010**, *10*, 1351-1363 [**Title:** Structural Diversity in Partially Fluorinated Metal Organic Frameworks (F-MOFs) Composed of Divalent Transition Metals, 1,10-Phenanthroline, and Fluorinated Carboxylic Acid]; *CrystEnggComm*, **2010**, *12,* 1600-1609 [**Title:** Synthesis and Structural Comparisons of Five New Fluorinated Metal Organic Frameworks (F-MOFs)] and *Chemistry-A European Journal*, **2012**, *18*, 688-694 [**Title:** Fluorinated Metal–Organic Frameworks: Advantageous for Higher H_2 and CO_2 Adsorption or Not?].

This publication was the result of collaboration between the group of Dr. Rahul Banerjee and his students Pradip Pachfule, Tamas Panda, Chandan Dey and the group of Dr. Pankaj Poddar with his student Raja Das from the Physical/Materials Chemistry Division at CSIR-National Chemical Laboratory in Pune, India. The group of Prof. Dr. Jianwen Jiang with his student Yifei Chen from the National University of Singapore, 117576 Singapore have actively contributed to the publication by performing computational studies on MOFs. The group of Dr. Pankaj Poddar was contributed in these publications by analyzing the magnetic properties of MOFs. Tamas Panda and Chandan Dey helped for single crystal X-ray diffraction data collection and analyses.

Pradip Pachfule was involved in the preparation of MOFs, characterization of MOFs which includes Single crystal X-ray diffraction studies, PXRD, FT-IR, TGA, NMR, Gas adsorption studies. Finally figure preparation and draft writing was carried out by him under the guidance of Dr. Rahul Banerjee.

Chapter 3

Effect of Fluorination on Hydrogen (H_2) Adsorption in Copper-Tetrazolate Based Metal Organic Frameworks (MOFs)

3.1 Introduction:

From last few years, active research for storing hydrogen is also proceeding on functionalized and non-functionalized carbon nanotubes,[1] zeolites,[2] activated carbon,[3] and metal hydrides.[4] Although, these materials has been broadly studied and potentially applied in H_2 storage applications, still there are limitations for using these materials as they are expensive, shows strong interaction with adsorbents, problems in regeneration of adsorbents, etc.[5] Recent years have witnessed huge research on the synthesis of porous functional MOF materials, using diverse organic spacers with different metals.[6] MOFs, on the other hand has shown promise over these materials due to their fascinating structures, exceptionally high surface areas, uniform yet tunable pore sizes and well-defined adsorbate-MOF interaction sites.[7] One of the major reasons for MOF research is the expectation of achieving the U.S. Department of Energy (DoE) targets on H_2 storage for on-board and vehicular applications.[8] Various strategies such as extending pore sizes comparable to the adsorbed molecules,[9] increasing surface area and pore volume,[10] utilizing catenation[11] and creation of open metal sites[12] have been explored to achieve the DoE target for H_2 storage. Similarly, insertion of functionalities like –F, –NH_2, –OH, –COOH, etc. on the organic spacer has also been proved to have good impact on enhancing the H_2 and CO_2 gas adsorption properties.[13] Recently, computational studies also proved that the choice of both ligand and metal center plays an important role in gas-framework interactions.[14] In recent reports, researchers have showed that porous MOFs with exposed fluorine atoms (*F*-MOFs), possess "*high*" physisorptive H_2 adsorption enthalpy resulting into the enhancement in the H_2 adsorption properties.[15] In previous chapter, as per our recent communications, we have demonstrated the advantage of fluorination for elevated H_2 uptake experimentally as well as computationally.[16] However, in an additional work on partially fluorinated MOFs, the explicit comparison of *F*-MOFs with its non-fluorinated analogues imparted

a "*disadvantage*" towards H_2 adsorption.[17] As a result, it is very difficult to draw any conclusion regarding the impact of fluorination on H_2 and CO_2 adsorption as there are very few systematic comparative study of gas storage in iso-structural fluorinated and non-fluorinated MOFs.

Utilization of carboxylate containing organic linkers for constructing MOFs has been extensively studied because of their excellent coordination potential and possibility of building up novel open architectures. Alternatively, tetrazole based linkers and their substituted derivatives having p*K*a values similar to carboxylate acids (~4) have attracted great attention and used as organic linkers in the construction of MOFs.[18,19] Followed by the convenient and environmental friendly synthetic route reported by Sharpless *et al.* for synthesis of 5-substituted-1*H*-tetrazoles; these tetrazolates have picked up researchers' attentions for several purposes including organic linkers for MOF synthesis.[18] Several tetrazolate-based MOFs with novel structures and interesting physical properties have been generated by *in-situ* hydrothermal methods.[19,20] Similarly, utilization of pre-synthesized tetrazole based linkers for MOF synthesis has been attempted due to the phenomenal applications shown by these MOFs in the fuel gas or CO_2 storage, catalysis, nonlinear optics, molecular magnets, and luminescent properties.[19] Carboxylate-containing 5-substituted tetrazolate ligands (so-called tetrazolate-5-carboxylates), contains at least four nitrogen and two oxygen atoms as electron-donating hetero-atoms, and thus can exhibit diverse coordination modes and have been used as

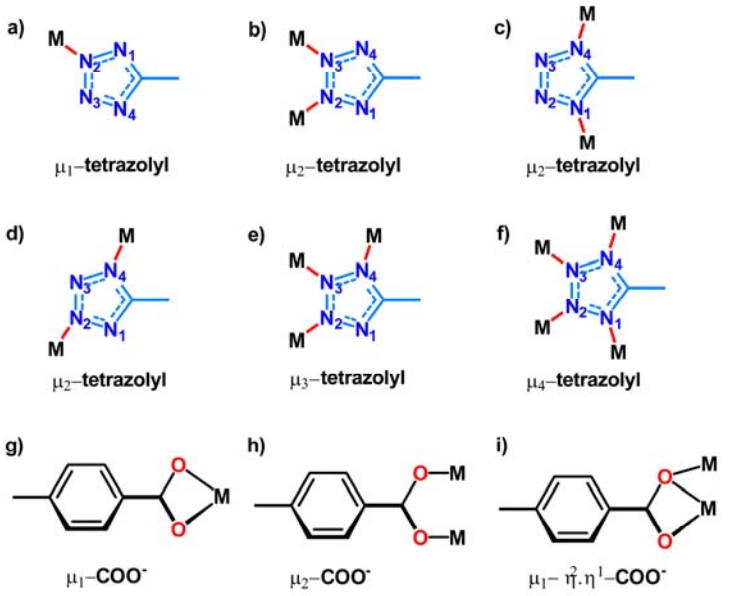

Figure 3.1 Possible modes of attachments commonly observed in tetrazolyl and carboxylate based linkers.

bridging building blocks in the formation of polymeric networks with charming structural varieties and peculiar performance (*Figure 3.1*). However, in contrast with carboxylate or tetrazolate, the investigation on chemistry of tetrazolate-5-carboxylate ligands having both functionalities (carboxylate and tetrazole) remains less developed, though they are expected to be a versatile bridge ligand. Since, the linkers possessing carboxylic acids and tetrazoles, exhibits a variety of coordination abilities (*Figure 3.1*) and the tendency to form architectures with multidimensional frameworks, these linkers are appealing for building new coordination compounds.[20] In these regards, in order to achieve the multidimensional MOFs, with superior gas adsorption properties, we have utilized the 4-(1*H*-tetrazole-5-yl) benzoic acid (4-TBA) as an organic linker for MOF synthesis. Also, to explore the effect of fluorine insertion on the gas uptake properties in MOFs, the fluorine containing linker 2-fluoro-4-(1*H*-tetrazole-5-yl)benzoic acid (2F-4-TBA) has been synthesized.

Herein, in continuation with our previous attempts towards the evaluation of effect of partial fluorination on H_2 uptake in MOFs,[16a] we represent the synthesis, structure and gas adsorption properties of three MOFs synthesized from predesigned ligands 4-TBA and 2F-4-TBA with $Cu(NO_3)_2.4H_2O$ and anhydrous CuCl as metal precursors.[16f] Among these MOFs, $Cu_9(4\text{-TBA})_{10}(C_2H_5OH)_2$ **(**Cu-TBA-1**)** and $Cu_2(4\text{-TBA})_2(DMF)(C_2H_5OH)$ **(**Cu-TBA-2**)** are structural isomers. Whereas, non-fluorinated $Cu_2(4\text{-TBA})_2(DMF)(C_2H_5OH)$ **(**Cu-TBA-2) and fluorinated $Cu_2(2\text{-F-4-TBA})_2(DMF)_2$ **(**Cu-TBA-2F**)** have similar crystal structure. The structure of MOFs was determined by single crystal X-Ray diffraction, phase purity was demonstrated by PXRD, FT-IR and elemental analysis. Whereas, thermal stability of these MOFs was analyzed using VT-PXRD/TGA analyses and N_2, H_2 and CO_2 adsorption studies were performed in order to determine the porosity. H_2 adsorption sites in Cu-TBA-2 and Cu-TBA-2F have been analyzed computationally by molecular simulations. To the best of our knowledge this is the first attempt, where effect of fluorination on structurally similar MOFs has been verified both experimentally and computationally.

3.2 Result and Discussion:

3.2.1 Synthesis of MOFs:

In the present context, we have used 4-TBA and it's partially fluorinated analogue 2-F-4-TBA as key linkers and presented a comparative study towards their gas adsorption properties. We chose tetrazole benzoic acids as the ligand for this study as:

a. These linkers possess two functional groups with different coordination modes. The carboxylate and tetrazole group can adopt versatile coordination conformations, from monodentate to tetradentate. Combination of both these functionalities can create a number of new MOFs with uncommon topologies.[20]

b. Elongated structure of the ligand with carboxylate and tetrazole functionality can create large pores for gas adsorption and other purposes.

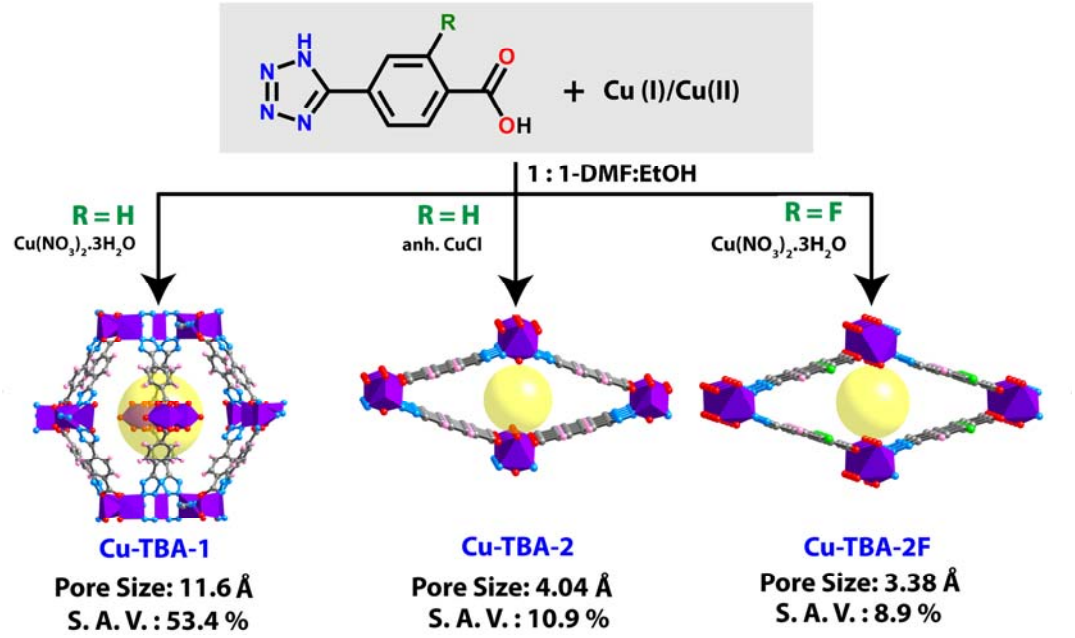

Figure 3.2 Scheme of synthesis for MOFs synthesized using of 4-tetrazole benzoic acid and 2-fluoro-4-tetrazole benzoic acid linkers. (S.A.V. = solvent accessible volume).

Since, thermodynamically and kinetically unfavorable room temperature reactions of these linkers with metals results into the precipitations of reactants, we have followed the solvothermal synthetic pathway using elevated temperature around 90 °C. Although, we could see the small crystallites in the reaction vessel after 12 h, in order to achieve the single crystal suitable for X-ray diffraction studies in large yield, we have

used prolonged heating upto 96 h to the same mixture. Due to the poor solubility of both 4-TBA and 2-F-4-TBA into water, we have used DMF as a solvent. The addition of alcohol into the reaction vial facilitated the crystal growth to form the single crystals mountable for X-ray diffraction studies. Since, the oxidation state of precursor metal in the reaction mixture affects the resulting crystal structure of MOFs diversely, in this context we have used both Cu(I) and Cu(II) as metal centers for the MOF synthesis. The effect of metal oxidation state, temperature and ligand functionalization on the resulting MOF structures has been validated by means of single crystal XRD structures. The MOFs formed in these series were further examined for gas adsorption studies.

3.2.2 Crystal Structure Descriptions:

Crystal Structure of Cu-TBA-1:

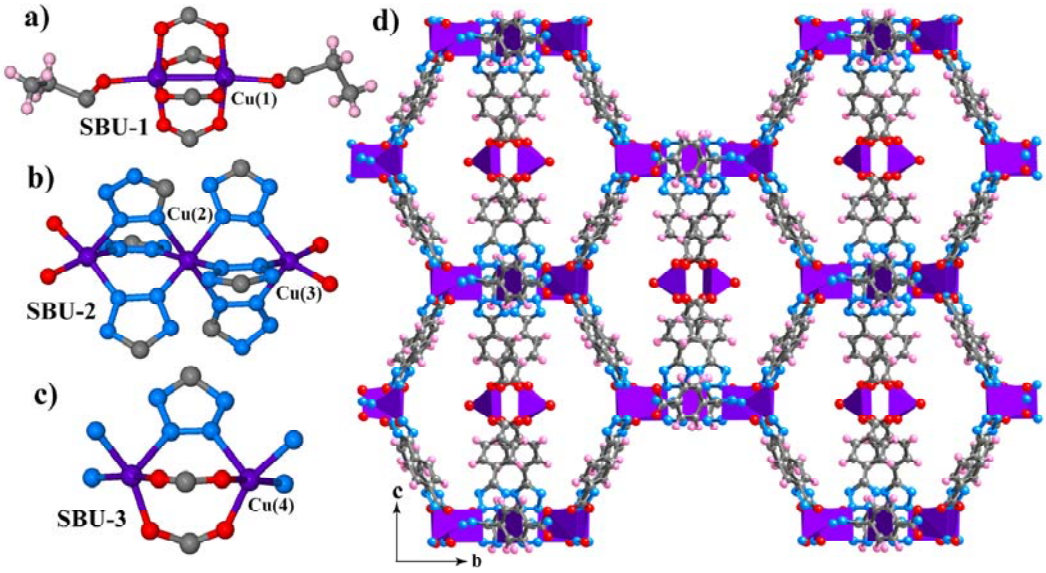

Figure 3.3 Crystal structure of $Cu_9(4\text{-TBA})_{10}(EtOH)_2$ (Cu-TBA-1). (a) Octahedral paddlewheel type SBU-1 along with 2 axial solvent molecules. (b) SBU-2 with octahedral Cu(II) (middle, coordinated to 6 nitrogen) surrounded by two trigonal bipyramidal Cu(II) (coordinated to 3 nitrogen and 2 oxygen). (c) Trigonal bipyramidal SBU-3 where Cu(II) is coordinated to 3 nitrogen and 2 oxygen. (d) Packing diagram showing formation of hollow cages through a axis. Solvent molecules are omitted for clarity. Color code: Cu (magenta), N (blue), O (red), C (grey), H (pink). [Reprinted with permission from (16f). Copyright 2011 American Chemical Society].

In the crystal structure of Cu-TBA-1, three types of SBUs are present (*Figure 3.3* and *Figure 3.4*), where Cu(II) metal centers are either in octahedral (SBU-1 and -2) or in trigonal bipyramidal coordination state (SBU-2 and SBU-3). It is noteworthy that,

octahedral metal centers [Cu(1) and Cu(2)] in the SBU-1 and -2 are coordinated exclusively to oxygen or nitrogen; while trigonal bipyramidal metal centers [Cu(3) and Cu(4)] are coordinated to both oxygen and nitrogen (*Figure 3.3*). Among the three SBUs, SBU-1 is a Cu paddlewheel type, where four μ_2-OCO^- carboxyl groups from different 4-TBA ligands join to two different Cu(II) atoms. Two axial positions of Cu(II) are coordinated by ethanol molecules as shown in Figure 3.3a and Figure 3.6. Removing coordinated solvent molecules from the paddlewheel SBU via solvent exchange followed by evacuation at elevated temperature, can create open metal sites.

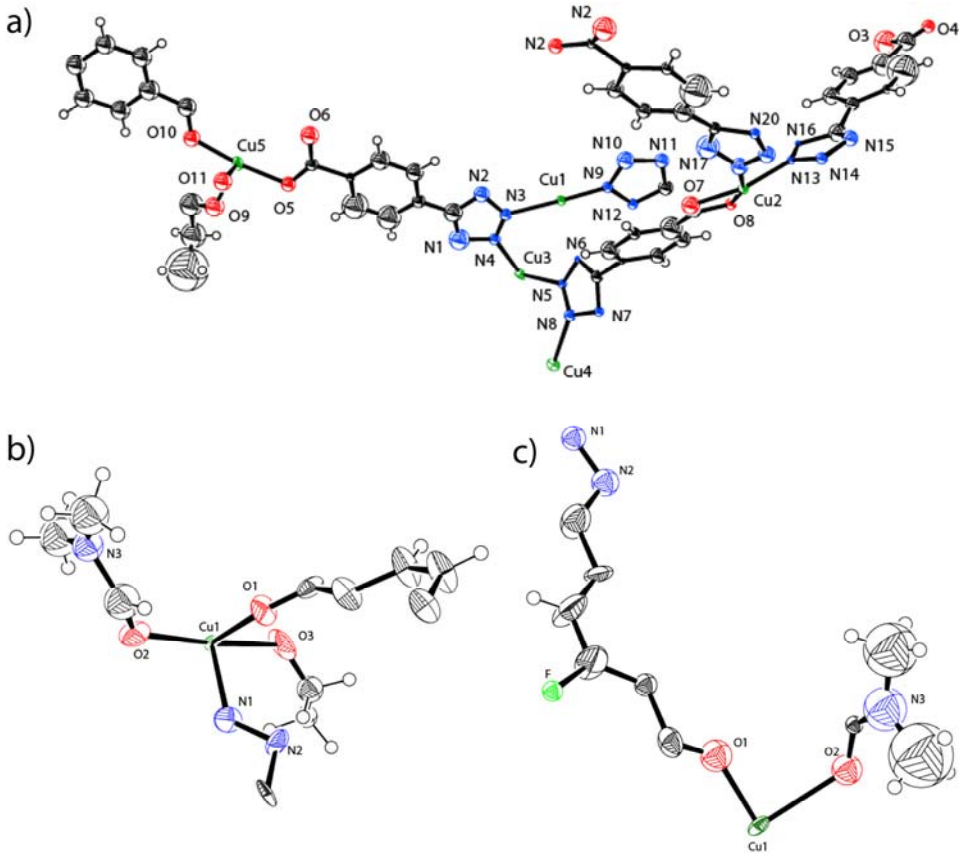

Figure 3.4 ORTEP drawings displayed at the 50 % probability level for, (a) Cu-TBA-1, (b) Cu-TBA-2, and (c) Cu-TBA-2F synthesized using 4-TBA and 2F-4-TBA linkers.

In SBU-2, there are two types Cu(II) atoms, in which Cu(2) is coordinated to four different μ_2-tetrazolyl and two different μ_4-tetrazolyl nitrogen (See *Figure 3.6* for modes of attachments). On the other hand, Cu(3) is coordinated to two nitrogen from two different μ_2-tetrazolyl groups, one nitrogen from μ_4-tetrazolyl group and two

oxygens from carboxylate functionality of 4-TBA ligand (*Figure 3.3b*). Similarly the SBU-3 is formed by coordination of three different μ_2-tetrazolyl, one μ_4-tetrazolyl nitrogen and two μ_2-OCO carboxylate functionality to Cu(4) as shown in Figure 3.3c.

In the crystal structure of Cu-TBA-1, the paddlewheel type SBU-1 extends in three dimensions through its μ_2-tetrazolyl group along *a* and *c* axis connecting to SBU-2 as shown in Figure 3.3d. Further, SBU-2 expands its coordination sphere along *ab* plane connecting it's both sides to the SBU-3 and thus creates a three dimensional architecture. Cu-TBA-1 forms highly connected porous structure due to the different binding modes of 4-TBA ligand. In the crystal structure, three types of SBUs with two different types of bridging modes for tetrazolyl group and carboxyl group gives highly connected structure with a large cages of 18.4 × 19.7 Å outer dimensions, with 11.6 Å pore radii inside it (*Figure 3.2*). These pores are accessible for gas adsorption as they have the pore aperture of 3.6 Å. The paddlewheel type SBU-1 forms the wall of cages and two solvent molecules attached to it protrude into the pores, which can be removed after evacuation for creation of large void space. The solvent accessible volume calculated for guest free Cu-TBA-1 using *PLATON* is as high as 51 %.[29] The structure of Cu-TBA-1 is highly stable till 230 ºC and maintains crystallinity at higher temperature as well.

Crystal Structure of Cu-TBA-2:

In the crystal structure of Cu-TBA-2, only one SBU has been observed with octahedral Cu(II) centers (*Figure 3.5b*). In Cu-TBA-2, two oxygen atoms from μ_2-OCO carboxylate groups are coordinated to two adjacent Cu(II) centers (*Figure 3.6*). These Cu(II) centers are also connected to four nitrogen atoms from ditopic μ_2-tetrazolyl groups. One oxygen atom from DMF and one oxygen atom from ethanol are coordinated to these Cu centers to form octahedral environment as shown in Figure 3.5. The structure of Cu-TBA-2 extends in the *ab* plane through the coordination of Cu(II) centers, ditopic tetrazolyl groups and DMF or ethanol in alternate fashion (*Figure 3.5a and 3.5c*). The joining of these carboxyl and tetrazolyl groups in ditopic fashion along the *c* axis creates one dimensional square shaped pores of 4.0 Å, where bridging disordered DMF and ethanol are pointing towards the pores (*Figure 3.5b*).

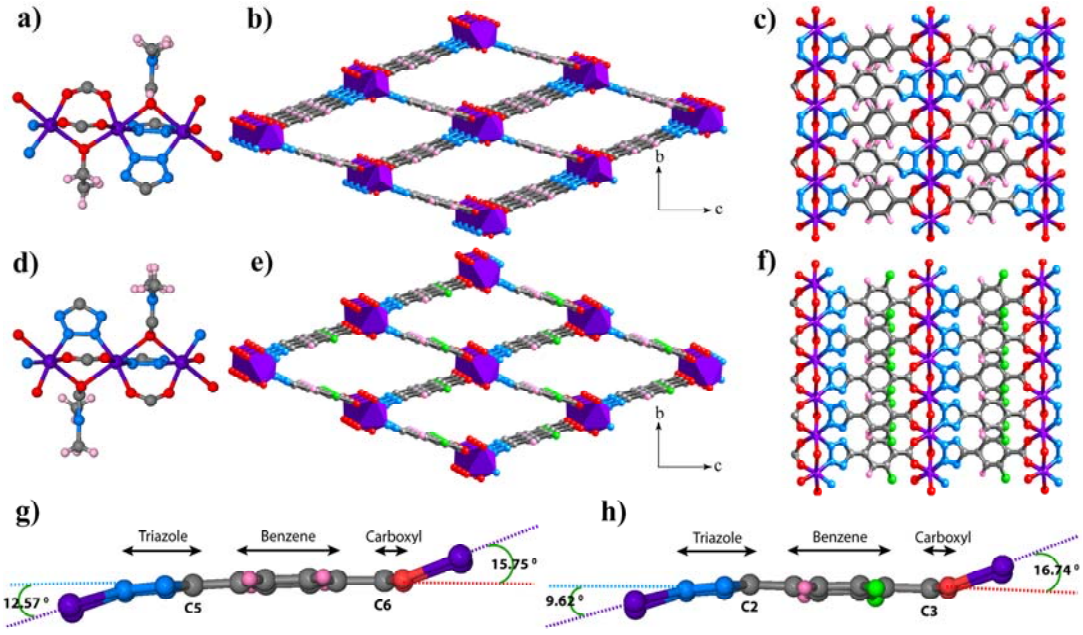

Figure 3.5 Crystal structure and structural deformation of $Cu_2(4\text{-TBA})_2(DMF)(EtOH)$ (Cu-TBA-2) and $Cu_2(2F\text{-}4\text{-TBA})_2(DMF)_2$(Cu-TBA-2F). (a) and (d) Octahedral Cu(II) SBU in Cu-TBA-2 and Cu-TBA-2F coordinated to 4 oxygen and 2 nitrogen. (b) and (e) Packing diagram showing formation of one-dimensional pores through a axis for Cu-TBA-2 and Cu-TBA-2F. (c) and (f) Packing diagram of Cu-TBA-2 and Cu-TBA-2F showing connectivity of metal centers with 4-TBA and 2-F-4-TBA linkers. (g) Formation of 12.5 Å and 15.7 Å angle between tetrazole ring with benzene ring plane and carboxyl group with benzene ring plane, respectively in Cu-TBA-2. (f) Formation of 9.6 Å and 16.7 Å angles between the tetrazole ring with the benzene ring plane and the carboxyl group with the benzene ring plane, respectively, in Cu-TBA-2F, showing variation in angle formation due to the effect of the protruding fluorine. Color code: Cu (magenta), N (blue), O (red), C (grey), H (pink), and F (green).

Crystal Structure of Cu-TBA-2F:

In the crystal structure of Cu-TBA-2F, only one type SBU has been observed (like Cu-TBA-2) with octahedral Cu(II) metal center. In the SBU of Cu-TBA-2F, two oxygen atoms from μ_2-OCO carboxylate groups, two nitrogen atoms from ditopic μ_2-tetrazolyl groups and two DMF molecules are coordinated to the two adjacent Cu centers to form the octahedral Cu(II) centers as shown in Figure 3.5d and Figure 3.6. Each Cu(II) atom in the structure is connected through carboxyl and tetrazolyl groups along *a* axis. The structure of Cu-TBA-2 extends in the *ab* plane through joining of μ_2-carboxyl and ditopic tetrazolyl groups in alternate ditopic fashion (*Figure 3.5f*) and creates the one dimensional, square shaped pores of 3.6 Å along the *a* axis (*Figure 3.5e*).

In Cu-TBA-2 and Cu-TBA-2F, both tetrazolate ring and carboxyl functionality adopts a bend conformation (*Figure 3.5g and 3.5h*). The tetrazolate ring for Cu-TBA-2 and -2F adopts an angle of 12.5° and 9.6º with respect to the plane of the benzene ring, while 15.7° and 16.7º are the angles of the carboxyl group. In Cu-TBA-2F, due to the steric hindrance of fluorine atom with solvent molecules, the bending angle increases from 15.7º to 16.7º for the coordinated carboxyl group. Due to the higher bending of carboxyl group, the pores formed in Cu-TBA-2F have smaller dimensions (3.3 Å) than Cu-TBA-2 (4.0 Å). Structures of Cu-TBA-2 and Cu-TBA-2F are very similar in nature, well simplified compared to Cu-TBA-1, and porous. Solvent accessible void calculated for solvent free Cu-TBA-2 and -2F using *PLATON* is 10 % and 8 %, respectively. In the crystal structure of the Cu-TBA-2F fluorine atoms are protruding in the pores, leading to the pore blockage and decreasing the solvent accessible volume.

3.2.3 Discussion on Crystal Structures:

Structural analysis of Cu-TBA-1, Cu-TBA-2 and Cu-TBA-2F reveals several interesting features. Cu-TBA-1 is highly porous and highly connected MOF with different connectivity's for tetrazolate (μ_2-tetrazolyl, μ_4-tetrazolyl) as well as carboxyl group (μ_1-OCO^-, μ_2-OCO^-). The Cu-TBA-1 has large elliptical cages possessing large pores of about 11.6 Å. On the other hand Cu-TBA-2, the structural isomer of Cu-TBA-1 is well simplified and contains only one octahedral SBU with μ_2-tetrazolyl group and μ_2-OCO^- group (*Figure 3.6*). The structure of Cu-TBA-2F is iso-structural to Cu-TBA-2 in terms of connectivity of the SBU and formation of extended

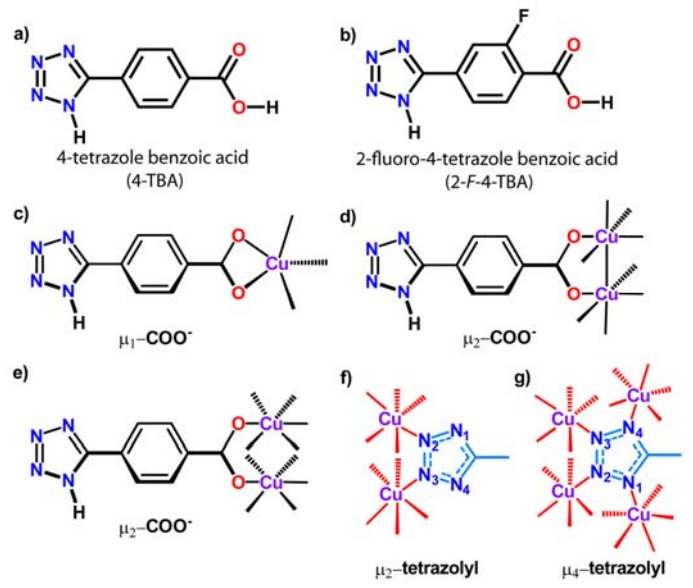

Figure 3.6 Schematic drawing and mode of coordination of TBA and 2F-4-TBA linkers observed in Cu-TBA-1, -2, and -2F.

3D structure. In this structure, due to insertion of highly electronegative fluorine atom into the system, bending of carboxyl group increases from 15.7 Å to 16.7 Å from the benzene ring plane, possibly due to the interaction of fluorine atoms with neighboring atoms resulting into the formation of smaller pores of 3.3 Å as compared to the Cu-TBA-2. Moreover, in the structure of Cu-TBA-2F, uncoordinated exposed fluorine atoms are protruding into the pores resulting in pore blockage.

By changing the metal precursor from Cu(II) to Cu(I), the structural isomers Cu-TBA-1 and Cu-TBA-2 has been isolated in crystalline form in quantitative amount. The discrete differences in pore size and modes of attachments observed in these MOFs, highlights the role of metal precursor in the determination of MOF structure. The structural isomerism, in which isomers retain their structural similarity before and after functionalization, is very rare in the literature and has not been reported in MOF literature frequently. Since, Cu-TBA-2 and Cu-TBA-2F are isostructural MOFs, the obvious structural similarities are observed in these cases. Most importantly, the Cu-TBA-2 synthesized from 4-TBA have the similar structure so as to Cu-TBA-2F synthesized from 2-F-4-TBA. Isostructural MOFs having exactly similar structures but with and without fluorine atoms pointing into the MOF pores in case of Cu-TBA-2 and Cu-TBA-2F, respectively; would be the best choice to study the effect of partial fluorination on gas uptake properties.

3.2.4 Thermo Gravimetric and Powder X-ray Diffraction Analyses:

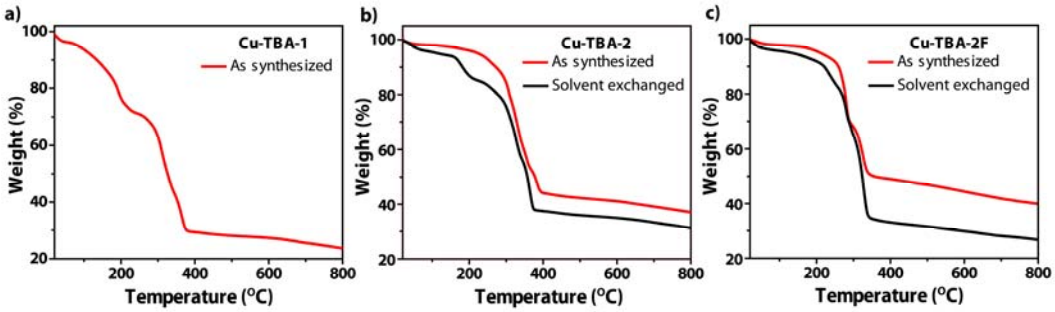

Figure 3.7 Thermal stability and the thermal gravimetric analysis (TGA) data of as synthesized samples of (a) Cu-TBA-1, (b) Cu-TBA-2, and (c) Cu-TBA-2F and solvent exchanged samples of Cu-TBA-2 and Cu-TBA-2F. The solvent exchanged samples show the higher weight loss at low temperature due removal low boiling guest solvent molecules from the framework.

We have prepared the Cu-TBA-1, Cu-TBA-2 and Cu-TBA-2F at the gram scale to allow detailed investigation of the thermo gravimetric properties and to examine the architectural stability and thermal stability. Thermo gravimetric analysis (TGA) performed on as-synthesized Cu-TBA-1, Cu-TBA-2 and Cu-TBA-2F revealed that these compounds have high thermal stability (*Figure 3.7*). The TGA trace for as synthesized Cu-TBA-1, Cu-TBA-2 and Cu-TBA-2F showed a gradual weight-loss step of 22.5 % (20–200 °C), 3.2 % (20–200 °C) and 3.0 % (20–200 °C), respectively; corresponding to escape of coordinated and guest solvent (DMF and ethanol) molecules in pores. This is followed by a sharp weight loss (200–390 °C) probably due to the decomposition of the framework. It is noteworthy that the TGA traces solvent exchanged Cu-TBA-2 show a larger weight loss of 12.5 % (20–200 °C) corresponding to escape of coordinated DMF, ethanol and non-coordinated guest solvent molecules in pores (*Figure 3.7b*). However, the same for Cu-TBA-2F doesn't change its TGA behavior in large extent [6.5 % (20–200 °C)]. A possible reason for this could be due to difficulty for the removal of coordinated DMF and ethanol molecules form Cu-TBA-2F framework (*Figure 3.7c*).

In order to confirm the phase purity of the bulk materials, powder X-ray diffraction (PXRD) experiments were carried out on all complexes. All major peaks of experimental PXRDs of Cu-TBA-1, Cu-TBA-2 and Cu-TBA-2F matches well with simulated PXRDs, indicating their reasonable crystalline phase purity (*Figure 3.8a, 3.8c and 3.8e*).[21] We have performed in situ variable temperature PXRD (VT-PXRD) of Cu-TBA-1, Cu-TBA-2 and Cu-TBA-2F to understand the structural changes at high temperature (*Figure 3.8b, 3.8d and 3.8f*). In situ VT-PXRD patterns of Cu-TBA-1, Cu-TBA-2 and Cu-TBA-2F have been collected at different temperature that coincides with the patterns simulated from single crystal structures. In situ VT-PXRD of all MOFs reported here indicate the stability and retention of crystallinity of these samples (230 °C) at high temperature. It also reveals that there are no possibilities of phase changes at higher temperature for these samples. Small differences in the intensities of the reflections are observed at higher temperatures due to the removal of residual solvent molecules.

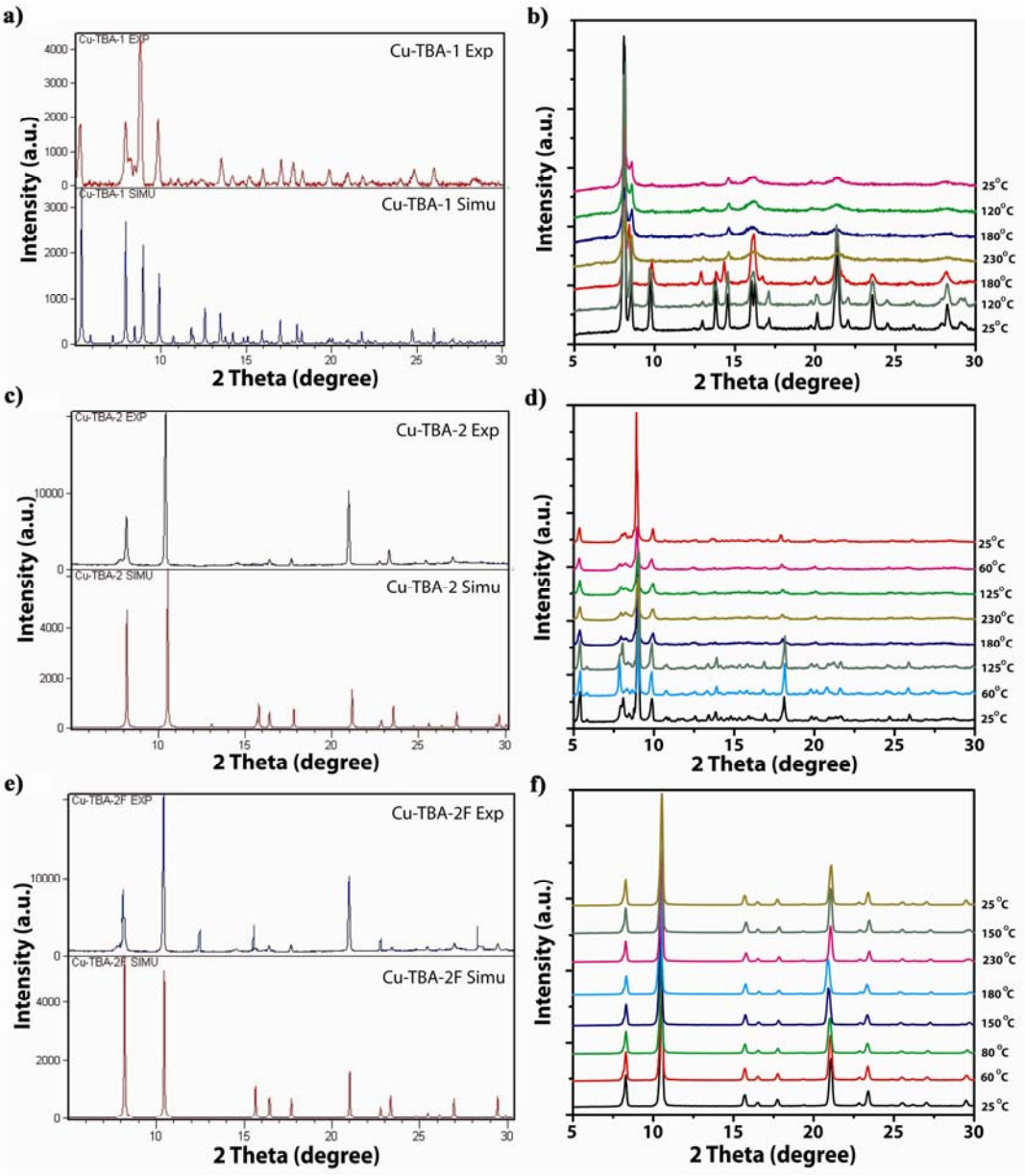

Figure 3.8 PXRD and VTPXRD patterns Cu-TBA-1, Cu-TBA-2 and Cu-TBA-2F. (a), (c) and (e) Comparison of the experimental PXRD pattern of as-synthesized Cu-TBA-1, Cu-TBA-2 and Cu-TBA-2F (top) with the one simulated from its single crystal structure (bottom), respectively. (b), (d) and (f) VT-PXRD patterns of Cu-TBA-1, Cu-TBA-2 and Cu-TBA-2F at different temperatures which coincides upto 230 °C, showing absence of phase change at high temperature.

3.3 Gas Adsorption Properties:

3.3.1 Experimental Results:

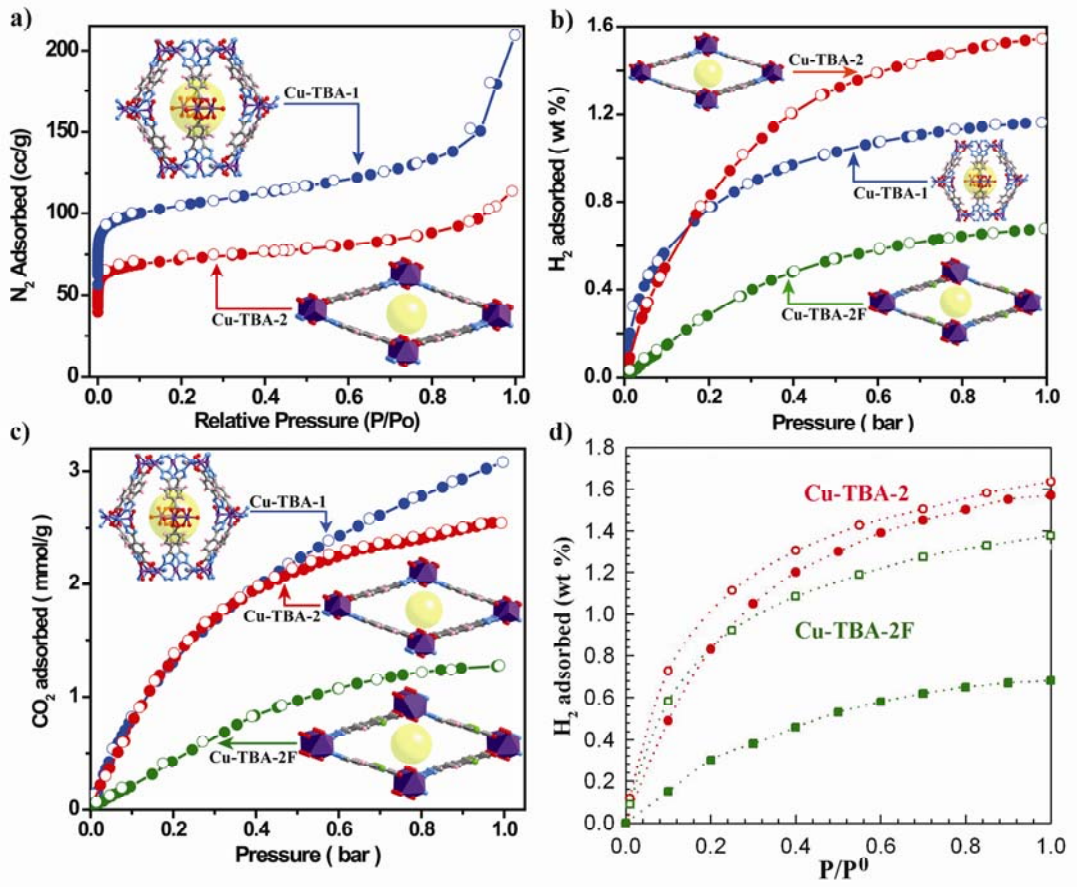

Figure 3.9 Experimental and computational gas adsorption isotherms for Cu-TBA-1, Cu-TBA-2 and Cu-TBA-2F. (a) N_2 adsorption isotherms below 1.0 bar for Cu-TBA-1 (blue) and Cu-TBA-2 (red) at 77 K. (b) H_2 adsorption isotherms below 1.0 bar for Cu-TBA-1 (blue), Cu-TBA-2 (red) and Cu-TBA-2F (green) at 77 K. (c) CO_2 adsorption isotherms below 1.0 bar for Cu-TBA-1 (blue), Cu-TBA-2 (red), and Cu-TBA-2F (green) at 298 K. (d) Simulated and experimental adsorption isotherms of H_2 in Cu-TBA-2 (red) and -2F (green) at 77 K. The open symbols are from simulation and the filled symbols are from experimental data. Pores available for N_2 gas adsorption in the Cu-TBA-1, Cu-TBA-2 and Cu-TBA-2F are shown with a yellow ball in the inset figures. Filled and open circles represent adsorption and desorption data for (a), (b) and (c), respectively. [Reprinted with permission from (16f). Copyright 2011 American Chemical Society].

In order to explore the gas storage properties of MOFs synthesized using 4-TBA and 2-F-4-TBA, we have performed the N_2, H_2 and CO_2 uptake studies (*Table 3.1*). The permanent porosity of Cu-TBA-1, Cu-TBA-2 and Cu-TBA-2F is confirmed by gas

adsorption studies. The N_2 adsorption isotherms of the activated sample of Cu-TBA-1 exhibit Type-I sorption behavior (*Figure 3.9*) with a Langmuir and BET surface area of 686 m^2/g and 616 m^2/g respectively. The activated sample of Cu-TBA-2 also shows type-I adsorption behavior with Langmuir and BET surface area of 402 m^2/g and 356 m^2/g, respectively. These results are justified as Cu-TBA-2 has less pore size (4.24 Å), low void space and less solvent accessible volume (10.9 %) as compared to Cu-TBA-1 (51.3 %). Although, Cu-TBA-2 and Cu-TBA-2F are iso-structural in terms of the connectivity of the SBU and formation of extended 3D structure, Cu-TBA-2F is non-porous to N_2 adsorption. The total reduction of surface area in Cu-TBA-2F is presumably due to the insertion of fluorine and subsequently inaccessibility of pores. Fluorine atom has considerably higher van der Waals radius (1.47 Å) than H_2 (1.20 Å). Also, as mentioned previously, the coordinated guest solvents present in the framework of Cu-TBA-2F are difficult to remove from the framework possibly due to highly electronegative nature of fluorine atom. The kinetic diameter of N_2 (3.65 Å) is higher than pore size of Cu-TBA-2F (3.52 Å), and the low kinetic energy of the N_2 molecules at 77 K resulting in N_2 molecules unable to effectively enter small pores of Cu-TBA-2F. However, Cu-TBA-2F is able to take up H_2 (2.89 Å) and CO_2 (3.4 Å) as it has the less kinetic diameter.

Table 3.1 Summary of gas adsorption analyses of Cu-TBA-1, Cu-TBA-2 and Cu-TBA-2F MOFs synthesized using 4-TBA and 2-F-4-TBA linkers:

Name of MOFs	**Surface Area (m^2/g)**		**H_2 Uptake**		**CO_2 Uptake (mmol/g)**
	Langmuir	**BET**	**Experimental**	**Computational**	
Cu-TBA-1	686	402	1.16	-	3.08
Cu-TBA-2	616	356	1.54	1.62	2.54
Cu-TBA-2F	-	-	0.67	1.36	1.27

The H_2 and CO_2 adsorption properties of Cu-TBA-1, Cu-TBA-2 and Cu-TBA-2F are shown in Figure 3.9b and 3.9c, respectively. All these MOFs show reversible type-I H_2 and CO_2 adsorption isotherms at 77K and 298 K, respectively. In addition, the absence of adsorption–desorption hysteresis indicates that H_2 and CO_2 is reversibly

adsorbed by all the MOFs discussed in this context. At 760 Torr and 77 K, Cu-TBA-1 and Cu-TBA-2 adsorbs 1.16 and 1.54 wt% H_2, while Cu-TBA-2F adsorbs 0.67 wt% H_2. The difference between the H_2 uptakes of Cu-TBA-1 and –2 is well anticipated as small pores of Cu-TBA-2 are more suitable for H_2 adsorption, which is well supported by previous reports.[22] Fluorine atoms protrude into the pores in case of Cu-TBA-2F, as a result due to decreased pore size and steric crowding; it shows less adsorption capacity for H_2. The CO_2 adsorption properties of Cu-TBA-1, –2 and –2F are shown in Figure 3.9c. Cu-TBA-1 and –2 adsorbs 3.08 and 2.54 mmol/g, while Cu-TBA-2F adsorbs 1.27 mmol/g of CO_2 at 298 K and 1 bar pressure. These reversible H_2 and CO_2 uptake at 1 atm pressure is comparable with previously reported ZIFs and well known MOFs materials.[23] The prominent difference in CO_2 uptake properties between the Cu-TBA-1 and –2 is well defined. As shown in Figure 3.9c, at low pressure upto the 0.45 bar both these MOFs adsorb CO_2 equally as Cu-TBA-1 and -2 have availability of adsorptive pores till that pressure. After 0.45 bar pressure, Cu-TBA-2 adsorbs less CO_2 gas as its pore size is less than Cu-TBA-1. The larger pores of Cu-TBA-1 adsorb more CO_2 as pressure increases from 0.45 to 1 bar. The availability of larger and suitable pores for CO_2 adsorption in Cu-TBA-1 over Cu-TBA-2 gives more adsorption capacity in it. Again as discussed earlier, due to blocking of pores, Cu-TBA-2F adsorbs less amount of CO_2, although it is iso-structural, in terms of the connectivity of the SBU and formation of extended 3D structure with Cu-TBA-2.

3.3.2. Computational/Theoretical Results:

Grand Canonical Monte Carlo (GCMC) simulations were carried out for H_2 adsorption in Cu-TBA-2 and Cu-TBA-2F; to unravel the effect of fluorine atoms on adsorption and to identify the adsorption sites in gas–loaded structures, as they are isostructural. The experimentally determined desolvated crystal structures were used in the simulations. The porosities of Cu-TBA-2 and Cu-TBA-2F are 0.540 and 0.531, respectively, evaluated using Materials Studio with a Connolly probe radius equal to zero. H_2 molecule was represented as a two-site rigid molecule with H–H bond length of 0.74 Å. The Lennard-Jones parameters of H-H interaction were σ = 2.59 Å and ε = 12.5 K.[31] The dispersion interactions of the framework atoms in Cu-TBA-2 and Cu-TBA-2F were modeled by the Universal Force Field (UFF).[32] The Lorentz-Berthelot combining rules

were used to calculate the cross LJ interaction parameters.

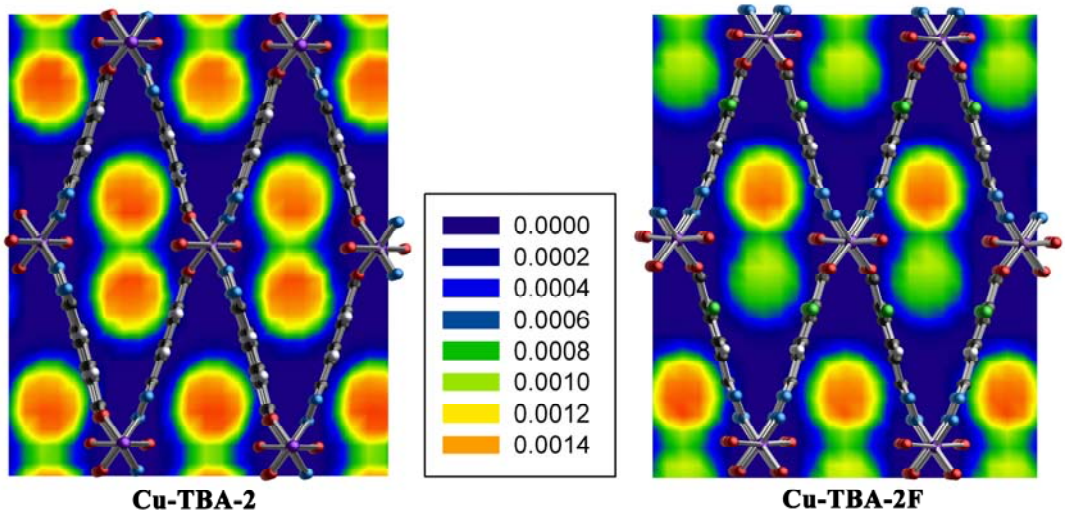

Figure 3.10 H_2 adsorption density contours for Cu-TBA-2 and Cu-TBA-2F on the *XY* plane for H_2 adsorption at 1 kPa. [Reprinted with permission from (16f). Copyright 2011 American Chemical Society].

In the GCMC simulations the frameworks and H_2 molecules were treated as rigid. The LJ interactions were evaluated using a spherical cutoff of 18 Å with the long-range corrections added. Five types of trial moves were conducted for H_2 molecules, namely, displacement, rotation, partial re-growth at a neighboring position, complete re-growth at a new position, and swap with the reservoir. The number of trial moves in the simulations was 2×10^7. The first 10^7 moves were used for equilibration and the subsequent 10^7 moves for production. The H_2 adsorption isotherms obtained in Cu-TBA-2 and Cu-TBA-2F at 77 K by experimental procedures and simulations are shown in Figure 3.10d. The simulated H_2 adsorption agrees fairly well with experimental in Cu-TBA-2. Specifically, the adsorption at 1 bar is 1.54 wt% from experiment and 1.62 wt% predicted by simulation. But the simulated isotherm in Cu-TBA-2F largely overestimates experimental data as the simulated adsorption is 1.36 wt%, whereas the experimental is 0.67 wt%. The deviations between experimental and simulation isotherms in Cu-TBA-2F are much larger than in Cu-TBA-2. This is possibly attributed to the interactions of protruding fluorine atoms in Cu-TBA-2F and difficulties in removing the coordinated and guest solvent molecules from the pores. At low pressures, both the simulated isotherms in Cu-TBA-2 and Cu-TBA-2F are nearly similar, due to

the availability of smaller pores in both MOFs. But as we move further to high pressures, due to the inaccessibility of pores for H_2 adsorption in Cu-TBA-2F over Cu-TBA-2, lower H_2 adsorption is observed in Cu-TBA-2F.

To identify the favorable binding sites for H_2 in Cu-TBA-2 and -2F, the density distributions of adsorbed H_2 molecules were estimated along the *YZ* plane at 77 K and 1 kPa. As illustrated in Figure 3.10, H_2 molecules are primarily adsorbed in the pores along the *X* axis and the binding sites are mostly located in the pore centers in both Cu-TBA-2 and -2F. More specifically, the density in Cu-TBA-2 equally distributes in the middle of the pores as protruding hydrogen atoms from ligand does not have strong effect on adsorbed H_2 gas molecules. The density in Cu-TBA-2F is lower; however, particularly in the regions near the fluorine atoms due to steric hindrance.

3.4 Conclusions:

In conclusion, we have synthesized solvothermally three new MOFs having three dimensional structures using the predesigned 4-TBA and 2-F-4-TBA ligands with a transition metal center Cu(I/II). These MOFs are highly porous and show high adsorption capacity for N_2, H_2 and CO_2 at 1 atm pressure. At 1 atm pressure, Cu-TBA-1 shows 1.16 wt% H_2 and 3.08 mmol/g CO_2 uptake; while Cu-TBA-2 shows uptake of 1.54 wt % H_2 and 2.54 mmol/g CO_2 at 77 and 298 K. These MOFs are highly stable and retain crystallinity until 230 °C which was confirmed by TGA and in situ VT-PXRD patterns. The phenomenon of structural isomerism has been observed in the Cu-TBA-1 and Cu-TBA-2 upon changing metal source during synthesis [$Cu(NO_3)_2.3H_2O$ to CuCl]. Also, iso-structural Cu-TBA-2 and Cu-TBA-2F were obtained by changing the ligand 4-TBA to 2-F-4-TBA. The utility of small sized pores than that of very large for high H_2 uptake is experimentally redefined using Cu-TBA-2 (1.54 wt %) and Cu-TBA-1 (1.16 wt %).

In continuation with our efforts to explore the effect of partial fluorination on H_2 uptake properties in MOFs from previous Chapter 2, herein using isostructural Cu-TBA-2 and Cu-TBA-2F MOFs, we have studied the same effect in more details by utilizing the experimental and computational results of H_2 adsorption isotherms. The direct comparison between gas adsorption properties of iso-structural partially fluorinated Cu-TBA-2F and non-fluorinated Cu-TBA-2 suggested that enhancement of H_2 adsorption due to fluorination in MOFs is not an universal phenomenon, but it is rather system specific and can differ from system to system. The density distributions of adsorbed H_2 molecules in Cu-TBA-2 and Cu-TBA-2F from simulation suggest that H_2 molecules are primarily adsorbed in the pores along the X axis and the binding sites are mostly located in the pore centers. Based on the simulation, protruding fluorine atoms from 2-F-4-TBA appear to cause a steric hindrance and a lower adsorption for H_2. Nevertheless, thorough research work is necessary on H_2 adsorption on iso-structural fluorinated/non-fluorinated MOFs before we can conclusively indicate a positive/negative effect of fluorination on enhancement of hydrogen adsorption in MOFs.

3.5 Experimental and Computational Materials and Methods:

3.5.1 General Procedures:

All reagents and solvents for syntheses and analyses were commercially available and used as received. 4-cyanobenoic acid, 2-Fluoro-4-cyanobenzoic acid, $Cu(NO_3)_2.3H_2O$, Sodium azide and Ammonium chloride were purchased from Aldrich Chemicals. DMF was purchased from Rankem chemicals. All experimental operations were performed in air and all the stock solutions were prepared in DMF. The Fourier transform (FT) IR spectra were recorded on a Bruker Optics ALPHA-E spectrometer with a universal Zn-Se ATR accessory in the 600–4000 cm^{-1} region. Powder X-ray diffraction (PXRD) patterns and insitu variable temperature PXRD (VT-PXRD) were recorded on a Phillips PANalytical diffractometer for Cu K_α radiation (λ= 1.54 Å), with a scan speed of 2° min^{-1} and a step size of 0.02° in 2θ. Thermo-gravimetric analyses (TGA) were carried out for the temperature range of 20–800 °C on a SDT Q600 TG-DTA analyzer under N_2 atmosphere at a heating rate of 10 °C min^{-1}. All low pressure gas adsorption experiments (up to 1 bar) were performed on a Quantachrome Quadrasorb automatic volumetric instrument.

3.5.2 Single Crystal X-Ray Diffraction Methods:

Single crystal data were collected on Bruker SMART APEX three circle diffractometer equipped with a CCD area detector and operated at 1500 W power (50 kV, 30 mA) to generate Mo K_α radiation (λ= 0.71 Å). The incident X-ray beam was focused and monochromated using Bruker Excalibur Gobel mirror optics. Crystals of all MOFs reported in the paper were mounted on nylon Cryo-Loop (Hampton Research) with Paraton-N (Hampton Research). Initial scans of each specimen were performed to obtain preliminary unit cell parameters and to assess the mosaicity (breadth of spots between frames) of the crystal to select the required frame width for data collection. In every case frame widths of 0.5° were judged to be appropriate and full hemispheres of data were collected using Bruker SMART software suite.[24] Following data collection, reflections were sampled from all regions of the Ewald sphere to redetermine unit cell parameters for data integration and to check for rotational twinning using CELL NOW. Following exhaustive review of the collected frames the resolution of the dataset was judged. Data were integrated using Bruker SAINT[25] software with a narrow frame

algorithm and a 0.40 fractional lower limit of average intensity. Data were subsequently corrected for absorption by the program SADABS.[26] The space group determinations and tests for merohedral twinning were carried out using XPREP.[27] In these cases, the highest possible space group was chosen.

Table 3.2 Comparison of crystal data and structure refinement for Cu-TBA-1, Cu-TBA-2 and Cu-TBA-2F MOFs.

MOFs	**Cu-TBA-1**	**Cu-TBA-2**	**Cu-TBA-2F**
Empirical formula	$C_{86}H_{50}Cu_9N_{40}O_{22}$	$C_{21}H_{23}Cu_2N_9O_6$	$C_{11.16}H_8CuF_{0.33}N_5O_3$
Formula weight	2567.5	624.5	330.0
Temperature	293(2) K	298(2) K	298(2) K
Wavelength	0.7107 Å	0.7107 Å	0.7107 Å
Crystal system	Orthorhombic	Orthorhombic	Orthorhombic
Space group	*Pnn*2	*Imm*2	*Ima*2
Unit cell dimensions	*a* = 13.46(8) Å, α = 90° *b* = 29.98(7) Å,β = 90° *c* = 19.71(11) Å, γ = 90°	*a* = 7.11(6) Å, α = 90° *b* = 21.58(2) Å, β = 90° *c* = 9.10(8) Å, γ = 90°	*a* = 7.185(15) Å, α = 90° *b* = 9.185(19) Å, β = 90° *c* = 21.544(5) Å, γ = 90°
Volume	7960 (8)	1398 (2)	1421.8 (5)
Z	2	2	4
Density (calculated)	1.071	1.477	1.540
Absorption coefficient	1.235	1.572	1.553
Goodness-of-fit on F^2	0.910	1.077	1.031
Final R indices [I>2sigma(I)]	R_1 = 0.0778, wR_2 = 0.1731	R_1 = 0.0604, wR_2 = 0.1503	R_1 = 0.0723, wR_2 = 0.1961
R indices (all data)	R_1 = 0.1304, wR_2 = 0.1943	R_1 = 0.0663, wR_2 = 0.1540	R_1 = 0.0933, wR_2 = 0.2091
CCDC	**811812**	**811813**	**811814**

Structures were solved by direct methods and refined by least square method using the SHELXTL 97 software suite.[28] Atoms were located from iterative examination of difference F-maps following least squares refinements of the earlier models. Final model was refined anisotropically (if the number of data permitted) until full convergence was achieved. Hydrogen atoms were placed in calculated positions (C–H = 0.93 Å) and included as riding atoms with isotropic displacement parameters 1.2–1.5 times U_{eq} of the attached C atoms. In some cases modeling of electron density

within the voids of the frameworks did not lead to identification of recognizable solvent molecules in these structures, probably due to the highly disordered contents of the large pores in the frameworks. Single crystal X-ray diffraction data for Cu-TBA-1, -2 and -2F was collected at 293(2) or 298(2) K. Structures were examined using the ADDSYM subroutine of PLATON to assure that no additional symmetry could be applied to the models.[29] All ellipsoids in ORTEP diagrams are displayed at the 50 % probability level unless noted otherwise. Crystal data and details of data collection, structure solution and refinement are summarized in Table 3.2. Crystallographic data (excluding structure factors) for the structures reported in this context have been deposited with the CCDC as deposition No. CCDC 811812 - 811814. Copies of the data can be obtained, free of charge, on application to the CCDC, 12 Union Road, Cambridge CB2 lEZ UK (fax: + 44 (1223) 336 033; e-mail: deposit@ccdc.cam.ac.uk).

3.5.3 Gas Adsorption Measurements:

Low pressure volumetric gas adsorption measurements involved in this work were performed at 77 K for H_2 and N_2, maintained by a liquid nitrogen bath, with pressures ranging from 0 to 760 Torr on Quantachrome Quadrasorb automatic volumetric instrument. While CO_2 adsorption measurements were done at room temperature (298 K) with same pressures range. In the all adsorption measurements, ultra high-purity H_2 was obtained by using calcium aluminosilicate adsorbents to remove trace amounts of water and other impurities before introduction into the system. The blue colored micro crystals of each MOF were soaked in 1:1 dry dichloromethane and methanol mixture for 12 h. Fresh 1:1 dry dichloromethane and methanol mixture was subsequently added and the crystals were allowed to stay for additional 48 h to remove co-ordinated and free solvates (DMF and EtOH) present in framework. The sample was dried under a dynamic vacuum (< 10^{-3} Torr) at room temperature for 12 h. The coordinated solvents DMF and EtOH on the secondary binding units (SBUs) remain in the framework at this stage. To remove coordinated solvents, samples were heated at 60 °C for 12 h and 100 °C for 12 h under a dynamic vacuum.

3.5.4 Simulation Model and Methods:

Grand canonical Monte Carlo (GCMC) simulations were carried out for H_2 adsorption in Cu-TBA-2 and –2F; to find the effect of fluorine atoms on adsorption and to identify

the adsorption sites in gas–loaded structures. The experimentally determined desolvated crystal structures were used in the simulations. The porosities of Cu-TBA-2 and -2F are 0.540 and 0.531, respectively, evaluated using Materials Studio[30] with a Connolly probe radius equal to zero. H_2 molecule was represented as a two-site rigid molecule with H–H bond length of 0.74 Å.[31] The dispersion interactions of the framework atoms in Cu-TBA-2 and –2F were modeled by the Universal Force Field (UFF).[32] The Lorentz-Berthelot combining rules were used to calculate the cross LJ–interaction parameters. GCMC simulations were conducted for H_2 adsorption in Cu-TBA-2 and -2F at 77 K. The LJ interactions were evaluated using a spherical cutoff with the long-range corrections added. The number of trial moves in the simulation was 2×10^7. The first 10^7 moves were used for equilibration and the subsequent 10^7 moves for production.

3.5.5 Synthesis of Linkers and MOFs:

Synthesis of 4-tetrazole benzoic acid (4-TBA) and 2-fluoro-4-tetrazole benzoic acid (2F-4TBA): Sodium azide (0.11 mol, 7.1 g) and ammonium chloride (0.11 mol, 5.8 g) were dissolved in 100 mL dry DMF. This solution was stirred for 30 min at room temperature. 4-cyano benzoic acid (0.1 mol, 14.7 g) was added with stirring to this solution. Then this mixture was refluxed with stirring at 120 °C for 18–20 h. After cooling to room temperature, this solution was acidified with 200 mL hydrochloric acid (1 M) solution with continuous stirring. White precipitate formed in the flask was filtered and ensuing product was washed with successive aliquots of distilled water (3 × 25 mL). The product 4-tetrazole benzoic acid obtained was re-crystallized in dry acetone (Yield: 90 %, 13.2 g).[33]

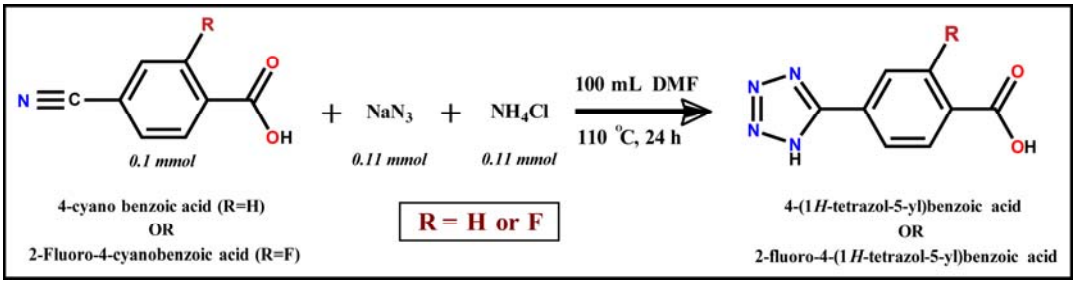

Scheme 1. Scheme of synthesis of 4-tetrazole benzoic acid and 2-fluoro-4-tetrazole benzoic acid linkers.

The synthesis of 2-F-4-TBA was performed by following the similar synthesis

protocol so as to 4-TBA except the use of 2-fluoro-4-cyano benzoic acid instead of 4-cyano benzoic acid (Yield: 58 %, 9.5 g).

4-tetrazole benzoic acid (4-TBA):

FT-IR: (KBr, 4000-600 cm^{-1}): 3066 (m), 2321 (m, br), 1885 (m, br), 1630 (m), 1415 (s), 1375 (s), 1200 (m), 1112 (m), 890 (s) and 744 (s).

^{1}H NMR (300 MHz, $CDCl_3$): δ 8.10 (d, 2H, J=7.8), 8.00 (d, 2H, J=7.8).

2-fluoro-4-tetrazole benzoic acid (2-F-4-TBA):

FT-IR: (KBr 4000-600 cm^{-1}): 3205 (m, br), 2958 (m), 2342 (m, br), 1802 (m), 1617 (m), 1401 (m), 1355 (s), 1287 (s), 1212 (s), 854 (m) and 713 (m).

^{1}H NMR (300 MHz, $CDCl_3$): δ 7.98 (d, 1H), 7.87 (d, 1H), 7.85 (d, 1H).

Synthesis of Cu_9(4-TBA)$_{10}$(C_2H_5OH)$_2$ (Cu-TBA-1): 2.0 mL 4-TBA solution (0.20 M) in 1:1 solution of *N*,*N*-dimethylformamide (DMF) and Ethanol (EtOH) was taken in a 5 mL vial. 0.5 mL $Cu(NO_3)_2 \cdot 3H_2O$ solution (0.20 M) in DMF was added to this solution. The vial was capped and heated to 85 °C for 96 h. The mother liquor was decanted and the octahedral blue crystals were filtered off, washed with EtOH. The unreacted ligand was removed by washing with DMF (3 mL, 4 times) as 4-TBA is highly soluble in DMF and afterwards resulting MOF was dried in air (10 min). [**Yield:** 0.013 g, 54 % depending on $Cu(NO_3)_2$. $3H_2O$].

FT-IR: (KBr 4000-600 cm^{-1}): 3039 (m, br), 2795 (w, br), 2356 (m), 1660 (s), 1611 (s), 1393 (s), 1246 (m), 1091 (s), 868 (m) and 742 (m).

Element analysis: Found (%) C= 39.20, H= 1.99, N= 22.24; Calc. (%) C= 40.24, H= 1.96, N= 21.82.

Synthesis of Cu_2(4-TBA)$_2$(DMF)(C_2H_5OH) (Cu-TBA-2): 2.0 mL 4-TBA solution (0.20 M) in 1:1(v/v) mixture of DMF and EtOH was taken in a 5 mL vial. 0.009 g (0.2 mmol) of anhydrous CuCl solid was added to this solution. Additional 0.5 ml DMF was added to this above mixture; vial was capped and heated at 90 °C for 72 h. After cooling to room temperature, two layers were seen, one is a plate light blue crystal of Cu-TBA-2 and other one is an unreacted white starting materials. Then collected Cu-TBA-2 crystals were washed with EtOH (2 mL, 3 times) and DMF (5 mL, 2 times) and dried in air (10 min). [**Yield:** 0.0054 g, 61 % depending on CuCl].

FT-IR: (KBr 4000-600 cm^{-1}): 3555 (m, br), 2811 (m), 2675 (w), 2361 (w), 1668 (s),

1614 (m), 1537 (w), 1401 (s), 1325 (m), 1098 (s), 860 (m) and 739 (s).

Element analysis: Found (%) C= 39.84, H= 3.59, N= 20.96; Calc. (%) C= 40.38, H= 3.71, N= 20.18

Synthesis of Cu_2(2-F-4-TBA)$_2$(DMF)$_2$ (Cu-TBA-2F):[34] 2.0 mL 2-F-4-TBA solution (0.20 M) in 1:1(v/v) mixture of DMF and EtOH was taken in a 5 mL vial. 0.5 mL $Cu(NO_3)_2.3H_2O$ solution (0.20 M) in DMF was added to this solution. The vial was capped and heated to 85 °C for 96 h. The mother liquor was decanted and plate like blue crystals were filtered off, washed with EtOH and dried in air (10 min). [**Yield:** 0.0139 g, 58 % depending on $Cu(NO_3)_2$• $3H_2O$].

FT-IR: (KBr 4000-600 cm^{-1}): 3561 (m, br), 2923 (m), 2853 (w), 2458 (w), 1745 (s), 1537 (s), 1380 (s), 1212 (s), 1090 (m), 1020 (s), 895 (m) and 752(s).

Element analysis: Found (%) C= 40.02, H= 2.31, N= 21.84; Calc. (%) C= 40.61, H= 2.44, N= 21.21.

3.6 References and Notes

1. (a) T. Huang, *Nanotechnology That Will Change the World*; Enlighten Noah Publishing: **2002**, 38. (b) P. Chen, X. Wu, J. Lin, K. L. Tan, *Science* **1999**, *285,* 91. (c) C. Liu, Y. Y. Fan, M. Liu, H. T. Cong, H. M. Cheng, M. S. Dresselhaus, *Science* **1999**, *286*, 1127. (d) A. C. Dillon, K. M. Jones, T. A. Bekkedahl, C. H. Kiang, D. S. Bethune, M. J. Heben, *Nature* **1997**, *386,* 377. (e) A. Chambers, C. Park, R. T. K. Baker, N. M. Rodriguez, *J. Phys. Chem. B* **1998**, *102*, 4253.

2. (a) R. T. Yang, *Adsorbents*: *Fundamentals and Applications*; Wiley: New York, **2003**, 280. (b) Y. Li, R. T. Yang, *J. Phys. Chem. B*, **2006**, *110,* 17175. (c) F. Darkrim, A. Aoufi, P. Malbrunot, D. Levesque, *J. Chem. Phys*, **2000**, *112*, 5991. (d) M. G. Nijkamp, J. E. Raaymakers, A. J. van Dillen, K. P. de Jong, *Appl. Phys. A*, **2001**, *72*, 619.

3. (a) M. A. de la Casa-Lillo, F. Lamari-Darkrim, D. Cazorla-Amoros, A. Linares-Solano, *J. Phys. Chem. B*, **2002**, *106*, 10930. (b) H. Wang, Q. Gao, J. Hu, *J. Am. Chem. Soc.*, **2009**, *131*, 7016. (c) S. Hynek, W. Fuller, J. Bentley, *Int. J. Hydrogen Energy* **1997**, *22*, 601. (d) R. Chahine, T. K. Bose, *Int. J. Hydrogen Energy* **1994**, *19*, 161. (e) C. Carpetis, W. Peschka, *Int. J. Hydrogen Energy* **1980**, *5*, 539. (f) J. S. Noh, R. K. Agarwal, J. A. Schwarz, *Int. J. Hydrogen Energy* **1987**, *12*, 693. (g) Y. Zhou, L. Zhou, *Sci. China, Ser. B* **1996**, *39*, 598. (h) Q. Wang, J. K. Johnson, *J. Chem. Phys.* **1999**, *110*, 577.

4. (a) Y. Fukai, In *The Metal−Hydrogen System;* Gonser, U., Ed.; Springer Series in Material Science; Springer-Verlag, New York, **1993**. (b) L. M. Das, *Int. J. Hydrogen Energy* **1996**, *21*, 789. (c) H. Imamura, N. Sakasai, *J. Alloys Compd.* **1995***, 231*, 810. (d) H. Imamura, N. Sakasai, Y. Kajii, *J. Alloys Compd.* **1996**, *232*, 218. (e) H. Imamura, N. Sakasai, T. Fujinaga, *J. Alloys Compd.* **1997**, 34, *253*. (f) G. Sandrock, *J. Alloys Compd.* **1999**, *293*, 877. (g) F. Schuth, B. Bogdanovi, M. Felderhoff, *Chem. Commun.* **2004**, 2249. (h) K. J. Gross, P. Spatz, A. Züttel, L. Schlapbach, *J. Swiss Soc. Surf. Mater.* **1996**, *5*, 22.

5. (a) A. Zuttel, *et.al.*, *Hydrogen Desorption From Lithiumtetrahydroboride (LiBH4)*, Proceedings, 14th World Hydrogen Energy Conference, June **2002**, Montreal, Canada. (b) J. Strom-Olsen, *Method of Hydrogen Generation for Fuel Cell Applications and a Hydrogen-Generating System*, Patent Filing WO0185606, May **2001**, McGill University. (c) J. Irvine, Theme issue: materials chemistry for hydrogen storage and generation, *J. Mater. Chem.*, **2008**, *18*, 2295.

6. (a) H. Furukawa, K. E. Cordova, M. O'Keeffe, O. M. Yaghi, *Science*, 2013, **341**, 1230444. (b)

H.-C. Zhou, J. R. Long, O. M. Yaghi, *Chem. Rev.*, **2012**, *112*, 673. (c) J. R. Long, O. M. Yaghi, *Chem. Soc. Rev.*, **2009**, *38*, 1213. (d) M. O'Keeffe, *Chem. Soc. Rev.*, **2009**, *38*, 1215. (e) J. J. P. IV, J. A. Perman, M. J. Zaworotko, *Chem. Soc. Rev.*, **2009**, *38*, 7761.

7. (a) M. O'Keeffe, M. A. Peskov, S. J. Ramsden, O. M. Yaghi, *Acc. Chem. Res.*, **2008**, *41*, 1782. (b) O. D. Friedrichs, M. O'Keeffe, O. M. Yaghi, *Phys. Chem. Chem. Phys.*, **2007**, *9*, 1035. (c) R. J. Hill, D. L. Long, N. R. Champness, P. Hubberstey, M. Schroder, *Acc. Chem. Res.*, **2005**, *38*, 337.(d) S. Natarajan, P. Mahata, *Chem. Soc. Rev.*, **2009**, *38*, 2304. (d) C. Janiak, *J. Chem. Soc. Dalton Trans*. **2003**, 2781. (e) B. Moulton, M. J. Zaworotko, *Chem. Rev*. **2001**, *101*, 1629. (f) M. Eddaoudi, D. B. Moler, H. Li, B. Chen, T. M. Reineke, M. O'Keeffe, O. M. Yaghi, *Acc. Chem. Res.* **2001**, *34*, 319. (g) R. Robson, *J. Chem. Soc., Dalton Trans*. **2000**, 3735. (h) O. M. Yaghi, *Nature Mat.* **2007**, *6*, 92. (i) I. G. Georgiev, L. R. MacGillivray, *Chem. Soc. Rev.* **2007**, *36*, 1239. (j) A. Corma, H. Garcia, F. X. L. Xamena, *Chem. Rev.* **2010**, *110*, 4606. (k) S. L. James, *Chem. Soc. Rev.* **2003**, *32*, 276. (l) O. M. Yaghi, H. Li, C. Davis, D. Richardson, T. L. Groy, *Acc. Chem. Res.* **1998**, *31*, 474. (m) C. Janiak, *Angew. Chem., Int. Ed. Engl.* **1997**, *36,* 1431. (n) A. J. Blake, N. R. Champness, P. Hubberstey, W.-S. Li, M. A. Withersby, M. Schroder, *Coord. Chem. Rev.* **1999**, *183,* 117. (o) B. Kesanli, Y. Cui, M. Smith, E. Bittner, B. Bockrath, W. Lin, *Angew. Chem., Int. Ed.* **2005**, *44,* 72.

8. (a) DoE Office of Energy Efficiency and Renewable Energy Hydrogen, Fuel Cells & Infrastructure Technologies Program Multi-Year Research, Development and Demonstration Plan. (b) FY **2006** *Annual Progress Report for the DoE Hydrogen Program*, Nov **2006**. (c) S. Satyapal, *et al*. FY **2006** *DoE Hydrogen Program Annual Merit Review and Peer Evaluation Meeting Proceedings*, Plenary Session.

9. (a) H. Deng, C. J. Doonan, H. Furukawa, R. B. Ferreira, J. Towne, C. B. Knobler, B. Wang, O. M. Yaghi, *Science* **2010**, *327*, 846. (b) K. Koh, A. G. Wong-Foy, A. J. Matzger, *J. Am. Chem. Soc,* **2009**, *131*, 4184. (c) D. Zhao, D. Yuan, D. Sun, H. C. Zhou, *J. Am. Chem. Soc.* **2009**, *131*, 9186. (d) H. Furukawa, N. Ko, Y. B. Go, N. Aratani, S. B. Choi, E. Choi, A. O. Yazaydin, R. Q. Snurr, M. O'Keeffe, J. Kim, O. M. Yaghi, *Science* **2010**, *329*, 427. (e) L. Ma, C. Abney, W. Lin, *Chem. Soc. Rev.* **2009**, *38,* 1248. (f) O. R. Evans, H. L. Ngo, W. Lin, *J. Am. Chem. Soc.* **2001**, *123*, 10395.

10. (a) D. Yuan, D. Zhao, D. Sun, H.-C. Zhou, *Angew. Chem., Int. Ed.* **2010**, *49*, 5357. (b) S. Q. Ma, D. F. Sun, M. Ambrogio, J. A. Fillinger, S. Parkin, H. C. Zhou, *J. Am. Chem. Soc.* **2007**, *129*, 1858. (c) B. Chen, M. Eddaoudi, S. T. Hyde, M. O'Keeffe, O. M. Yaghi, *Science* **2001**, *291*, 1021. (d) K. Koh, A. G. Wong-Foy, A. J. Matzger, *J. Am. Chem. Soc.* **2009**, *131*, 4184. (e)

H. Furukawa, N. Ko, Y. B. Go, N. Aratani, S. B. Choi, E. Choi, A. O. Yazaydin, R. Q. Snurr, M. O'Keeffe, J. Kim, O. M. Yaghi, *Science* **2010**, *329*, 424. (f) A. G. Wong-Foy, O. Lebel, A. J. Matzger, *J. Am. Chem. Soc.* **2007**, *129*, 15740. (g) X. Lin, J. Jia, P. Hubberstey, M. Schröder, N. R. Champness, *CrystEngComm* **2007**, *9*, 438.

11. (a) R. Banerjee, H. Furukawa, D. Britt, C. Knobler, M. O'Keeffe, O. M. Yaghi, *J. Am. Chem. Soc.* **2009**, *131*, 3875. (b**)** A. Blomqvist, C. M. Araujo, P. Srepusharawoot, R. Ahuja, *PNAS.* **2007**, *104,* 20173. (c) Z. Li, G. Zhu, G. Lu, S. Qiu, X. Yao, *J. Am. Chem. Soc.* **2010**, *132*, 1490. (d) J.-R. Li, R. J. Kuppler, H.-C. Zhou, *Chem. Soc. Rev.* **2009**, *38*, 1477. (e) Y.-S. Bae, O. K. Farha, A. M. Spokoyny, C. A. Mirkin, J. T. Hupp, R. Q. Snurr, *Chem. Commun.* **2008**, 4135. (f) Y.-S. Bae, O. K. Farha, J. T. Hupp, R. Q. Snurr, *J. Mater. Chem.* **2009**, *19*, 2131. (g) M. Dinca, A. Dailly, Y. Liu, C. M. Brown, D. A. Neumann, J. R. Long, *J. Am. Chem. Soc.* **2006**, *128,* 16876. (h) K. Sumida, S. Horike, S. S. Kaye, Z. R. Herm, W. L. Queen, C. M. Brown, F. Grandjean, G. J. Long, A. Dailly, J. R. Long, *Chem. Sci.* **2010**, *1,* 184. (i) M. Dinca, A. Dailly, C. Tsay, J. R. Long, *Inorg. Chem.* **2008**, *47,* 11. (j) Y.-S. Bae, K. L. Mulfort, H. Frost, P. Ryan, S. Punnathanam, L. J. Broadbelt, J. T. Hupp, R. Q. Snurr, *Langmuir* **2008**, *24*, 8592. (k) H. J. Choi, M. Dinca, A. Dailly, J. R. Long, *Energy Environ. Sci.* **2010**, *3,* 117.

12. (a) B. Chen, N. W. Ockwig, A. R. Millward, D. S. Contreras, O. M. Yaghi, *Angew. Chem. Int. Ed.* **2005**, *44*, 4745. (b) S. S.-Y. Chui, S. M.-F. Lo, J. P. H. Charmant, A. G. Orpen, I. D. Williams, *Inorg. Chem. Commun.,* **1999***, 283*, 1148. (c) J. R. Karra, K. S. Walton, *Langmui***r 2008***, 24*, 8620. (d) K. Schlichte, T. Kratzke, S. Kaskel, *Microporous Mesoporous Mater.* **2004***, 73*, 81. (e) C. Prestipino, L. Regli, J. G. Vitillo, F. Bonino, D. C. Lamberti, A. Zecchina, P. L. Solari, K. O. Kongshaug, S. Bordiga, *Chem. Mater.* **2006***, 18*, 1337. (f) N. L. Rosi, J. Kim, M. Eddaoudi, B. L. Chen, M. O'Keeffe, O. M. Yaghi, *J. Am. Chem. Soc.* **2005***, 127*, 1504. (g) P. D. C. Dietzel, Y. Morita, R. Blom, H. Fjellvag, *Angew. Chem., Int. Ed.* **2005***, 44*, 6354. (h) P. D. C. Dietzel, B. Panella, M. Hirscher, R. Blom, H. Fjellvag, *Chem. Commun.* **2006**, 959. (i) S. R. Caskey, A. G. Wong-Foy, A. J. Matzger, *J. Am. Chem. Soc.* **2008***, 130*, 10870.

13. (a) S. Couck, J. F. M. Denayer, G. V. Baron, T. Remy, J. Gascon, F. Kapteijn, *J. Am. Chem. Soc.* **2009**, *131*, 6326. (b) Z. Chen, S. Xiang, H. D. Arman, P. Li, S. Tidrow, D. Zhao, B. Chen, *Eur. J. Inorg. Chem.* **2010**, 3745. (c) T. Panda, P. Pachfule, Y. Chen, J. Jiang, R. Banerjee, *Chem. Commun.* **2011**, *47*, 2011. (d) F. Debatin, A. Thomas, A. Kelling, N. Hedin, Z. Bacsik, I. Senkovska, S. Kaskel, M. Junginger, H. Muller, U. Schilde, C. Jager, A. Friedrich, H.-J. Holdt, *Angew. Chem., Int. Ed.* **2010**, *49*, 1258. (e) J. An, S. J. Geib, N. L. Rosi, *J. Am. Chem. Soc.* **2010**, 132, 38. (f) R. Vaidhyanathan, S. S. Iremonger, K. W. Dawson, G. K. H.

Shimizu, *Chem. Commun.* **2009**, 5230. (g) B. Arstad, H. Fjellvag, K. O. Kongshaug, O. Swang, R. Blom, *Adsorption* **2008**, *14*, 755. (h) P. D. C. Dietzel, V. Besikiotis, R. Blom, *J. Mater. Chem.*, **2009**, *19*, 7362. (i) J.-B. Lin, J.-P. Zhang, X.-M. Chen, *J. Am. Chem. Soc.* **2010**, *132*, 6654. (j) A. Torrisi, R. G. Bell, Mellot- C. Draznieks, *Cryst. Growth Des.* **2010**, *10*, 2839. (k) A. Demessence, D. M. D'Alessandro, M. L. Foo, J. R. Long, *J. Am. Chem. Soc.* **2009**, *131*, 8784. (l) A. Sayari, Y. Belmabkhout, *J. Am. Chem. Soc.*, **2010**, *132*, 6312. (m) X. Gu, Z.–H. Lu, Q. Xu, *Chem. Commun.* **2010**, *46*, 7400. (n) A. O. Yazaydin, R. Q. Snurr, T.-H. Park, K. Koh, J. Liu, M. D. LeVan, A. I. Benin, P. Jakubczak, M. Lanuza, D. B. Galloway, J. J. Low, R. R. Willis, *J. Am. Chem. Soc.* **2009**, *131*, 18198. (o) J. An, R. P. Fiorella, S. J. Geib, N. L. Rosi, *J. Am. Chem. Soc.* **2009**, *131*, 8401.

14. (a) O. Hubner, A. Gloss, M. Fichtner, W. Klopper, *J. Phys. Chem. A* **2004**, *108*, 3019. (b) T. Yildirim, M. R. Hartman, *Phys. Rev. Lett.* **2005**, *95*, 215504. (c) V. K. Peterson, Y. Liu, C. M. Brown, C. J. Kepert, *J. Am. Chem. Soc.* **2007**, *128*, 15578. (d) J. L. C. Rowsell, J. Eckert, O. M. Yaghi, *J. Am. Chem. Soc.* **2005**, *127*, 14904. (e) Y. Liu, C. M. Brown, D. A. Neumann, V. K. Peterson, C. J. Kepert, *J. Alloys Compd.* **2007**, *446–447*, 385. (f) M. R. Hartman, V. K. Peterson, Y. Liu, S. S. Kaye, J. R. Long, *Chem. Mater.* **2006**, *18*, 3221. (g) H. Wu, W. Zhou, T. Yildirim, *J. Am. Chem. Soc.* **2007**, *129*, 5314.

15. (a) C. Yang, X. Wang, M. A. Omary, *J. Am. Chem. Soc.* **2007**, *129,* 15454. (b) L. Pan, M. B. Sander, X. Huang, J. Li, M. Smith, E. Bittner, B. Bockrath, J. K. Johnson, *J. Am. Chem. Soc.* **2004**, *126,* 1308. (c) R. A. Fischer, C. Woll, *Angew. Chem., Int. Ed.*, **2008**, *47,* 8164. (d) C. Yang, X. P. Wang, M. A. Omary, *Angew. Chem., Int. Ed.* **2009**, *48*, 2500. (e) Z. Hulvey, D. A. Sava, J. Eckert, A. K. Cheetham, *Inorg. Chem.* **2011,** *50*, 403. (f) Z. Hulvey, E. H. L. Falcao, J. Eckert, A. K. Cheetham, *J. Mater. Chem.* **2009**, *19,* 4307. (g) C. A. Fernandez, P. K. Thallapally, R. K. Motkuri, S. K. Nune, J. C. Sumrak, J. Tian, J. Liu, *Cryst. Growth Des.* **2010**, *10,* 1037. (h) W. Yang, X. Lin, A. J.;Blake, C. Wilson, P. Hubberstey, N. R. Champness, M. Schroder, *Inorg. Chem.* **2009**, *48,* 11067.

16. (a) P. Pachfule, Y. Chen, J. Jiang, R. Banerjee, *Chem. Eur. J.*, **2012**, *18*, 688. (b) P. Pachfule, R. Das, P. Poddar, R. Banerjee, *Inorg. Chem.,* **2011**, *50*, 3855. (c) P. Pachfule, R. Das, P. Poddar, R. Banerjee, *Cryst. Growth & Design*, **2011**, *11*, 1215. (d) P. Pachfule, C. Dey, T. Panda, K. Vanka, R. Banerjee, *Cryst*. *Growth & Design*, **2010**, *10*, 1351. (e) P. Pachfule, C. Dey, T. Panda, R. Banerjee, *CrystEnggComm*, **2010**, *12,* 1600. (f) P. Pachfule, Y. Chen, S. C. Sahoo, J. Jiang, R. Banerjee, *Chem. Mater.*, **2011**, *23*, 2908.

17. Chun, H.; Dybtsev, D. N.; Kim, H.; Kim. K. *Chem. Eur. J.* **2005**, *11,* 3521.

18. (a) Z. P. Demko, K. B. Sharpless, *Angew. Chem., Int. Ed.*, **2002**, 41, 2110. (b) Z. P. Demko, K. B. Sharpless, *J. Org. Chem.*, **2001**, 66, 7945. (c) Z. P. Demko, K. B. Sharpless, *Angew. Chem., Int. Ed.*, **2002**, 41, 2113.

19. (a) J. J. Perry IV; J. A. Perman, M. J. Zaworotko, *Chem. Soc. Rev.*, **2009**, 38, 1400. (b) F. Nouar, J. F. Eubank, T. Bousquet, L. Wojtas, M. J. Zaworotko, M. Eddaoudi, *J. Am. Chem. Soc.*, **2008**, 130, 1833. (c) M. H. Alkordi, J. A. Brant, L. Wojtas, V. Ch. Kravtsov, A. J. Cairns, M. Eddaoudi, *J. Am. Chem. Soc.*, **2009**, 131, 17753.

20. (a) A. L. Gavrilova, B. Bosnich, *Chem. Rev.*, **2004**, *104*, 3553. (b) J. P. Zhang, X. M. Chen, *Chem. Commun.*, **2006**, 1689. (c) M. Dinca, A. F. Yu, J. R. Long, *J. Am. Chem. Soc.*, **2006**, *128*, 8904. (d) K. S. Park, Z. Ni, A. P. Cote, J. Y. Choi, R. Huang, F. J. Uribe-Romo, H. K. Chae, M. O'Keeffe, O. M. Yaghi, *Proc. Natl. Acad. Sci. U. S. A.*, **2006**, *103*, 10186. (e) H. Hagashi, A. P. Cote, H. Furukawa, M. O'Keeffe, O. M. Yaghi, *Nat. Mater.*, **2007**, *6,* 501. (f) M. Dinca, A. Dailly, J. R. Long, *Chem.–Eur. J.*, **2008**, *14*, 10280. (g) M. Dinca, A. Dailly, Y. Liu, C. M. Brown, D. A. Neumann, J. R. Long, *J. Am. Chem. Soc.*, **2006**, *128*, 16876.

21. The experimental pattern of Cu-TBA-1 has a few diffraction lines that are unindexed and some that are slightly broadened in comparison with those simulated patterns. This is probably due to the loss of either DMF or EtOH molecules from the lattice or phase change due to grinding while analysis.

22. (a) D. J. Collins, H.-C. Zhou, *J. Mater. Chem.* **2007**, *17*, 3154. (b) D. Sun, S. Ma, Y. Ke, D. J. Collins, H.-C. Zhou, *J. Am. Chem. Soc.* **2006**, *128*, 3896. (c) M. Kondo, M. Shimamura, S.-I. Noro, S. Minakoshi, A. Asami, K. Seki, S. Kitagawa, *Chem. Mater.* **2000**, *12*, 1288. (d) S. Bourrelly, P. L. Llewellyn, C. Serre, F. Millange, T. Loiseau, G. Ferey, *J. Am. Chem. Soc.* **2005**, *127*, 13519. (e) T. Dueren, L. Sarkisov, O. M. Yaghi, R. Q. Snurr, *Langmuir* **2004**, *20*, 2683. (f) X. Zhao, B. Xiao, A. J. Fletcher, K. M. Thomas, D. Bradshaw, M. J. Rosseinsky, *Science* **2004**, *306*, 1012. (g) B. Panella, M. Hirscher, *Ad*V. *Mater*. **2005**, *17*, 538. (h) D. W. Breck, *Zeolite molecular sieves*: John Wiley and Sons: New York, **1974**. (i) J. Wegrzyn, M. Gurevich, *Appl. Energy.* **1996**, *55*, 71. (j) S. Ma, D. Sun, J. M. Simmons, C. D. Collier, D. Yuan, H.-C. Zhou, *J. Am. Chem. Soc.* **2008**, *130*, 1012. (k) J. L. C. Rowsell, O. M. Yaghi, *Angew. Chem., Int. Ed.* **2005**, *44*, 4670.

23. (a) B. L. Chen, S. Q. Ma, E. J. Hurtado, E. B. Lobkovsky, H. C. Zhou, *Inorg. Chem.* **2007**, *46*, 8490. (b) B. L. Chen, C. D. Liang, J. Yang, D. S. Contreras, Y. L. Clancy, E. B. Lobkovsky, O. M. Yaghi, S. Dai, *Angew. Chem., Int. Ed.* **2006**, *45*, 1390. (c) D. Zhao, D. Yuan, H.-C. Zhou, *Energy Environ. Sci.* **2008**, *1*, 222. (d) K. S. Park, Z. Ni, A. P. Cote, J. Y. Choi, R. D. Huang, F.

J. Uribe-Romo, H. K. Chae, M. O'Keeffe, O. M. Yaghi, *Proc. Natl. Acad. Sci. U. S. A*. **2006**, *103*, 10186. (e) W. Zhou, H. Wu, M. R. Hartman, T. Yildirim, *J. Phys. Chem. C,* **2007**, *111*, 16131. (f) A. G. Wong-Foy, A. J. Matzger, O. M. Yaghi, *J. Am. Chem. Soc.* **2006**, *128*, 3494. (g) J. L. C. Rowsell, O. M. Yaghi, *J. Am. Chem. Soc.* **2006**, *128*, 1304. (h) A. Dailly, J. J. Vajo, C. C. Ahn, *J. Phys. Chem. B* **2006**, *110*, 1099.

24. *SMART, Version 5.05*; Bruker AXS, Inc.: Madison, Wisconsin, **1998**.

25. Bruker **(2004)**. *SAINT-Plus* (Version 7.03). Bruker AXS Inc., Madison, Wisconsin, USA.

26. G. M. Sheldrick, **(2002)**. *SADABS* (Version 2.03) and *TWINABS* (Version 1.02).University of Göttingen, Germany.

27. G. M. Sheldrick, **(1997)**. *SHELXS '97*. University of Göttingen, Germany.

28. G. M. Sheldrick, **(1997)**. *SHELXTL '97*. University of Göttingen, Germany.

29. A. L. Spek, **(2005)**. PLATON, *A Multipurpose Crystallographic Tool*, Utrecht University, Utrecht, The Netherlands.

30. Materials Studio, v., Accelrys: San Diego, **2007**.

31. R. F. Cracknell, *Phys. Chem. Chem. Phys.* **2001**, *3*, 2091.

32. A. K. Rappe, C. J. Casewit, K. S. Colwell, W. A. Goddard, W. M. Skiff, *J. Am. Chem. Soc.* **1992**, *114*, 10024.

33. M. Koyama, N. Ohtani, F. Kai, I. Moriguchi, S. Inouye, *J. Med. Chem.* **1987**, *30*, 552.

34. We replaced the 2-F-4-TBA with 3-F-4-TBA, which is the 3-substituted fluorinated analogue of 4-TBA. The reaction of 3-F-4-TBA with $Cu(NO_3)_2$ was resulted into the formation of plate like blue crystals similar to Cu-TBA-2 and Cu-TBA-2F. But in this case, we are unable to grow proper sized crystals for single crystal X-Ray Diffraction studies after several attempts. The formation of same phase like Cu-TBA-2 and Cu-TBA-2F was confirmed by PXRD studies in the case of Cu-TBA-3F.

Memorandum

The results of this chapter have already been published in *Chemistry of Materials*, **2011**, *23*, 2908–2916; with the title: "Structural Isomerism and Effect of Fluorination on Gas Adsorption in Copper-Tetrazolate Based Metal Organic Frameworks".

This publication was the result of collaboration between the group of Dr. Rahul Banerjee and his students Pradip Pachfule, Subash Chandra Sahoo from the Physical/Materials Chemistry Division at CSIR-National Chemical Laboratory in Pune, India and the group of Prof. Dr. Jianwen Jiang with his student Yifei Chen from the National University of Singapore, 117576 Singapore. Prof. Dr. Jianwen Jiang with his student Yifei Chen have actively contributed to the publication by performing computational studies on MOFs. Subash Sahoo helped for single crystal X-ray diffraction data collection and analyses.

Pradip Pachfule was involved in the preparation of MOFs, characterization of MOFs which includes Single crystal X-ray diffraction studies, PXRD, FT-IR, TGA, NMR, Gas adsorption studies. Finally figure preparation and draft writing was carried out by him under the guidance of Dr. Rahul Banerjee.

Chapter 4

Functionalized Interpenetrated Metal Organic Frameworks (MOFs) for Reversible Hydrogen (H_2) Uptake

4.1 Introduction:

The decreasing amount of fossil fuels and increasing warning of global warming due to the pollutant emissions from traditional energy sources like coal, natural gas, gasoline, etc. have driven the search for clean energy sources like solar, wind and geothermal power sources.[1] Although, Department of Energy (DoE) has launched the Hydrogen Fuel Initiative project, the commercialization of hydrogen powered vehicles still remains a challenge as it is difficult to create a technology for on board hydrogen storage due to complications in H_2 storage systems.[2] As a result, energy sources from fossil fuels still remains in the forefront despite being a major source of increased CO_2 content in the atmosphere.[3] Due to these reasons, the capture and storage of CO_2 emitted from coal fired power plants and vehicle exhausts has also emerged as another major research area, wherein materials having physisorptive adsorption of CO_2 are mostly preffered.[4] The currently employed carbon capture method from flue gas involves alkanolamine based solvents that act as CO_2 absorber by formation of N–C bonded carbamate species.[5] Amine regeneration requires cleavage of this covalent bond by heating (at 100 to 150 °C) and has high operational cost. In these regards, MOFs have emerged as promising materials for H_2 storage and CO_2 sequestration due to its completely physisorptive adsorption behaviour.[6] Several factors influencing the gravimetric H_2 uptake of porous MOFs such as surface area, catenation, ligand functionalization, doping with alkali metals and unsaturated metal centers have been extensively studied in order to achieve the elevated H_2 uptake.[7] In other efforts, CO_2 uptake in amine-functionalized porous solids like zeolitic materials, mesoporous silica, porous carbon, etc. has also been tried since long time.[8] As these materials have the lack of order, large voids, flexible amine groups, and random adsorption sites, the CO_2 adsorption is unfeasible due to undefined and random gas adsorption sites. In contrary, well defined periodicity and tunable pore sizes along with less basic amino functional

groups ($–NH_2$) in MOFs enables them as a favorable candidate for fast and reversible CO_2 gas adsorption at low partial pressure and room temperature.[9] In previous reported examples of amino functionalized MOFs, it has been showed that these MOFs can perform better for selective and reversible CO_2 adsorption at very low heat of adsorption range.[10]

In these regards, although many successful strategies exist towards the design of MOFs for simultaneous high CO_2 and H_2 uptake, there are only a handful of MOFs reported that can do both the jobs efficiently.[11] Several researchers studied the phenomenon of interpenetration (or catenation) in MOFs for high H_2 uptake[12,7] and amino-functionalization for high CO_2 uptake separately.[9,10] As a result, each time a separate MOF becomes necessary to achieve these both H_2 and CO_2 uptake efficiently. There are very limited reports available in literature for the MOFs, wherein single MOFs can perform both these functions efficiently as a result of their intrinsic structural magnificence. This will not only minimize the efforts to synthesize various MOFs but also emerge as one of the effective strategy for the utilization of any MOF for multiple applications. In view of all these aspects, any MOF having interpenetrated structure with free functional groups like $–NH_2$, –CONH-, etc. will be the best choice to achieve both H_2 and CO_2 uptake in same MOF material.[13] In former case interpenetration in MOFs can show high adsorption of H_2 and in later case amino functionalization in MOFs can show high CO_2 uptake at very low pressure range. To achieve these functionalized interpenetrated MOFs, the organic linker with rigid structure and free functional groups can emerge as best choice, since the MOFs derived from these pyridine carboxylate linkers usually forms the porous structures, with or without interpenetration. The considerably high length (~9 Å) of these pyridine carboxylate linkers favors the MOFs with gas/solvent accessible pores or channels, which motivated us to use these linkers for MOF synthesis.

In these regard, we have selected 2-amino-isonicotinic acid (2-amino-4-pyridylcarboxylic acid) as an organic linker having free $–NH_2$ groups on its backbone due to its rigid structure with sufficient length and capability to form fascinating coordination modes (*Figure 4.1*). The longer backbone length of organic linkers favors the formation of interpenetrated framework after reaction with transition metal in

suitable solvent.[7i,7j] In addition to the interpenetrated framework in these MOFs, free functional groups (here, $-NH_2$ groups) present on the linker restrict the higher degree of interpenetration in resulting MOFs.[14] The partially or doubly interpenetrated MOFs

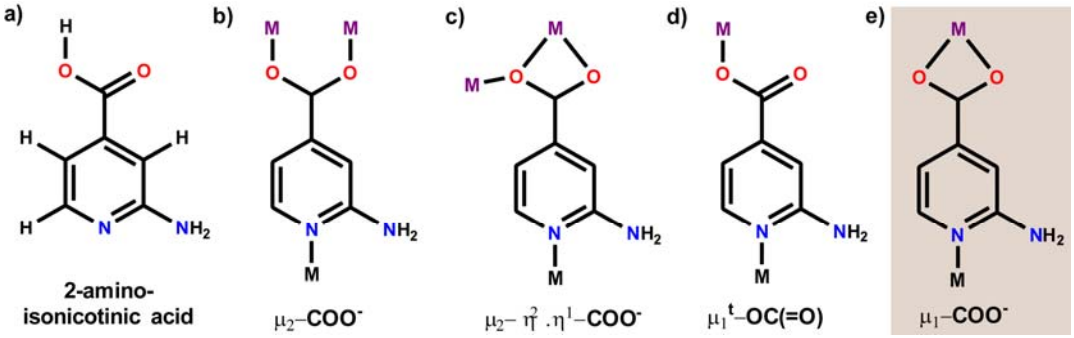

Figure 4.1 (a) Structure of 2-amino-isonicotinic acid and (b), (c), (d) and (e) commonly observed coordination modes in 2-amino-isonicotinic acid linker.

having porous structures with free amine groups into its backbone poking into the pore, may be ideal candidate for simultaneously high H_2 and CO_2 uptake in same MOF.[15] In this context, using 2-amino-isonicotinic acid (ANIC) linker, we report the blending of amino-functionalization and interpenetration in two isostructural porous MOFs having diamondoid (*dia*) topology for simultaneous high H_2 and CO_2 uptake. As a result of long backbone length of ANIC linker, the formation of the partially interpenetrated structure of MOFs, in the midst of pore size of ~3.9 Å with free amine groups into the backbone was achieved.

4.2 Interpenetration/catenation in MOFs:

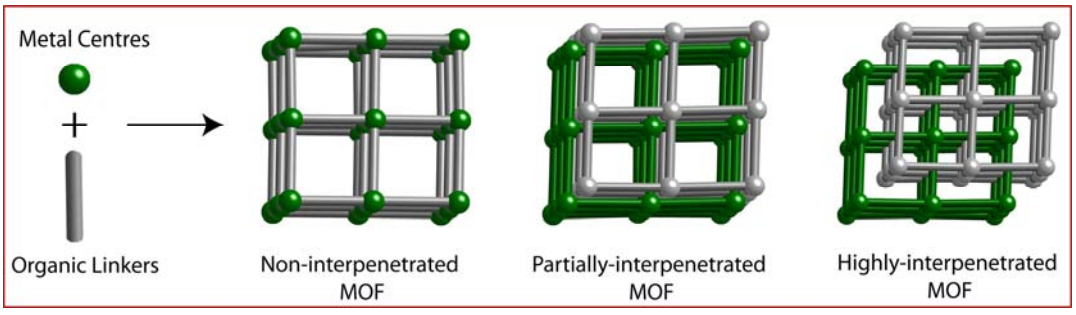

Figure 4.2 Schematic representations of non-interpenetrated and interpenetrated MOFs depending on the degree on interpenetration. The individual MOF nets are showed in green and grey colors for visualization.

The ongoing attempts for the overall increase in the H_2 uptake properties of MOFs

includes the creating exposed/open metal sites, functionalization with organic groups, catenation/interpenetration, spillover, doping of metal nanoparticles, etc.[7] From the literature reports, it is clear that very large pores within MOFs are ultimately unfavorable to H_2 storage.[7a,11e] Since, H_2 molecules near the center of the pore are unlikely to experience any attraction from the potential surface of the pore walls, small sized pores with availability of large number of adsorption sites are recommended for high H_2 uptake in MOFs.[7i,7j] Although, for improved H_2 uptake in MOFs, the methods followed like functionalization and creation of open metal sites were fruitful to some extent; the partial or doubly interpenetrated MOFs having pore sizes fitable to the kinetic diameter of H_2 showed very high uptake, at very low coverage (*Figure 4.2*). Framework interpenetration, by which the pores of one framework are inter-grown by one or more independent frameworks, is a commonly observed phenomenon in MOFs (*Figure 4.2*).[16] While it may be a negative phenomenon from the surface area point of view, because it significantly reduces the available void space; the interpenetration bears positive effects, including enhanced framework stability, increased heat of adsorption, and size selectivity.[7] The studies on the adsorption of small molecules (such as H_2, CH_4, O_2, etc.) by microporous interpenetrated MOFs pioneered the successful utilization of these MOFs for gas uptake. It was believed that favorable interactions exist between aromatic rings of MOFs and H_2 molecules. Since, microporous interpenetrated MOFs would be ideal candidates for the sorption of small gaseous molecules, interpenetration can be utilized to strengthen the interaction between the gaseous molecule and the framework by an entrapment mechanism, in which a hydrogen molecule is in close proximity with several aromatic rings from interpenetrating networks.[16] In addition to the experimental results, from the computational outcomes, it is clear that a large micropore volume composed of small voids is more desirable for an efficient storage.[7j] Ideally, a material with interpenetrated frameworks (or partial interpenetration), but still exhibiting a moderate surface area would adsorb H_2 more strongly as well as in high amount. Although, interpenetration can reduce the pore size of MOFs increasing the micropore volume, which helps to improve the H_2 uptake significantly; the higher degree of interpenetration can reduce the pore size drastically creating the non-porous MOFs. Thus, in order to improve the H_2

uptake in MOFs, partially interpenetrated or interpenetrated MOFs with pore sizes higher than kinetic diameter of H_2 are favorable (*Figure 4.2*).

In MOFs, it is possible to reduce the number of large voids conceivably in a given structure *via* framework interpenetration. Although, in synthetic manner, it is extremely difficult to control the interpenetration, which further leads to the formation of non-porous MOFs (*Figure 4.2*); the small pores formed *via* partial or sometimes two, three or four fold interpenetration shows the ability to adsorb the H_2 in large quantity. The 0.6 wt% improvement in H_2 storage achieved in interpenetrated MOF PCN-6 as compared to its non-interpenetrated counterpart PCN-6' showed the advantages of framework interpenetration for improved H_2 uptake in MOFs (*Figure 4.3*).[7b] In such cases, MOFs having smaller pore diameters show moderately stronger adsorbent−adsorbate interactions, leading towards the uptake improvement.[17] Hypothetically, one should expect that the surface area for an interpenetrated framework will be reduced relative to its non-interpenetrated analogue, owing to the framework–framework interactions that should arise upon desolvation. But, in practical aspects, catenation can sometimes lend a material enhanced thermal stability, reducing the degree of framework collapse during desolvation.[18] The recent calculations on interpenetrated MOFs suggest that the amount of H_2 adsorbed correlates with the heat of adsorption only at low loadings, and surface area as well as total free volume become more important at intermediate and high loadings, respectively. So, in order to seize the extra advantage of framework interpenetration, for improved H_2 uptake in amino functionalized MOFs, herein we have synthesized the MOFs having partial interpenetrated framework with moderate porosity. The H_2 and CO_2 uptake properties of these MOFs have been studied experimentally as well as computationally.

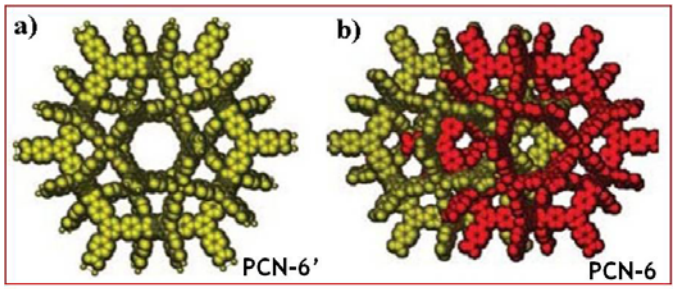

Figure 4.3 (a) Space-filling model of the non-interpenetrated net in PCN-6′; (b) two interpenetrated nets in PCN-6 forming interpenetrated MOF structure (Adopted with permission from XX). [Reprinted with permission from (7b). Copyright 2007 American Chemical Society].

4.3 Result and Discussion:

4.3.1 Synthesis of MOFs:

The rational design and appropriate use of the characteristic ligands is critical in the construction of the desired MOFs. Among various organic ligands, multidentate *N*- or *O*-donor ligands such as pyridine or pyrazine-carboxylic acids have drawn extensive attention in the construction of coordination polymers owing to their versatile coordination modes and structural stability. Pyridyl carboxylic acids with various functional groups on its backbone are especially useful in this regard, but the exploitation of the ligands in the construction of open framework materials is still in its infancy. The anions of these acids may bond to metal centers via their *N*- and *O*-donor atoms. Thus, one would expect higher flexibility and more versatile coordination modes compared to the original ligand (*Figure 4.1*). Furthermore, the separation of the bridging sites is definitely larger, which can further induce the interpenetration into resulting MOFs. However, studies on such ligand behavior towards coordination polymers are limited, and only a few transition metal-, lanthanide metal-, and main group metal-based coordination polymers incorporating pyridyl carboxylic acid have been structurally examined.[19] By the successful employment of pyridine carboxylate (nicotinic acid, isonicotinic acid, etc.) as multifunctional ligands a variety of MOFs with diverse topologies and interesting properties have been obtained. However, compared with other pyridine based acids, 4-pyridine carboxylate derived organic linkers having functional groups (*Figure 4.1*) are rarely employed as a linkage ligand. In an attempt to address this point, we have introduced an effective strategy to synthesize the interpenetrated MOFs with functional groups, in which the 2-amino isonicotinic acid is used to construct a basic skeleton. The advantages of having both interpenetration and functional groups in same MOF structure for higher H_2 and CO_2 uptake can be achieved by judicial selection of organic linker 2-amino isonicotinic acid for the MOF synthesis.

4.3.2 Crystal Structure Description.

Crystal structure of Cd-ANIC-1 and Co-ANIC-1:

Single crystal X-ray diffraction studies reveal that isostructural Cd-ANIC-1 and Co-ANIC-1 crystallizes in F*ddd* Space Group with octahedral Cd or Co secondary building units (SBUs) linked by ANIC linkers (*Figure 4.4*). Four O atoms from two μ_2-CO_2^-

functionality and two N atoms of two unidentate pyridyl groups provide the four connecting nodes resulting in an adamantanoid unit (*Figure 4.5*). The distance between two Cd(II) metal centers is determined by the length of ANIC ligands (9.1 Å). In Cd-ANIC-1, each Cd(II) centre is coordinated to four ANIC links in octahedral geometry, which are in turn bound to four other Cd(II) centers (See *Table 4.2* for more structural details).

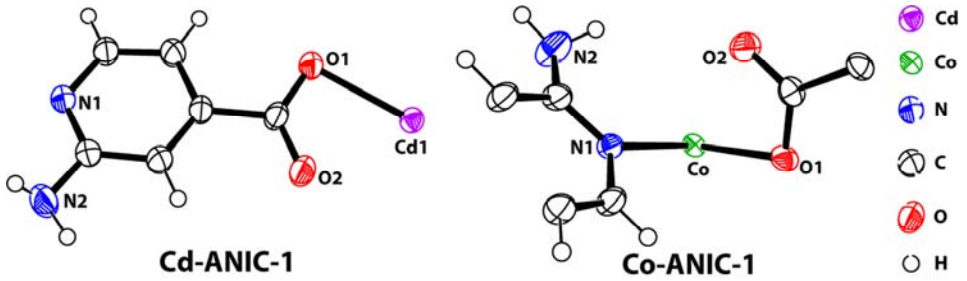

Figure 4.4 ORTEP diagrams of Cd-ANIC-1 and Co-ANIC-1 at 50 % probability factor showing coordination of linkers with metal centers.

The three-dimensional structure of Cd-ANIC-1 and Co-ANIC-1 (*Figure 4.5c-4.5f*) builds through the formation of edge-sharing adamantoid units. The single adamantoid cage consists of 10 Cd(II) or Co(II) ions and 12 ANIC ligands. Figure 4.5c–4.5f shows the interpenetration within the MOF structure with two independent equivalent networks (twofold interpenetration) (*Figure 4.6*). The separation between adjacent adamantoid cages is further controlled by N–H•••O hydrogen bonding (*D*, 3.0 Å; *d*, 2.2 Å; θ_1, 116.3°) between the sets of ANIC carboxylate oxygen atoms and $–NH_2$ group present on the organic linkers. Hydrogen bonding[20] interaction is clearly important in the overall control of this extended structure and the presence of this interaction along the direction in which the adamantoid cages propagate. Due to the two fold interpenetration, pore size decreases from the dimensions of 5.4 Å × 5.4 Å to 3.9 Å × 3.9 Å (*Figure 4.5f*). Although, the reason for Cd-ANIC-1 and Co-ANIC-1 adopting the diamondoid (*dia)* topology is not very clear to us; probably L–M–L angle is responsible for the creation of *dia* topology into the framework (L, ANIC linker; M, Cd/Co metal centers). There are three types (out of 18) of L–M–L angles present in the adamantanoid cage, each 6 being 138.9º, 99.7º and 94.4º. The angles between each corners of the hexagonal circuit (99.7º and 94.4º) are less than angles at the middle (138.9º). Overall, moderately porous Cd-ANIC-1 and Co-ANIC-1 MOFs with

considerable solvent accessible voids, free functional groups and partially interpenetrated networks has been isolated. These kind of porous functionalized frameworks with partially interpenetrated nets and *dia* topology are very rare in literature and structurally interesting.

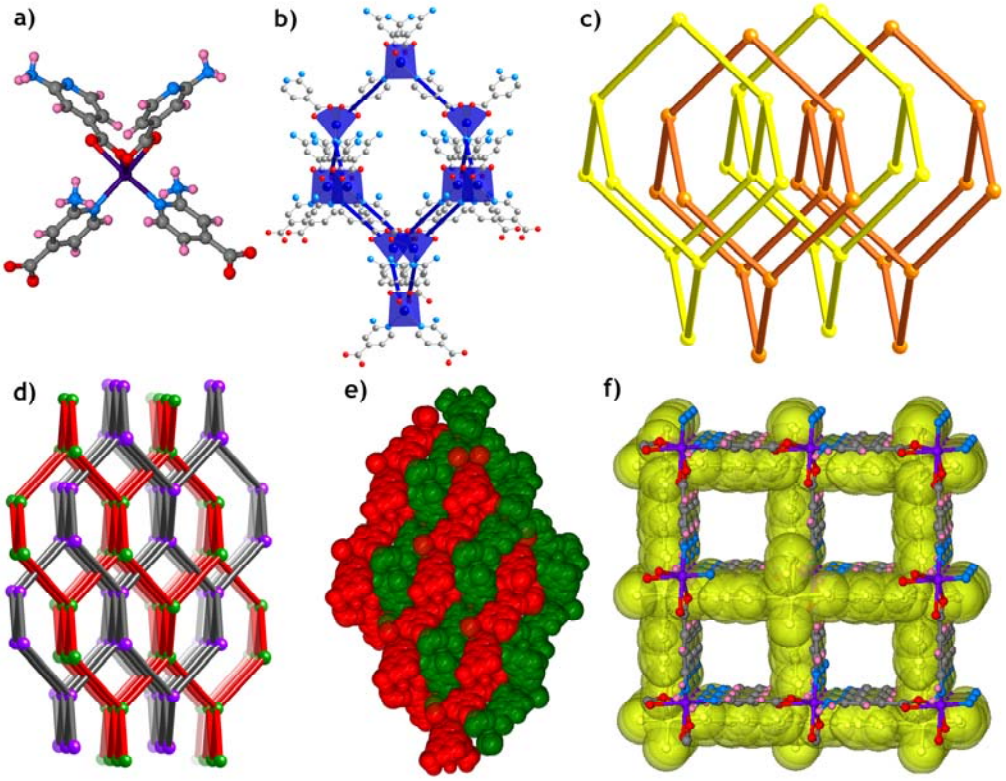

Figure 4.5 Crystal structures of Cd-ANIC-1 and Co-ANIC-1. (a) Octahedral SBU in Cd-ANIC-1 and Co-ANIC-1, where each octahedral Cd(II) or Co(II) metal is connected to two $\mu 2$-OCO carboxylate groups and two nitrogen atoms from ANIC ligand. (b) A single adamantanoid cage of Cd-ANIC-1 and Co-ANIC-1. (c) Interpenetrated adamantanoid cages in Cd-ANIC-1 and Co-ANIC-1. (d) A topological representation of the two fold interpenetration in Cd-ANIC-1, where red and grey lines represents the ligands and green and violet balls represents the metal centers. (e) Formation of the interpenetrated framework in Cd-ANIC-1 and Co-ANIC-1, where separate green and red colored layers are interweaving to form the interpenetrated framework through *c* axis. (f) Packing diagram of Cd-ANIC-1 and Co-ANIC-1, where each layer is distinguished in space filling (yellow) and ball and stick models showing two fold interpenetrating frameworks through *a* axis. (Color code: Cd: violet, O: red, H: pink, N: light blue, C: grey). [Reprinted with permission from (15). Copyright 2011 Royal Society of Chemistry].

The structure of Co-ANIC-1 is isostructural with Cd-ANIC-1 except shorter M–M distance (Co–Co = 8.85 Å) and smaller L–M–L angles (137.5º, 98.8º and 96.2º) compared to Cd-ANIC-1. Solvent accessible volume in Cd-ANIC-1 (38.2 %) is higher

compared to Co-ANIC-1 (36.3 %) as the degree of interpenetration is less in the former compound. As discussed earlier, less M–M distance, more distance between two independent interweaving layers and smaller L–M–L angles, increases the degree of interpenetration in Co-ANIC-1 resulting into the pores of the dimensions 3.7 × 3.7 Å.

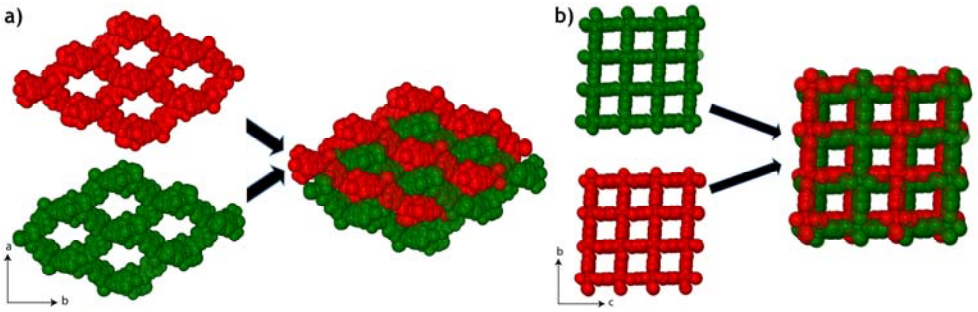

Figure 4.6 Formation of the interpenetrated framework in Cd-ANIC-1 and Co-ANIC-1, where separate green and red colored layers are interweaving to form the interpenetrated framework through (a) *c* axis, and (b) *a* axis.

4.3.3 Discussion on Crystal Structures.

The closer structural analysis of these MOF structures depicts the presence of only μ_1-CO_2^- coordination mode selectively, although these pyridine carboxylate linkers can show several coordination modes (*Figure 4.1*). The crystal structure of Cd-ANIC-1 and Co-ANIC-1 show one-dimensional channels of 3.9 × 3.9 Å and 3.7 × 3.7 Å running through *a* axis, respectively. These channels present in these structures are densely lined by free $–NH_2$ groups, which usually show high affinity towards the adsorbing CO_2 molecules. Since, these MOFs have the free amino groups and two fold interpenetrated framework structure, the pore size is lower as compared to the non-interpenetrated and non-functionalized isonicotinic acid based MOFs. Although, we have used the transition metals Co(II) and Cd(II) for MOF synthesis, the electronic factors of these metals affects the M–L–M distances and angles (M = Cd and Co; L= ANIC) to large extent. This change in metal to metal distances further influence on the pore sizes in the resulting MOFs.

The crystalline MOFs have currently attracted considerable attention because of their enormous variety of fascinating structural topologies through self-organization and great potential applications as functional solid materials. Especially, some MOFs with the *dia* topology that are usually assembled by the copolymerization of 4-connected

mononuclear metal-carboxylate SBUs with organic linkers have been synthesized. In the case of Cd-ANIC-1 and Co-ANIC-1, we have observed very rare *dia* topology as a result of coordination behavior of polyatomic ANIC linkers. Most surprisingly, as shown in figure 4.5b, 4.5c, 4.5d and 4.6a, we have successfully isolated the two fold interpenetrated, amino functionalized MOFs with *dia* topology, which is obviously very rare in the literature.

4.3.4 Thermal properties, X-ray powder diffraction and FT-IR analyses:

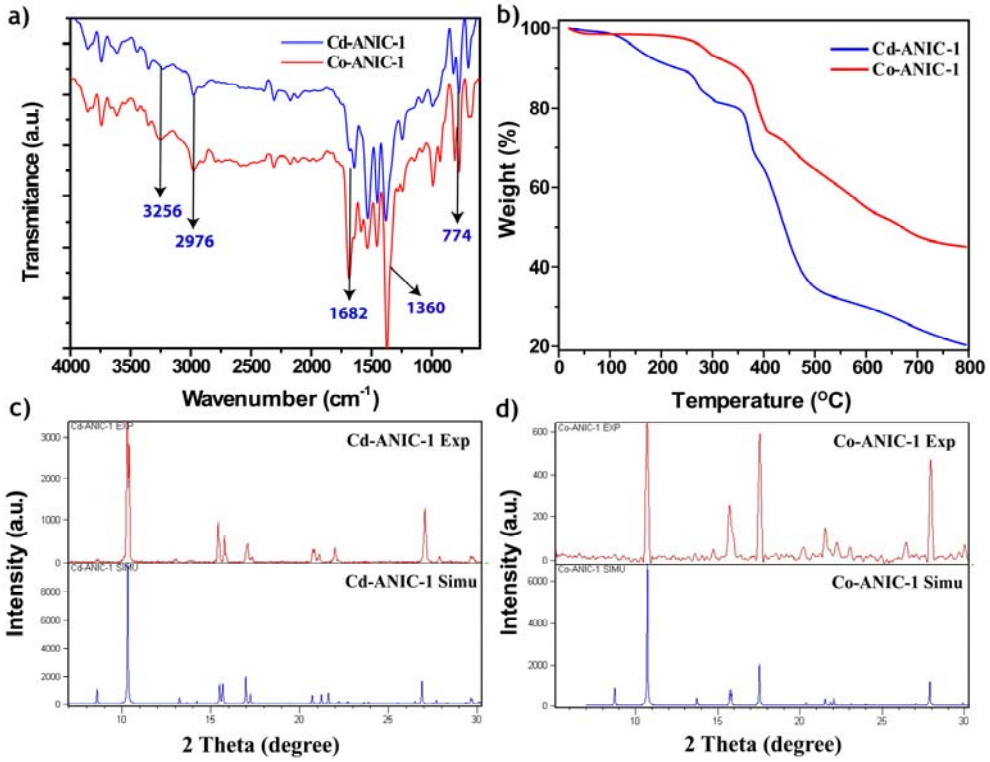

Figure 4.7 Characterizations of Cd-ANIC-1 and Co-ANIC-1. (a) IR absorption spectrums of Cd-ANIC-1 (blue) and Co-ANIC-1 (red). IR stretching indicates the presence of uncoordinated $–NH_2$ functionality in the MOFs. (b) Thermal stability and the thermal gravimetric analysis (TGA) data of Cd-ANIC-1 and Co-ANIC-1. (c) Comparison of the experimental PXRD pattern of as-synthesized Cd-ANIC-1 (top) with the one simulated from its single crystal structure (bottom). (d) Comparison of the experimental PXRD pattern of as-synthesized Co-ANIC-1 (top) with the one simulated from its single crystal structure (bottom).

In the purpose to analyze the framework architecture and thermal stability of Cd-ANIC-1 and Co-ANIC-1, we have examined the thermal gravimetric analyses (TGA) of these samples. From TGA, it was revealed that these compounds have high thermal stability. The TGA traces for as synthesized Cd-ANIC-1 and Co-ANIC-1 showed a

gradual weight-loss step of 9.5 % (20–200 °C), 4.75 % (20–200 °C), respectively; corresponding to escape of solvent of crystallization present in pores (*Figure 4.7b*). This is followed by a sharp weight loss (270–390 °C) probably due to the decomposition of the framework. The TGA trace of Cd-ANIC-1 indicates the loss of solvent molecules in the range of 20–200 °C in 2 steps. The first weight loss step of ~2.5 % occurring at 20–90 °C is possibly due to removal of ethanol molecules from the framework as this temperature. Following to this weight loss in Cd-ANIC-1, a weight loss of ~7.0 % is possibly due to removal of higher boiling DMF molecules. Similarly, in case of Co-ANIC-1 also first solvent removal steps of ~3.0 % has been observed, which may arise due to removal of ethanol molecules at temperature range 20–90 °C. Following to this, the weight loss observed may be due to the removal of DMF molecules.

Further, powder X-ray diffraction (PXRD) analyses of Cd-ANIC-1 and Co-ANIC-1 performed to confirm the phase purity of the bulk samples show the formation of phase pure MOF samples. All major peaks of experimental PXRDs match well with simulated PXRDs, indicating their reasonable crystalline phase purity (*Figure 4.7c and 4.7d*). Also the PXRD patterns of the solvent exchanged and the activated samples show the crystallinity and the retention of the framework. The presence of strong characteristic peaks for $-NH_2$ groups (~3256 cm^{-1}) in addition to the other featured starching and bending assignments in MOFs proves the presence of free $-NH_2$ groups in the MOF structure (*Figure 4.7a*).

4.4 Gas Adsorption Properties:

4.4.1 Experimental Results:

Although, the Cd-ANIC-1 and Co-ANIC-1 are formed by the interweaving of the two nets, these MOFs are still porous, with solvent-accessible void of 38.2 % and 36.3 % as calculated using PLATON.[31] Prior to gas sorption experiments, guest (DMF and ethanol) solvent molecules are removed by solvent exchange (1:1 mixture of CH_2Cl_2: MeOH) followed by thermal activation at an optimized temperature of 120 °C, for 48 h. Compounds Cd-ANIC-1 and Co-ANIC-1 exhibit permanent porosity, which has been confirmed by nitrogen gas sorption isotherms collected at 77 K and 1 atm pressure. The N_2 adsorption isotherm of Cd-ANIC-1 (*Figure 4.8a*) indicates typical Type-I sorption behavior, with a Langmuir and BET surface area of 504 m^2/g and 329 m^2/g,

respectively. The Co-ANIC-1, on the other hand has a lower Langmuir and BET surface area of 412 m^2/g and 274 m^2/g, respectively.

Table 4.1 Gas uptake properties of MOFs reported in this chapter collected at 1 atm pressure.[a,b]

Name of MOF	Surface Area (m^2/g)		H_2 uptake (77 K) (Wt %)	CO_2 uptake (mmol/g)	
	BET	Langmuir		273 K	298 K
Cd-ANIC-1	329.3	504.9	1.84	4.72	3.84
Co-ANIC-1	274.0	412.6	1.64	4.22	3.48

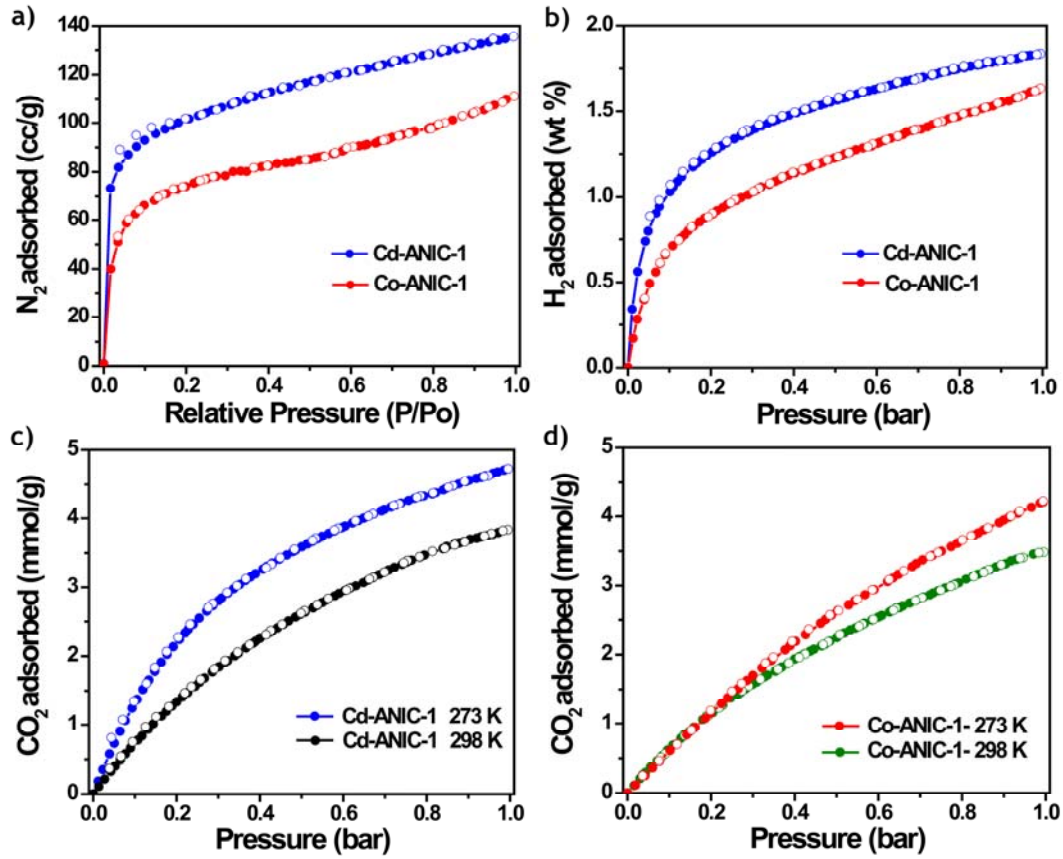

Figure 4.8 Gas adsorption isotherms of Cd-ANIC-1 and Co-ANIC-1. (a) N_2 adsorption isotherms for Cd-ANIC-1 (blue circles) and Co-ANIC-1 (red circles) at 77 K and 1 atm pressure. (b) H_2 adsorption isotherms for Cd-ANIC-1 (blue circles) and Co-ANIC-1 (red circles) at 77 K. (c) CO_2 adsorption isotherms for Cd-ANIC-1 at 273 K (blue circles) and 298 K (black circles). (d) CO_2 adsorption isotherms for Co-ANIC-1 at 273 K (red circles) and 298 K (green circles). The filled and open circles represent adsorption and desorption, respectively. [Reprinted with permission from (15). Copyright 2011 Royal Society of Chemistry].

Several researchers proposed and proved that rather than a number of extremely large pores, a larger number of small pores which closely "*fit*" the dihydrogen molecule are most favorable for adsorption.[21] Catenation or interpenetration divides the large pores into smaller ones and has the ability of increasing surface area to pore volume ratio and the overall stability of the network along with increased hydrogen adsorption capacity.[7, 12, 21] It has been previously reported that, porous interpenetrated MOFs like IRMOF-9,[7e] IRMOF-13,[7e] PCN-6,[7b] etc. outperform the non-interpenetrated ones regarding the H_2 adsorption properties. This fact motivated us to check the H_2 uptake for Cd-ANIC-1 and Co-ANIC-1. The activated samples of Cd-ANIC-1 and Co-ANIC-1 show typical Type-I H_2 adsorption isotherm at 77 K temperature, with steep rise at very low pressure. As expected, the Cd-ANIC-1 shows the H_2 adsorption nearly 1.84 wt% at 1 atm pressure, which is higher than the Co-ANIC-1 (1.64 wt% of H_2 adsorption) at same conditions (*Figure 4.8b*). These adsorption capacities are well justified as these MOFs have the interpenetrated frameworks with suitable pores for H_2 adsorption. Also from the previous reports and theoretical calculations, it was confirmed that the porous MOFs having free $–NH_2$ groups, can adsorb large amount of CO_2 at room temperature.[9,10] The pores of Cd-ANIC-1 and Co-ANIC-1 are densely lined with basic amino functionality (*Figure 4.5*). This feature prompted us to examine the CO_2 adsorption properties. We firstly collected the CO_2 isotherm at 273 K and later at 298 K. For Cd-ANIC-1, the isotherm is completely reversible, exhibits a steep rise at low pressures, and reaches a maximum of 4.72 mmol/g (273 K) and 3.84 mmol/g (298 K) as pressure reach to the 1 bar (*Figure 4.8*). Also Co-ANIC-1 shows similar behavior like Cd-ANIC-1, with 4.22 mmol/g (273 K) and 3.48 mmol/g (298 K) CO_2 uptake at 1 bar pressure (*Figure 4.8*). Again these results are well anticipated as free $–NH_2$ groups can drastically increase the CO_2 adsorption capacities at ambient temperature. Pores present into interpenetrated Cd-ANIC-1 and Co-ANIC-1 allow dihydrogen molecule to interact with multiple portions of the framework rather than just one SBU or organic linker, increasing the interaction energy between the framework and H_2. This increased interaction between adsorbing gas molecules and framework ingredients like SBU, linkers, etc. results into the improvement in isosteric heat (Q_{st}) of H_2 adsorption giving high uptake at low pressure.

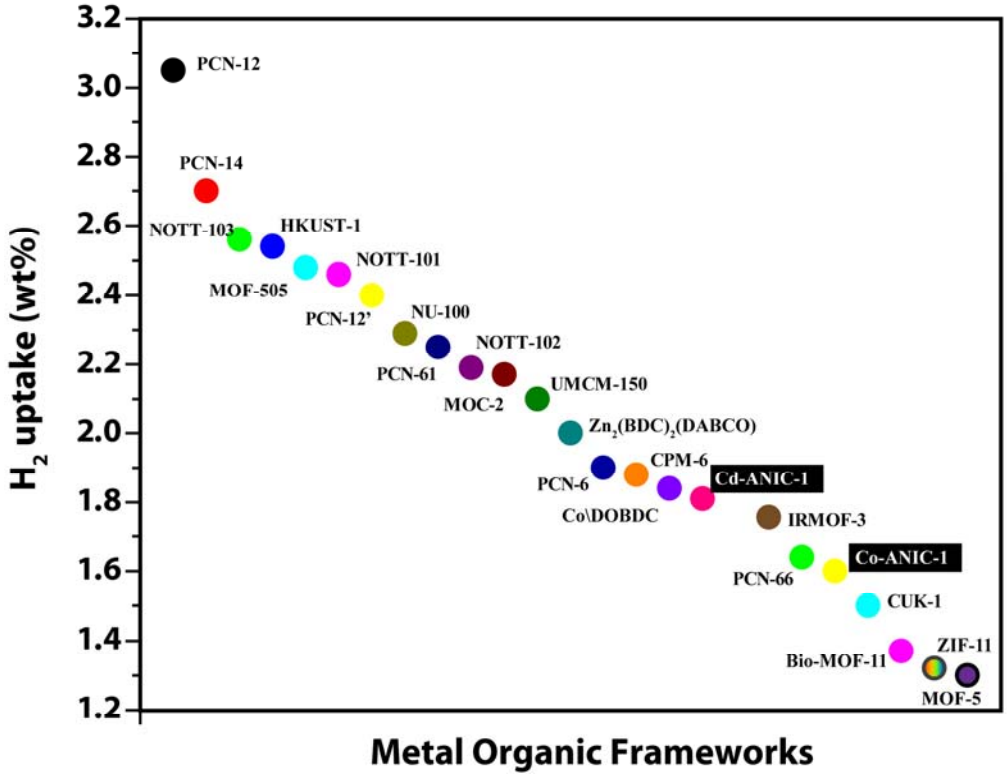

Figure 4.9 Comparison of H_2 adsorption capacity of literature reported MOFs with Cd-ANIC-1 and Co-ANIC-1. H_2 uptake data collected at 77 K and 1atm pressure is represented here.

As discussed earlier, the H_2 adsorption capacity of Cd-ANIC-1 and Co-ANIC-1 is greatly enhanced by the interpenetrating framework and comparable pore size with H_2 molecule. The recent experimental and computational studies have demonstrated that the smaller pore size and multiplicity of networks allows the dihydrogen molecule to interact with the central phenyl rings and functional group of multiple linkers present therein, thus increasing the relevance of the non-coordinating portion of the ligand to H_2 storage.[7] Both experimental and computational studies performed for Cd-ANIC-1 and Co-ANIC-1 agree that interpenetrated networks present into MOFs along with functional groups are responsible for high H_2 uptake. The H_2 adsorption capacity of Cd-ANIC-1 at 1 bar pressure is comparable to the previously reported MOFs like Co\DOBDC,[7g] CPM-6,[11d] PCN-68,[17] PCN-66,[22a] IRMOF-3,[7h] and outperforms some well known MOFs and ZIFs like ZTF-1,[22b] Zn-DOBDC,[7g] Bio-MOF-1,[22c] MOF-177,[11a] ZIF-11[6d] and ZIF-8[22d] (*Figure 4.9*).

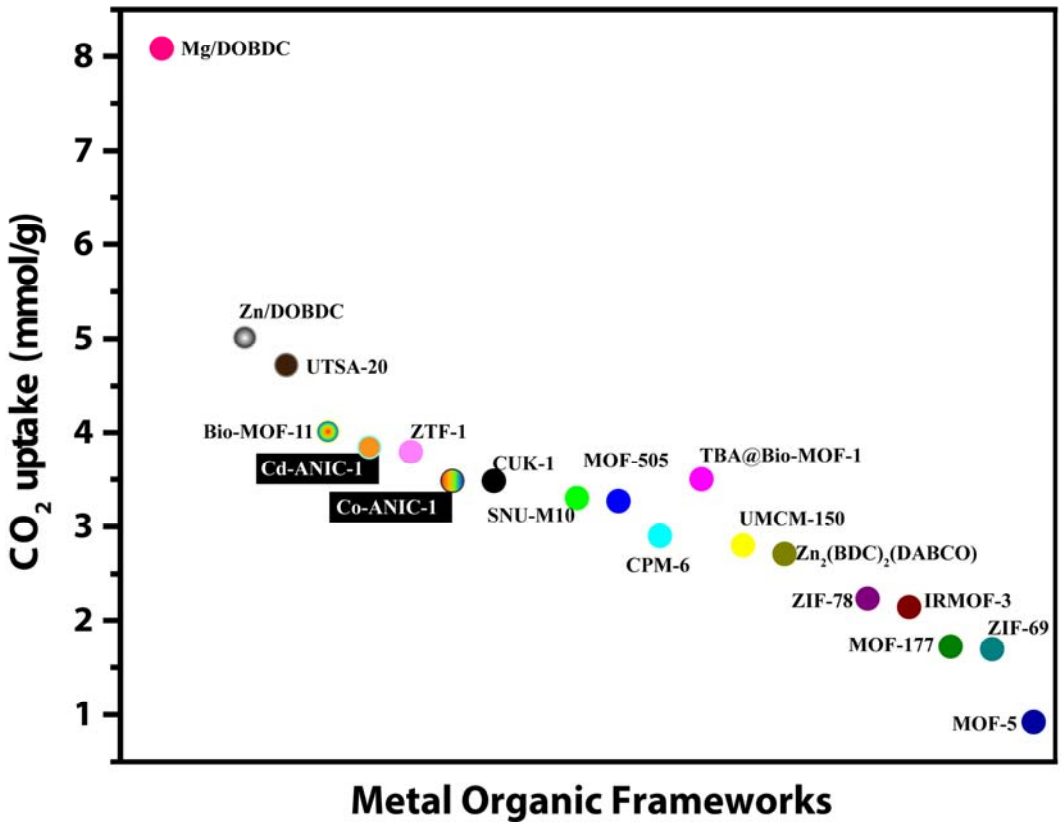

Figure 4.10 Comparison of CO_2 adsorption capacity of literature reported MOFs with Cd-ANIC-1 and Co-ANIC-1. CO_2 uptake data collected at 298 K and 1atm pressure is represented here.

Also, CO_2 adsorption capacity at 298 K and 1 bar pressure for Cd-ANIC-1 is higher than ZTF-1, $Zn_2(C_2O_4)(C_2N_4H_3)_2$. $(H_2O)_{0.5}$,[23a] MOF-505,[7c] $(In_3O)(OH)$ $(ADC)_2$ $(NH_2IN)_2$. $2.67H_2O$,[9j] CPM-6, TMA@ Bio-MOF-1,[11d] UMCM-150,[11c] IRMOF-3, MOF-177 and ZIFs like ZIF-78,[6c] -96,[23c] -69.[6c] (*Figure 4.10*). Although, MOFs like PCN-12,[23d] –14,[23e] –11, –10, –6,[12b] HKUST-1,[10b] Cu_2(tptc),[23f] NOTT-103,[23h] –100,[23h] –140, –101,[23h] –105,[23h] UTSA-20,[23h] NU-100,[21c] MOF-505,[23f] $Cu_6O(tzi)_3(NO_3)$,[23i] UMCM-150, Ni/DOBDC,[7g] Zn_2(BDC)(TMBDC)(DABCO),[11e] $Ni_3(BTC)_2(3\text{-PIC})_6(PD)_3$,[23e] Mg\DOBDC,[7g] etc. outperforms the Cd-ANIC-1 in H_2 adsorption at aforementioned pressure and MOFs like Mg\DOBDC, Co\DOBDC, Ni\DOBDC, Zn\DOBDC, UTSA-20, HKUST-1, Bio-MOF-1, $Zn_3(OH)$(*p*-CDC)$_{2.5}$,[22e] etc. outperforms the same in terms of their CO_2 uptake, only few MOFs like Ni\DOBDC, UTSA-20, HKUST-1 and Mg\DOBDC withstands higher H_2 as well as CO_2 adsorption capacity over Cd-ANIC-1

(*Figure 4.11*).

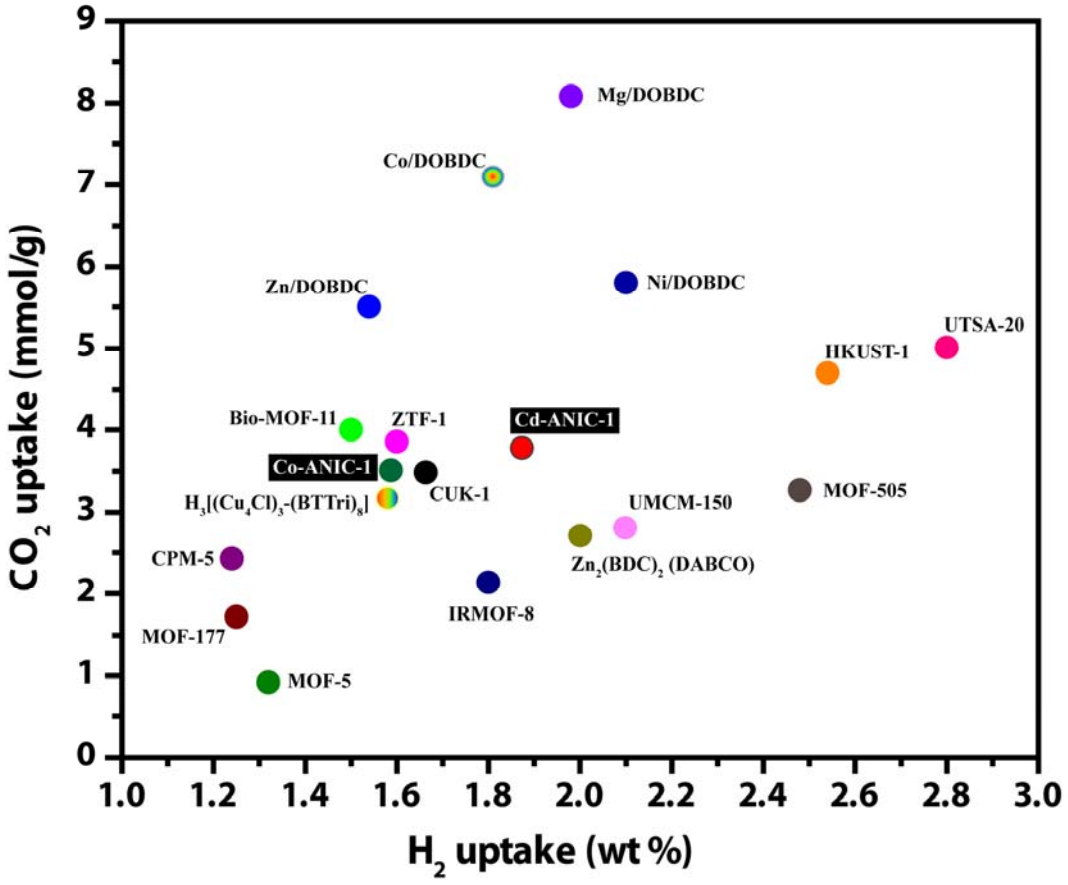

Figure 4.11 Plot of H_2 uptake (X axis) and CO_2 uptake (Y axis) in literature reported MOFs with comparison to Cd-ANIC-1 and Co-ANIC showing the utility of functionalized interpenetrated MOFs for subsequent H_2 and CO_2 uptake. The represented H_2 and CO2 uptake data is collected at 77 K and 298 K, respectively; at 1 atm pressure.

High H_2 adsorption by the interpenetration or CO_2 adsorption by $–NH_2$ functionalization previously achieved by MOFs only stands better in separate cases. But in the case of Cd-ANIC-1 and Co-ANIC-1 by the blending of interpenetration and $–NH_2$ functionalization, we could successfully achieve a significantly high H_2 and CO_2 uptake despite the limited surface area of these MOFs. Since, Cd-ANIC-1 and Co-ANIC-1 have the low surface area; we acknowledge that high pressure H_2 and CO_2 uptake could be moderate. But this particular work implies that, it is possible to blend interpenetration and amino functionalization in one MOF, which successfully impose their individual effect enhancing both H_2 and CO_2 uptake.

4.4.2 Computational/Theoretical Results:

Figure 4.12 shows the comparison between experimental and simulated H_2 and CO_2 adsorption isotherms for Cd-ANIC-1 and Co-ANIC-1 at 77 K and 298 K, respectively. The simulated results of H_2 agree fairly well with the experimental data in both Cd-ANIC-1 and Co-ANIC-1 structures. However, the simulated results of CO_2 are overestimated at low pressures and underestimated at high pressures. For both H_2 and CO_2, the extent of adsorption in Cd-ANIC-1 is greater than in Co-ANIC-1, because the former has a larger porosity as confirmed from single crystal structure and porosity studies using gas adsorption as well as Materials Studio software.[24]

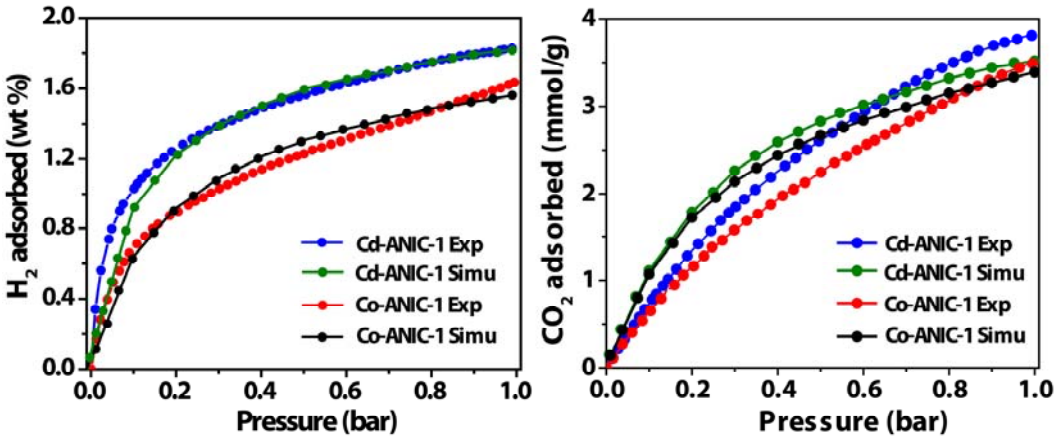

Figure 4.12 Comparison between experimental and simulated adsorption isotherms in Cd-ANIC-1 and Co-ANIC-1 (a) H_2 at 77 K; (b) CO_2 at 298 K. (Desorption branches for isotherms has been removed for clarity).

As mentioned earlier these deviations in experimental and simulated gas uptake properties could be attributed to a number of possible factors as:

a. The framework structures used in simulations are perfect crystals without any defects; however, experimental samples usually contain impurities.

b. Activation of experimental samples may not be complete and solvent is not fully evacuated.

c. The force field used may be inaccurate to describe the interactions.

Figure 4.13d shows the density contours of H_2 adsorption at 77 K and 1 kPa in Cd-ANIC-1 and Cd-ANIC-1. The contours are viewed from the [100] plane and generated by accumulating 100 equilibrium configurations. It is observed that H_2 molecules are

primarily adsorbed in pore centers in both Cd-ANIC-1 and Cd-ANIC-1. The density contours for CO_2 adsorption also shows similar results like those observed in the case of H_2 adsorption studies.

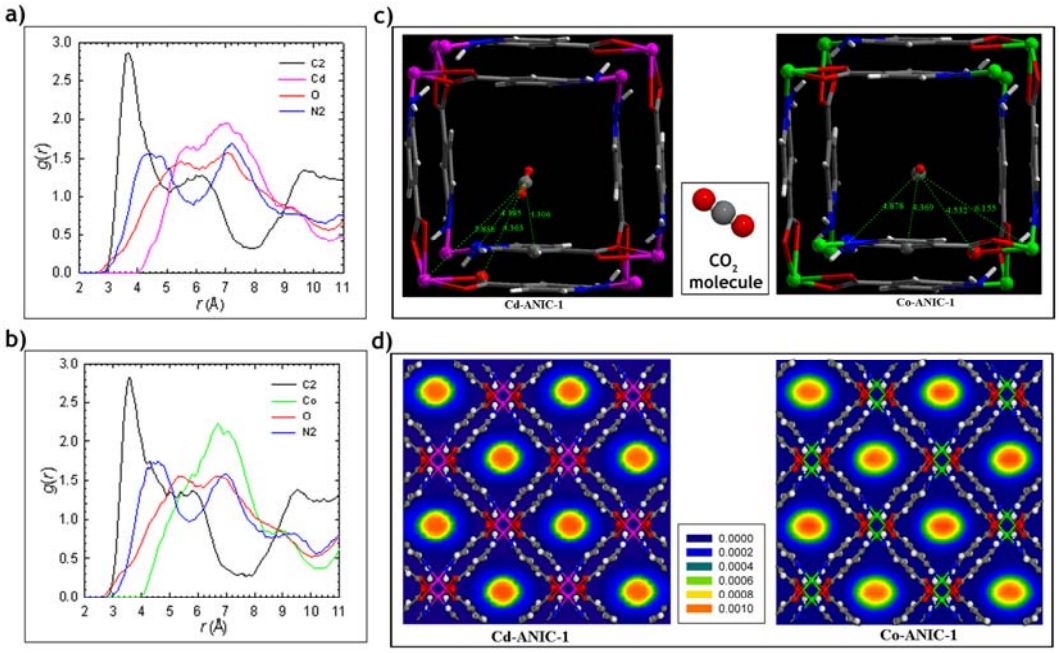

Figure 4.13 Computational results for Cd-ANIC-1 and Co-ANIC-1. (a) and (b) Radial distribution functions for Cd-ANIC-1 and Co-ANIC-1, respectively. (c) Distances between CO_2 and framework atoms (C2, Cd/Co, O, N2) in Cd-ANIC-1 and Co-ANIC-1, respectively. (d) Density contours of H_2 adsorption at 1 kPa in Cd-ANIC-1 and Co-ANIC-1, respectively. [Reprinted with permission from (15). Copyright 2011 Royal Society of Chemistry].

To better understand the nature of adsorption sites, we have performed further simulations using single crystal X-ray diffraction derived structures of Cd-ANIC-1 and Co-ANIC-1. Figure 4.13a shows the radial distribution functions $g(r)$ between CO_2 and the framework atoms (C2, Cd, O, N2) in Cd-ANIC-1.[24] The $g(r)$ was calculated by,

$$g_{ij}(r) = \frac{\Delta N_{ij}\, V}{4\pi r^2 \Delta r\, N_i N_j}$$

Where, r is the distance between species i and j, ΔN_{ij} is the number of species j around i within a shell from r to $r + \Delta r$, V is the volume, N_i and N_j are the numbers of species i and j. It is observed CO_2 is the closest to C2 atom and the $g(r)$ of CO_2–C2 has the highest peak. This reveals that phenyl ring has the strongest affinity with CO_2 because

of the framework interpenetration. CO_2 is closer to N2 atom than to Cd and O atoms, implying $–NH_2$ group plays a more important role than Cd and O atoms for CO_2 adsorption. Figure 4.13c schematically shows the distances between a single CO_2 molecule and the framework atoms. Figure 4.13a and 4.13b shows the radial distribution functions and distances between CO_2 and the framework atoms (C2, Co, O, N2) in Co-ANIC-1. Similar to figure 4.13c and 4.13d, CO_2 is the closest to C2 atom, followed by N2 atom, and finally O and Co atoms. Again, this suggests CO_2 is preferentially adsorbed near phenyl ring and then $–NH_2$ group.

These overall experimental and computational studies performed suggest the advantages of framework interpenetration and functionalization for H_2 uptake studies. The partial interpenetrated frameworks of Cd-ANIC-1 and Co-ANIC-1 having moderate porosity, where higher degree of interpenetration is controlled by hydrogen bonding between functional groups and oxygen atoms from carboxylate groups show high uptake of H_2 as well as CO_2 at 77 K and 298 K, respectively. The combined effect of interpenetration and presence of functional groups on H_2 uptake demonstrate the utility of these kinds of porous materials for H_2.

4.5 Conclusions:

In conclusion, we have successfully achieved isolation of the interpenetrated, porous, functionalized MOFs with diamondoid topology that shows high H_2 uptake. The two fold interpenetrated structures of Cd-ANIC-1 and Co-ANIC-1 have one dimensional channels of dimensions 3.9 Å × 3.9 Å and 3.7 Å × 3.7 Å running through *a* axis, respectively. The higher degree of interpenetration in these structures is probably restricted due to the N–H•••O hydrogen bonding present between free $–NH_2$ groups and oxygen atoms of the ANIC linkers. By the successful utilization of functionalized organic linker ANIC, for the first time, we have isolated the porous amino functionalized and interpenetrated MOFs having *dia* topology.

Cd-ANIC-1 and Co-ANIC-1 have high H_2 and CO_2 adsorption capacities which outperform previously reported well known MOFs and ZIFs. We attribute these favorable H2 and CO_2 adsorption properties to the presence of the Lewis basic amino groups of 2-amino-4-pyridine carboxylic acid and interpenetrated frameworks in Cd-ANIC-1 and Co-ANIC-1. Specially, as other amino functionalized MOFs and ZIFs lack the high H_2 adsorption, we could successfully achieve high H_2 adsorption as well, which is contributed by interpenetration in the frameworks of Cd-ANIC-1 and Co-ANIC-1. H_2 and CO_2 adsorption in Cd-ANIC-1 and Co-ANIC-1 have also been validated by simulations, which show good agreement with experimental data. Collectively, these results points towards the discovery of new materials with functionalized interpenetrated frameworks synthesized from a simple isonicotinic acid derived link for high H_2 and CO_2 adsorption capacities.

4.6 Experimental Materials and Methods:

4.6.1 General Procedures:

All reagents and solvents for synthesis and analysis were commercially available and used as received. 2-amino-4-pyridylcarboxylic acid (2-amino-isonicotinic acid) was purchased from Alfa Aesar and $Cd(NO_3)_2.4H_2O$, $Co(NO_3)_2.6H_2O$ were purchased from Aldrich Chemicals. *N*,*N*-dimethylformamide (DMF) was purchased from Rankem chemicals. All starting materials were used without further purification. All experimental operations were performed in air and all the stock solutions were prepared in *N*,*N*-dimethylformamide (DMF). The Fourier transform (FT) IR spectra were taken on a Bruker Optics ALPHA-E spectrometer with a universal Zn-Se ATR accessory in the 600–4000 cm^{-1} region. Powder X-ray diffraction (PXRD) patterns and insitu variable temperature PXRD (VT-PXRD) were recorded on a Phillips PANalytical diffractometer for Cu K_α radiation (λ = 1.5406 Å), with a scan speed of 2° min^{-1} and a step size of 0.02° in 2θ. Thermo-gravimetric experiments (TGA) were carried out in the temperature range of 20–800 °C on a SDT Q600 TG-DTA analyzer under N_2 atmosphere at a heating rate of 10 °C min^{-1}. All low pressure gas adsorption experiments (up to 1 bar) were performed on a Quantachrome Quadrasorb automatic volumetric instrument.

4.6.2 Single Crystal X-Ray Diffraction Methods:

Single crystal data were collected on Bruker SMART APEX three circle diffractometer equipped with a CCD area detector and operated at 1500 W power (50 kV, 30 mA) to generate Mo-K_α radiation (λ=0.71073 Å). The incident X-ray beam was focused and monochromated using Bruker Excalibur Gobel mirror optics. Crystals of all Cd-ANIC-1 and Co-ANIC-1 reported in the paper was mounted on nylon Cryo-Loop (Hampton Research) with Paraton-N (Hampton Research). Initial scans of each specimen were performed to obtain preliminary unit cell parameters and to assess the mosaicity (breadth of spots between frames) of the crystal to select the required frame width for data collection. In every case frame widths of 0.5° were judged to be appropriate and full hemispheres of data were collected using the *Bruker SMART*[25] software suite. Following data collection, reflections were sampled from all regions of the Ewald sphere to re-determine unit cell parameters for data integration and to check for

rotational twinning using CELL_NOW.[26] Data were integrated using Bruker SAINT[27] software with a narrow frame algorithm and a 0.400 fractional lower limit of average intensity. Data were subsequently corrected for absorption by the program SADABS.[28] The space group determinations and tests for merohedral twinning were carried out using XPREP.[29] In these cases, the highest possible space group was chosen using WINGX.[30]

Table 4.2 Comparison of crystal data and structure refinement for Cd-ANIC-1 and Co-ANIC-1 MOFs.

MOFs	**Cd-ANIC-1**	**Co-ANIC-1**
Empirical formula	C12 H12 Cd N4 O4	C12 H10 Co N4 O4
Formula weight	388.67	333.17
Temperature	298(2) K	298(2) K
Wavelength	0.71073	0.71073
Crystal system	Orthorhombic	Orthorhombic
Space group	F*ddd*	F*ddd*
Unit cell dimensions	a = 12.869(5) Å, α = 90° b = 23.643(10) Å, β = 90° c = 24.900(11) Å, γ = 90°	a = 12.819(2) Å, α = 90° b = 23.058(4) Å, β = 90° c = 23.654(4) Å, γ = 90°
Volume	7576(5)	6992(2)
Z	16	16
Density (calculated)	1.363	1.266
Absorption coefficient	1.192	0.998
Goodness-of-fit on F^2	1.340	1.110
Final R indices [I>2sigma(I)]	R_1 = 0.0659, wR_2 = 0.1822	R_1 = 0.0335, wR_2 = 0.1087
R indices (all data)	R_1 = 0.0688, wR_2 = 0.1853	R_1 = 0.0437, wR_2 = 0.1108
CCDC No.	**822054**	**822055**

Structures were solved by direct methods and refined using the SHELXTL 97[29] software suite. Atoms were located from iterative examination of difference F-maps following least squares refinements of the earlier models. Final model was refined anisotropically (if the number of data permitted) until full convergence was achieved. Hydrogen atoms were placed in calculated positions (C–H = 0.93 Å) and included as

riding atoms with isotropic displacement parameters 1.2–1.5 times U_{eq} of the attached C atoms. Single Crystal X-ray Diffraction data for Cd-ANIC-1 and Co-ANIC-1 was collected at 298(2) K. Structures were examined using the ADDSYM[30] subroutine of PLATON[32] to assure that no additional symmetry could be applied to the models. All ellipsoids in ORTEP diagrams are displayed at the 50 % probability level unless noted otherwise (Figure 4.4). Table 4.2 contains crystallographic data for the Cd-ANIC-1 and Co-ANIC-1 MOFs. Crystallographic data (excluding structure factors) for the structures reported in this chapter have been deposited with the CCDC as deposition No. 822054 and 822055. Copies of the data can be obtained, free of charge, on application to the CCDC, 12 Union Road, Cambridge CB2 lEZ UK (fax: + 44 (1223) 336 033; E-mail: deposit@ccdc.cam.ac.uk).

4.6.3 Gas Adsorption Measurements:

Low pressure volumetric gas adsorption measurements involved in this work were performed at 77 K for H_2 and N_2, maintained by a liquid nitrogen bath, with pressures ranging from 0 to 760 Torr on Quantachrome Quadrasorb automatic volumetric instrument. While CO_2 adsorption measurements were done at 273 K and 293 K temperature with same pressures range. In the all adsorption measurements, ultra high-purity H_2 was obtained by using calcium aluminosilicate adsorbents to remove trace amounts of water and other impurities before introduction into the system. The micro crystals of each MOF were soaked in 1:1 dry dichloromethane and methanol mixture for 12 h. Fresh 1:1 dry dichloromethane and methanol mixture was subsequently added and the crystals were allowed to stay for additional 48 h to remove co-ordinated and free solvates (DMF and Ethanol) present in framework. The sample was dried under a dynamic vacuum ($<10^{-3}$ Torr) at room temperature overnight. Prior to gas sorption experiments, thermal activation at an optimized temperature of 120 °C, for 48 h has been done to remove co-ordinated and free solvates (DMF and Ethanol) present in framework.

4.6.4 Simulation Model and Methods:

Grand-canonical Monte Carlo (GCMC) simulations were carried for the adsorption of H_2 at 77 K and CO_2 at 273 and 298 K in Cd-ANIC-1 and Co-ANIC-1. H_2 was

represented as a two-site rigid molecule with H–H bond length of 0.74 Å. The Lennard-Jones parameters of H–H interaction were σ = 2.59 Å and ε = 12.5 K.[24a] CO_2 was represented as a three-site rigid molecule and its intrinsic quadrupole moment was described by a partial-charge model. The partial charges on C and O atoms were q_C = 0.576*e* and q_O = –0.288*e* (*e* = 1.602 $\times 10^{-19}$ is the elementary charge). The C–O bond length was 1.18 Å and the bond angle O–C–O was 180°. The LJ parameters for CO_2 were σ_C = 2.789 Å, ε_C = 29.66 K, σ_O = 3.011 Å, ε_O = 82.96 K.[24b] The experimentally determined crystal structures were used in simulations. The porosities of Cd-ANIC-1 and Co-ANIC-1 were estimated to be approximately 0.516 and 0.488 using Materials Studio[24c] with a Connolly probe radius equal to zero. The atomic charges of the framework atoms were calculated from periodic density functional theory (DFT) using the primitive cells of Cd-ANIC-1 and Co-ANIC-1. The DFT calculations used the Becke exchange plus Lee-Yang-Parr correlation functional and all-electron core potentials. The double-ξ numerical polarization (DNP) basis set was adopted. The Mulliken population analysis was used to estimate the atomic charges as listed in Table 4.4. The dispersion interactions of the framework atoms in Cd-ANIC-1 and Co-ANIC-1 were modeled using the parameters based on the DREIDING force field.[24d] However, the DREIDING force field parameters are not available for Cd and Co atoms; thus the parameters from the Universal force field were adopted.[24e] With these LJ parameters, the predicted isotherms were found not to agree well with experimental data. As a simple alternative, the parameters of carbon atoms were adjusted.

Table 4.3 LJ Potential parameters for the framework atoms in Cd-ANIC-1 and Co-ANIC-1.

Atom type	**Cd**	**Co**	**C *in* (Cd-ANIC-1)**	**C *in* (Co-ANIC-1)**	**O**	**N**	**H**
σ(Å)	2.537	2.559	3.473	3.473	3.033	3.263	2.846
ε/k_B (K)	114.631	7.039	40.813	32.813	48.115	38.914	7.642

Table 4.3 lists the set of LJ parameters used in this study. The Lorentz-Berthelot combining rules were used to calculate the cross LJ interaction parameters. In the GCMC simulations, the frameworks were treated as rigid and the adsorbent-adsorbate

interactions were pre-tabulated. The LJ interactions were evaluated using a spherical cutoff of 11.5 Å with the long-range corrections added. For the Coulombic interactions, the Ewald sum with a tin-foil boundary condition was used. The real/reciprocal space partition parameter and the cutoff for reciprocal lattice vectors were chosen to be 0.2 $Å^{-1}$ and 8, respectively, to ensure the convergence of the Ewald sum. Five types of trial moves were conducted for gas molecules, namely, displacement, rotation, partial re-growth at a neighboring position, complete re-growth at a new position, and swap with the reservoir. The number of trial moves in the simulation was 2×10^7 with the first 10^7 moves for equilibration and the subsequent 10^7 moves for production.

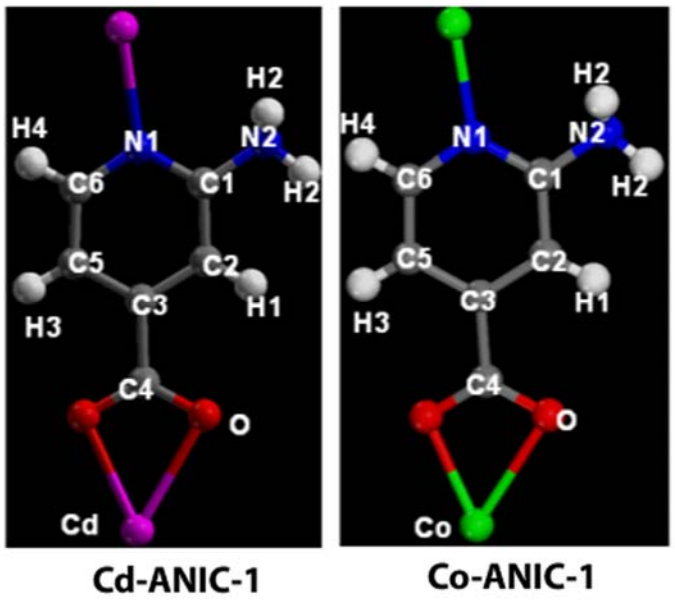

Figure 4.14 Atomic types in Cd-ANIC-1 and Co-ANIC-1 MOF represented during the simulation studies.

Table 4.4 Atomic charges in Cd-ANIC-1 and Co-ANIC-1 MOFs as per atomic types labeled in Figure 4.14.

(a) Cd-ANIC-1							
Atom type	C1	C2	C3	C4	C5	C6	Cd
Charge	0.314	0.030	-0.059	0.525	-0.048	0.213	0.953
Atom type	H1	H2	H3	H4	N1	N2	O
Charge	0.079	0.255	0.136	0.029	-0.476	-0.565	-0.581

(**b) Co-ANIC-1**							
Atom type	C1	C2	C3	C4	C5	C6	Co
Charge	0.271	-0.028	-0.051	0.553	-0.041	0.189	0.711
Atom type	H1	H2	H3	H4	N1	N2	O
Charge	0.074	0.175	0.144	0.046	-0.700	-0.246	-0.574

4.6.5 Synthesis of Cd-ANIC-1 and Co-ANIC-1 MOFs:

Synthesis of [Cd(ANIC)$_2$] ($C_{12}H_{12}N_4O_4Cd$) (Cd-ANIC-1):

A solution of $Cd(NO_3)_2 \cdot 4H_2O$ (37 mg, 0.12 mmol) and ANIC (69 mg, 0.50 mmol) in DMF/Ethanol (6:1 (v/v), 7 mL) was heated under controlled heating at 120 ºC for 2 days in a Teflon-lined steel bomb. The resulting colorless crystals were collected, washed with DMF, and dried at room temperature (yield: 19 mg, 54 % based on Cd).

FT-IR: (KBr 4000-600 cm^{-1}): 3256 (m, br), 2976 (w), 2308 (w), 1675 (s), 1642 (s), 1530 (s), 1452 (m), 1360 (s), 1244 (m) and 774 (m).

Elemental analysis (%) calcd: C 37.08, H 3.11, N 18.62; found: C 36.35, H 2.96, N 18.96.

Synthesis of [Co(ANIC)$_2$] ($C_{12}H_{12}N_4O_4Co$) Co-ANIC-1:

A solution of $Co(NO_3)_2 \cdot 6H_2O$ (35 mg, 0.12 mmol) and ANIC (69 mg, 0.50 mmol) in DMF/Ethanol (6:1 (v/v), 7 mL) was heated under controlled heating at 120 ºC for 2 days in a Teflon-lined steel bomb. The resulting pink colored crystals were collected, washed with DMF, and dried at room temperature (yield: 17 mg, 48 % based on Co).

FT-IR: (KBr 4000-600 cm^{-1}): 3258 (m, br), 2977 (w), 2311 (w), 1682 (s), 1586 (s), 1534 (s), 1454 (m), 1371 (s), 1243 (m), 990 (m), 808 (m) and 771 (m).

Elemental analysis (%) calcd: C 43.25, H 3.02, N 16.80; found: C 42.63, H 2.99, N 17.04.

4.7 References and Notes:

1. (a) Meehl *et. al.*, Chap. 10: Global Climate Projections, in IPCC AR4 WG1, **2007**. (b) D. Zhao, D. Yuan, H.–C. Zhou, *Energy Environ. Sci.* **2008**, *1*, 222. (c) G. Lota, K. Fic, E. Frackowiak, *Energy Environ. Sci.* **2011**, *4*, 1592. (d) S. Keskin, D. S. Sholl, *Energy Environ. Sci.* **2010**, *3*, 343. (e) Y. H. Hu, L. Zhang, *Adv. Mater*. **2010**, *22*, E117. (f) T. L. Frölicher, M. Winton, J. L. Sarmiento, *Nature Climate Change,* **2014***, 4*, 40.

2. (a) *Basic Research Needs for the Hydrogen Economy*; United States Department of Energy, Report of the Basic Energy Sciences Workshop on Hydrogen Production, Storage, and Use, May 13-15, **2003**, available at http://www.sc.doe.gov/ bes/hydrogen.pdf. (b) L. Schlapbach, A. Zuttel, *Nature* **2001**, *414*, 353. (c) M. Dinca, J. R. Long, *J. Am. Chem. Soc.* **2005***, 127,* 9376. (d) C. Read, J. Petrovic, G. Ordaz, S. Satyapal, *Mater. Res. Soc. Symp. Proc*. **2006**, *885*, 125. (e) M. S. Dresselhaus, I. L. Thomas, *Nature* **2001**, *414*, 332. (f) M. Takimoto, Z. Hou, *Nature,* **2006**, *443*, 400.

3. (a) E. Kintisch, *Science* **2007**, *317*, 184. (b) H. E. D. Herzog, E. Adams, *CO_2 Capture, Reuse, and Storage Technologies for Mitigating Global Climate Change*; Report No. DE-AF22-96PC01257; U.S. Department of Energy: Washington, D.C., **1997**.

4. (a) U.S. Department of Energy (DoE). *Carbon Sequestration: State of the Science. A working paper on carbon sequestration science and technology.* Office of Science, Office of Fossil Energy, U.S. Department of Energy, Washington, DC, **1999.** (b) D. Reichle, *et al*. *Carbon Sequestration Research and Development*; Department of Energy: Washington, D.C., **1999**; Chapter 2.

5. (a) F. Barzagli, F. Mani, M. Peruzzini, *Energy Environ. Sci.*, **2010**, *3*, 772. (b) S. Chakravarti, A. Gupta, B. Hunek, *First National Conference on Carbon Sequestration,* Washington, DC, **2001**. (c) G. Vallee, P. Mougine, S. julian, W. Furst, *Ind. Eng. Chem. Res*. **1999**, *38*, 3473.

6. (a) A. J. Fletcher, K. M. Thomas, M. J. Rosseinsky, *J. Solid State Chem.*, **2005**, *178*, 2491. (b) M. Dinca, J. R. Long, *J. Am. Chem. Soc.* **2007***, 129,* 11172. (c) R. Banerjee, H. Furukawa, D. Britt, C. Knobler, M. O'Keeffe, O. M. Yaghi, *J. Am. Chem. Soc.* **2009**, *131*, 3875. (d) R. Banerjee, A. Phan, B. Wang, C. Knobler, H. Furukawa, M. O'Keeffe, O. M. Yaghi, *Science* **2008**, *319,* 939. (e) N. L. Rosi, J. Eckert, M. Eddaoudi, D. T. Vodak, J. Kim, M. O'Keefe, O. M. Yaghi, *Science*, **2003**, *300*, 1127. (f) G. Ferey, C. Mellot-Draznieks, C. Serre, F. Millange, J. Dutour, S. Surble, I. Margiolaki, *Science* **2005**, *309*, 2040. (g) F. Salles, H. Jobic, G. Maurin, M. M. Koza, T. Devic, C. Serre, G. Ferey, *Phys. Rev. Lett.* **2008**, *100*, 245901. (h) B. Chen, M.

Eddaoudi, S. T. Hyde, M. O'Keeffe, O. M. Yaghi, *Science* **2001**, *291*, 1021. (i) N. L. Rosi, J. Kim, M. Eddaoudi, B. Chen, M. O'Keeffe, O. M. Yaghi, *J. Am. Chem. Soc.* **2005***, 127*, 1504.

7. (a) B. Kesanli, Y. Cui, M. R. Smith, E. W. Bittner, B. C. Bockrath, W. Lin, *Angew. Chem., Int. Ed.*, **2005**, *44*, 72. (b) S. Ma, D. Sun, M. W. Ambrogio, J. A. Fillinger, S. Parkin, H.-C. Zhou, *J. Am. Chem. Soc.*, **2007**, *129*, 1858. (c) B. Chen, N. W. Ockwig, A. R. Millward, D. S. Contreras, O. M. Yaghi, *Angew. Chem., Int. Ed.*, **2005**, *44*, 4745. (d) S. T. Batten, R. Robson, *Angew. Chem., Int. Ed.*, **1998**, *37*, 1460. (e) J. L. C. Rowsell, O. M. Yaghi, *J. Am. Chem. Soc.* **2006**, *128*, 1304. (f) C. Tan, S. Yang, N. R. Champness, X. Lin, A. J. Blake, W. Lewis, M. Schroder, *Chem. Commun*. **2011**, *47*, 4487. (g) S. R. Caskey, A. G. Wong-Foy, A. J. Matzger, *J. Am. Chem. Soc.* **2008**, *130*, 10870. (h) F. Debatin, A. Thomas, A. Kelling, N. Hedin, Z. Bacsik, I. Senkovska, S. Kaskel, M. Junginger, H. Muller, U. Schilde, C. Jager, A. Friedrich, H. J. Holdt, *Angew. Chem. Int. Ed.* **2010**, *49*, 1258. (i) H. Frost, T. Duren, R. Q. Snurr, *J. Phys. Chem. B*, 2006, 110, 9565. (j) P. Ryan, L. J. Broadbelt, R. Q. Snurr, *Chem. Commun.*, **2008**, 4132.

8. (a) C. Chen, S.-T. Yang, W.-S. Ahn, R. Ryoob, *Chem. Commun*. **2009**, 3627. (b) R. V. Siriwardane, M. S. Shen, E. P. Fisher, J. Losch, *Energy Fuels* **2005**, *19*, 1153. (c) A. Zukal, I. Dominguez, J. Mayerová, J. Cejka, *Langmuir* **2009**, *25*, 10314. (d) Y. Belmabkhout, A. Sayari, *Adsorption,* **2009**, *15*, 318. (e) S. Kim, J. Ida, V. V. Guliants, J. Y. S. Lin, *J. Phys. Chem. B,* **2005**, *109*, 6287. (f) B. J. Kim, K. S. Cho, S. J. Park, *J. Colloid Interface Sci*. **2010**, *342*, 575. (g) S. N. Kim, W. J. Son, J. S. Choi, W. S. Ahn, *Microporous Mesoporous Mater*. **2008**, *115*, 497.

9. (a) O. M. Yaghi, Q. Li, *MRS Bull.*, **2009**, *34*, 682. (b) L. J. Murray, M. Dinca, J. R. Long, *Chem. Soc. Rev.*, **2009**, *38*, 1294. (c) J. R. Li, R. J. Kuppler, H. C. Zhou, *Chem. Soc. Rev.*, **2009**, *38*, 1477. (d) J. Y. Lee, O. K. Farha, J. Roberts, K. A. Scheidt, S. T. Nguyen, J. T. Hupp, *Chem. Soc. Rev.*, **2009**, *38*, 1450. (e) Y. Q. Zou, A. I. Abdel-Fattah, H. W. Xu, Y. S. Zhao, D. D. Hickmott, *CrystEngComm*, **2010**, *12*, 1337. (f) G. Ferey, C. Serre, T. Devic, G. Maurin, H. Jobic, P. L. Llewellyn, G. De Weireld, A. Vimont, M. Daturif, J. S. Chang, *Chem. Soc. Rev.*, **2011**, *40*, 550. (g) S. Keskin, T. M. Van Heest, D. S. Sholl, *ChemSusChem*, **2010**, *3*, 879. (h) S. Couck, J. F. M. Denayer, G. V. Baron, T. Remy, J. Gascon, F. Kapteijn, *J. Am. Chem. Soc.* **2009**, *131*, 6326. (i) A. Demessence, D. M. D'Alessandro, M. L. Foo, J. R. Long, *J. Am. Chem. Soc.* **2009**, *131*, 8784. (j) X. Gu, Z.–H. Lu, Q. Xu, *Chem. Commun.* **2010**, *46*, 7400. (k) R. Vaidhyanathan, S. S. Iremonger, G. K. H. Shimizu, P. G. Boyd, S. Alavi, T. K. Woo, *Science*, **2010**, *330*, 650.

10. (a) L. J. Murray, M. Dinca, J. R. Long, *Chem. Soc. Rev.*, **2009**, *38*, 1294. (b) L. Hamon, E. Jolimaitre, G. D. Pirngruber, *Ind. Eng. Chem. Res.*, **2010**, *49*, 7497. (c) J. R. Li, Y. Tao, Q. Yu, X. H. Bu, H. Sakamoto, S. Kitagawa, *Chem.–Eur. J.*, **2008**, *14*, 2771. (d) A. Martin-Calvo, E. Garcia-Perez, J. M. Castillo, S. Calero, *Phys. Chem. Chem. Phys.*, **2008**, *10*, 7085. (e) B. Liu, B. Smit, *Langmuir*, 2009, 25, 5918. (f) Q. Y. Yang, C. L. Zhong, *ChemPhysChem*, **2006**, *7*, 1417. (g) D. Wu, Q. Xu, D. H. Liu, C. L. Zhong, *J. Phys. Chem. C*, **2010**, *114*, 16611. (h) Q. Y. Yang, L. L. Ma, C. L. Zhong, X. H. An, D. H. Liu, *J. Phys. Chem. C*, **2011**, *115*, 2790. (i) S. Couck, J. F. M. Denayer, G. V. Baron, T. Remy, J. Gascon, F. Kapteijn, *J. Am. Chem. Soc.*, **2009**, *131*, 6326. (j) Q. Y. Yang, L. L. Ma, C. L. Zhong, X. H. An, D. H. Liu, *J. Phys. Chem. C*, **2011**, *115*, 2790. (k) V. Finsy, L. Ma, L. Alaerts, D. E. De Vos, G. V. Baron, J. F. M. Denayer, *Microporous Mesoporous Mater.*, **2009**, *120*, 221.

11. (a) J. L. C. Rowsell, A. R. Millward, K. S. Park, O. M. Yaghi, *J. Am. Chem. Soc*. **2004**, *126*, 5666. (b) Q. M. Wang, D. Shen, M. Bulow, M. L. Lau, S. Deng, F. R. Fitch, N. O. Lemcoff, J. Semanscin, *Microporous and Mesoporous Mater.,* ***2002***, *55*, 217. (c) A. G. Wong-Foy, O. Lebel, A. J. Matzger, *J. Am. Chem. Soc.* **2007**, *129*, 15740. (d) S.-T. Zheng, J. T. Bu, Y. Li, T. Wu, F. Zuo, P. Feng, X. Bu, *J. Am. Chem. Soc.* **2010**, *132*, 17062. (e) H. Chun, D. N. Dybtsev, H. Kim, K. Kim, *Chem. Eur. J.* **2005**, *11*, 3521.

12. (a) P. K. Thallapally, J. Tian, M. R. Kishan, C. A. Fernandez, S. J. Dalgarno, P. B. McGrail, J. E. Warren, J. L. Atwood, *J. Am. Chem. Soc.*, **2008**, *130*, 16842. (b) D. Sun, S. Ma, Y. Ke, D. J. Collins, H.-C. Zhou, *J. Am. Chem. Soc*. **2006**, *128*, 3896. (c) B. Chen, M. Eddaoudi, S. T. Hyde, M. O'Keeffe, O. M. Yaghi, *Science*, **2001**, *291*, 1021. (d) J. L. C. Rowsell, O. M. Yaghi, *J. Am. Chem. Soc.*, **2006**, *128*, 1304. (e) D. J. Collins, H.-C. Zhou. *J. Mater. Chem.* **2007**, *17*, 3154. (f) B. Liu, Q. Yang, C. Xue, C. Zhong, B. Chen, B. Smit, *J. Phys. Chem. C*, **2008**, *112*, 9854. (g) H. Furukawa, M. A. Miller, O. M. Yaghi, *J. Mater. Chem*. **2007**, *17*, 3197. (h) S. Keskin, D. S. Sholl, *Langmuir*, **2009**, *25*, 11786.

13. (a) F. Luo, M.-S. Wang, M.-B. Luo, G.-M. Sun, Y.-M. Song, P.-X. Li, G.-C. Guo, *Chem. Commun.*, **2012**, *48*, 5989. (b) B. Yuan, D. Ma, X. Wang, Z. Li, Y. Li, H. Liu, D. He, *Chem. Commun.*, **2012**, *48*, 1135.

14. O. K. Farha, C. D. Malliakas, M. G. Kanatzidis, J. T. Hupp, *J. Am. Chem. Soc*., **2010**, *132*, 950.

15. P. Pachfule, Y. Chen, J. Jiang, R. Banerjee, *J. Mater. Chem.*, **2011**, *21*, 17737.

16. L. R. MacGillivray, *Metal-Organic Frameworks: Design and Application*, Wiley: Hoboken,

NJ, **2010**.

17. S. Ma, J. Eckert, P. M. Forster, J. W. Yoon, Y. K. Hwang, J.-S. Chang, C. D. Collier, J. B. Parise, H.-C. Zhou, *J. Am. Chem. Soc.* **2008**, *130*, 15896.

18. M. P. Suh, Y. E. Cheon, E. Y. Lee, *Chem.–Eur. J.* **2007**, *13*, 4208.

19. (a) S. R. Miller, D. Heurtaux, T. Baati, P. Horcajada, J.-M. Grenèche, C. Serre, *Chem. Commun.*, **2010**, 46, 4526. (b) J. Y. Yu, E. Kohler, *Inorg. Chem. Commun.*, **2002**, *8*, 600. (c) J. Lou, F. Jiang, R. Wang, L. Han, Z. Lin, R. Cao, M. Hong, *J. Mol. Struct.*, **2004**, *1–3*, 211. (d) W.-J. Feng, G.-P. Zhou, X.-F. Zheng, Y.-G. Liu, Y. Xu, *Acta Crystallogr., Sect. E: Struct. Rep. Online*, **2006**, *62*, m2033. (e) Y. S. Song, Y. Bing, Z. X. Chen, *J. Solid State Chem.*, **2006**, *179*, 4037. (f) J. Y. Lu, A. M. Babb, Inorg. *Chem. Commun.*, **2001**, *4*, 716. (g) C. T. Dziobkowski, T. J. Wrobleski, D. B. Brown, *Inorg. Chem.*, **1982**, *21*, 671.

20. (a) G. R. Desiraju, *Acc. Chem. Res.*, **2002**, *35*, 565. (b) S. Sarkhel, G. R. Desiraju, *Proteins: Struct., Funct., Genet.,* **2004**, *54*, 247. (c) G. R. Desiraju, T. Steiner, *The Weak Hydrogen Bond, In Structural Chemistry and Biology*, Oxford University Press, **2001**.

21. (a) H. Kim, S. Das, M. G. Kim, D. N. Dybtsev, Y. Kim, K. Kim, *Inorg. Chem.* **2010,** *50,* 3691. (b) S. Ma, *Pure Appl. Chem*. **2009**, *81*, 2235. (c) O. K. Farha, A. O. Yazaydın, I. Eryazici, C. D. Malliakas, B. G. Hauser, M. G. Kanatzidis, S. T. Nguyen, R. Q. Snurr, J. T. Hupp, *Nature Chem.* **2010**, *2*, 944. (d) P. Ryan, L. J. Broadbelt, R. Q. Snurr, *Chem. Commun*. **2008**, 4132. (e) S. Ma, J. Eckert, P. M. Forster, J. W. Yoon, Y. K. Hwang, J.-S. Chang, C. D. Collier, J. B. Parise, H.-C. Zhou, *J. Am. Chem. Soc*. **2008**, *130*, 15896. (f) B. Chen, S. Ma, F. Zapata, E. B. Lobkovsky, J. Yang, *Inorg. Chem*. **2006**, *45*, 5718. (g) M. Xue, S. Ma, Z. Jin, R. M. Schaffino, G.-S. Zhu, E. B. Lobkovsky, S.-L. Qiu, B. Chen, *Inorg. Chem.* **2008**, *47*, 6825. (h) B. Chen, M. Eddaoudi, S. T. Hyde, M. O'Keeffe, O. M. Yaghi, *Science* **2001**, *291*, 1021.

22. (a) D. Yuan, D. Zhao, D. Sun, H.-C. Zhou, *Angew. Chem. Int. Ed.* **2010**, *49,* 5357. (b) T. Panda, P. Pachfule, Y. Chen, J. Jiang, R. Banerjee, *Chem. Commun.* **2011**, *47*, 2011. (c) J. An, S. J. Geib, N. L. Rosi, *J. Am. Chem. Soc.*, **2010**, *132*, 38. (d) D. Britt, H. Furukawa, B. Wang, T. G. Glover, O. M. Yaghi, *Proc. Natl. Acad. Sci. U. S. A.* **2006**, *103*, 10186. (e) Y. S. Bae, O. K. Farha, A. M. Spokoyny, C. A. Mirkin, J. T. Hupp, R. Q. Snurr, *Chem. Commun*. **2008**, 4135.

23. (a) R. Vaidhyanathan, S. S. Iremonger, K. W. Dawson, G. K. H. Shimizu, *Chem. Commun.* **2009**, 5230. (b) J. An, N. L. Rosi, *J. Am. Chem. Soc.*, **2010**, *132*, 5578. (c) W. Morris, B. Leung, H. Furukawa, O. K. Yaghi, N. He, H. Hayashi, Y. Houndonougbo, M. Asta, B. B. Laird, O. M. Yaghi, *J. Am. Chem. Soc.*, **2010**, *132*, 11006. (d) X.-S. Wang, S. Ma, P. M. Forster, D. Yuan, J.

Eckert, J. J. Lopez, B. J. Murphy, J. B. Parise, H.–C. Zhou, *Angew. Chem. Int. Ed.* **2008**, *47*, 7263. (e) S. Ma, D. Sun, J. M. Simmons, C. D. Collier, D. Yuan, H.-C. Zhou, *J. Am. Chem. Soc.*, **2008**, *130,* 1012. (f) X. Lin, J. H. Jia, X. B. Zhao, K. M. Thomas, A. J. Blake, G. S. Walker, N. R. Champness, P. Hubberstey, M. Schroder, *Angew. Chem. Int. Ed.* **2006**, *45,* 7358. (g) X. Lin, I. Telepeni, A. J. Blake, A. Dailly, C. M. Brown, J. M. Simmons, M. Zoppi, G. S. Walker, K. M. Thomas, T. J. Mays, P. Hubberstey, N. R. Champness, M. Schroder, *J. Am. Chem. Soc*. **2009**, *131*, 2159. (h) Z. Guo, H. Wu, G. Srinivas, Y. Zhou, S. Xiang, Z. Chen, Y. Yang, W. Zhou, M. O'Keeffe, B. Chen, *Angew. Chem. Int. Ed.* **2011**, *50*, 3178. (i) F. Nouar, J. F. Eubank, T. Bousquet, L. Wojtas, M. J. Zaworotko, M. Eddaoudi, *J. Am. Chem. Soc.* **2008**, *130*, 1833.

24. (a) R. F. Cracknell, *Phys. Chem. Chem. Phys.* **2001**, *3*, 2091. (b) A. Hirotani, K. Mizukami, R. Miura, H. Takaba, T. Miya, A. Fahmi, A. Stirling, M. Kubo, A. Miyamoto, *Appl. Surf. Sci.* **1997**, *120*, 81. (c) Materials Studio, v.4.4, *Accelrys: San Diego*, **2007**. (d) S. L. Mayo, B. D. Olafson, W. A. Goddard, *J. Phys. Chem.* **1990**, *94*, 8897. (e) A. K. Rappe, C. J. Casewit, K. S. Colwell, W. A. Goddard, W. M. Skiff, *J. Am. Chem. Soc.* **1992**, *114*, 10024.

25. Bruker, **2005**, *APEX2*. Version 5.053. Bruker AXS Inc., Madison, Wisconsin, USA.

26. G. M. Sheldrick, **2004**, *CELL_NOW*. University of Göttingen, Germany.

27. Bruker, **2004**, *SAINT-Plus* (Version 7.03). Bruker AXS Inc., Madison, Wisconsin, USA.

28. G. M. Sheldrick, **2002**, *SADABS* (Version 2.03) and *TWINABS* (Version 1.02).University of Göttingen, Germany.

29. G. M. Sheldrick, **1997**, *SHELXS '97* and *SHELXL '97*. University of Göttingen, Germany.

30. WINGX

31. A. L. Spek, **2005**, *PLATON-A Multipurpose Crystallographic Tool*, Utrecht University, Utrecht, The Netherlands.

Memorandum

The results of this chapter have already been published in *Journal of Materials Chemistry*, **2011**, *21*, 17737–17745; with the title: "Experimental and computational approach of understanding the gas adsorption in amino functionalized interpenetrated metal organic frameworks (MOFs)".

This publication was the result of collaboration between the group of Dr. Rahul Banerjee and his student Pradip Pachfule from the Physical/Materials Chemistry Division at CSIR-National Chemical Laboratory in Pune, India and the group of Prof. Dr. Jianwen Jiang with his student Yifei Chen from the National University of Singapore, 117576 Singapore. Prof. Dr. Jianwen Jiang with his student Yifei Chen have actively contributed to the publication by performing computational studies on MOFs.

Pradip Pachfule was involved in the preparation of MOFs, characterization of MOFs which includes Single crystal X-ray diffraction studies, PXRD, FT-IR, TGA, NMR, Gas adsorption studies. Finally figure preparation and draft writing was carried out by him under the guidance of Dr. Rahul Banerjee.

Chapter 5

Carbon Nanofiber-Metal Organic Framework (CNF-MOF) Hybrids for Enhanced Hydrogen (H_2) Uptake

5.1 Introduction:

Hybrid materials design for specified applications *Viz.* gas adsorption, gas and solvent separation, electronic and optical properties, catalysis, etc; has been emerged as the most modish research topics in recent years as it often results in new or modified properties than that of individual counterparts.[1] These kinds of hybrid materials may be considered as multifunctional materials, wherein two (or more) functional properties not only just simply co-exist, but can also be found strongly coupled with each other. This brings advantages for the multiple applications with enhanced activities. Research on MOFs as well as carbon nanomorphologies like carbon nanotubes (CNTs), graphene (GE) and carbon nanofibers (CNFs) has picked up attention due to variety of applications like gas storage, sensing, drug delivery, catalysis, oxygen reduction reactions (ORR), etc.[2,3] Many attempts have been devoted so far to improve the properties of these materials individually as well as by preparing the hybrids. Some of the specific examples aiming at the property modulation of MOFs include increasing and controlling functionality, introduction of exposed metal sites, doping the MOFs with alkali-metal ions, etc.[4] Similarly, for nanocarbon morphologies, various strategies like surfactant encapsulation, polymer wrapping and attachment of various metal and metal oxide nanoparticles have been attempted.[5] MOFs and nanocarbon morphologies so far have been well exploited in the literature for several applications including improvement in gas adsorption, enhanced ORR activity, etc. The recent progresses in the construction of novel MOF-nanocarbon hybrid structures through different strategies aimed at the improvement in the gas adsorption properties highlights the capabilities and convenience of such hybrids for those applications.[6] In this aspect, the nature of interaction between the MOF and nanocarbon components still possesses a limitation to the versatile exploration of such hybrids. However, most of the hybrids are physical mixtures and they lack a proper chemical interaction between the individual counterparts.[7] These materials having loose interaction among the individual

constituents suffer from the separation from each other upon utilization for targeted applications of these materials, which results into poor performance due to phase separation. But, the long term use of these materials needs modifications in the properties by synergistic effects by chemical interactions between ingredients to meet the real time requirements.

In this context, in continuation with our efforts to improve the H_2 uptake capacities of MOFs,[8] we report a facile move toward the synthesis of a Zn-terephthalate MOF-CNF hybrid [MOF@CNF]. Since, in-situ approach for hybrid synthesis mostly results into the intimate interactions between individual counterparts, we have synthesized MOF-CNF hybrids *via* in-situ MOF growth mechanism.[9] As the confinement and insulation within nanosized hollow structures are expected to show intriguing property modulations and unusual stability, we have selected CNFs, which are still much unexplored as a wide-diameter carbon container and may also present exceptional encapsulating capacity.[10] By rational tailoring of the experimental parameters, we achieved the selective one-dimensional confinement of highly crystalline and nanosized MOFs in inner cavity and both in the inner cavity as well as on the outer walls of CNF. We have endeavoured to unravel the intimate interaction between the CNFs and the encapsulated MOFs using TEM and XPS analysis and thermal stability using variable temperature PXRD analysis (VT-PXRD) and Thermogravimetric analysis (TGA). To the best of our knowledge, it is the first successful report where a metal organic framework in the nanoregime is effectively encapsulated in a one-dimensional nanocarbon material for improved H_2 uptake.

5.2 MOF and Carbon Nanotube/Graphene Oxide based Hybrids:

Many efforts are conducted worldwide to find out efficient and cost-effective H_2 storage materials for various applications including transportation and distributed generation.[11] Although, extensive storage methods have been inspected including liquid H_2, metal hydrides, electrosorption, high-pressure H_2 and physisorption in porous materials; none of these methods have a clear technical and commercial future.[12] Storing molecular H_2 in porous media is one of the promising ways for H_2 storage, among which the physisorption of H_2 remains an attractive alternative due to its reversible storage reaction and safety. Many researchers have investigated several materials like CNTs,

activated carbon, CNFs, graphitic materials, zeolites, MOFs, etc. for physisorptive H_2 storage.[12b] The interest in these materials lies in the fact that they can be optimized for H_2 storage through various physical and chemical treatments. These carbon containing materials like CNTs, CNFs and graphitic compounds are known to offer many advantages due to its low mass density and high surface area.[5,6] The narrow pore size distribution of in these carbon containing materials makes them attractive candidates as adsorbents for H_2.[13] Their cylindrical structure would be increases the adsorption potential on the tube core leading to capillary forces and to enhanced storage capability.[13d]

Similarly, porous MOFs have attracted much attention due to their potential applications in heterogeneous catalyst, separations, sensors, electronics, gas storage, etc. In these regards, as discussed in earlier chapters, we have shown the uses of MOFs as strong candidates for hydrogen storage with or without structural modifications. Therefore, porous MOFs with various functionalities or active metal centers naturally became initial target for the hybrid composites preparation for H_2 storage. The H_2 storage behaviors of carbon nanotubes and MOF hybrid composites (CNTs/MOF-5) were studied (*Figure 5.1*).[14a] The preparation and enhanced hydrostability and H_2 storage capacity of CNT@MOF-5 hybrid composite has been reported in subsequent reports. Similarly, i*n-situ* synthesis of zeolitic imidazolate frameworks/carbon nanotubes composites for enhanced CO_2 adsorption has been reported recently (*Figure 5.2b*).[14b] Few literature reports have showcased utilization of these MOF@CNF or graphene-CNF hybrids for improved gas uptake, with enhanced thermal and chemical stability.[14c,14d]

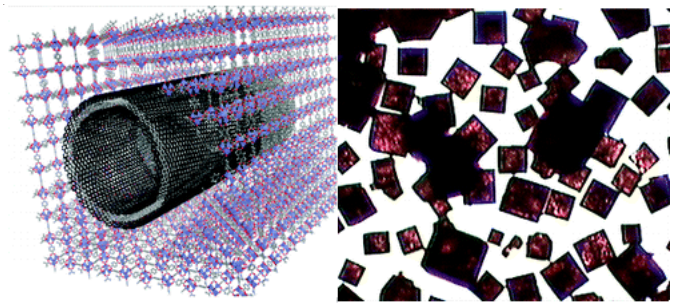

Figure 5.1 Scheme illustrating the synthesis of CNT@MOF-5 hybrid composites and optical image of CNT incorporated MOF-5 crystals. [Reprinted with permission from (14a). Copyright 2009 American Chemical Society].

Since, graphene oxide (GO) is the solution-dispersible form of graphene with

presence of epoxy and hydroxyl functional groups on either side of the GO sheet, it imparts bifunctional properties on the material allowing it to act as structural nodes in MOFs.[15a] The higher conductivity and other supporting properties of GO for Oxygen Reduction Reactions (ORR) helps to improve activity many folds. The change in crystallization process of iron−porphyrin in the MOF by the addition of pyridine functionalized graphene, which increases its porosity and enhances the electrochemical charge transfer rate of iron−porphyrin has been reported in literature (*Figure 5.2a*).[15b] Composites of MIL-100 (Fe) and GO were prepared with various ratios of the two components and tested for ammonia removal in dynamic conditions.[15c] Since, it has been demonstrated that introduction of CNTs into solar cell enhances the electric field of the devices; CNTs were introduced into the Cu-based MOF sensitized solar cell in an attempt to improve the performance of the cell.

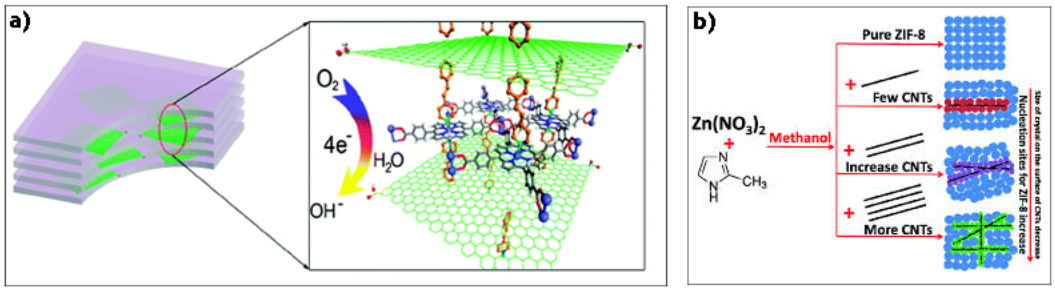

Figure 5.2 Scheme illustrating the synthesis of, (a) electrocatalytically active graphene−porphyrin MOF composite, and (b) ZIF@CNF composite for enhanced CO_2 uptake. [5.2a: Reprinted with permission from (15b). Copyright 2012 American Chemical Society; 5.2b: Reprinted with permission from (14b). Copyright 2014 Royal Society of Chemistry].

From the aforementioned examples of MOF based hybrid materials, it is clear that these materials show very promising properties with enhanced chemical and thermal stabilities. The carbon based materials which have ultimate chemical interaction with decorated or incorporated MOFs, show high stability as well as potential applications in various avenues. Although, there are several reports available for the hybrid materials synthesized using CNTs, graphene based materials; hybrid materials derived from nanosized hollow structures named CNFs are not reported till date. Since, CNFs have wide-diameter and exceptional encapsulating capacity due to higher diameter; the MOF-CNF hybrid materials may pave applications for gas uptake.

5.3 Result and Discussion:

5.3.1 Synthesis of MOF@PCNF and MOF@FCNF:

The commonly used methods for synthesis of MOFs are hydrothermal and solvothermal pathways. For most of the terephthalic acid based MOFs, generally solvothermal methods were followed, since these organic linkers and metal precursors get easily dissolved and deprotonation of organic linkers happens quite easily. In the case of hybrid materials preparation, although methods like mechanochemical grinding, layered growth, etc. are followed in literature, the intimate interactions necessary to hold these both (or more) materials is not sufficient to bind them together.

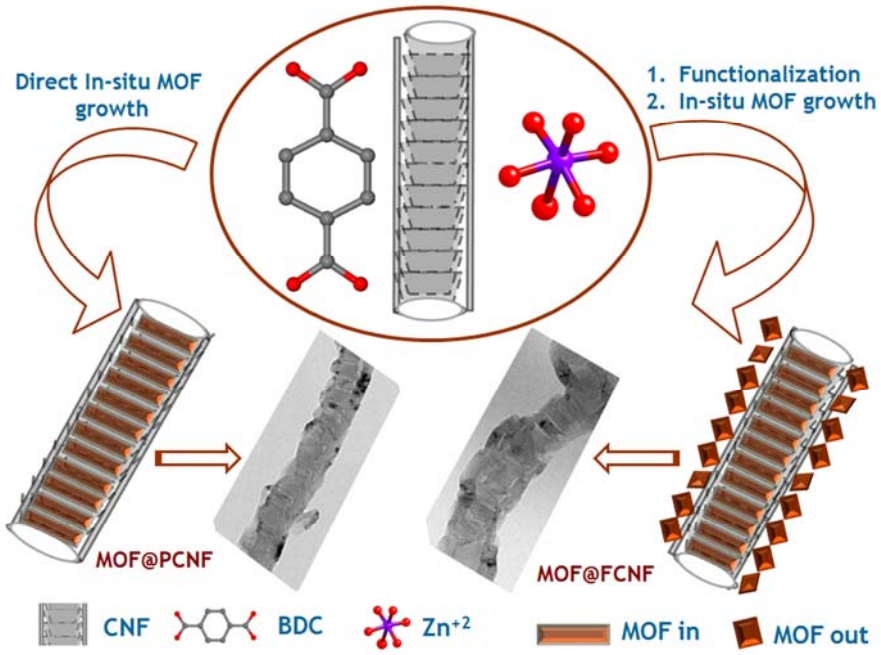

Figure 5.3 Scheme illustrating the synthesis for hybrid MOF@PCNF and MOF@FCNF using pristine CNFs (PCNF) and functionalized CNFs (FCNF), respectively. [Reprinted with permission from (16). Copyright 2012 Royal Society of Chemistry].

In these regards, we have followed *in-situ* approach for hybrid preparation, wherein during the MOF synthesis itself, we have added the CNFs; in order to achieve the hybrids having proper interactions among MOFs and CNFs (*Figure 5.3*).[16] The addition of Pristine Carbon Nanofibres (PCNF) into the reaction mixture resulted into the formation of MOF@PCNF hybrid, wherein loading was selectively achieved into the inner cavity of CNFs, due to the absence of interaction sites and functional groups.

The proof of concept for the necessity of functional groups or interaction sites for MOF-CNF hybrid preparation was further confirmed by the addition of FCNF into the reaction mixture for MOF synthesis (*Figure 5.3*). The inside-out loading of MOF-2 on the FCNF confirmed using TEM and XPS and FT-IR data proved the necessity of functionalization for hybrid preparation. The reaction conditions for good quality hybrid preparation were optimized using different amount of MOF precursors, CNFs, temperature, etc. Finally in order to achieve the uniform loading of MOF into the CNF cavity, to facilitate the entry of MOF precursor solution into the hollow CNF, the probe sonication was followed to the reaction mixture. The pure MOF@PCNF and MOF@FCNF hybrids were isolated following the centrifugation method, since pure MOF crystals have considerably high density than that of CNFs and hybrids synthesized. The low dense hybrids MOF@PCNF and MOF@FCNF collected by filtration were dried in air and used without further purification.

5.3.2 Morphology and structure of MOF@PCNF and MOF@FCNF:

The SEM images of the pristine CNFs shown in Figure 5.4a clearly depict that the length of these nanofibers is in few micrometers and diameter is ~ 100 ± 20 nm. As shown in Figure 5.4b, SEM images of pure MOF-2 indicates that the size of the MOF is in micrometers, typically in the range of 100 μm. It is also clear from the image that the growth of MOFs is not uniform and there is polydispersity in size as well as in shape. The SEM image of MOF@FCNF (*Figure 5.4c*) demonstrates a clear enhancement in the diameter of the CNFs after the incorporation and loading of MOF on/in CNFs. The observed diameter is ~150 ± 20 nm and this enhancement in the diameter gives an indication for the incorporation of the MOF inside as well as outer walls of CNFs. However, the presence of MOF in and out of CNF cannot be detected from the SEM images due to its nanosized morphology, which will be explained in the latter sections. From the SEM images of the hybrid material it can also be confirmed that the unattached MOFs are not present in the sample, which implies the effectiveness of the washing strategy we adopted for the purification and separation of the material from the unattached MOFs. Since, the SEM could not detect the quantity and accessibility of MOFs for the inner cavity of CNFs, we have moved further for TEM analyses of as synthesized samples.

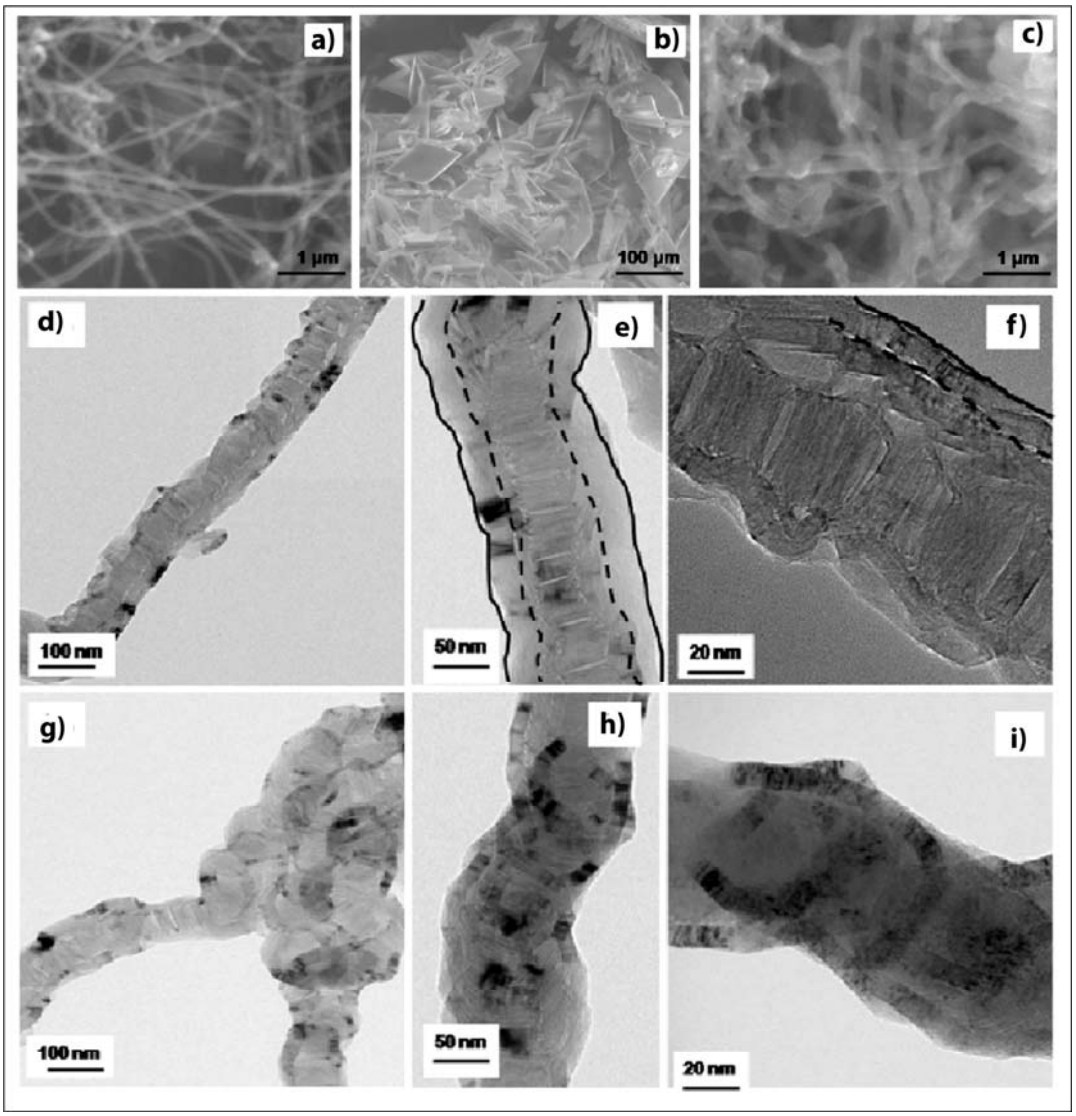

Figure 5.4 Comparison of the SEM images of (a) pristine CNF, (b) pure MOF-2 and (c) MOF@FCNF. (d) HRTEM images of MOF@PCNF showing the one dimensional confinement of MOF in the inner cavity. (e) and (f) are the high-magnification images and the marked black lines show the empty outer wall. (g) MOF@FCNF showing the attachment of MOF in the inner cavity as well as on the outer walls. (h) and (i) are the high magnification images showing stacking of MOF crystals inside the CNFs. [Reprinted with permission from (16). Copyright 2012 Royal Society of Chemistry].

HRTEM is used as an effective tool to authenticate the incorporation of MOF-2 crystals in the CNFs. Accordingly, Figure 5.5a and 5.5b show the HRTEM images of pristine carbon nanofibers at different magnifications. The peculiar morphological features of these CNFs; i.e. active terminal graphene edges in the inner cavity, open tips

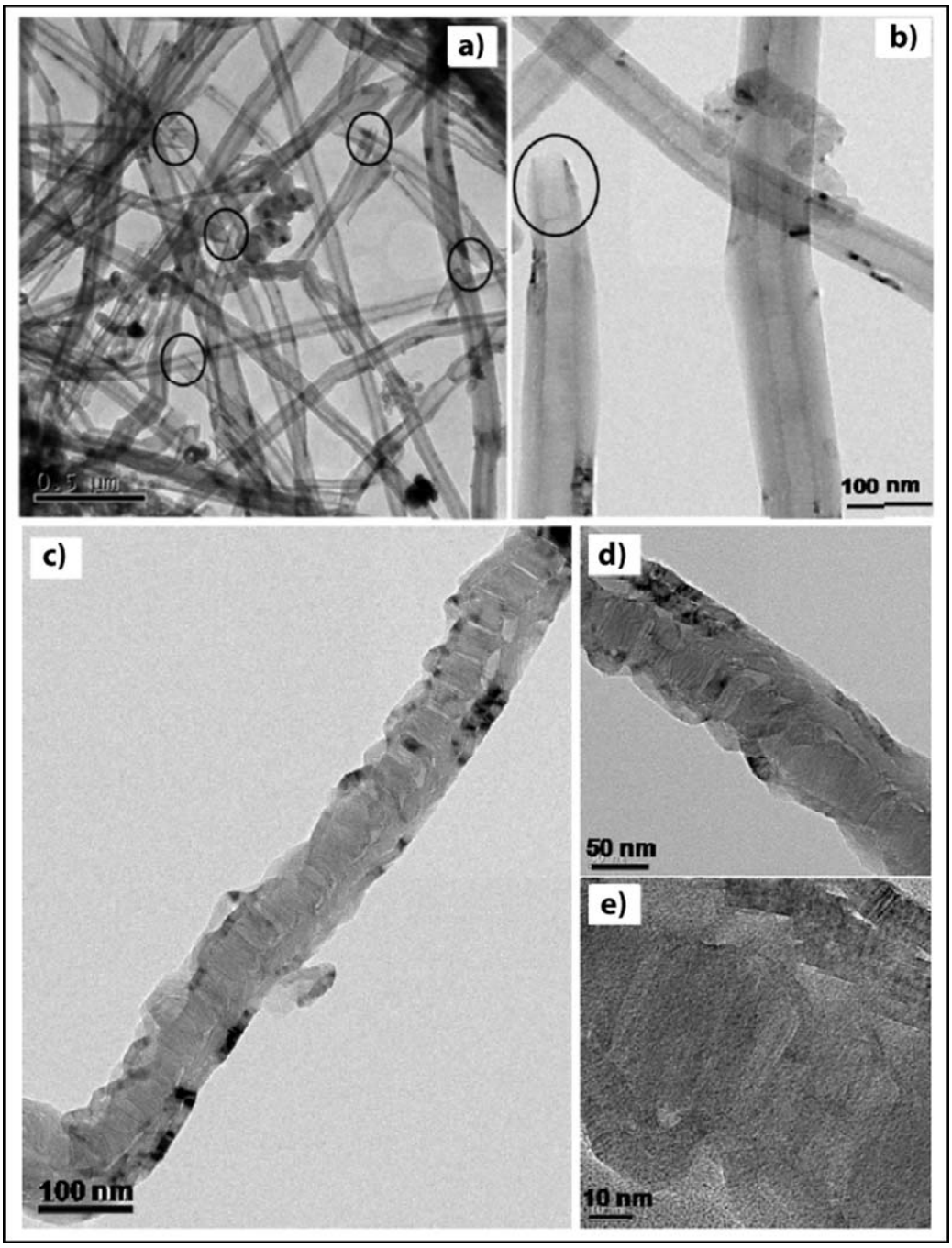

Figure 5.5 HRTEM images of pristine CNF at different magnifications, (a) pristine carbon nanofiber [PCNF]; encircled regions represent the open tips of the carbon nanofiber support. (b) images of carbon nanofiber clearly depicting the active terminal graphene edges and the deactivated outer wall due to the deposition of a pyrolytic carbon layer. (c) and (d) HRTEM images of MOF@PCNF at different magnifications are clearly showing the one-dimensional confinement of nanosized MOFs in the inner cavity of CNFs. (f) HRTEM image showing the continuous lattice fringes clearly indicating the crystalline nature of the MOFs.

with large inner diameter, inherently inactive outer surface which results from the covering of the slanting graphene edges by a duplex layer etc. are evident from the images.[17] The HRTEM images of MOF@PCNF, shown in Figure 5.4d–5.4f and Figure 5.5c–5.5e, clearly show the one dimensional stacking of MOF crystals in the entire length of the inner cavity of the CNFs. The high magnification image of the same given in Figure 5.4f indubitably confirms that regular hexagonal shaped MOF crystals are stacked together in an organized way. Moreover, these MOF crystals are strictly in the nanoregime with size ~20–30 nm, which correlates closely with the inner diameter of the CNFs. The completely unoccupied outer wall of the CNFs, marked with the black lines (*Figure 5.4e*), clearly gives an unambiguous evidence for the initial prediction that MOF crystals are exclusively incorporated in the inner cavity.

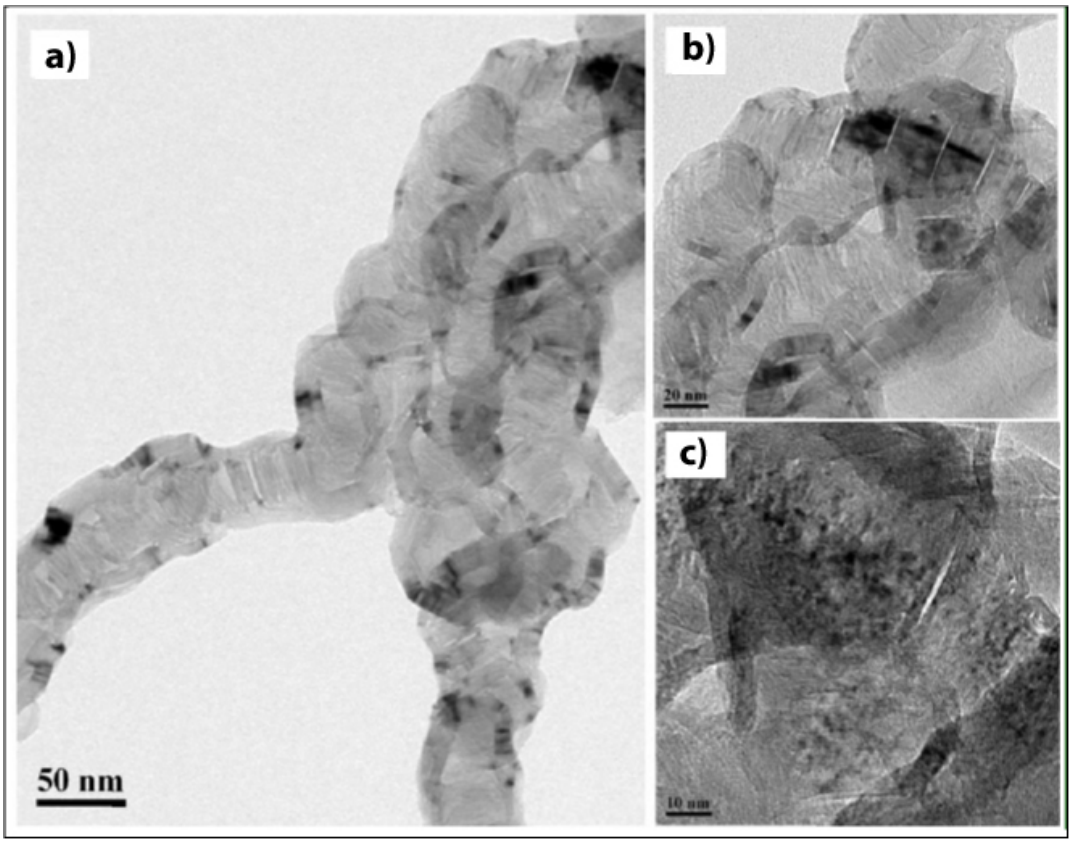

Figure 5.6 (a) and (b) HRTEM images of MOF@FCNF at different magnifications are depicting the attachment of MOFs on the outer walls along with its confinement in the inner cavity. (c) HRETEM image showing the continuous lattice fringes clearly indicating the crystalline nature of the MOFs both in the inner cavity as well as on the outer walls.

The attachment of MOF crystals with FCNFs in hybrid MOF@FCNF was also

explored using TEM imaging and the respective images are shown in 5.4g–5.4i and Figure 5.6. The images clearly demonstrate that the FCNF host is homogeneously loaded with the MOF crystals on the outer wall along with their stacking in the inner cavity. The high magnification images shown in Figure 5.4i and Figure 5.6b–5.6c indicate the highly crystalline nature of these particles. The size of the MOF crystals on the outer wall is slightly larger (~50–60 nm), as compared to those in the inner cavity. This can be attributed to the more freedom for growth on the outer surface compared to the restricted inner cavity of CNF. The distortion of the CNF walls as apparent from Figure 5.4 and 5.6, clearly demonstrates the stress induced during the restricted growth of MOFs along the inner cavity of CNFs.

5.3.3 X-ray powder diffraction analysis and thermal stability of hybrids:

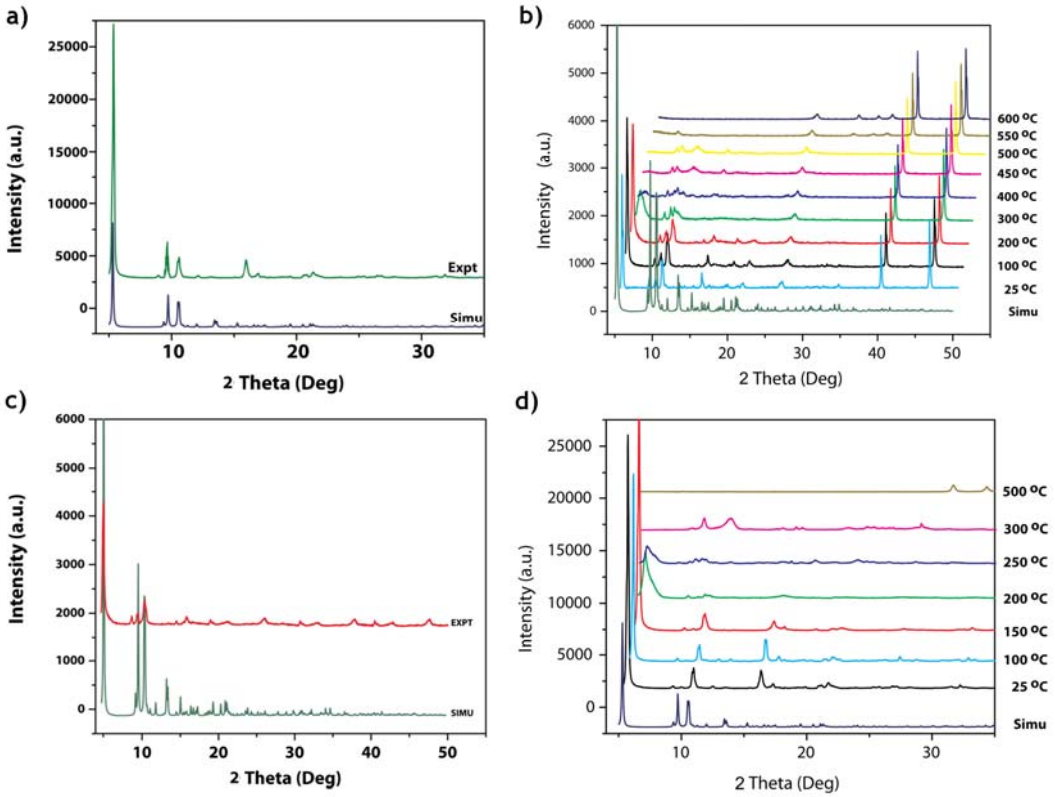

Figure 5.7 Characterizations of MOF-2 and MOF@FCNF. (a) Comparison of the experimental PXRD pattern of as-synthesized MOF-2 (green) with the simulated from single crystal structure of MOF-2 (blue). (b) VT-PXRD analysis of MOF@FCNF. (c) Comparison of the experimental PXRD pattern of as-synthesized MOF@FCNF (red) with the simulated from single crystal structure of MOF-2 (green). (d) VT-PXRD analysis of MOF-2. [Reprinted with permission from (16). Copyright 2012 Royal Society of Chemistry].

To confirm the content and the phase purity of samples, PXRD analyses of the hybrid materials were performed. Although, we attempted the synthesis of the MOF-5 based hybrid,[18] the PXRD patterns of the resulting MOF crystals as well as the MOF@CNF hybrid show that all the major peaks of experimental PXRD match well with the simulated PXRD pattern of another Zn–terephthalate based MOF (MOF-2) synthesized under acidic conditions (*Figure 5.7* and *5.9*).[19] To find out the lowest threshold of CNFs at which the structure directing occurs, we used the amount of FCNF as small as 1 mg in 10 mL Zn–terephthalate solution. It is fascinating to note that this minimum amount itself is sufficient to change the growth of the crystal from MOF-5 to MOF-2, which is also confirmed from PXRD analysis. Though, the exact reason for this structure directing role of CNFs is unclear at this point, we speculate that the lowering of pH (~ 4.3) of the DEF solution of $Zn(NO_3)_2.6H_2O$ and terephthalic acid by induction of CNFs may play a crucial role for the final structure determination.

To validate the thermal stability of the MOF@FCNF hybrid, we performed *in-situ* VT-PXRD analyses of MOF-2 and MOF@FCNF samples at temperatures ranging from 25 °C to 600 °C (*Figure 5.7b* and *5.7d*). The VT-PXRD analysis of MOF-2 obtained, clearly indicates that MOF-2 is stable and retains crystallinity up to 200 °C without any phase change. Small differences in the intensities of the reflections are observed at higher temperatures probably because of the removal of residual solvent molecules. However, the VT-PXRD analysis of MOF@FCNF depicts that the hybrid material is stable even above 300 °C and this additional thermal stability by 100 °C can be attributed to the synergistic effect between the MOF-2 and FCNFs. Similarly, TGA of these samples also suggests the additional thermal stability of hybrid MOF@FCNF over pristine MOF-2. The TGA analysis for the as synthesized MOF@FCNFs hybrid shows stability up to 180 °C, which is followed by a gradual weight-loss step of 4.5% (180–275 °C), corresponding to escape of the trapped solvent of crystallization present in the pores and CNFs. This is followed by a sharp weight loss (275–340 °C) probably due to the decomposition of the framework. The TGA trace of as synthesized MOF-2 indicates the loss of solvent molecules in the range of 20–220 °C in 2 steps possibly due to removal of free and trapped DEF molecules from the framework. This is followed by the sharp weight loss step of 13.8%

(220–280 °C) probably due to decomposition of bridging terephthalate molecules resulting into decomposition of the framework.

5.3.4 FT-IR and XPS analyses of MOF-2 and hybrids:

The FT-IR analyses of the samples of F-CNF, MOF-2 and MOF-@FCNF hybrids were performed to confirm the interactions between MOF-2 and FCNF into the hybrid materials. The presence of characteristic peaks for acid functionalized CNFs at ~1690 cm^{-1} and ~3110 cm^{-1} confirmed the existence of coordination sites for MOF-2 anchoring (*Figure 5.8*). Similarly, the distinct appearance of peaks for uncoordinated carbonyl and –OH groups in the IR-spectrum MOF-2 has been noticed. The FT-IR spectra of MOF-2@FNCF showed the presence of all the characteristic peaks for both FCNF and MOF-2, with additional peaks for coordination between Zn-metal and functional groups from FCNF as expected (*Figure 5.8*). From the FT-IR an analysis of these samples, interactions of MOF-2 with CNFs was confirmed, which was further authenticated using XPS analysis of as synthesized samples of MOF-2 and MOF@FCNF (vide infra).

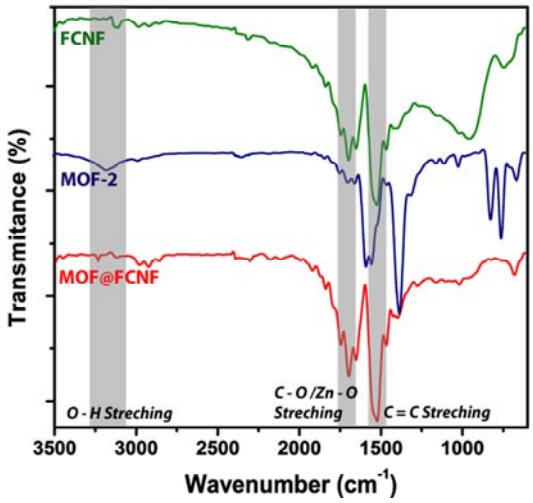

Figure 5.8 FT-IR spectra for FCNF, MOF-2 and MOF-2@FCNF showing characteristic peaks for the confined MOF-2 in FCNF.

The intimate interaction between the FCNFs and MOF-2 is unraveled using XPS analysis. Figure 5.9b and 5.9c respectively, show the comparison of the deconvoluted Zn 2p levels of MOF-2 and MOF@FCNF. The Zn 2p spectra of MOF-2 exhibit two intense peaks at 1022.2 and 1045.2 eV, respectively; which can be assigned to the $2p_{3/2}$ and $2p_{1/2}$ components, revealing the presence of Zn^{2+} cations in MOF-2. The Zn 2p spectrum of MOF@FCNF shows two doublets at peak positions 1023, 1045.8, 1015.5 and 1037.5 eV, respectively. The additional two peaks observed at lower binding energy indicate that Zn is present in two chemical environments in MOF@FCNF. This doublet can be attributed to the Zn present in the MOF-2 crystals which are directly

linked to the FCNF support.[20] The observed shift in the binding energy of Zn by *ca.* 8 eV indicates the strong chemical interaction between the carbon in the FCNF and the Zn in the MOF-2. The regular doublet observed in pure MOF-2 is retained in the hybrid also. Interestingly, a slight shift in the peak position of *ca.* 0.8 eV is observed in this case as well. This elucidates that a liable interaction is still present even in MOF crystals which are not in immediate contact with the FCNF. Further, additional evidences for the interaction between FCNF and MOF-2 can be deduced from a comparison of the full survey XP spectra (*Figure 5.9a*), C 1s (*Figure 5.9d–5.9f*) and O 1s (*Figure 5.9g–5.9i*) spectra of the FCNF, MOF-2 and MOF@FCNF.

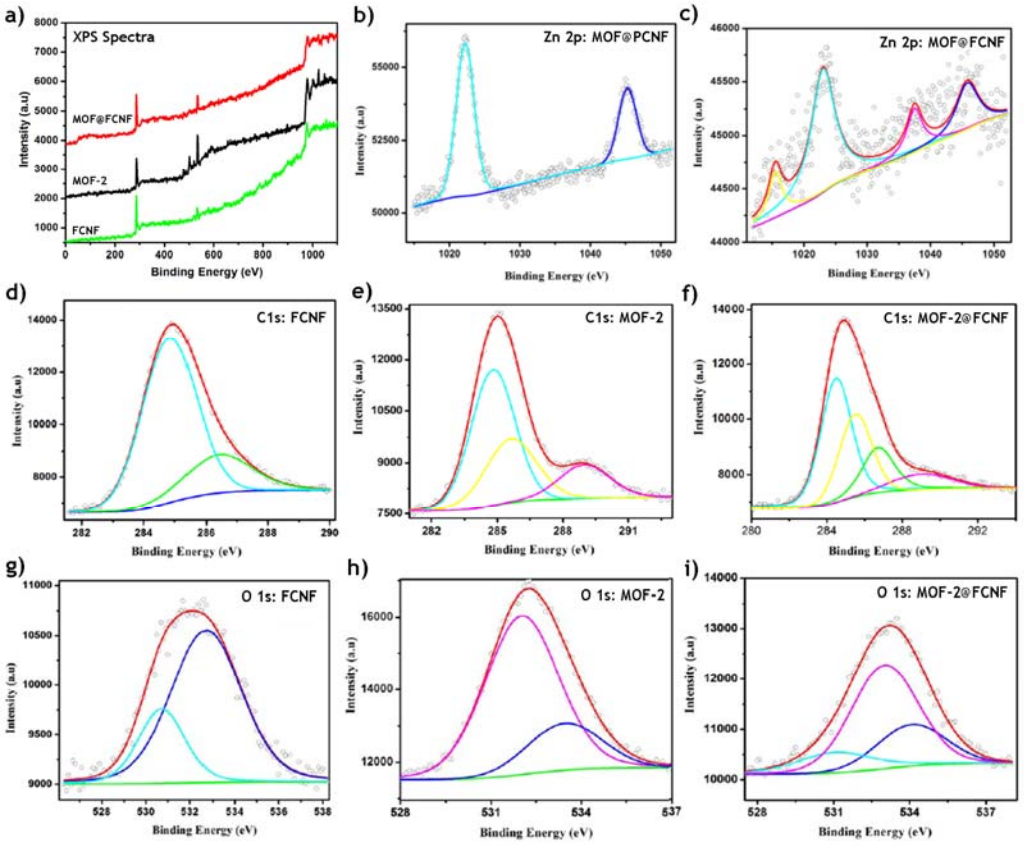

Figure 5.9 XPS analyses of FCNF, MOF-2, MOF@PCNF and MOF@FCNF. a) Comparison of the full survey X-ray photoelectron spectra obtained for FCNF, MOF-2 and MOF@FCNF. b) and c) Deconvoluted XP spectra of Zn 2p levels in MOF@PCNF and MOF@FCNF, respectively. d), e) and f) XP spectra of C 1s core level of F-CNF, MOF-2 and MOF@FCNFs after deconvolution, respectively. g), h) and i) Comparison of XP spectra of O 1s core level of F-CNF, MOF-2 and MOF@FCNFs after deconvolution, respectively. (The circles represent the experimental data, red line represents the fitting data for the overall signal and the dotted lines are the deconvoluted individual peaks for different species present in the sample).

5.3.5 Crystal structure description of MOF-2:

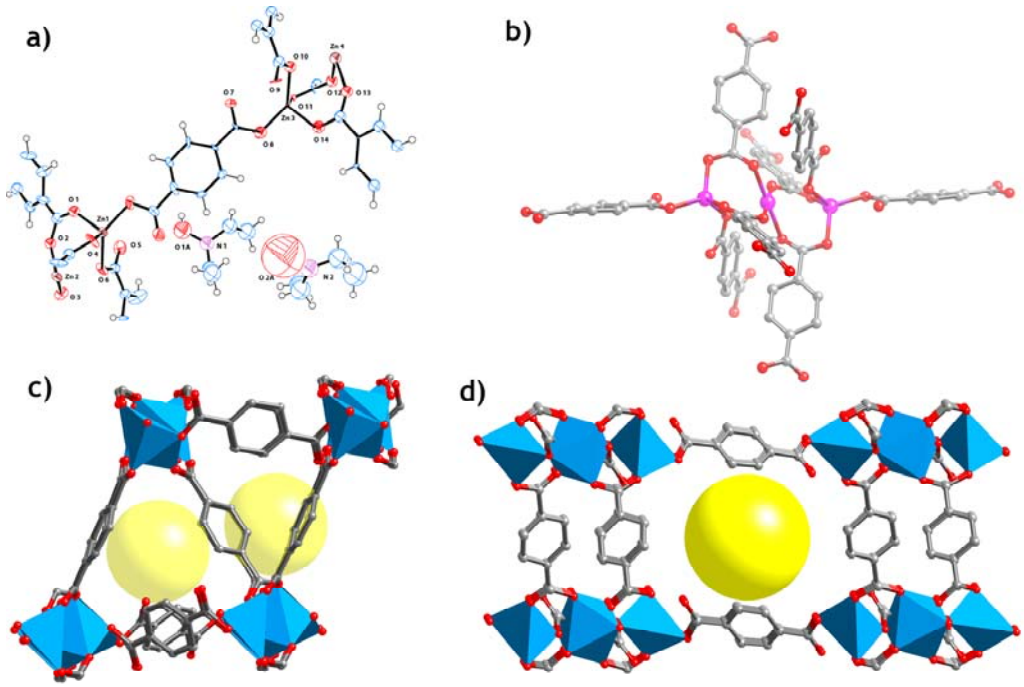

Figure 5.10 Crystal structure of MOF-2. a) ORTEP drawing of the asymmetric unit of MOF-2 drawn at 50% probability level. b) Tetrahedral SBU's in MOF-2 where each tetrahedral Zn is connected to the next Zn through bridging carboxylate groups. c) and d) Packing diagram of MOF-2 through *a* and *c* axis showing one dimensional channels running through structure.

Further, in order to confirm the formation of MOF-2 despite of MOF-5, single crystal X-ray analyses were performed using single crystals of MOFs obtained during the hybrid synthesis.[19] A open-framework zinc terephthalate $(H_2NEt_2)_2[Zn_3(BDC)_4]\cdot 3DEF$ (BDC = 1,4-benzendicarboxylate, DEF=*N*,*N*′-diethylformamide) was obtained under slightly acidic condition developed by addition of FCNF into the reaction mixture through the reaction of 1,4-benzendicarboxylic acid (H_2BDC) with Zn(II) in a DEF solution. The structure was obtained by single crystal X-ray diffraction and consists of trimetallic zinc building units, that are interconnected by eight BDC units each as previously reported by Stock and co-workers (*Figure 5.10*). Six BDC ions together with the trimetallic Zn-units form a two-dimensional (3,6)-net while the other two BDC unit pillar these layers. Thus a three-dimensional anionic framework with a 2D pore system is formed. The pore space is occupied by solvent molecules (DEF) and diethylammonium ions, produced by *in situ* hydrolysis of DEF. These DMA cations are interconnected with each other as well as connected to the framework by H-bonds.

5.4 Gas Adsorption Properties:

In order to study the porosity and gas uptake properties of FCNF, MOF-2 and MOF@FCNF, these samples were activated to make them free from other guest entities. The permanent porosity of the activated samples of FCNF, MOF-2 and MOF@FCNFs is confirmed by N_2 adsorption study. The N_2 adsorption isotherms for the activated samples of FCNF, MOF-2 and MOF@FCNF exhibit type-I sorption behavior (*Figure 5.11a*) with Langmuir surface areas of 37, 68 and 81 $m^2 g^{-1}$ and BET surface areas of 23, 39 and 50 $m^2 g^{-1}$, respectively. Further, all these samples show reversible type-I H_2 and CO_2 adsorption isotherms at 77 and 298 K, respectively, at 1 atm pressure indicating reversible adsorption (*Figure 5.11b* and *5.11c*). At 1 atm pressure and 77 K, FCNF and MOF-2 adsorb 0.27 and 0.63 wt% H_2, while MOF@FCNF adsorbs 0.84 wt% H_2. In the case of CO_2 adsorption, at 298 K, FCNF and MOF-2 adsorb 0.70 and 1.20 mmol g^{-1} CO_2 as the pressure approaches 1 atm, while MOF@FCNF adsorbs 1.61 mmol g^{-1} CO2 at 298 K and 1 atm pressure. So, there is a significant increase of ~30% in the H_2 uptake and ~25% increase of CO_2 uptake in the case of hybrids in comparison with pristine MOF-2 (*Figure 5.11d*).

This overall increase in the gas uptake properties can be attributed to the modulated property characteristics of the hybrid material *via* gas diffusion in the MOF@CNF hybrid. Since CNFs are hollow structure with a large central hollow core and comparatively larger inner diameter (60 ± 10 nm), diffusion of guest molecules into the inner cavity will not be a major problem. On the other hand, adsorption of tiny gas molecules like N_2 (Kinetic diameter–3.65 Å), CO_2 (Kinetic diameter–3.4 Å) and H_2 (Kinetic diameter: 2.85 Å) is also difficult in case of CNFs, as they have very high diameter compared to the kinetic diameter of the adsorbing molecules. Form the synthesis part; it is clear that relatively viscous DEF solution has entered in the inner cavity without any diffusional limitation resulting into the formation of MOF-2 crystals in the inner cavity. Since, in case of gas uptake the molecules are in the gaseous state, diffusional limitation will be less as compared to that in the liquid phase. Moreover, the CNF is not completely packed with the MOFs thus leaving path for gas diffusion. During the mass-transport process, the guest molecules can either diffuse through the

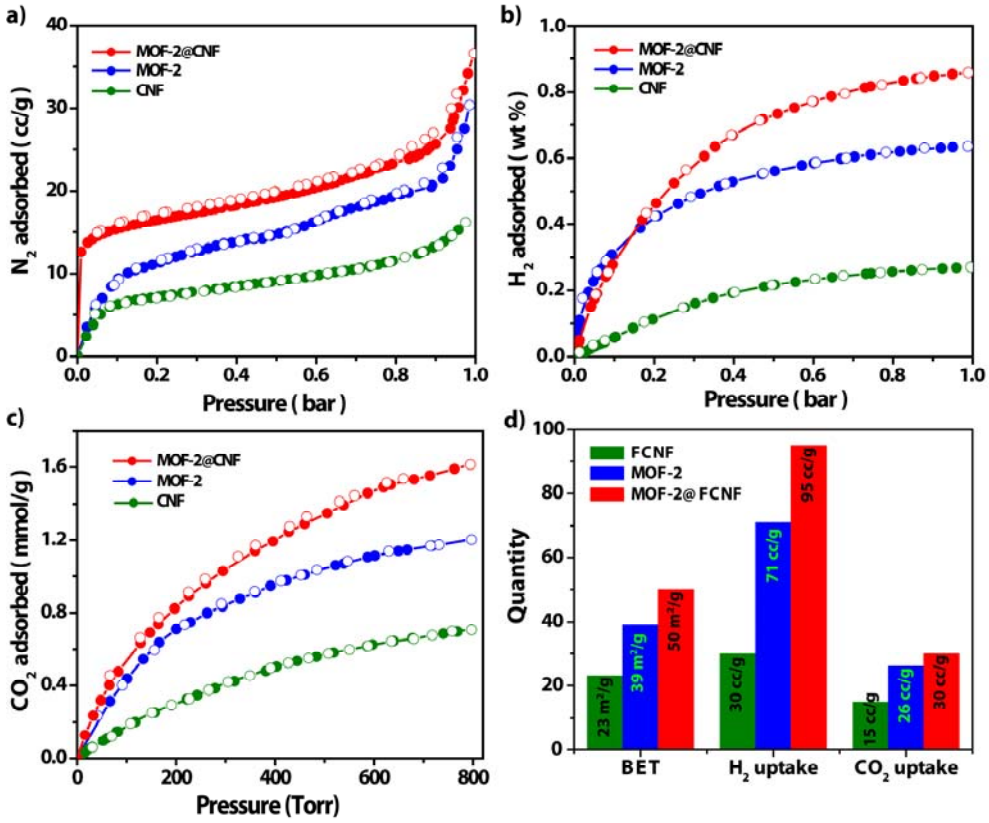

Figure 5.11 Gas adsorption analyses of FCNF, MOF-2 and MOF@FCNF. (a) N_2 adsorption isotherms for FCNF, MOF-2 and MOF@FCNF. (b) H_2 adsorption isotherms for FCNF, MOF-2 and MOF@FCNF. c) CO_2 adsorption isotherms for FCNF, MOF-2 and MOF@FCNF. d) Bar chart representation of comparison of the BET, H_2 and CO_2 uptake capabilities in the FCNF, MOF-2 and MOF@FCNF. [Reprinted with permission from (16). Copyright 2012 Royal Society of Chemistry].

pore (Knudson diffusion or bulk diffusion), on the pore wall (surface diffusion) or a combination through desorption/adsorption processes.[21] In this context, although CNFs are partially or completely filled with the MOF-2, the active graphene edges which are still present inside the CNFs, which acts as adsorption sites. As MOF-2 itself is porous, it can easily adsorb or allow the diffusion of gas molecules through its pores and through the CNFs. MOF@CNF although have limited channels, the overall increase in the gas uptake can be attributed to the creation of the new adsorption sites (active graphene edges) as well synergetic effect of both MOF as well as CNFs. But, we would like to mention that the exact mechanism of the adsorption of gases on the MOF@CNF is still not clear, we are still finding the ways to analyze the reason behind the overall increase in the gas uptake rather than FCNF and MOF-2.

5.5 Conclusions:

The utilization of carbon nanofibers, having one dimensional tubular, nanosized hollow structure has been demonstrated, as a host for MOFs to improve the gas uptake as well as thermal stability. The selective one dimensional confinement of MOF-2 in the inner cavity of CNF has been achieved by the utilization of pristine CNFs as a host, whereas the loading of MOF-2 in inner cavity as well as on outer surface of CNFs was accomplished in the case of functionalized CNFs. The presence of anchoring sites in the FCNFs to achieve the both in and out growth of MOFs was explored. This study outlines a new strategy for the well ordered assembly of an otherwise thermodynamically less stable MOF in the inner cavity as well as on the outer wall of a CNF template. The 1D confinement restricts the growth of such MOFs to nanodimensions giving superior properties over pristine MOF and CNFs. The hybrid material shows improved thermal stability as well as gas uptake over FCNF and MOF-2. The overall increase in the gas uptake properties attributed by the modulated property characteristics of the hybrid material *via* gas diffusion in the MOF@CNF hybrid was realized for the first time in MOF literature. The advantages of hybrid synthesis using two promising materials for betterment of gas uptake and thermal stability of MOFs by achieving increased interactions between indivisual counterparts was also reveled. The stabilization of the thermodynamically less stable variety of the MOF observed in our study may pave the way for future applications of these materials in unforeseen fields.

5.6 Experimental Materials and Methods:

5.6.1 General Procedures:

All reagents and solvents for synthesis and analysis were commercially available and used as received. 1,4-Benzene dicarboxylic acid (Terephthalic acid), *N*,*N*-Diethylformamide (DEF) and $Zn(NO_3)_2.6H_2O$ were purchased from Aldrich Chemicals. All starting materials were used without further purification. All experimental operations were performed in air and all the stock solutions were prepared in DEF. *N*,*N*-dimethylformamide (DMF) was purchased from Rankem chemicals. Powder X-ray diffraction (PXRD) patterns were recorded on a Phillips PANalytical diffractometer for Cu Kα radiation (l = 1.5406 Å), with a scan speed of 0.5° min^{-1} and a step size of 0.02° in 2θ. Fourier transform infrared (FT-IR) spectra were taken on a Bruker Optics ALPHA-E spectrometer with a universal Zn-Se ATR (attenuated total reflection) accessory in the 600-4000 cm^{-1} region or using a Diamond ATR (Golden Gate). Thermogravimetric analyses (TGA) were carried out on a TG50 analyzer (Mettler-Toledo) or a SDT Q600 TG-DTA analyzer under N_2 atmosphere at a heating rate of 10 ºC min^{-1} within a temperature range of 30–900 °C. SEM images were obtained with a Zeiss DSM 950 scanning electron microscope and FEI, QUANTA 200 3D. Scanning Electron Microscope with tungsten filament as electron source operated at 10 kV was used to get SEM images. The samples were sputtered with Au (nano-sized film) prior to imaging by a SCD 040 Balzers Union as well as by sprinkling the powder on carbon tape. Microscopy analyses were performed using a LEICA Stereoscan 440 scanning electron microscope (SEM) equipped with Phoenix energy dispersive analysis of X-ray (EDAX). To investigate the microstructure and morphology of the nanoparticles, we used the FEI (model Tecnai F30) high resolution transmission electron microscope (HRTEM) equipped with field emission source operating at 300 KeV to image the nano-crystals on carbon-coated copper TEM grids. The nanoparticles were dispersed in *i*-PrOH and drop casted on the TEM grids. X-Ray photoelectron spectroscopic (XPS) measurements were carried out on a VG Micro Tech ESCA 3000 instrument at a pressure of $>1 \times 10^{-9}$ Torr (pass energy of 50 eV, electron take-off angle of 60°, and overall resolution was 0.1 eV).

5.6.2 Single Crystal X-Ray Diffraction Methods:

Single crystal data for MOF-2 was collected on Bruker SMART APEX three circle diffractometer equipped with a CCD area detector and operated at 1500 W power (50 kV, 30 mA) to generate Mo K_α radiation (λ= 0.71073 Å). The incident X-ray beam was focused and monochromated using Bruker Excalibur Gobel mirror optics. Crystal of MOF-2, which data is reported in this work, was mounted on nylon CryoLoop (Hampton Research) with Paraton-N (Hampton Research). Initial scans of each specimen were performed to obtain preliminary unit cell parameters and to assess the mosaicity (breadth of spots between frames) of the crystal to select the required frame width for data collection. In every case frame widths of 0.5° were judged to be appropriate and full hemispheres of data were collected using the *Bruker SMART*[22] software suite. Following data collection, reflections were sampled from all regions of the Ewald sphere to re-determine unit cell parameters for data integration and to check for rotational twinning using *CELL_NOW.*[23] Following exhaustive review of the collected frames the resolution of the dataset was judged. Data were integrated using Bruker *SAINT*[24] software with a narrow frame algorithm and a 0.400 fractional lower limit of average intensity. Data were subsequently corrected for absorption by the program *SADABS.*[25] The space group determinations and tests for merohedral twinning were carried out using *XPREP.*[26] In these cases, the highest possible space group was chosen.

Structure was solved by direct methods and refined using the *SHELXTL 97*[26] software suite. Atoms were located from iterative examination of difference *F*-maps following least squares refinements of the earlier models. Final model was refined anisotropically (if the number of data permitted) until full convergence was achieved. Hydrogen atoms were placed in calculated positions (C–H = 0.93 Å) and included as riding atoms with isotropic displacement parameters 1.2-1.5 times U_{eq} of the attached C atoms. Single Crystal X-ray Diffraction data for MOF-2 was collected at 298(2) K. Structures were examined using the *ADDSYM*[27] subroutine of *PLATON*[28] to assure that no additional symmetry could be applied to the models. All ellipsoids in *ORTEP* diagrams are displayed at the 50 % probability level unless noted otherwise (*Figure 5.10a*).

5.6.3 Gas Adsorption Measurements:

Low pressure volumetric gas adsorption measurements involved in this work were performed at 77 K for H_2 and N_2, maintained by a liquid nitrogen bath, with pressures ranging from 0 to 1 bar on Quantachrome Quadrasorb automatic volumetric instrument. While, CO_2 adsorption measurements were done at 273 K and 293 K temperature with same pressures range. In the all adsorption measurements, ultra high-purity H_2 was obtained by using calcium aluminosilicate adsorbents to remove trace amounts of water and other impurities before introduction into the system. The samples of MOF-2, MOF@FNCF and MOF@PCNF were soaked in 1:1 dry dichloromethane and methanol mixture for 12 h. Fresh 1:1 dry dichloromethane and methanol mixture was subsequently added and the crystals were allowed to stay for additional 48 h to remove co-ordinated and free solvates (DEF and H_2O) present in framework. The sample was dried under a dynamic vacuum ($<10^{-3}$ Torr) at room temperature overnight. Prior to gas sorption experiments, thermal activation at an optimized temperature of 120 °C, for 48 h has been done to remove free solvates (DMF and EtOH) present in framework.

5.6.4 Synthesis of MOF-CNF Hybrids by Solvothermal Method.

Synthesis of MOF@PCNF:

As shown in Figure 5.3, $Zn(NO_3)_2.6H_2O$ (0.1 g) and terephthalic acid (0.4 g) were dissolved in 10 mL DEF and mixed well by ultra-sonication (5 min) to get a clear solution in a glass vial. To this solution a weighed amount of the PCNF (45 mg) was added. To facilitate the entry of the precursor solution in the inner cavity of the CNFs, this was subjected to extensive sonication using a probe type sonicator (10 sec pulse for 5 times). This slurry was then kept at 90 °C for 48 h for the complete formation of MOF crystals. The resulting hybrid material was purified and separated from the unattached MOFs by repeated centrifugation (5 times) at 2000 rpm in the same solvent used for the synthesis. Since, there is considerable difference in the density of pure MOFs and the hybrid material, during centrifugation pure MOFs were settled down at the bottom and could be separated from the hybrid material easily. The resulting hybrid material MOF@PCNF was collected and dried in atmospheric conditions.

Synthesis of MOF@FCNF:

$Zn(NO_3)_2.6H_2O$ (0.1 g) and terephthalic acid (0.4 g) were dissolved in 10 mL DEF and

mixed well by ultra-sonication (5 min) to get a clear solution in a glass vial. To this solution, a weighed amount of the FCNF (45 mg) was added. In this case, PCNF activated by an H_2O_2 treatment at 60 °C for 6 h to introduce functional groups (FCNF) was used. The same synthesis approach was performed to load MOF-2 on FCNF and to get the phase pure MOF@FCNF (*Figure 5.3*).

5.7 References and Notes:

1. (a) G. Kickelbick, *Hybrid Materials: Synthesis, Characterization, and Applications*, Wiley-VCH Verlag GmbH & Co. KGaA, **2007**. (b) L. Taberna, S. Mitra, P. Poizot, P. Simon, J. M. Tarascon, *Nat. Mater.*, **2006**, *5*, 567. (c) P. J. Hagrman, D. Hagrman, J. Zubieta, *Angew. Chem. Int. Ed.* **1999**, *38*, 2638. (d) F. Mammeri, E. Le Bourhis, L. Rozes, C. Sanchez, *J. Mater. Chem.* **2005**, *15*, 3787.

2. (a) S. J. Loeb, *Chem. Soc. Rev*. **2007**, *36*, 226. (b) H. Deng, M. A. Olson, J. F. Stoddart, O. M. Yaghi, *Nat. Chem.* **2010**, *2*, 439. (c) V. N. Vukotic, S. J. Loeb, *Chem. Soc. Rev.* **2012**, *41*, 5896. (d) A. Coskun, M. Banaszak, R. D. Astumian, J. F. Stoddart, B. A. Grzybowski, *Chem. Soc. Rev.* **2012**, *41*, 19. (e) J. Lee, O. K. Farha, J. Roberts, K.A. Scheidt, S. T. Nguyen, J. T. Hupp, *Chem. Soc. Rev*., **2009**, *38*, 1450. (f) S. T. Meek, J. A. Greathouse, M. D. Allendorf, *Adv. Mater.*, **2011**, *23*, 249.

3. (a) A. Shaikjee, N. J. Coville, *J. Adv. Res.*, **2012**, *3*, 195. (b) Timothy D. Burchell, *Carbon Materials for Advanced Technologies*, Elsevier, **1999**. (c) G. Messina, S. Santangelo, *Carbon: The Future Material for Advanced Technology Applications Series*, Springer, **2006**. (d) Ashutosh Tiwari, S. K. Shukla, *Advanced Carbon Materials and Technology*, Wiley, **2014**. (e) K. Balasubramanian, M. Burghard, *Small*, **2005**, *1*, 180. (f) C. N. R. Rao, K. Biswas, K. S. Subrahmanyam, A. Govindaraj, *J. Mater. Chem.*, **2009**, *19*, 2457.

4. (a) S. Ma, D. Sun, M. W. Ambrogio, J. A. Fillinger, S. Parkin, H.-C. Zhou, *J. Am. Chem. Soc.*, **2007**, *129*, 1858. (b) J. L. C. Rowsell, O. M. Yaghi, *J. Am. Chem. Soc.* **2006**, *128*, 1304. (c) C. Tan, S. Yang, N. R. Champness, X. Lin, A. J. Blake, W. Lewis, M. Schroder, *Chem. Commun*. **2011**, *47*, 4487. (d) B. Chen, N. W. Ockwig, A. R. Millward, D. S. Contreras, O. M. Yaghi, *Angew. Chem., Int. Ed.*, **2005**, *44*, 4745. (e) S. T. Batten, R. Robson, *Angew. Chem., Int. Ed.*, **1998**, *37*, 1460. (f) S. R. Caskey, A. G. Wong-Foy, A. J. Matzger, *J. Am. Chem. Soc.* **2008**, *130*, 10870. (g) P. Ryan, L. J. Broadbelt, R. Q. Snurr, *Chem. Commun.*, **2008**, 4132.

5. (a) H. Itoi, H. Nishihara, T. Kogure, T. Kyotani, *J. Am. Chem. Soc*. **2011**, *133*, 1165. (b) Z. Yang, Y. Xia, R. Mokaya, *J. Am. Chem. Soc.* **2007**, *129*, 1673. (c) T. Kyotani, *Carbon* **2000**, *38*, 269. (d) R. Ryoo, S. H. Joo, M. Kruk, M. Jaroniec, *Adv. Mater*. **2001**, *13*, 677. (e) M. Kang, S. H. Yi, H. I. Lee, J. E. Yie, J. M. Kim, *Chem. Commun.* **2002**, 1944. (f) A. C. Dillon, K. M. Jones, T. A. Bekkedahl, C. H. Kiang, D. S. Bethune, M. J. Heben, *Nature* **1997**, *386*, 377. (g) Z. Yang, Y. Xia, R. Mokaya, *Adv. Mater.* **2004**, *16*, 727. (h) J. Lee, S. Han, T. Hyeon, *J. Mater. Chem.* **2004**, *14*, 478. (i) H. F. Yang, D. Y. Zhao, *J. Mater. Chem.* **2005**, *15*, 1217. (j) Y. Xia, G. S. Walker, D. M. Grant, R. Mokaya, *J. Am. Chem. Soc.* **2009**, *131*, 16493. (k) Y. Xia, Z. Yang,

R. Mokaya, *Nanoscale* **2010**, *2*, 639.

6. (a) R. T. Yang, Y. Wang, *J. Am. Chem. Soc.* **2009**, *131*, 4224. (b) Z. Ma, T. Kyotani, Z. Liu, O. Terasaki, A. Tomita, *Chem. Mater.* **2001**, *13*, 4413. (c) H. Nishihara, P.-X. Hou, L.-X. Li, M. Ito, M. Uchiyama, T. Kaburagi, A. Ikura, J. Katamura, T. Kawarada, K. Mizuuchi, T. Kyotani, *J. Phys. Chem. C* **2009**, *113*, 3189. (d) B. Hu, K. Wang, L. Wu, S.-H. Yu, M. Antonietti, M.-M. Titirici, *Adv. Mater.* **2010**, *22*, 813. (e) K. Matsuoka, Y. Yamagishi, T. Yamazaki, N. Setoyama, A. Tomita, T. Kyotani, *Carbon,* **2005**, *43*, 876. (f) S. A. Johnson, E. S. Brigham, P. J. Ollivier, T. E. Mallouk, *Chem. Mater.,* **1997**, *9*, 2448. (g) S. Flandrois, B. Simon, *Carbon,* **1999**, *37*, 165. (h) Z. Hu, M. P. Srinivasan, Y. Ni, *Adv. Mater.,* **2000**, *12*, 62. (i) P.-X. Hou, T. Yamazakia, H. Orikasa, T. Kyotani, *Carbon,* **2005**, *43*, 2624. (j) J. Lee, J. Kim, T. Hyeon, *Adv. Mater.,* **2006**, *18*, 2073. (k) K. M. Thomas, *Catal. Today,* **2007**, *120*, 389.

7. (a) C. Petit, T. J. Bandosz, *Adv. Mater.* **2009**, *21*, 4753. (b) Y. E. Cheon, M. P. Suh, *Angew. Chem. Int. Ed.* **2009**, *48*, 2899. (c) S. J. Yang, J. Y. Choi, H. K. Chae, J. H. Cho, K. S. Nahm, C. R. Park, *Chem. Mater.* **2009**, *21,* 1893. (d) Z. Xiang, Z. Hu, D. Cao, W. Yang, J. Lu, B. Han, W. Wang, *Angew. Chem. Int. Ed.* **2011**, *50,* 491.

8. (a) A. Mallick, S. Saha, P. Pachfule, S. Roy, R. Banerjee, *J. Mater. Chem.*, **2010**, *20*, 9073. (b) T. Panda, P. Pachfule, Y. Chen, J. Jiang, R. Banerjee, *Chem. Commun.*, **2011**, *47*, 2011. (c) P. Pachfule, Y. Chen, S. C. Sahoo, J. Jiang, R. Banerjee, *Chem. Mater.,* **2011**, *23*, 2908. (d) P. Pachfule, Y. Chen, S. C. Sahoo, J. Jiang, R. Banerjee*, J. Mater. Chem.,* **2011***, 21*, 17737. (e) P. Pachfule, Y. Chen, S. C. Sahoo, J. Jiang, R. Banerjee, *Chem.–Eur. J.*, **2012***, 18*, 688.

9. (a) Y.-R. Lee, J. Kim, W.-S. Ahn, *Korean J. Chem. Eng.*, 2013, 30, 1667. (b) N. Stock, S. Biswas, *Chem. Rev.*, **2012**, *112*, 933. (c) J. J. Perry IV, J. A. Perman, M. J. Zaworotko, *Chem. Soc. Rev.*, **2009**, *38*, 1400.

10. (a) A. N. Khlobystov, D. A. Britz, G. A. D. Briggs, *Acc. Chem. Res.* **2005**, *38*, 901. (b) G. Sui, W.-H. Zhong, M. A. Fuqua, C. A. Ulven, *Macromol. Chem. Phys.,* **2007**, *208*, 1928.

11. National Hydrogen Association; United States Department of Energy. "*The History of Hydrogen*". *Hydrogenassociation.org*. National Hydrogen Association, **2010**.

12. (a) J. Yang, A. Sudik, C. Wolverton, D. J. Siegel, *Chem. Soc. Rev.*, **2010**, *39*, 656. (b) A. Züttel, *Mater. Today,* **2003**, *6*, 24.

13. (a) J. Lee, J. Kim, T. Hyeon, *Adv. Mater.*, **2006**, *18*, 2073. (b) N. Alam, R. Mokaya, *Energy Environ. Sci.*, **2010**, *3*, 1773. (c) A. Chambers, C. Park, R. T. K. Baker, N. M. Rodriguez, *J. Phys. Chem. B*, **1998**, *102*, 425. (d) B. Panella, M. Hirscher, S. Roth, *Carbon*, **2005**, *43*, 2209.

14. (a) S. J. Yang, J. Y. Choi, H. K. Chae, J. H. Cho, K. S. Nahm, C. R. Park, *Chem. Mater.*, **2009**, *21*, 1893. (b) Y. Yang, L. Ge, V. Rudolph, Z. Zhu, *Dalton Trans.*, **2014**, *43*, 7028. (c) R. Kumar, K. Jayaramulu, T. K. Maji, C. N. R. Rao, *Chem. Commun.,* **2013**, *49*, 4947. (d) S.-J. Park, S.-Y. Lee, *Carbon Letters*, **2009**, *10*, 19.

15. (a) Y. Zhu, S. Murali, W. Cai, X. Li, J. W. Suk, J. R. Potts, R. S. Ruoff, *Adv. Mater.*, **2010**, *22*, 3906. (b) M. Jahan, Q. Bao, K. P. Loh, *J. Am. Chem. Soc.*, **2012**, *134*, 6707. (c) C. Petit, T. J. Bandosz, *Adv. Funct. Mater.* **2011**, *21*, 2108.

16. P. Pachfule, B. K. Balan, S. Kurungot, R. Banerjee, *Chem. Commun.*, **2012**, *48*, 2009.

17. K. B. Beena, M. U. Sreekuttan, K. Sreekumar, *J. Phys. Chem. C.* **2009**, *113*, 17572.

18. H. Li, M. Eddaoudi, M. O'Keeffe, O. M. Yaghi, *Nature*, **1999**, *402*, 276.

1**9.** E. Biemmi, T. Bein, N. Stock, *Solid State Sci.*, **2006**, *8*, 363.

20. M. Müller, S. Turner, O. I. Lebedev,Y.Wang, G.Tendeloo, R. A. Fischer, *Eur. J. Inorg. Chem.* **2011**, 1876.

21. (a) S. C. Reyes, J. H. Sinfelt, G. J. DeMartin. *J. Phys. Chem. B*, **2000**, *104*, 5750. (b) S. Y. Lim, M. Sahimi, T. T. Tsotsis, N. Kim, *Phys. Rev. E*, 2007, 76, 011810.

22. Bruker, **2005**, *APEX2*. Version 5.053. Bruker AXS Inc., Madison, Wisconsin, USA.

23. G. M. Sheldrick, **2004**, *CELL_NOW*. University of Göttingen, Germany.

24. Bruker, **2004**, *SAINT-Plus* (Version 7.03). Bruker AXS Inc., Madison, Wisconsin, USA.

25. G. M. Sheldrick, **2002**, *SADABS* (Version 2.03) and *TWINABS* (Version 1.02).University of Göttingen, Germany.

26. G. M. Sheldrick, **1997**, *SHELXS '97* and *SHELXL '97*. University of Göttingen, Germany.

27. WINGX

28. A. L. Spek, **2005**, *PLATON-A Multipurpose Crystallographic Tool*, Utrecht University, Utrecht, The Netherlands.

Memorandum

The results of this chapter have already been published in *Chemical Communications*, **2012**, *48*, 2009–2011; with the title: "One-dimensional Confinement of a Nanosized Metal Organic Framework in Carbon Nanofibers for Improved Gas Adsorption".

This publication was the result of collaboration between the group of Dr. Rahul Banerjee and his student Pradip Pachfule from the Physical/Materials Chemistry Division at CSIR-National Chemical Laboratory in Pune, India and group Dr. Sreekumar Kurungot and his student Beena K. Balan from same place. Dr. Sreekumar Kurungot with his student Beena Balan has actively contributed to the publication in characterization of hybrids by TEM, SEM and XPS analyses.

Pradip Pachfule was involved in the preparation of MOF based hybrids, characterization of hybrids which includes Single crystal X-ray diffraction studies, PXRD, FT-IR, TGA, Gas adsorption studies, etc. Finally figure preparation and draft writing was carried out by him under the guidance of Dr. Rahul Banerjee and Dr. Sreekumar Kurungot.

Chapter 6

Conclusions and Future Prospects

6.1 Conclusions:

Physisorption of H_2 in porous materials at cryogenic conditions is a viable mechanism for H_2 storage in mobile applications, in which storage mechanism has the advantage of possessing fast kinetics, low heat of adsorption and being completely reversible. Although there are several porous materials reported into the literature, MOFs are the best candidates for H_2 adsorption, since they consist of lighter elements, are highly porous and their pore dimensions can be tailored by chemical engineering. Different properties of the material, like specific surface area, composition and pore size can influence the storage capacity. Therefore, an understanding about the correlation between adsorption properties and structure of MOFs is necessary to specifically improve these materials for H_2 storage.[2] The main achievements acquired during the course of time of the investigation for H_2 storage in MOFs are discussed, limitations of the present investigation are defined and some of the future prospects are proposed.

The intriguing structural aspects like high surface area, tunable pore sizes and functionalizable pore walls makes MOFs as a suitable candidate for H_2 adsorption over other literature reported materials like porous carbons, metal hydrides, zeolites, porous silica materials, etc. MOFs are considered as eligible materials for gas adsorption, gas separation, catalysis, drug delivery, luminescence and sensors, etc. Although, these materials are utilized for various applications, MOFs have been used frequently for H_2 storage in order to achieve DoE targets. Several attempts are followed for improvement in H_2 uptake capacities in MOFs, which includes increasing pore size, pore volume and surface area, creation of open metal sites, MOF functionalization, interpenetration or catenation, doping of metal nanoparticles and alkali metals in MOFs, etc. Despite of the promising achievements in terms of H_2 storage in MOFs, the weak interaction between H_2 molecules and framework ingredients is the main obstacle for its further application and achievement of DoE targets. From the literature survey and expert reviews, it seems that in order to reach the DoE set targets for room temperature adsorption a strong initial heat of adsorption and large surface area and pore volume is desirable. This may

be achieved by synthesis of highly porous MOFs with the incorporation of functional groups like –OH, –F, $–CF_3$, $–SO_3H$, –COOH, etc. *via* linkers or post-synthetic modifications. The initial heat of adsorption necessary for high H_2 uptake at low pressure can be achieved *via* highly electronegative groups present into the MOF pores and further uptake at high pressure can be accomplished by presence of high porosity.

In the initial attempts, as desired in previous literature outcomes, in order to improve the H_2 uptake properties of MOFs *via* increased interactions among the framework components and adsorbing H_2 molecules, synthesis of new *F*-MOF was performed. In these aspects, using a flexible fluorinated dicarboxylates building block 4,4′-hexafluoroisopropilidine bis-benzoic acid; 3-methyl pyridine/1,10-phenanthroline co-ligands, and different transition metal cations [Zn(II), Co(II), Mn(II), and Cu(II)] several *F*-MOFs have been synthesized. The moderate H_2 uptake shown by these materials, despite of its very limited or negligible surface area could possibly emerge as H_2 storage materials. The further attempts to improve the gas uptake in these *F*-MOFs were unsuccessful due the V-shaped twisted conformation and flexible nature of 4,4′-hexafluoroisopropilidine bis-benzoic acid, which restricts the expansion of cavities into the MOF structure. To overcome these issues, highly robust and porous MOFs using isonicotinic acid and 3-fluoro isonicotinic acid for high H_2 uptake proved to be rewarding to increase the overall H_2 uptake. The H_2 uptake data collected in two pairs of isostructural fluorinated and non-fluorinated MOFs, Co-INA-1 and Co-*F*INA-1, fluorination resulted in almost similar H_2 uptake, whereas in Co-INA-2 and Co-*F*INA-2, fluorination resulted in an overall increase in H_2 uptake. From these results, it is clear that as fluorine atoms in *F*-MOFs are weakly interacting with gas molecules, other factors, such as pore size, curvature, and open metal sites, can also play crucial roles in the gas uptakes in these *F*-MOFs. The comparison of H_2 uptake in these isostructural MOFs using experimental and simulation methods, emphasizes that improvement in H_2 uptake in *F*-MOFs is not a universal phenomenon, but is rather system-specific and differs from system to system.

In order to reassert the effect of partial fluorination on H_2 uptake properties of MOFs, we have synthesized new MOFs using the predesigned 4-tetrazole benzoic acid (4-TBA) and fluorine containing 2-fluoro-4-tetrazole benzoic acid (2-F-4-TBA) linkers

with a transition metal center Cu(I/II), solvothermally. The exploration of H_2 uptake properties in isostructural Cu-TBA-2 and Cu-TBA-2F was performed in more details by utilizing the experimental and computational results of H_2 adsorption isotherms. At 1 atm pressure, Cu-TBA-2 shows uptake of 1.54 wt % H_2, whereas Cu-TBA-2F shows uptake of 0.67 wt% at same conditions. The direct comparison between gas adsorption properties of iso-structural partially fluorinated Cu-TBA-2F and non-fluorinated Cu-TBA-2 suggested that enhancement of H_2 adsorption due to fluorination in MOFs is not an universal phenomenon, but it is rather system specific and can differ from system to system. The density distributions of adsorbed H_2 molecules in Cu-TBA-2 and Cu-TBA-2F from simulation suggest that H_2 molecules are primarily adsorbed in the pores along the X axis and the binding sites are mostly located in the pore centers. Based on the simulation, protruding fluorine atoms from 2-F-4-TBA appear to cause a steric hindrance and a lower adsorption for H_2. Nevertheless, thorough research work is necessary on H_2 adsorption on iso-structural fluorinated/non-fluorinated MOFs before we can conclusively indicate a positive/negative effect of fluorination on enhancement of hydrogen adsorption in MOFs.

As per the studies based on fluorinated MOFs for enhanced H_2 uptake showed promising results, we have moved further for the synthesis of functionalized MOFs having framework interpenetration. Framework interpenetration is a phenomenon, where the pores of one framework are inter-grown by one or more independent frameworks, which hold favorable interactions between aromatic rings of MOFs and H_2 molecules. Since, microporous interpenetrated MOFs would be ideal candidates for the sorption of small gaseous molecules, interpenetration has been utilized to strengthen the interaction between the gaseous molecule and the framework by an entrapment mechanism, in which hydrogen molecules remains in close proximity with several aromatic rings from interpenetrating networks. In these regards, the successful isolation of the interpenetrated, porous, functionalized Cd-ANIC-1 and Co-ANIC-1 MOFs with diamondoid topology having one dimensional channels of dimensions 3.9 Å × 3.9 Å and 3.7 Å × 3.7 Å running through *a* axis, respectively; synthesized using 2-amino-isonicotinic acid (ANIC). The porous, interpenetrated and functionalized Cd-ANIC-1 and Co-ANIC-1 have high H_2 adsorption capacities of 1.84 wt% and 1.64 wt%,

respectively; which can be attributed to the presence of the Lewis basic amino groups of ANIC linkers and interpenetration. Specially, as other amino functionalized MOFs and ZIFs lack the high H_2 adsorption, we could successfully achieve high H_2 adsorption as well, which is contributed by interpenetration in the frameworks of Cd-ANIC-1 and Co-ANIC-1. The H_2 adsorptions in Cd-ANIC-1 and Co-ANIC-1 have also been validated by simulations, which show good agreement with experimental data. Collectively, these results points towards the discovery of new materials with functionalized interpenetrated frameworks synthesized from a simple isonicotinic acid derived link for high H_2 adsorption capacities.

Lastly, to achieve the enhanced H_2 uptake in MOFs, synthesis of hybrid materials using functionalized carbon nanofibers (*F*-CNF) has been performed. The utilization of carbon nanofibers, having one dimensional tubular, nanosized hollow structure has been demonstrated, as a host for MOFs to improve the gas uptake as well as thermal stability. The selective one dimensional confinement of MOF-2 in the inner cavity of CNF has been achieved by the utilization of pristine CNFs as a host, whereas the loading of MOF-2 in inner cavity as well as on outer surface of CNFs was accomplished in the case of functionalized CNFs. This study outlines a new strategy for the well ordered assembly of an otherwise thermodynamically less stable MOF in the inner cavity as well as on the outer wall of a CNF template. The 1D confinement restricts the growth of such MOFs to nanodimensions giving superior properties over pristine MOF and CNFs. The hybrid material shows improved thermal stability as well as H_2 uptake over FCNF and MOF-2. At 1 atm pressure and 77 K, FCNF and MOF-2 adsorb 0.27 and 0.63 wt% H_2, while MOF-2@FCNF adsorbs 0.84 wt% H_2. The significant increase of ~30% in the H_2 uptake in the case of hybrids in comparison with pristine MOF-2, which can be attributed to the modulated property characteristics of the hybrid material *via* gas diffusion in the MOF@CNF hybrid. The advantages of hybrid synthesis using two promising materials for betterment of gas uptake and thermal stability of MOFs by achieving increased interactions between indivisual counterparts was also revealed. The stabilization of the thermodynamically less stable variety of the MOF observed in our study may pave the way for future applications of these materials in unforeseen fields.

In summary, MOFs have versatile structures, high surface areas, and high pore volumes, and thus can be regarded as good candidate materials for H_2 storage. To develop MOFs as H_2 storage materials that meet the DoE targets for an on-board hydrogen system, a serious challenge is still present in the design and synthesis of the MOF materials. We may expect that highly stable MOFs having a large surface area and pore volume, together with many open metal sites or embedded catalysts for hydrogen spillover or functional groups having high affinity to H_2 molecules would provide positive results for H_2 storage at ambient temperature. Looking through the impact of MOFs for social cause, these materials are applied in several avenues for gas separation, proton conductivity, charge carrier mobility, magnetism, drug delivery, luminescence and sensors, etc. Due to the intriguing structural and inherent properties, MOFs may pave future application for several unseen field for the good of the society.

6.2 Future Prospects:

Finally, some of the future prospects for the applications of MOFs within the broad perspective of storage materials and its societal impact are as follows:

Proposal-I: Synthesis of Hydrophobic Fluorinated Metal Organic Frameworks for Hydrocarbon Storage, Adsorption of Nerve agents and Mustard Gases

Synthesis of hydrophobic adsorbing materials has picked researchers attention due to its significant applications in gas adsorption, hydrocarbon adsorption/separation, capture of Nerve agents and Mustard gas analogues.[1] As discussed earlier, as a result of high elctronegativity and hydrophobic nature fluorine atoms, the utilization of *F*-MOFs for gas adsorption and hydrocarbon separation and sorption are demonstrated in literature. The capture of Nerve agents is also important in order to maintain the environmental balance, since these gases disrupt the mechanism by which nerves transfer messages to organs. Similarly, the mustard gas compound readily eliminates a chloride ion by intramolecular nucleophilic substitution to form a cyclic sulfonium ion, which tends to permanently alkylate the guanine nucleotide in DNA strands, which prevents cellular division and generally leads directly to programmed cell death or development of cancer.[2] MOFs with hydrophobic groups have been utilized to capture the Nerve agents and Mustard gas analogues owing to their highly ordered, crystalline architectures with

tunable porosities. MOFs/ZIFs having functional groups (–CH_3, –C_2H_5, –CHO, etc.) anchored to the coordinating linkers studied extensively for their hydrophobic nature.[3] Similarly, the fluorine functionalized MOFs having fluorine lined channels showed great promise for hydrocarbon adsorption/separation and gas uptake as well, probably due to the high thermal stability, high selectivity, and excellent recyclability of these materials originating from the highly electronegative fluorine atoms.[4] Although, these materials are of great interest, they are not studied well in the literature due to limited diversity of fluorine containing linkers.

In light of these issues associated with the synthesis of fluorinated MOFs (*F*-MOFs), herein we propose the synthesis of fluorinated MOFs having fluorine lined channels. The synthesis of fluorine containing ligands can be achieved by simple click chemistry or coupling reaction. As shown in Figure 6.1, the reaction of these fluorine containing ligands with metal centers like Zn(II), Cu(II), Co(II), etc. will result into the formation of highly porous *F*-MOFs possessing fluorine lined channels. As these ligands can coordinate into the similar fashion of 1,4-benzene dicarboxylate showed in MOF-5 or 3,5-dimethyl-4-carboxypyrazolate showed in [Zn_4O(3,5-dimethyl-4-carboxypyrazolato)$_3$] MOF, hence possibility of getting highly porous structures is maximum.

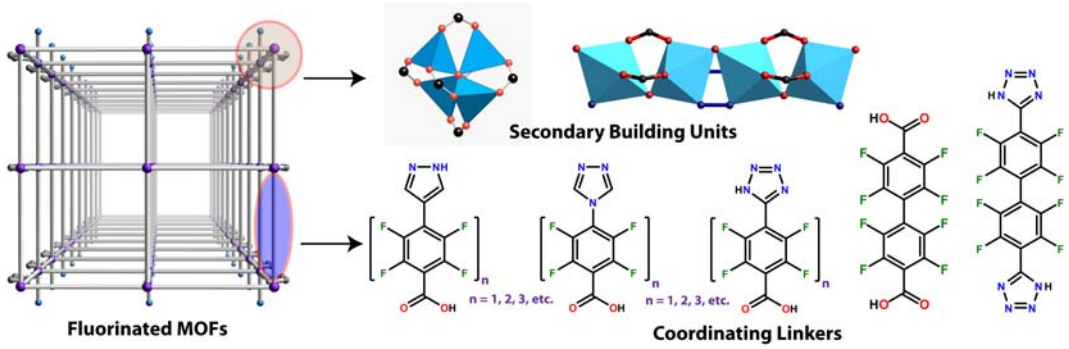

Figure 6.1 Synthesis of MOF-5 analogues fluorinated MOFs from pyrazolate, triazolates, tetrazolate or carboxylate based coordinating linkers.

The highly ordered and porous architectures with hydrophobic channels present in these FMOFs can be further utilized for the hydrocarbon adsorption/separation and H_2 adsorption also. The similar approach of utilization of hydrophobic channels can be extended for the capture of G/V-series Nerve agents and Mustard gas analogues as well.

The harmful volatile compounds including tear agents, vomiting agents, lethal agents, etc. will be successfully captured by these *F*-MOFs as these materials possesses the high attraction towards these kind of gases.

Proposal-II: Design and Synthesis of New Proton Conducting Materials Based on Metal-Organic Framework-Carbon Nanofiber (PC-MOF@CNF) Hybrids

Research on Metal–organic frameworks (MOFs)[5] and carbon nanomorphologies like carbon nanotubes (CNTs), graphene (GE) and carbon nanofibers (CNFs) derived hybrid materials[6] has picked up attention due to variety of applications like gas storage, sensing, drug delivery, catalysis, proton conduction, etc. MOFs and nanocarbon morphologies so far have been well exploited in the literature separately; and despite the recent progresses in the construction of novel MOF-nanocarbon hybrid structures through different strategies and the improvement in the properties of such hybrids.[7] However, most of the hybrids are physical mixtures and they lack proper chemical interactions between the individual counterparts. But, the modifications in the properties by synergistic effects need such chemical interactions to meet the real time requirements. On the other hand, the search for new highly proton-conducting materials has been a subject of intense research because of their potential applications in fuel cells, sensors and other areas as the traditional proton conducting nafion membranes suffers a limitation of operating in temperature above 80 °C.[8] In order to replace these membranes several materials like MOFs, organic molecular porous materials, biopolymer composite materials, anodic nanofilms, etc. have been tried previously.[9] Despite the several materials studied for proton conduction, MOFs showed promising results over other materials due to hallow channels inside the flexible structure and competence of accommodating small molecules like water, imidazole, triazole helping in proton conduction.[10] In this context, we propose a facile move toward the synthesis of a MOF-CNF hybrid by an in-situ approach for high proton conduction. As the confinement and insulation within nanosized hollow structures are expected to show interesting property modulations and unusual stability, we have selected CNFs, which has a such as high flexibility, high tensile strength, low weight, high resistance, high temperature tolerance, low thermal expansion and high thermal conductivity. By rationally tailoring the experimental parameters, it is possible that the selective one-

dimensional confinement of highly crystalline and nanosized proton conductive MOFs (PC-MOF) in inner cavity and in inner cavity as well as on the outer walls of CNF.[11]

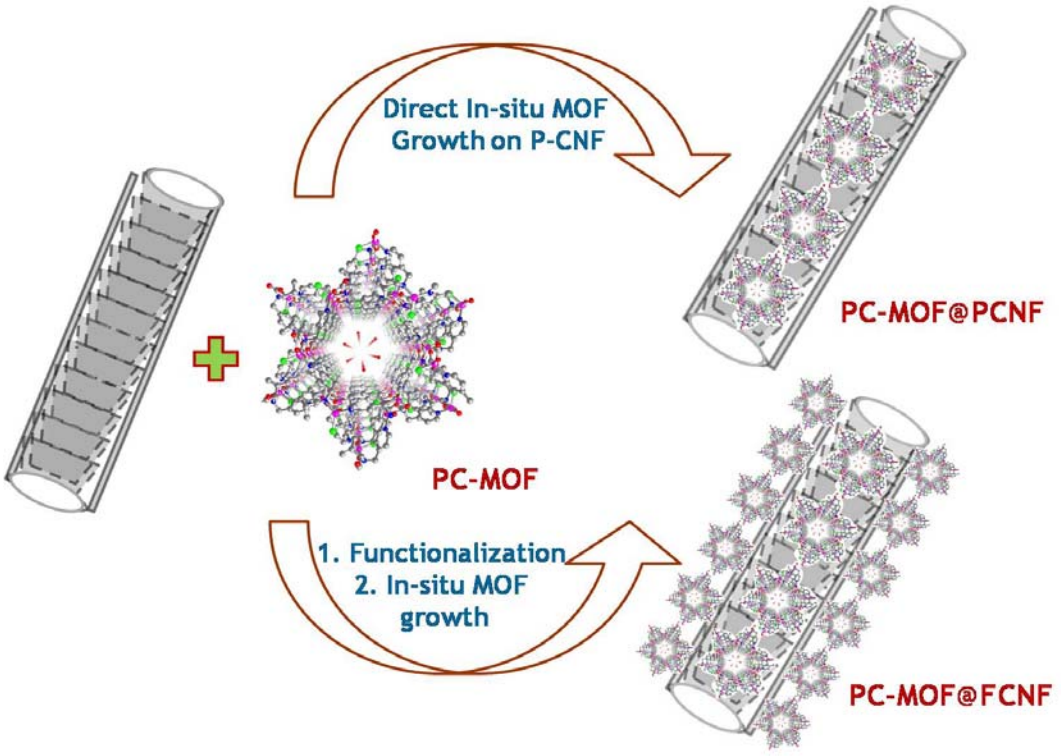

Figure 6.2 Proposed scheme of synthesis illustrating the synthesis for hybrid PC-MOF@PCNF and PC-MOF@FCNF using pristine CNFs (PCNF) and functionalized CNFs (FCNF), respectively.

The proposed research intends to create a new route to synthesize PC-MOF@CNFs hybrid by an insitu MOF growth approach.[12] Figure 6.2 illustrates the idea behind the proposed work, where selective decoration of PC-MOF inside and inner as well as outer surface of CNFs can be achieved by using prestine and functionalized CNFs, respectively; as functionalizations of CNFs can procure binding sites for MOFs. As CNFs possesses active terminal graphene edges in the inner cavity, open tips with large inner diameter, inherently inactive outer surface which results from the covering of the slanting graphene edges by a duplex layer, the chemical interaction between PC-MOF and FCNF is obvious, which usually results into the improved chemical as well as thermal stability. The incessant loading of PC-MOFs on outer as well as inner surface of

CNFs with improved thermal stability can be achieved, as CNFs possesses high thermal conductivity and low thermal expansion with high temperature tolerance, it is expected that confinement of proton PC-MOFs inside as well as on the outside surface on CNFs could result into the thermally stable hybrid PC-MOF@CNF materials.

We have in our laboratory already synthesised a Zn-terephthalate MOF-CNF hybrid by an in-situ [MOF@CNF] approach.[13] By rationally tailoring the experimental parameters, we expect the selective one-dimensional confinement of highly crystalline and nanosized MOFs in inner cavity and in inner cavity as well as on the outer walls of CNF. The hybrid material may show improved thermal stability as well as gas uptake over individual precursors. One dimensional continuous confinement of MOF inside the hollow CNFs can facile the movement of the charge carrier molecules like water, imidazole, triazole, etc. by following the Grotthuss hopping mechanism for proton conduction. To achieve the real time need of materials which will show the proton conduction at high as well as low temperature, the hybrid materials PC-MOF@PCNF and PC-MOF@FCNF will be the best materials to replace the thermally unstable traditional proton conduction materials like nafion.

6.3 References and Notes:

1. C. Montoro, F. Linares, E. Q. Procopio, I. Senkovska, S. Kaskel, S. Galli, N. Masciocchi, E. Barea, J. A. Navarro, *J. Am. Chem. Soc.* **2011**, *133*,11888.

2. *Mustard agents: description, physical and chemical properties, mechanism of action, symptoms, antidotes and methods of treatment.* Organization for the Prohibition of Chemical Weapons.

3. K. Zhang, R. P. Lively, M. E. Dose, A. J. Brown, C. Zhang, J. Chung, S. Nair, W. J. Koros, R. R. Chance, *Chem. Commun.,* **2013**, *49*, 3245.

4. C. Yang, U. Kaipa, Q. Z. Mather, X. Wang, V. Nesterov, A. F. Venero, M. A. Omary, *J. Am. Chem. Soc.* **2011**, *133*, 18094.

5. V. N. Vukotic, S. J. Loeb, *Chem. Soc. Rev.* **2012**, *41*, 5896.

6. A. Shaikjee, N. J. Coville, *J. Adv. Res.*, **2012**, *3*, 195.

7. T. D. Burchell, *Carbon Materials for Advanced Technologies*, Elsevier, **1999**.

8. K.-D. Kreuer, *Chem. Mater.*, **1996**, *8*, 610.

9. K.-D. Kreuer, S. J. Paddison, E. Spohr, M, Schuster, *Chem. Rev.*, **2004**, **104**, 4637.

10. M. Yoon, K. Suh, S. Natarajan, K. Kim, *Angew. Chem. Int. Ed.*, **2013**, *52*, 2688.

11. S. C. Sahoo, T. Kundu, R. Banerjee, *J. Am. Chem. Soc.*, **2011**, *133*, 17950.

12. A. N. Khlobystov, D. A. Britz, G. A. D. Briggs, *Acc. Chem. Res.* **2005**, *38*, 901.

6. P. Pachfule, B. K. Balan, S. Kurungot, R. Banerjee, *Chem. Commun.*, **2012**, *48*, 2009.

List of Publications and Patents

List of Publications

1. Pradip Pachfule, Chandan Dey, Tamas Panda and Rahul Banerjee* *"Synthesis and structural comparisons of five new fluorinated metal organic frameworks (F-MOFs)"* **CrystEngComm,** *2010*, 12, 1600–1609.

[***Among Top 10 most downloaded CrystEngComm articles for May 2010***]

2. Pradip Pachfule, Tamas Panda, Chandan Dey and Rahul Banerjee* *"Structural diversity in a series of metal–organic frameworks (MOFs) composed of divalent transition metals, 4,4'-bipyridine and a flexible carboxylic acid"* **CrystEngComm,** *2010*, 12, 2381–2389.

[Published as part of a virtual special issue on crystallography named "NEW TALENT"]

3. Pradip Pachfule, Chandan Dey, Tamas Panda, Kumar Vanka and Rahul Banerjee* *"Structural diversity in partially fluorinated metal organic frameworks (F-MOFs) composed of divalent transition metals, 1,10-phenanthroline, and fluorinated carboxylic acid"* **Cryst. Growth Des.,** *2010*, 10, 1351–1363.

[Most Accessed Articles Published by Indian Authors for 2010-Rank 4]

4. Pradip Pachfule, Raja Das, Pankaj Poddar and Rahul Banerjee* "*Structural, magnetic, and gas adsorption study of a two-dimensional tetrazole-pyrimidine based metal−organic framework"* **Cryst. Growth Des.,** *2010*, 10, 2475–2478.

[***Among Top 10 most-accessed articles published in Crystal Growth & Design during the second quarter of 2010***]

[Most Accessed Articles Published by Indian Authors for 2010-Rank 2]

5. Arijit Mallick, Subhadeep Saha, **Pradip Pachfule,** Sudip Roy and Rahul Banerjee* *"Selective CO_2 and H_2 adsorption in a chiral magnesium-based metal organic framework (Mg-MOF) with open metal sites"*

J. Mater. Chem., *2010*, 20, 9073–9080.

6. Chandan Dey, Raja Das, **Pradip Pachfule**, Pankaj Poddar, and Rahul Banerjee* *"Structural and selective gas adsorption studies of polyoxometalate and tris(ethylenediamine) cobalt(III) based ionic crystals"*

Cryst. Growth Des., *2011,* 11, 139–146.

7. Pradip Pachfule, Raja Das, Pankaj Poddar and Rahul Banerjee* "*Solvothermal synthesis, structure, and properties of metal organic framework isomers derived from a partially fluorinated link"*

Cryst. Growth Des., *2011*, 11, 1215–1222.

[Published as part of a virtual special issue on "Structural Chemistry in India: Emerging Themes"]

8. Arijit Mallick, Subhadeep Saha, **Pradip Pachfule**, Sudip Roy, and Rahul Banerjee* *"Structure and gas sorption behavior of a new three dimensional porous magnesium formate"*

Inorg. Chem. *2011*, 50, 1392–1401.

[***Among Top 10 most-accessed articles published in Inorganic Chemistry during the First quarter of 2011***]

9. Pradip Pachfule, Raja Das, Pankaj Poddar and Rahul Banerjee* "*Structural, magnetic, and gas adsorption study of a series of partially fluorinated metal-organic frameworks (HF-MOFs)"*

Inorg. Chem. *2011*, 50, 3855–3865.

10. Tamas Panda, **Pradip Pachfule**, Yifei Chen, Jianwen Jiang and Rahul Banerjee* "*Amino functionalized zeolitic tetrazolate framework (ZTF) with high capacity for storage of carbon dioxide*"

Chem. Commun., *2011*, 47, 2011–2013.

11. Tamas Panda, **Pradip Pachfule** and Rahul Banerjee* "*Template induced structural isomerism and enhancement of porosity in manganese (II) based metal–organic frameworks (Mn-MOFs)*"

Chem. Commun., *2011*, 47, 7674–7676.

12. Pradip Pachfule, Yifei Chen, Subash Chandra Sahoo, Jianwen Jiang and Rahul

Banerjee* "*Structural isomerism and effect of fluorination on gas adsorption in copper-tetrazolate based metal organic frameworks*"

Chem. Mater., *2011*, 23, 2908-2916.

13. Mandakini Biswal , Vivek Dhas , Vivek Mate , Abhik Banerjee , **Pradip Pachfule** , Kanika Aggarwal , Satishchandra B. Ogale , and Chandrashekhar V. Rode, "*Selectivity tailoring in liquid phase oxidation over MWNT-Mn_3O_4 nanocomposite catalysts"*

J. Phys. Chem. C, *2011,* 115, 15440-15448.

14. Vitthal A. Kawade, Avinash S. Kumbhar,* Andrea Erxleben, **Pradip Pachfule** and Rahul Banerjee* *"Hydrogen bond directed honeycomb-like porous network structure of tris(bipyridyl-glycoluril)cobalt(III) chloride"*

CrystEngComm, *2011,* 13, 5289-5291.

15. Pradip Pachfule and Rahul Banerjee* "*Structural and gas adsorption study of a two dimensional copper-tetrazole based metal-organic framework"*

Current Science, *2011,* 101, 894-899.

16. Pradip Pachfule, Yifei Chen, Jianwen Jiang and Rahul Banerjee* "*Experimental and computational approach of understanding the gas adsorption in amino functionalized interpenetrated metal organic frameworks (MOFs)*"

J. Mater. Chem., *2011,* 21, 17737–17745.

17. Pradip Pachfule, and Rahul Banerjee* "*Porous nitrogen rich cadmium-tetrazolate based metal organic framework (MOF) for H_2 and CO_2 uptake"*

Cryst. Growth Des., *2011*, 11, 5176–5181.

18. Pradip Pachfule, Yifei Chen, Jianwen Jiang and Rahul Banerjee* "*Fluorinated metal organic frameworks (F-MOFs): advantageous for higher H_2 and CO_2 adsorption or not?*"

Chem.–Eur. J., *2012,* 18, 688-694.

19. Raja Das, **Pradip Pachfule,** Rahul Banerjee* and Pankaj Poddar* "*Metal and Metal Oxide Nanoparticle synthesis from metal organic frameworks (MOFs): finding the border of metal and metal oxides"*

Nanoscale, *2012*, 4, 591-599.

20. Manas K. Bhunia, Swapan K. Das, **Pradip Pachfule**, Rahul Banerjee and Asim

Bhaumik* "*Nitrogen-rich porous covalent imine network (CIN) material as an efficient catalytic support for C–C coupling reactions"*

Dalton Trans, *2012*, 41, 1304-1311.

21. Sarika A. Kelkar, Parvez A. Shaikh, **Pradip Pachfule**, Satishchandra B. Ogale* "*Nanostructured Cd_2SnO_4 as an energy harvesting photoanode for solar water splitting"*

Energy Environ. Sci., *2012,* 5, 5681-5685.

22. Pradip Pachfule, Beena K. Balan, Sreekumar Kurungot* and Rahul Banerjee* *"One-dimensional confinement of nanosized metal organic framework in carbon nanofibers for improved gas adsorption"*

Chem. Commun., *2012*, 48, 2009-2012.

23. Pradip Pachfule, Bishnu P. Biswal and Rahul Banerjee* "*Control over Porosity using isoreticular zeolitic imidazolate frameworks (IRZIFs) as template for porous carbon synthesis*"

Chem. Eur. J., *2012*, 18, 11399-11408.

[Highlighted In A Hot Topic Entitled "CARBON" by Wiley-VCH]

24. Pramod Kumar Yadav, Neeraj Kumari, **Pradip Pachfule**, Rahul Banerjee and Lallan Mishra,* "*Metal [Zn(II), Cd(II)], 1,10-phenanthroline containing coordination polymers constructed on the skeleton of polycarboxylates : synthesis, characterization, micro structural and CO_2 gas adsorption studies*"

Cryst. Growth Des., *2012*, 12, 5311–5319.

25. Pradip Pachfule, Vishal M. Dhavale, Sharath Kandambeth, Sreekumar Kurungot* and Rahul Banerjee* "*Porous organic framework templated nitrogen rich porous carbon as proficient electrocatalyst than Pt/C for the electrochemical oxygen reduction activity"*

Chem. Eur. J., *2013*, 19, 974-980.

26. Biswajit Bhattacharya, Rajdip Dey, **Pradip Pachfule**, Rahul Banerjee,* and Debajyoti Ghoshal,* "*Four 3D Cd(II)-based metal organic hybrids with different N,N'-donor spacers: syntheses, characterizations, and selective gas adsorption properties*"

Cryst. Growth Des., *2013*, 13, 731–739.

27. Sumi Ganguly, **Pradip Pachfule**, Sukhen Bala, Arijit Goswami, Sudeshna Bhattacharya, Raju Mondal* "*Azide-functionalized lanthanide-based metal−organic frameworks showing selective CO_2 gas adsorption and postsynthetic cavity expansion*"
Inorg. Chem. *2013*, 52, 3588−3590.

28. Harshitha Barike Aiyappa, **Pradip Pachfule**, Rahul Banerjee,* and Sreekumar Kurungot* "*Porous carbons from nonporous MOFs: influence of ligand characteristics on intrinsic properties of end carbon*"
Cryst. Growth Des., *2013, 13*, 4195–4199.

29. Anup Bhunia, Tony Roy, **Pradip Pachfule**, Pattuparambil R. Rajamohanan and Akkattu T. Biju,* "*Transition-metal-free multicomponent reactions involving arynes, N-heterocycles, and isatins*"

Angew. Chem. Int. Ed. *2013*, 52, 10040-10043.

30. Arijit Goswami, Sukhen Bala, **Pradip Pachfule,** Raju Mondal,* "*Comprehensive study on mutual interplay of multiple V-shaped ligands on the helical nature of a series of coordination polymers and their properties*"

Cryst. Growth Des., *2013*, 13, 5487–5498.

31. Rajdip Dey, Biswajit Bhattacharya, **Pradip Pachfule**, Rahul Banerjee,* Debajyoti Ghoshal,* "*Flexible dicarboxylate based pillar-layer metal organic frameworks: differences in structure and porosity by tuning the pyridyl based N,N' linkers*"

CrystEngComm, *2014*, 16, 2305-2316.

32. Pradip Pachfule, Sharath Kandambeth, David Díaz Díaz, Rahul Banerjee,* "*Highly stable covalent organic framework-Au nanoparticles hybrids for enhanced activity for nitrophenol reduction*"

Chem. Commun., *2014*, 50, 3169-3172.

33. Pradip Pachfule, Manas K. Panda, Sharath Kandambeth, S. M. Shivaprasad, David Díaz Díaz, and Rahul Banerjee,* *"Multifunctional and robust covalent organic framework-nanoparticles hybrids"*
J. Mater. Chem. A, *2014*, 2, 7944-7952.

34. Udai P. Singh,* Shikha Narang, **Pradip Pachfule** and Rahul Banerjee,* "*Variation of CO_2 adsorption in isostructural Cd(ii)/Co(ii) based MOFs by anion modulation"*

CrystEngComm, *2014*, 16, 5012-5020.

34. Biswajit Bhattacharya, Dilip Kumar Maity, **Pradip Pachfule**, Enrique Colacioc and Debajyoti Ghoshal,***** "*Syntheses, X-ray structures, catalytic activity and magnetic properties of two new coordination polymers of Co(II) and Ni(II) based on benzenedicarboxylate and linear N,N'-donor Schiff base linkers"*
Inorg. Chem. Front.*, 2014*, 1, 414-425.

List of Patents

Pradip Pachfule, Beena K. Balan, Sreekumar Kurungot and Rahul Banerjee**;** **"**Confinement of nanosized metal organic framework in nano carbon morphologies"
US Provisional Patent, US2013/0157837.

List of Conferences and Symposia Attended

1. Poster entitled "**Porous Metal Organic Frameworks for Hydrogen Storage and Carbon dioxide Sequestration**" was represented in the symposium ***CRSI Zonal Meeting, 2011***, arranged at National chemical Laboratory; Pune.

2. Poster entitled **"Structural, Magnetic and Gas Adsorption Study of A Series of Partially Fluorinated Metal-Organic Frameworks (F-MOFs): Effect of Fluorine Insertion on H_2 Uptake"** was represented in ***The International Conference on the Chemistry of Organic Solid (ICCOSS XX), 2011,*** arranged at IISC, Bangalore.

3. Poster entitled **"Effect of Fluorination on Gas Adsorption of Partially Fluorinated Metal-Organic Frameworks (F-MOFs)"** was represented in ***The International Conference Modern Trends in Inorganic Chemistry-XIV (MTIC-XIV)***, 2011, arranged at School of Chemistry, University of Hyderabad, Hyderabad.

4. Poster entitled **"Effect of Fluorination on Gas Adsorption of Partially Fluorinated Metal-Organic Frameworks (F-MOFs)"** was represented at ***CSIR-NCL, Pune*** on National Science Day, 2012.

Erratum